Chemical Vapour Deposition

of Tin Oxide Thin Films

Proefschrift

ter verkrijging van de graad van doctor
aan de Technische Universiteit Eindhoven,
op gezag van de Rector Magnificus, prof.dr. R.A. van Santen,
voor een commissie aangewezen door het College
voor Promoties in het openbaar te verdedigen op
dinsdag 18 november 2003 om 16.00 uur

door

Antonius Maria Bernardus van Mol

geboren te Eindhoven

Dit proefschrift is goedgekeurd door de promotoren:

prof.dr.ir. J.C. Schouten
en
prof.dr. M.L. Hitchman

Copromotor:
dr. M.H.J.M. de Croon

Aan mijn ouders

Aan Elle

Contents

Samenvatting

Eigenschappen van materialen en producten kunnen over het algemeen verbeterd worden door het aanbrengen van een coating. Eén van de meest voorkomende coatingmaterialen zijn transparant geleidende oxides, in het Engels afgekort naar TCO. De naam zelf geeft al weer welke eigenschappen deze coatings hebben: ze zijn transparant voor visueel licht en zijn elektrisch geleidend. Andere gunstige eigenschappen van deze lagen zijn, dat ze infrarood licht reflecteren en dat ze moeilijk beschadigbaar zijn door chemisch of mechanische behandeling.
Door deze combinatie van eigenschappen worden TCO's in een groot aantal producten verwerkt, zoals in zonnecellen en isolatie glas (HR++ glas).

Dit proefschrift behandelt één van de meest gebruikte TCO's, namelijk tinoxide. Dunne lagen van tinoxide worden voornamelijk geproduceerd via chemische dampafzetting (Engelse afkorting: CVD). Dit betekent dat verschillende chemische stoffen (precursoren) in gasvorm een reactor worden binnengebracht, waar ze onder invloed van de temperatuur van een verwarmd substraat met elkaar reageren, zodat er een coating op het substraat gevormd wordt. Deze technologie heeft als voordeel dat het toegepast kan worden in een continu proces waar met hoge snelheid, uniforme en homogene dunne lagen op grote oppervlakken afgezet moeten worden. Mogelijke precursoren voor het afzetten van tinoxide zijn $SnCl_4$, $Sn(CH_3)_4$, $(CH_3)_2SnCl_2$, $Sn(C_4H_9)_2(CH_3COO)_2$ en $(C_4H_9)SnCl_3$. Via reactie met zuurstof en/of water vormen deze stoffen een tinoxide-laag. Door gebruik te maken van geschikte dotering precursoren, kunnen deze lagen gedoteerd worden met fluor of antimoon om zo de elektrische geleiding te verbeteren.

Tinoxide CVD heeft echter ook enkele nadelen, zoals een lage conversie van de precursoren en een lage procesopbrengst. Om deze zaken te verbeteren is het noodzakelijk een beter inzicht te verkrijgen in de ingewikkelde interactie tussen gasfase hydrodynamica, gasfase reacties en de oppervlakte reacties, die uiteindelijk voor de vorming van de tinoxide-laag zorgen.

Dit proefschrift behandelt de studie naar de intrinsieke kinetiek van dimethyltindichloride (DMTC), zuurstof en water uitgevoerd in een daarvoor speciaal ontworpen geroerde reactor (CSTR). De resultaten van deze studie zijn geïmplementeerd in een computational fluid dynamics (CFD) model voor de beschrijving van verschillende typen CVD-reactoren.

Dit onderzoek is uitgevoerd bij TNO TPD in Eindhoven en is onderdeel van een Europees Brite-Euram R&D-project. In dit project werkten tien Europese bedrijven en instituten samen met als doel om beheersing van CVD-processen in het algemeen te verbeteren door toepassing van "in-situ monitoring" technieken.

De kinetiek van het DMTC-O_2 mechanisme wordt bepaald in een CSTR, waaraan FTIR en massaspectrometers gekoppeld zijn. De reactor is zodanig ontworpen dat de stroming binnenin volledig turbulent is, zodat de mengsnelheden tussen de verschillende deeltjes veel groter zijn dan de reactiesnelheden.

De tin-precursoren worden naar de reactor gevoerd via "bubbler"-systemen. Om de hoeveelheid tin-precursor naar de reactor te kunnen kwantificeren, zijn de dampspanningen van een aantal tin-precursoren bepaald bij verschillende temperaturen. Voor dit doel is een nieuwe experimentele opstelling gebruikt om de dampspanning bij constante temperatuur te meten. Deze opstelling maakt het mogelijk om corrigeren voor verscheidene storingseffecten zoals: verdamping van ontledingsproducten, ontgassen van de wanden en kleine lekken. De tin-precursoren, die doorgemeten zijn, zijn: $SnCl_4$, CH_3SnCl_3, $(CH_3)_2SnCl_2$, $(CH_3)_3SnCl$, $Sn(CH_3)_4$ en $(C_4H_9)SnCl_3$. Voor CH_3SnCl_3, $(CH_3)_2SnCl_2$, $(CH_3)_3SnCl$, en $(C_4H_9)SnCl_3$ zijn tot nu toe geen dampspanningen gepubliceerd.

Via bepaling van de samenstelling van de gasfase in de CSTR onder verschillende condities, zoals precursorconcentraties en temperatuur, is een mechanisme voorgesteld voor DMTC + O_2. De snelheidsbepalende stap vindt plaats in de gasfase via verbreking van de Sn-C binding. De radicalen die hieruit gevormd worden, CH_3 en OH, reageren direct weer met DMTC, zodat de conversie van DMTC versneld wordt. De gevormde tin-intermediair, $SnCl_2$, reageert op het oppervlak met geadsorbeerd –O of –OH tot SnO_2. Toevoeging van water aan het precursormengsel verhoogt de depositiesnelheid enorm. Door de aanwezigheid van water wordt het totale mechanisme complex doordat water verscheidene complexen kan vormen met tin deeltjes, zoals $SnCl_2$.

Een stagnerende punt reactor (SPFR) is gebruikt om de depositiesnelheden en laageigenschappen van tinoxide coatings te vergelijken, die gemaakt zijn uit vijf verschillende tin precursoren. De deposities zijn uitgevoerd op zowel glas als aluminiumsubstraten en gebruik makend van de precursoren monobutyl-tintrichloride (MMTC), dimethyltinchloride (DMTC), monomethyltintrichloride (MBTC), tintetrachloride (TTC) en tetramethyltin (TMT). Zuurstof is bij iedere precursor gebruikt als oxidant. De waargenomen activeringsenergieën zijn berekend met behulp van de Arrheniusvergelijking. Hierbij is opvallend dat deze activeringsenergieën verschillend zijn voor glas en aluminium als substraat. De hoogste depositiesnelheid voor temperaturen beneden 650°C op zowel glas als aluminium is behaald met monobutyltintrichloride. De optimale weerstand van 1.2×10^{-3} Ohm.cm is behaald met monomethyltintrichloride voor een 550 nm dikke laag gedeponeerd bij 675°C.

De resultaten van de kinetische studie in de CSTR zijn gebruikt om een eenvoudig mechanisme samen te stellen voor DMTC en O_2. Het bestaat uit twee reactiestappen, waarbij de eerste de snelheidsbepalende stap in de gasfase weergeeft en de tweede stap de zeer snelle vorming van tinoxide op het oppervlak weergeeft. Dit mechanisme is gebruikt om de depositie van tinoxide in twee

verschillende reactoren te simuleren met behulp van het CFD software pakket Fluent®. De eerste reactor is de al besproken SPFR, de tweede is een koude wand laminaire stroming reactor, welke in het Brite-Euram project gebruikt is door een andere partner om tinoxide te deponeren. De depositiesnelheden die berekend zijn met de simulaties zijn in uitstekende overeenstemming met de experimenteel bepaalde waarden.

De depositiesnelheden in de laminaire-stroming-reactor zijn ook bestudeerd door gebruik te maken van benaderde analytische oplossingen van de hydrodynamische vergelijkingen, die de stroming in de reactor beschrijven. Hierbij zijn drie cases onderzocht:
(1)   diffusie gelimiteerde groei
(2)   oppervlaktereactie gelimiteerde groei
(3)   gasfase reactie gelimiteerde groei

Zoals verwacht wordt de groeisnelheid in het geval van cases (1) en (2) lager over de lengte van de reactor. Voor een gasfase gelimiteerd proces, case (3), bereikt de groeisnelheid zijn maximum pas aan het einde van de reactor. De resultaten van de Fluent® simulatie (en de experimentele trend) vallen precies tussen de analytische oplossingen in voor een vergelijkbare isotherme reactor met, respectievelijk, een temperatuur van de topplaat en het substraat.

Dit proefschrift geeft inzicht in het zeer gecompliceerde mechanisme van tinoxide depositie. De eenvoudige kinetiek, die bepaald is uit de CSTR experimenten, kan gebruikt worden om de depositiesnelheid in verschillende tinoxide reactoren te simuleren om zo tot een beter ontwerp te komen.

Summary

Tin oxide thin films have some very beneficial properties, such as transparency for visible light, reflectivity for infrared light, and a low electrical sheet resistance, making them suitable for a wide variety of applications as low-E coatings on glass, gas sensors, and electrodes in solar cells. One of the major production techniques is chemical vapour deposition (CVD). It has the advantage to be used in a continuous process for depositing uniform, homogeneous coatings on large surface areas at high deposition rates. Possible precursors are $SnCl_4$, $Sn(CH_3)_4$, $(CH_3)_2SnCl_2$, $Sn(C_4H_9)_2(CH_3COO)_2$, and $(C_4H_9)SnCl_3$. By oxidation with O_2 or hydrolysis with H_2O, these precursors form a SnO_2 layer. Using suitable dopant-precursors the films can be doped with fluorine or antimony to enhance electrical conductivity.

Disadvantages of tin oxide CVD are low conversion of raw material and low process yield. In order to overcome these problems more insight is necessary in the complicated interaction between gas phase reaction, surface reactions, and the hydrodynamics of the reactor system, which controls the deposition process.

This thesis presents the results of a study of the intrinsic reaction kinetics of the dimethyltin dichloride (DMTC) - O_2 - H_2O system in a specially designed continuously stirred tank reactor (CSTR), and implementation of the kinetics in a computational fluid dynamics (CFD) model of different types of CVD reactors.
This research was carried out at TNO TPD (Eindhoven, The Netherlands) as a part of a large Brite-Euram R&D-project. In this project 10 European companies and institutes participated with the objective to improve CVD process control by in-situ monitoring tools.

The chemical kinetics of the reaction between DMTC and O_2 are determined in a CSTR reactor equipped with an FTIR spectrometer, a mass spectrometer, and an in-situ mass balance. The reactor is designed in such a way that the flow inside is completely turbulent and the mixing rate between species is much higher than the reaction rate.
The precursors are fed to the reactor by a bubbler system. In order to quantify the flow of tin precursor to the reactor, the vapour pressures of a number of tin precursors were determined at various temperatures. For this purpose, a new experimental set-up was used for measuring vapour pressure at constant temperature. With this set-up, disrupting effects due to evaporation of volatile decomposition products, degassing of gas particles from walls, and small leaks can be readily detected and compensated for. The precursors studied were $SnCl_4$, CH_3SnCl_3, $(CH_3)_2SnCl_2$, $(CH_3)_3SnCl$, $Sn(CH_3)_4$, $(C_4H_9)SnCl_3$. For CH_3SnCl_3,

$(CH_3)_2SnCl_2$, $(CH_3)_3SnCl$, and $(C_4H_9)SnCl_3$, no vapour pressure data have been previously reported.

By measuring the composition of the gas phase under various conditions such as different precursor concentrations and reactor temperatures, a mechanism for the intrinsic reaction kinetics is proposed. In the reaction between DMTC and O_2 the rate-limiting step takes place in the gas phase through the cleavage of the Sn-C bond. The radicals formed in subsequent reactions, i.e. CH_3 and OH, react directly with DMTC, thereby accelarating the conversion rate. The resulting intermediate from the gas phase reactions, $SnCl_2$, reacts on the surface with absorbed -O or -OH to form SnO_2. Addition of water to the precursor mixture greatly increases the deposition rate. In the presence of water, the reaction mechanism becomes much more complicated because water can form various complexes with $SnCl_2$.

A stagnant point flow reactor was used to compare the deposition kinetics and film properties of tin oxide films grown from five different tin precursors at atmospheric pressure. Deposition was performed on glass and aluminum substrates using the precursors monobutyltin chloride (MMTC), dimethyltin chloride (DMTC), monomethyltin trichloride (MBTC), tin tetrachloride (TTC), and tetramethyltin (TMT) with oxygen as an oxidant. Apparent activation energies were calculated for each precursor using the Arrhenius equation, giving different activation energies for both substrates. The highest deposition rates on both glass and aluminum substrates at temperatures below 650° C were achieved using monobutyltin trichloride. Optimum film resistivity of 1.2×10^{-3} ohm.cm was found for a tin oxide layer of 550 nm grown at 675 °C from monomethyltin trichloride.

The results from the kinetics study in the CSTR were used to construct a lumped mechanism for the reaction between DMTC and O_2, consisting of two reaction steps, where the first step represents the rate-limiting step in the gas phase, and the second step is the very fast formation of tin oxide on the surface. This mechanism is used to simulate the deposition of tin oxide in two different reactors with the aid of the CFD-package Fluent®. The first reactor is the stagnant point flow reactor mentioned earlier. The second reactor is a cold wall laminar flow reactor, which has been used by a partner in the project to deposit tin oxide. The deposition rates obtained by modelling are in very good agreement with the experimentally determined deposition rates, thereby enhancing the validity of the chemical mechanism proposed.

The growth behaviour was also studied in the laminar flow reactor using approximate analytical solutions by comparing (1) diffusion limited growth, (2) surface reaction rate limited growth, and (3) gas phase reaction limited growth. As expected for case (1) and (2) the growth decreases over the length of the reactor. For a gas phase reaction limited process the growth rate reaches its maximum at the end of the reactor. The Fluent simulation (and experimental trend) falls exactly between analytical solutions for a similar isothermal reactor with, respectively, the average top plate and average substrate temperature.

This thesis gives insight in the complicated mechanism of tin oxide deposition. The lumped mechanism given here can be used to simulate and optimise future reactor or injector designs for tin oxide thin film depositions.

Chapter 1. Introduction

The past decades, thin solid films have found their use in a multitude of applications because of the more stringent specifications of modern materials and the evolution of multilayer devices such as integrated circuits. Through the use of a coating on a bulk material, composite materials can be produced which exhibit a combination of various and sometimes conflicting properties. A typical example is the use of a low-E coating on architectural glass to add the property of reflectivity to infrared radiation to the property of transparency to visible light. Another use of thin layers is the fabrication of hi-tech devices such as integrated circuits or photovoltaic cells, which consists of several thin layers of different materials stacked in a specific manner. All these applications require deposition processes, which are able to produce layers with reproducible and precisely defined properties. The most common techniques are sputtering, evaporation, spray pyrolysis, and chemical vapour deposition.

The topic of this thesis is the chemical vapour deposition of tin oxide, which is a semiconducting transparent material, used in various applications, such as solar cells and low-E glass. The primary objective is to gain more fundamental knowledge about the process itself in terms of chemistry and kinetics. This knowledge is used to simulate the process in a real reactor system with the help of computational fluid dynamic methods. These simulations should give more insight in the operation of a commercial process, and can therefore aid in the optimisation of such processes, and in the development of in-situ monitoring control tools for them. Some of the major applications of tin oxide layers are discussed in the next section. Sections 1.2 and 1.3 will provide some background in chemical vapour deposition and the equipment used in such a process. The last section will go into more detail in the objectives of this thesis and the methods of approach to achieve the goals set.

1.1 Tin oxide coatings

Tin oxide films have, besides a high transparency and a low electrical resistivity, various other beneficial properties, such as high reflectivity for infrared light, high mechanical hardness, and good environmental stability. This results in a variety of applications for tin oxide films, e.g.:

➢ Heating elements in aircraft windows [1, 2].
   A thin tin oxide coating is applied on the window. By applying a potential over the tin oxide coating, it becomes heated and any ice or fog on the window will evaporate. Antistatic coatings on instrument panels [3, 4].
➢ Transparent electrodes in electroluminescent lamps and displays [5 - 7]

- ➢ Gas sensors [8 - 11].

  If a tin oxide surface is exposed to air, oxygen absorbs onto it as O^{2-} or O^-. When reducing gases, such as H_2, CO, CH_4, or C_2H_5OH, are introduced, the absorbed oxygen species are removed through the oxidation of such reducing gases and the captured electrons are restored to the conduction band. This results in a decrease of the resistance of the material, which can be recorded easily.

- ➢ Solar cells [12 - 18].

  Because of its transparent and conductive properties, fluorine doped tin oxide layers are often used as top electrode in e.g. amorphous silicon solar cells.

- ➢ Protective and wear-resistant coating on glass containers [19].

  Most of the glass bottles produced nowadays are coated with a 10-100 nm thin layer of tin oxide. The bottles have equal or higher strength as non-coated bottles but can weigh till 20% less, and can be recycled more often.

- ➢ Infrared reflectors for glass windows [20 - 27].

  The insulating properties of a glass window can be improved by applying a fluorine doped tin oxide coating. The coating reflects infrared radiation emitted by objects in a room (around 10 μm), almost doubling the insulating property of the window.

Tin oxide, SnO_2, has a tetragonal rutile structure. Its unit cell contains two tin and four oxygen atoms as is shown in figure 1.1. The tin atom is at the centre of six oxygen atoms placed at the corners of a regular octahedron. Every oxygen atom is surrounded by three tin atoms at the corners of an equilateral triangle. If tin oxide was completely stoichiometric, it would be an insulator. However, in practice, deposited tin oxide layers contain a reasonable number of oxygen vacancies, making electrons available for conduction. In applications such as low-E coatings and solar cells, the tin oxide layers are chemically doped, for example, by fluorine or antimony, to further enhance the conductivity.
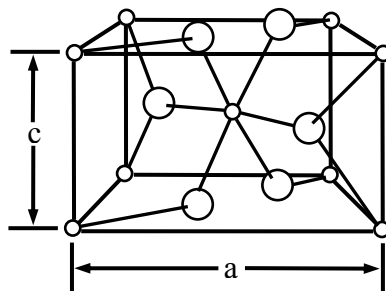
Figure 1.1: *Unit cell of the crystal structure of SnO_2. Large circles are oxygen atoms and the smaller ones are tin atoms (a = b = 4.737 Å, c = 3.185 Å) [28].*

1.2 Chemical Vapour Deposition

The most common technique for depositing tin oxide coatings, especially on glass, is chemical vapour deposition (CVD). It has the advantage that it can be used in a continuous process for depositing uniform, homogeneous coatings on large areas at

large deposition rates. It is also a common technique in the fabrication of IC's. With CVD, chemically reacting gases are used to deposit a thin solid film an a substrate. The energy required to drive the reaction is most often supplied by heat transfer, although, alternatively, photons from a light source or from a laser (PCVD) as well as energetic electrons in plasmas (PECVD) are also used. Figure 1.2 shows the basic steps that can occur during the CVD process:

1. Mass transport of the gaseous reactants from the reactor inlet to the deposition zone.
2. Chemical reactions in the gas phase leading to new reactive species and by-products.
3. Mass transport of the initial reactants and reaction products to the substrate surface.
4. Adsorption of these species to the substrate surface.
5. Surface diffusion of adsorbed species over the surface to the growth centre.
6. Surface reactions at the growth centre.
7. Desorption of by-products.
8. Diffusive mass transport of the by-products away from the surface.
9. Mass transport of the by-products to the outlet of the reactor.
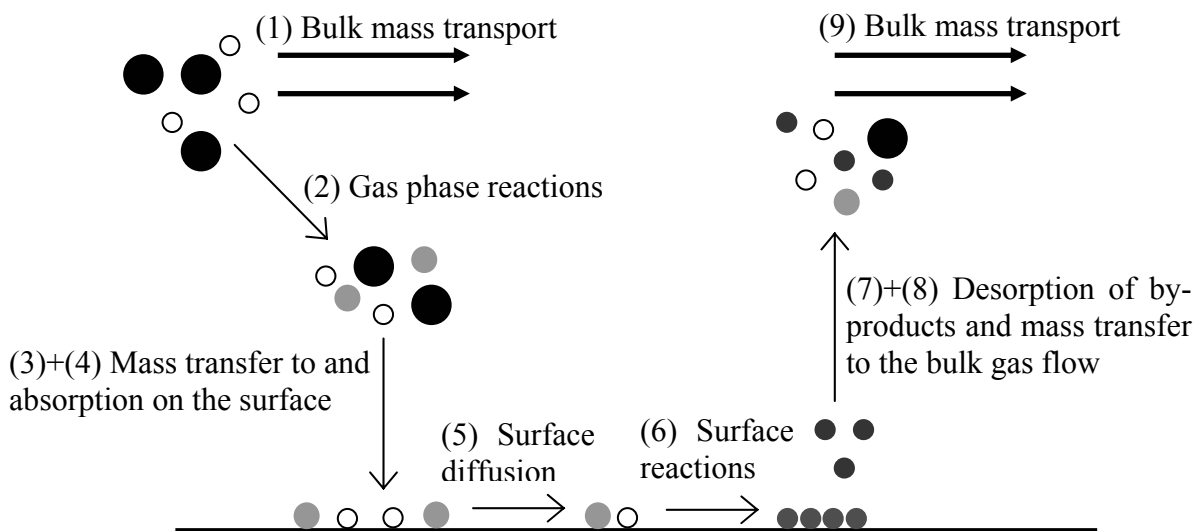
Figure 1.2: Schematic representation of the basic steps in a Chemical Vapour Deposition process.

1.3 CVD Equipment

The essential functions of CVD equipment are to create an appropriate vapour or gas mixture, and to make it flow over the substrate at an appropriate temperature. In most applications for coating large areas, CVD processes are carried out at normal atmospheric pressure. In some specialised applications, particularly in the

semiconductor industry, CVD is carried out at lower pressures. If the reactants are gases, then an appropriate gas mixture can be formed using standard mass flow controllers. If the reactant is a liquid or a solid, it must first be vaporised. Often the vaporisation is done in a bubbler, by passing a carrier gas through the precursor, which is heated if necessary to increase its vapour pressure. Alternatively, the liquid is supplied by a liquiflow controller, and subsequently, instantly evaporated.

In most products, a coating with uniform thickness is desired. If CVD is carried out in a laminar flow reactor on a stationary substrate at atmospheric pressure, the thickness of the coating varies with position along the substrate. In order to produce a uniformly thick coating over a flat substrate, the substrate is usually moved in the same direction as the gas flow, so each part of the substrate is exposed to the entire profile of non-uniform coating rates. If the gas is distributed uniformly across the substrate width (in the direction perpendicular to the motion of the gas and the glass), a 2D-uniformly thick coating will result. In order to achieve this result, not only must the reactant gas mixture be injected at a uniform flow rate across the width of the substrate, but also the depleted gas must be uniformly removed by an exhaust slot or slots going across the width of the substrate. Especially large glass manufacturers have designed a variety of on-line coating equipment for making uniform coatings on their glass during the float glass production, of which an example is depicted in figure 1.3.
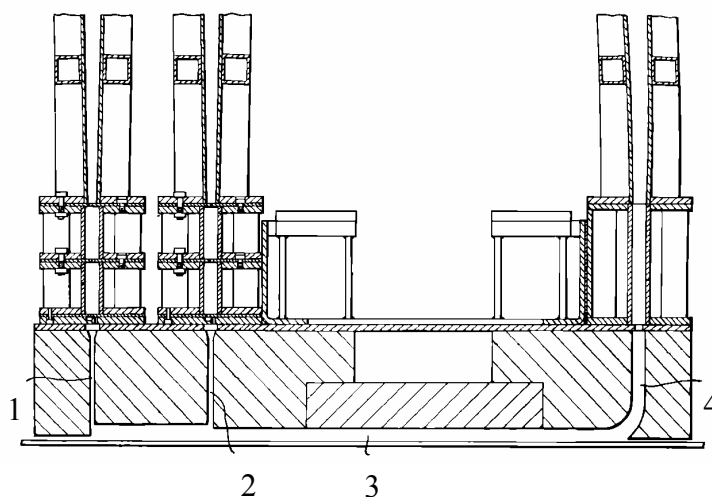
Figure 1.3: Schematic cross-section of an on-line CVD coater with uni-directional gas flow from two different gas inlet slots 1 and 2, along the gas flow path 3 to the exhaust slot 4 [29].

A typical reactor used for deposition of coatings on glass bottles is depicted in figure 1.4. This is an example of the Certincoat® system developed by Elf-Atofina for deposition of tin oxide on glass bottles [30].

In the semiconductor industry and also in a research laboratory, where the substrate size is much smaller compared to the applications mentioned previously, often use is made of a batch type reactor such as the stagnant point flow reactor as depicted in figure 1.5. The inlet flow is directed at a right angle to the substrate. Above the substrate a boundary layer is formed. By rotation of the substrate table and choosing the right set of process conditions very uniform layers can be obtained.
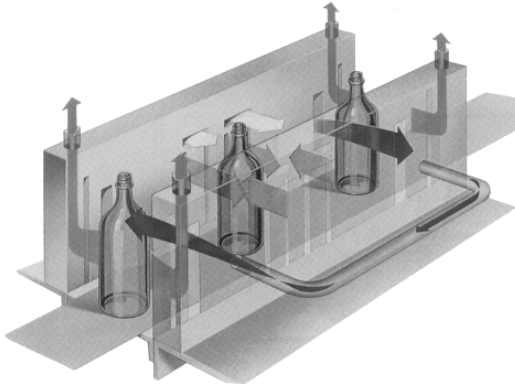
Figure 1.4: *Schematic representation of the Certincoat® process developed by Elf-Atofina for coating glass bottles [30].*
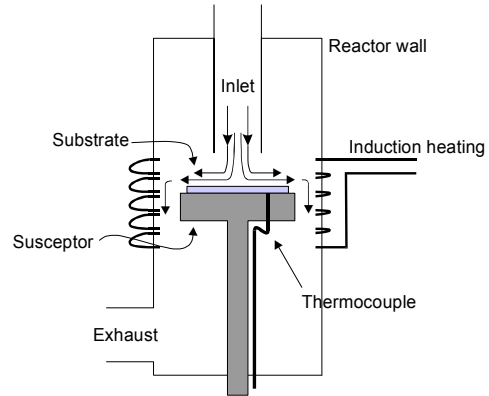
Figure 1.5: *A schematic of a stagnant point flow reactor.*

1.4 Scope of this thesis

As is clear from the scheme shown in paragraph 1.2 and the reactor geometries shown in paragraph 1.3, the CVD process is a complicated process, involving gas phase reactions, surface reactions, and the hydrodynamics of the reactor system. The design of CVD processes in industry is therefore often not based on a scientific approach, but more on empiricism and experience. However, as a result these processes may have some disadvantages as a low process yield, and high product fall out. The lack of more fundamental understanding of the coating process was identified as one of the major problems in this industry by a workshop held in January 2000 and attended by 42 experts from the glass and coating industries, universities, and national laboratories [31,32]. The need for substantial improvement of the coating manufacturing process was illustrated by some typical examples:

➢ In the deposition of coatings, such as tin oxide on flat glass, a best case yield of around 70% is achieved using CVD, but can be as low as 50%. If the coating was not applied, the yield is typically 75-80%. This means that an extra large portion of the glass is rejected, ground, and remelted. Such high reject rates represent an enormous cost in energy. On average, roughly $4 \cdot 10^{10}$ kJ/year per float line, must be expended to remelt this glass.
➢ The efficiency of reactant utilisation in CVD on float glass can be as low as 10%, necessitating the installation of multi-million dollar chemical scrubbing units or incinerators and requiring landfill of more than one million kg/year of waste.

In order to overcome these problems, knowledge about the reaction chemistry, and its interaction with the reactor hydrodynamics is necessary. With this knowledge, commercial deposition processes can be simulated on computers, thereby giving

more insight in the real world process. These simulations can aid in the development of more efficient reactor systems, or in the use of in-situ monitoring tools to control the process.

This thesis describes the chemistry of tin oxide deposition from one of the most industrially used tin-precursor, dimethyltin dichloride. It uses the obtained deposition mechanism to simulate various labscale reactors with computational fluid dynamic methods. This research was carried out at TNO TPD (Eindhoven, The Netherlands) as a part of a large Brite-Euram R&D-project. In this project 10 European companies and institutes, among which Pilkington, a large manufacturer of low-E glass, participated with the objective to improve CVD process control by in-situ monitoring tools. The tasks of TNO-TPD in this project are two-fold:

a) Development of a reaction mechanism for the deposition of tin oxide on glass from dimethyltin dichloride, oxygen, and water.
b) Implementation of this reaction mechanism in a computational model of a labscale tin oxide reactor, which mimics the characteristics of the commercial plant.

The work done in the frame of the TNO TPD tasks in this project constitutes the basis for this PhD thesis.

Chapter 2 gives a literature review of tin oxide CVD with an emphasis on the chemistry of the process and the influence of process parameters on the properties of the resulting layer. Chapter 3 describes the experimental set-up that is used to measure the intrinsic reaction kinetics of the tin oxide CVD process. In chapter 4 the vapour pressure measurements of the tin precursors that were investigated are described. These measurements were necessary to deduce the actual concentration of the tin precursor that enters the reactor. In chapter 5 the results of the quantitative mechanistic study of tin oxide deposition from dimethyltin dichloride (DMTC), oxygen, and water are given. In chapter 6 the deposition characteristics of five different precursors, i.e. tin tetrachloride (TTC), monobutyltin trichloride (MBTC), methyltin trichloride (MMTC), dimethyltin dichloride (DMTC), and tetramethyltin (TMT), are compared. Chapters 7 discusses the computational models, including the chemistry, of two different reactors, i.e. a stagnant point flow reactor, and a laminar flow reactor. For validation of these models, the results of the numerical simulations will be compared with results from real-life experiments. The stagnant point flow reactor is a typical lab-scale reactor. It is used to compare the differences in growth rate and sheet resistance of tin oxide layers grown from five different precursors as described in chapter 6. The growth rate of tin oxide obtained from dimethyltin dichloride and oxygen is compared with the simulation results. The laminar flow reactor is also a lab-scale reactor and is designed to mimic the performance of a commercial reactor of Pilkington for low-E glass production. In this reactor the growth rate profile of a tin oxide layer grown from dimethyltin dichloride and oxygen and/or water on a glass substrate is measured and compared with simulated growth rates. Also the methane concentration in this reactor is mapped in two dimensions using a laser diode. This concentration profile will again be used to validate the modelling results. The thesis will end with the

conclusions of the presented work and some recommendations for improving reactor performance.

References

1. Clough, T. J. , Grosvenor, V. L., Pinsky, N. *US Patent 5317132* **1994**.
2. Mukherjee, A. *US Patent 4959257* **1990**.
3. Tong, H., Hu, C., Hsu, M. *US Patent 5652477* **1997**.
4. Cahill, J. W. *US Patent 5284705* **1994**.
5. Houng, K. H. *Bull. Inst. Chem., Acad. Sin.* **1982**, *29*, 19.
6. Gazdag, R., Seyfried, E., Ligeti, Z. Adv. *Liq. Cryst. Res. Appl., Proc. Liq. Cryst. Conf. Soc. Countries, 3rd* **1981**, *Vol. 2*, 1137.
7. Kane, J. , Ling, M. *US Patent 4728581* **1988**.
8. Berger, F., Beche, E., Berjoan, R., Klein, D., Chambaudet, A. *Appl. Surf. Sci.* **1996**, *93*, 9.
9. Kim, K. H., Park, C. G. *J. Electrochem. Soc.* **1991**, *138(8)*, 2408.
10. Dimeo, F., Jr., Semancik, S., Cavicchi, R. E., Suehle, J. S., Chaparala, P., Tea, N. H. *Mater. Res. Soc. Symp. Proc.* **1996**, *415*, 231.
11. Brown, J.R., Cheney, M.T., Haycock, P.W., Houlton, D.J., Jones, A.C., Williams, E.W. *J. Electrochem. Soc.* **1997**, *144(1)*, 295.
12. Gordon, R. G., Proscia, J., Ellis Jr., F. B., Delahoy, A. E. *Sol. Energy Mater.* **1989**, *18*, 263.
13. Plättner R., Stetter W., Köhler P. *Siemens Forsch.- u. Entwick.-Ber.* **1988**, *17(3)*, 138.
14. Boiko, B.T., Kopach, G.I., Klochko, N.P., Kopach, V.R., Khripunov, G.S., Chernikov, A.I. *Applied Solar Energy* **1990**, *26(5)*, 40.
15. Greenwald, A., Bragagnolo, J., Leonard, M. *Conf. Rec. IEEE Photovoltaic Spec. Conf.* **1987**, *19th*, 621.
16. Saxena, A. K., Singh, S. P., Agnihotri, O. P. *Sol. Cells* **1986**, *19(2)*, 163.
17. Sato, K., Gotoh, Y., Hayashi, Y., Adachi, K., Nishimura, H. *Reports Res. Lab. Asahi Glass Co., Ltd.* **1990**, *40 (2)*, 233.
18. Singh, K., Tamakloe, R. Y. *Sol. Energy* **1996**, *56(4)*, 343.
19. Nakagawa, M., Amano, T., Yokokura, S., *J. Non-Cryst. Solids* **1997**, *218*, 100.
20. Lindner, G.H. *US Patent 4737388* **1988**.
21. Gerhardinger, P.F., McCurdy, R.J., *Mat. Res. Soc. Symp. Proc.* **1996**, *426*, 399.
22. Neumann, G.A., Stewart-Davis, R.L. *US Patent 5395698* **1995**.
23. Soubeyrand, M. J., Halliwell, A.C. *US Patent 5698262* **1997**.
24. Athey, P. R., Dauson, D. S., Lecocq, D.E., Neuman, G. A., Sopko, J. F., Stewart-Davie, R. L. *US Patent 5464657* **1995**.
25. Goodman, R. D., Greenberg, W. M., Tausch, P. J., *US Patent 4847157* **1989**.
26. Henery, V. A. *US Patent 4853257* **1989**.
27. Middleton, D. J., Grenier, J. I. *US Patent 4548836* **1985**.
28. Hartnagel, H.L., Dawar, A.L., Jain, A.K., Jagadish, C. *Semiconducting Transparent Thin Films*, IOP Publishing Ltd (Bristol), **1995**.

29. Gordon, R. J. *Non-crystalline solids* **1997**, *218*, 81.
30. Folder Elf-Atofina, *Certincoat*, **1999**.
31. Allendorf, M. *Proc. 3rd Int. Conf. Coatings on Glass***, 2000**, 3.
32. Allendorf, M. *Coatings on Glass, Technology Roadmap Workshop*, **2000**, Sandia National Laboratories, Livermore, USA.

Chapter 2. A Literature Review on the Chemical Vapour Deposition of Tin Oxide

Abstract

Tin oxide thin films have various beneficial properties, which make them very suitable for applications such as low-E coatings on glass, gas sensors, and electrodes in solar cells. These films can be prepared by chemical vapour deposition (CVD). The CVD process has the advantage that it can be used in a continuous process for depositing uniform, homogenous coatings on large surface areas at high deposition rates. Possible precursors are $SnCl_4$, $Sn(CH_3)_4$, $(CH_3)_2SnCl_2$, $Sn(C_4H_9)_2(CH_3COO)_2$, and $(C_4H_9)SnCl_3$. By oxidation with O_2 or hydrolysis with H_2O, these precursors form a SnO_2 layer. Using suitable dopant-precursors the films can be doped with fluorine or antimony to enhance electrical conductivity.

The specific properties of the film are determined by a complicated interplay between gas phase reactions, surface reactions, and the fluid dynamics of the CVD reactor. This chapter reviews the relationship between the process parameters, the hydrodynamics of the system, and the properties of the layer as published in literature. Dependent on the application, tin oxide thin films with the required set of properties can be produced by using the appropriate set of deposition conditions.

2.1 Introduction

Early work until 1976, covering tin oxide in general, has been reviewed by Jarzebski and Marton [1-3]. Other authors [4, 5] have given reviews covering tin oxide as a transparent conducting oxide (TCO). This review aims to provide an up-to-date picture on particularly CVD of tin oxide with a focus on the influence of the deposition parameters on the properties of the layer. Dependent on the application, a typical set of properties is required. For example, a low-E coating needs a high infrared reflectivity and a high in-line optical transmission. However, in a solar cell the diffusive transmission needs to be high.

Section 2.2 discusses the chemical kinetics occurring during the CVD of tin oxide starting from various precursors. The subsequent sections will discuss the influence of deposition parameters, such as precursor composition, deposition temperature, deposition time, substrate type, precursor flow rate, and of annealing, on the

electrical and optical properties of tin oxide layers. Section 2.6 deals with the properties that are required by two main applications of tin oxide layers, low-E coatings and solar cells. Also attention will be paid to methods to control these properties by means of the deposition parameters. Section 2.7 presents the main conclusions and ends with an outlook on future research.

2.2 Precursor chemistry

The quality of tin oxide layers and the economics of producing them in terms of adequate deposition rates are not only limited by process conditions, but also by the precursor system used. The chemistry and kinetics of the precursor system have a large influence on the possibility of incorporation of impurities, such as C or Cl, in the deposited layer as well as on the growth rate of the layer. In the following, some of these deposition reactions will be discussed in more detail.

2.2.1 $SnCl_2 + O_2$

Although tin dichloride has a very low volatility some authors have used it as precursor for tin oxide deposition by applying the following oxidation reaction:

$$SnCl_2 + O_2 \rightarrow SnO_2 + Cl_2 \tag{2.1}$$

Reddy et al. [6] showed that at a reactor temperature of 500 °C with excess oxygen, this reaction proceeds first order in $SnCl_2$. The reaction has rather a low apparent activation energy of 58 kJ/mole [7]. Because the dissociation energy for the ClSn-Cl bond is about 370 kJ/mole [8], it is likely that the reaction completely occurs at the surface. Also the large grains reported [9], indicate that growth proceeds through the chemisorption of $SnCl_2$ to a growing tin oxide grain, and subsequent reaction with absorbed oxygen atoms.

Figure 2.1 shows the growth rate as a function of temperature as is measured by various authors. All authors used a horizontal hot wall reactor. Yusta et al. [7], and Sundaram and Bhagavat [10] used a mole fraction of about 0.011 $SnCl_2$ and excess oxygen. Their growth rates are also of comparable order. Murty et al. [11] used a mole fraction of 0.0026 $SnCl_2$, which is about four times lower, causing their growth rates also to be a factor of about four lower.

2.2.2 $SnCl_4 + O_2$

The oxidation of tin tetrachloride proceeds according to the following overall reaction [12] :

$$SnCl_4 + O_2 \rightarrow SnO_2 + 2Cl_2 \tag{2.2}$$
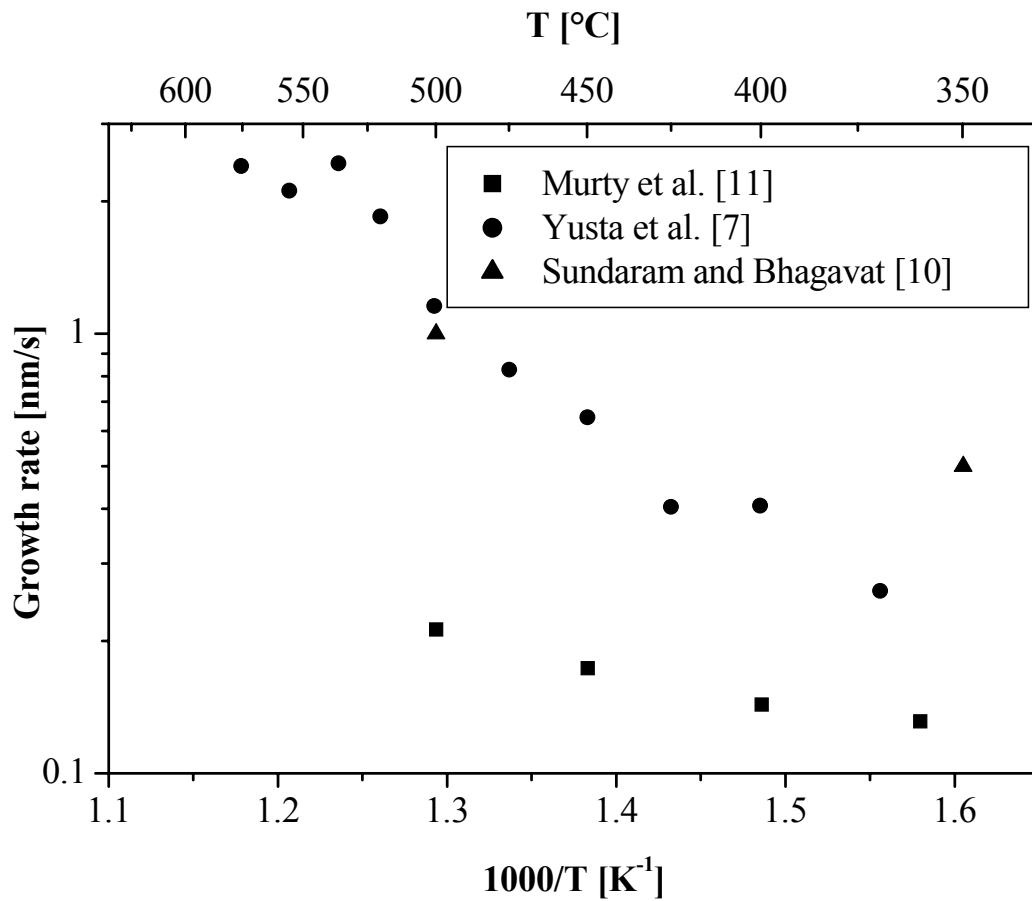
Figure 2.1: *Growth rate of tin oxide from SnCl$_2$ + O$_2$ as reported by Murty et al.[11], Yusta et al.[7], and Sundaram and Bhagavat [10].*
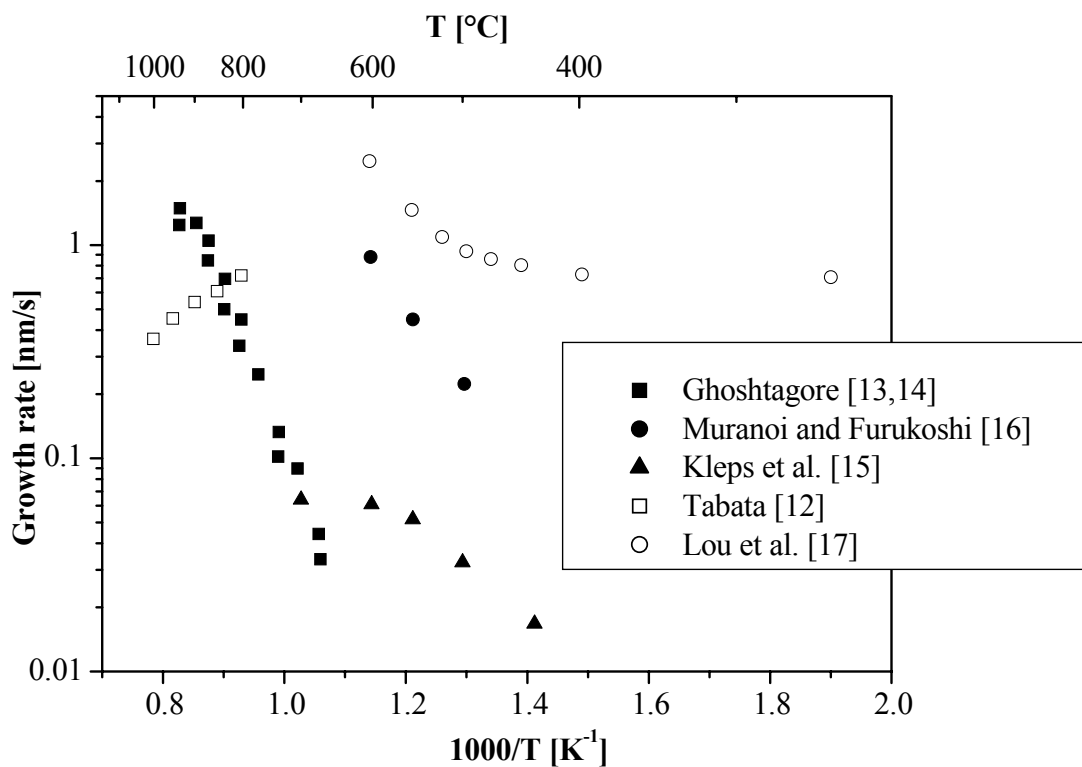
Figure 2.2: *Reported growth rate of tin oxide, prepared from SnCl$_4$ + O$_2$, as a function of temperature.*

Ghoshtagore [13, 14] postulated that this reaction proceeds via an Eley-Rideal mechanism, where oxygen is chemisorbed at the surface and reacts with gaseous $SnCl_4$ or $SnCl_2$. He reported an activation energy of 144.8 kJ/mole and the following relations between deposition rate and partial pressures of the reactants in the kinetically limited region were found:

low P_{O2} and all P_{SnCl4}: $\quad R \propto (P_{O2})^{\frac{1}{2}} (P_{SnCl4})^{0.26\pm0.01}$

high P_{O2} and all P_{SnCl4}: $\quad R \propto (P_{SnCl4})^{0.26\pm0.01}$

However, the exponent of the $SnCl_4$ partial pressure dependence suggests that prior to reaction with adsorbed oxygen, this precursor dissociates on the surface into adsorbed $SnCl_x$ and Cl. This would imply a Langmuir-Hinshelwood mechanism.
Other values reported for the activation energy are 73.22 kJ/mole between 500 and 640 °C [15], and 96.2 kJ/mole between 370 and 600 °C [16]. However, in these studies hot wall reactors were used, which favour gas phase reactions and formation of film precursors with a lower activation energy, such as $SnCl_2$. Ghoshtagore [13, 14] used a cold wall reactor with only the susceptor being heated, which suppresses gas phase reactions.

Figure 2.2 shows the reported growth rates as a function of the reciprocal temperature. The difference in growth rate behaviour between various authors is striking and cannot only be explained by differences in reactor system and process conditions. The overall rate of deposition via the oxidation reaction is relatively slow compared to the hydrolysis reaction, so most attention in literature has gone to the reaction between water and tin tetrachloride.

2.2.3 $SnCl_4 + H_2O$

The hydrolysis of tin tetrachloride can be written as [18]:

$$SnCl_4 + 2H_2O \rightarrow SnO_2 + 4HCl \quad\quad\quad (2.3)$$

This reaction allows tin oxide to be grown at temperatures as low as 250 °C [12], which is not possible for the O_2 based reaction. According to Ghoshtagore [13, 14] the hydrolysis reaction proceeds also via a Rideal-Eley mechanism with water as the chemisorbed species and $SnCl_4$ as the gaseous species. From the experiments he concluded that the reaction is zero order in the water concentration if the ratio $P(H_2O)/P(SnCl_4)$ is higher than 4. He suggested the following dependence for the deposition rate:

low P_{H2O} and all P_{SnCl4}: $\quad R \propto P_{H2O} P_{SnCl4}$

high P_{H2O} and all P_{SnCl4}: $\quad R \propto P_{SnCl4}$

As is shown in figure 2.3, Ghoshtagore [13, 14] found that above 400 °C no activation energy is required for the hydrolysis reaction. These results are in

agreement with the results of Advani et al. [19], who compared their experimental results with a thermodynamic analysis. They suggest that the reaction proceeds essentially under equilibrium conditions. Also Gotoh et al. [20] found similar characteristics as reported by Ghoshtagore, with some quantitative differences due to a different experimental set-up. Below 500 °C, reported activation energy varies between 39 [16] and 74 kJ/mol [21]. These results suggest that Gotoh et al. [20] and Ghoshtagore [13, 14] were working in the diffusion controlled region.

Wartenberg et al. [22] proposed a more detailed mechanism where water adsorbs on the active sites of the glass surface followed by a hydrolytic reaction to Si-OH groups. These groups react with gaseous $SnCl_4$ to form Si-O-Sn bonds. After formation of a very thin continuous layer of $Si-O-(SnO_2)_n$, further film growth occurs through the reaction between chemisorbed water onto free tin co-ordination sites and gas phase $SnCl_4$ to a continuous layer. Studies using surface monitoring techniques have as yet failed to confirm or contradict the postulated mechanism of Ghoshtagore [13, 14].

In some publications also the effect of methanol addition is studied. Methanol improves the electrical properties of SnO_2 coatings, but decreases the deposition rate [20]. This decrease in deposition rate is believed to be caused by the adsorption of methanol molecules on the surface, thereby reducing the number of active sites for water molecules [20].

2.2.4 $Sn(CH_3)_4 + O_2$

The second tin precursor that often has been the object of study is tetramethyltin (TMT). Because of the lack of chlorine ligands, only oxygen is used as the oxidant. The reported activation energies for this process range from 106 to 174 kJ/mole. As is shown in figure 2.4, some of these investigations were performed at conditions where the deposition rate is also dependent on the mass transfer of precursors from the bulk gas phase to the substrate. The value reported by Borman et al. [23], 165.7 ± 12 kJ/mole, should be the best indication for the actual activation energy of the reaction, as can be seen in figure 2.4.

Ghoshtagore [13,14] determined the order of the reaction to be:

low P_{O2} and all P_{TMT}: $R \propto P_{O2}^{1/2} P_{TMT}$

high P_{O2} and all P_{TMT}: $R \propto P_{TMT}$

The latter relation was also found by Vetrone et al. [24], Aleksandrov et al. [25], and Kamimori et al. [26]. Both relations are confirmed by Wan et al. [27]. Harrison et al. [28] recorded FTIR spectra of reactions carried out in a gas cell, and concluded that the reaction is zero order in TMT. However, they used a mixture of 10% TMT and 90% oxygen, and a operating pressure of about 100 Torr, while the other studies used a much lower concentration of TMT and had an operating pressure of 760 Torr. These findings already indicate that the mechanism of tin
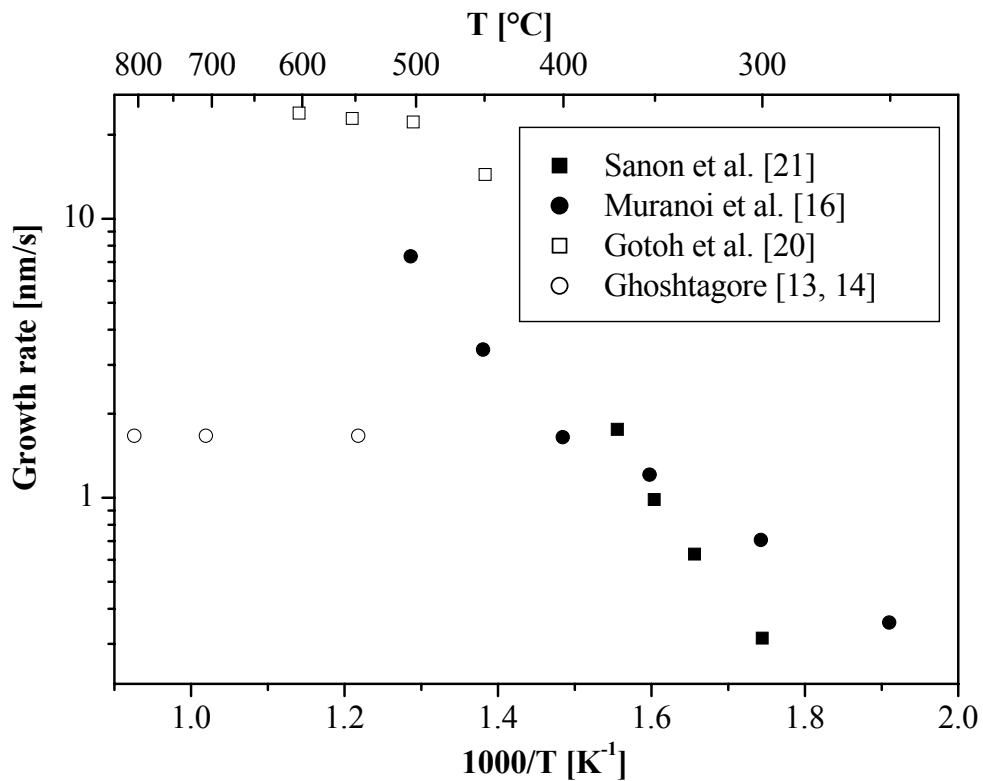
Figure 2.3: *Reported growth rate of tin oxide, prepared from SnCl₄ + H₂O, as a function of temperature.*
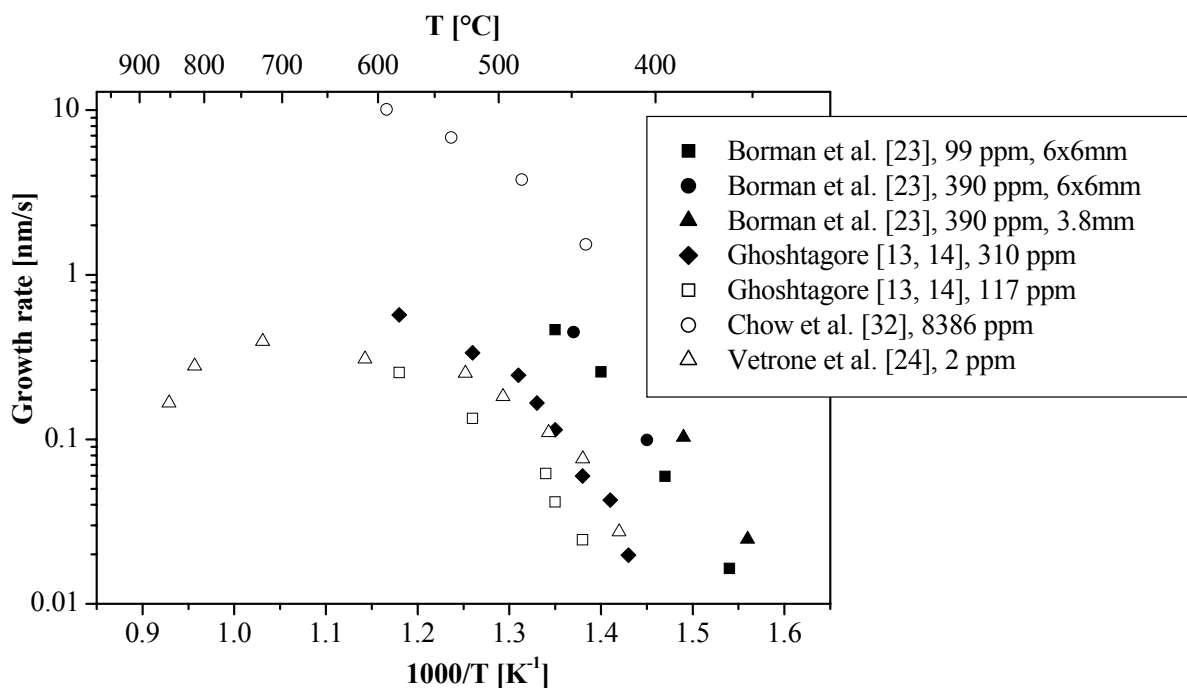
Figure 2.4: *Reported growth rate of tin oxide, prepared from (CH₃)₄Sn + O₂, as a function of temperature. Borman et al. [23] used a hot wall reactor with various diameters shown in the legend, [TMT]=99-390 ppm. Ghostagore [13, 14] used a horizontal cold wall reactor with [TMT]=117-310 ppm. Chow et al.[32] used a stagnant point flow reactor, and Vetrone et al.[24] a horizontal hot wall reactor with a tilted substrate.*

oxide deposition from TMT and oxygen is quite complicated and roughly three different types of mechanisms have been reported in literature.

Ghoshtagore [13, 14] investigated the tetramethyl tin oxidation in a cold-wall reactor. For deposition temperatures between 425 and 490 °C he proposed a reaction mechanism similar to the oxidation of $SnCl_4$: a Rideal-Eley mechanism with TMT as the virtually undissociated gaseous reaction species and atomic oxygen as the adsorbed species.

Also Harrison et al. [28] suggested a Rideal-Eley mechanism with the rate limiting step being the dissociative chemisorption of TMT at two adjacent oxygen surface sites, giving a surface trimethylstannyloxy, $-OSn(CH_3)_3$, species and a surface methoxide, $-OCH_3$.

The second mechanism that has been reported is from Aleksandrov et al. [25], who suggest that the rate limiting step occurs in the gas phase with the cleavage of the first methyl group from TMT. Based on a mass spectral analysis of the gas phase during deposition performed at pressures of 6000 Pa, they proposed the following mechanism:

$$(CH_3)_4Sn \rightarrow (CH_3)_3Sn\cdot + CH_3\cdot$$
$$CH_3\cdot + O_2 \rightarrow H_2CO + OH\cdot$$
$$(CH_3)_3Sn\cdot + O_2 \rightarrow (CH_3)_2SnO + CH_3O\cdot$$
$$CH_3O\cdot + (CH_3)_4Sn \rightarrow (CH_3)_3SnOCH_3\cdot + CH_3\cdot$$
$$OH\cdot + (CH_3)_4Sn \rightarrow (CH_3)_3SnOH + CH_3\cdot$$
$$(CH_3)_3SnOH \rightarrow CH_4 + (CH_3)_2SnO$$
$$(CH_3)_2SnO \rightarrow 2\,CH_3\cdot + SnO$$
$$OH\cdot \rightarrow \text{chain termination at walls}$$
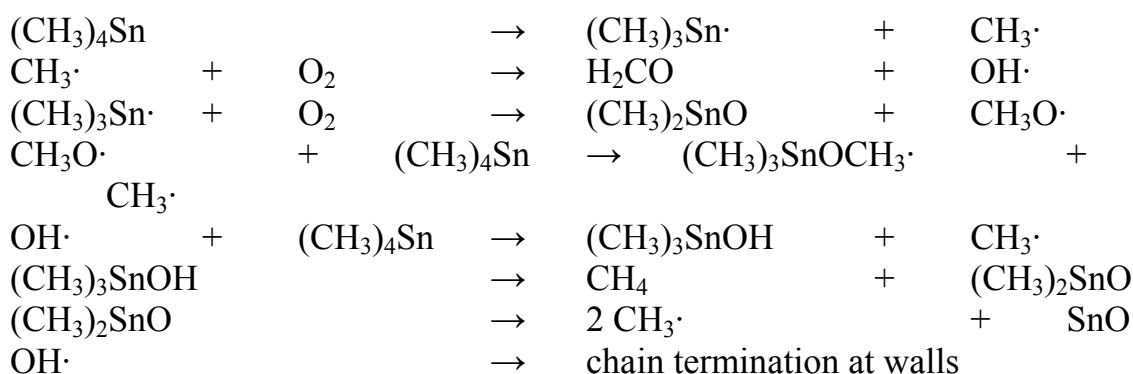
On the surface, intermediates such as SnO, are rapidly oxidised to SnO_2.

Borman and Gordon [23] investigated the gas phase chemistry of the process with Gas Chromatography-Mass Spectrometry (GC-MS) in a hot wall laminar flow reactor. They found various by-products of gas-phase free radical reactions, such as CO, CO_2, CH_2O, CH_4, H_2O, C_2H_4, C_2H_6, and C_2H_2. They also observed that the highest growth rate was not at the gas inlet of the reactor, where the concentration of precursor is highest. This implies that the species which stick to the surface were not present in the input gas stream, but were formed by gas phase reactions. Varying the flow velocities of the precursors led to proportional variation of the spatial position of the peak film growth. Like Aleksandrov et al. [25], they assume therefore that the rate limiting step for film formation occurs in the gas phase. Their hypothesis was also supported by the fact that they used additives which inhibited the film growth, but which are also known as free radical chain inhibitors.

Zawadski et al. [29] proposed a detailed kinetic model for the observations of Borman and Gordon [23] for the formation of undoped SnO_2. This is shown schematically in figure 2.5.

Figure 2.5: *Major reaction path ways in the oxidation of TMT by O₂ [29].*
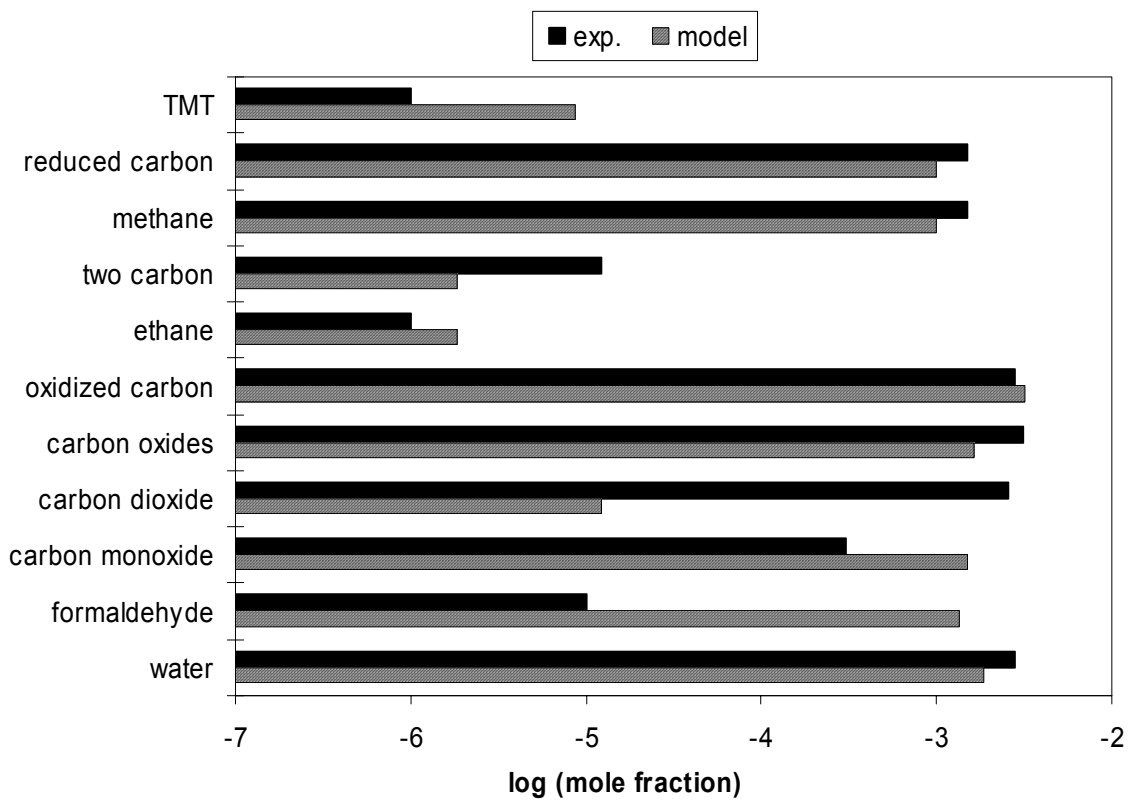
Figure 2.6: *By-product concentration from 0.1% TMT + 21% O₂ at T = 741K [23] and 3.5 s reactor residence time.*

The mechanism comprises 96 chemical reactions, involving 27 gas-phase species. The rate-limiting chemistry is proposed to occur in the gas phase, leading to species which diffuse to the film surface where they are adsorbed and rapidly oxidised. The model was divided in three subsets: hydrogen oxidation reactions, hydrocarbon reactions, and alkyltin reactions. The model parameters were as much as possible taken from kinetic data from previously studied processes. Only four of the model parameters were adjusted to fit the experimental data of Borman and Gordon [23].

The initial step in the model of Zawadski et al. [29], not shown in figure 2.5, is the pyrolysis of TMT [30], forming CH_3 radicals. Gas phase oxidation of CH_3 produces radicals, which rapidly attack TMT, starting further reaction in secondary initiation processes. The organotin radical, formed by these processes, reacts reversibly with oxygen to form a peroxide species. This peroxy species, $(CH_3)_3SnCH_2OO$, then undergoes β-elimination to form $(CH_3)_3SnO$ and CH_2O. $(CH_3)_3SnO$ subsequently abstracts hydrogen from HO_2, CH_4, or CH_2O to form the key intermediate, $(CH_3)_3SnOH$. This species decomposes and oxidises to SnO or SnO_2, which are believed to be the film precursors, because of lack of carbon incorporation in the film [28].

The model also predicts that radical scavengers as bromine containing species and alkenes inhibit film growth which agrees with the experimental results found by Borman and Gordon [23]. Their prediction of the by-product composition agrees reasonably well with experiments, except for the specific concentrations of CO, CO_2, and CH_2O (figure 2.6). However, the prediction of the sum of the concentrations of CO and CO_2 did agree rather well with the experiments. This may be caused by the fact that tin oxide surfaces catalyse the oxidation of CO [31].

The main difference between the mechanism of Zawadski et al. [29] and Aleksandrov et al. [25] is the formation of $(CH_3)_3SnOH$. More detailed investigations, such as detection of radical species via LIF, are necessary to decide which elementary reaction steps are more probable.

The chemistry and kinetics of the deposition process may be altered if dopants are used. Addition of Sb with trimethylantimony enhances the deposition rate and lowers the activation energy from 37.7 to 25.5 kcal/mol [32]. Adding dopants as phosphorous (ex PH_3) and arsenic (ex AsH_3) decreases the deposition growth rate [33, 34]. Borman and Gordon [23] also investigated the formation of fluorine doped tin oxide using CF_3Br as the F-precursor. Besides the additional by-products which they detected, HF, HBr, CH_3Br, CH_2CF_2, and CF_3H, and an increased CO/CO_2 ratio, they also found that the growth rate was accelerated by addition of CF_3Br.

2.2.5 $(CH_3)_2SnCl_2 + O_2$

Adachi and Mizuhashi [35, 36] investigated the oxidation of dimethyltin dichloride (DMTC) in a cold wall reactor. They reported that the order of reaction is about one half in both oxygen and DMTC, almost similar as was found by Ghoshtagore
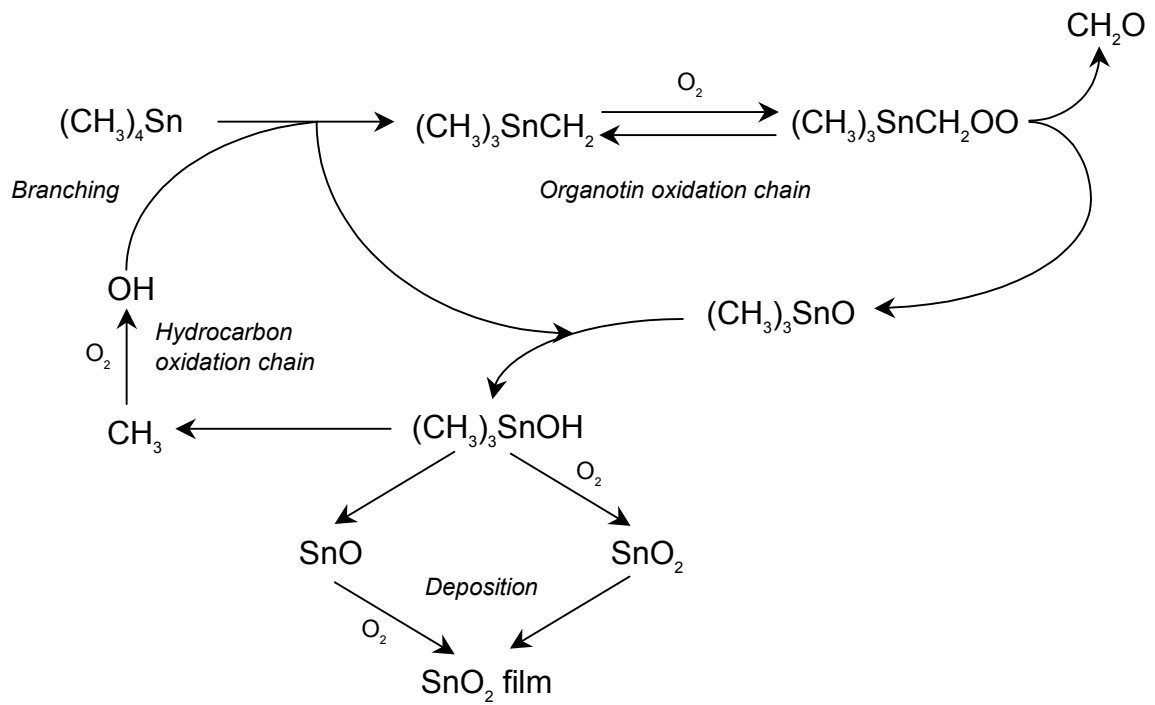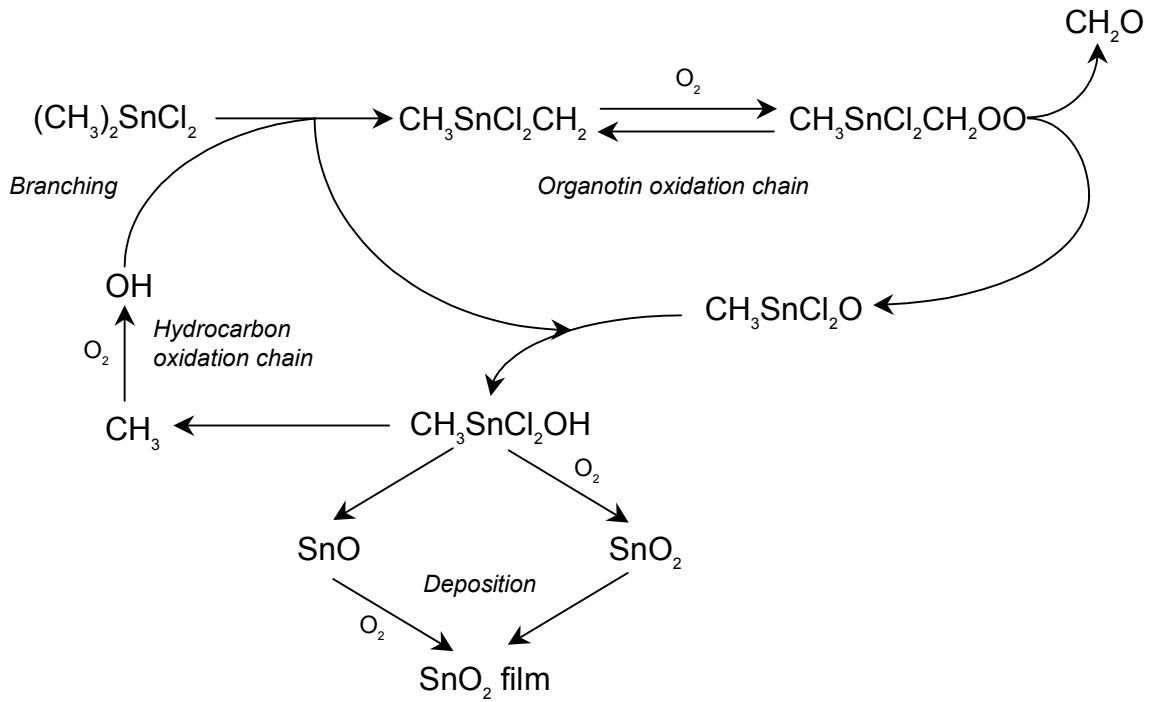
Figure 2.7: *Major reaction path ways in the oxidation of DMTC by O_2 [38].*
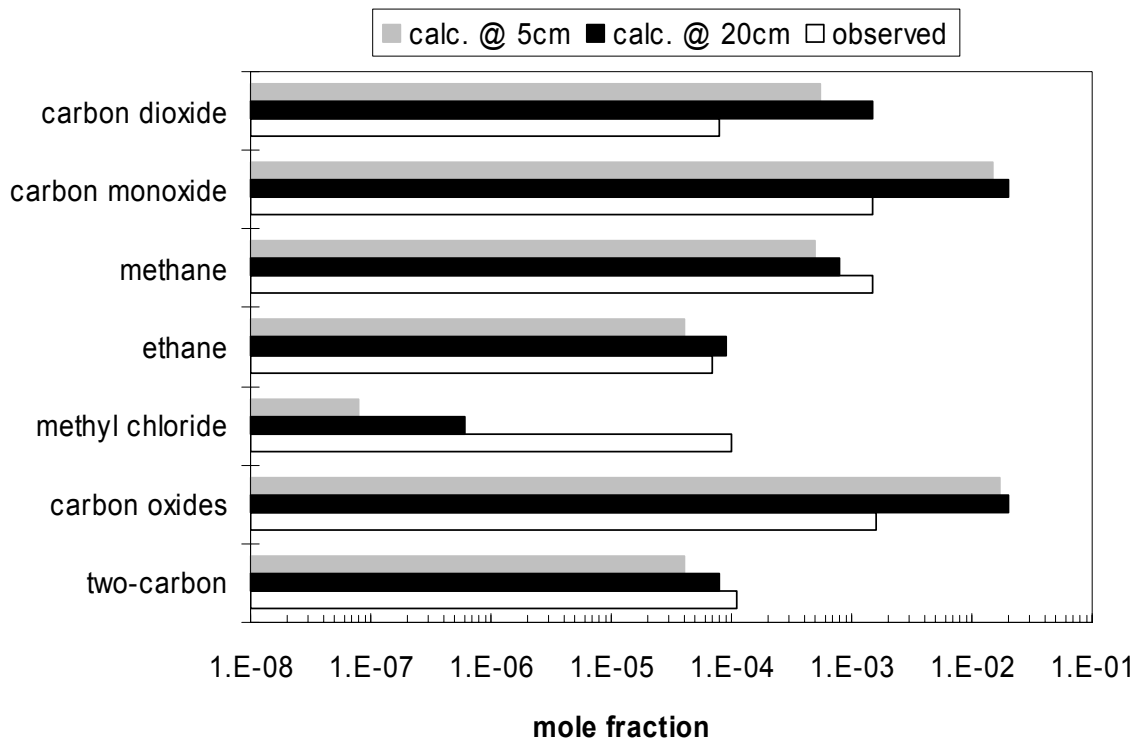
Figure 2.8*: By-product concentration for 1.3% DMTC + 20% O_2 at T = 893K and two positions along the flow direction [37].*

[13, 14] for the oxidation of $SnCl_4$. Like Ghoshtagore [13, 14], they also proposed that the reaction was diffusion limited at higher temperatures and surface reaction limited at lower temperatures. They found an activation energy of 142 kJ/mol for the kinetically limited region.

Strickler [37] used also a cold wall reactor to investigate the oxidation of DMTC to form SnO_2. With a GC he investigated the gas phase products formed during deposition. He found a variety of species including H_2, CO_2, CO, CH_4, C_2H_6, and CH_3Cl. His results suggest a complex mechanism for film formation involving not only surface reactions, but also various radical reactions in the gas phase. Giunta et al. [38] proposed a model for this mechanism, as depicted in figure 2.7, based on the mechanism developed by Zawadski et al. [29] for the oxidation of tetramethyl tin with an additional subset of reactions with chlorine.

The distribution of gas phase by-products at different process conditions obtained by this model follows the same trends as measured by Strickler [37], but the absolute concentrations were often over- or underestimated. Figure 2.8 shows the results of the model [38] and experiments [37].

The activation energy, calculated for the whole process, 21.8 kcal/mol, agrees well with the observed activation energy, 22.1 kcal/mol. Sanders [39] investigated the gas-product composition in a cold wall reactor with FTIR. She found almost the same products as Strickler [37], except H_2, which is IR inactive, and C_2H_6, which could not be identified unambiguously. Also formaldehyde and methanol were detected. Formaldehyde was predicted by the model of Giunta et al. [38], but methanol was not. This could mean that some radical reactions are more important than the mechanism of Giunta et al. [38] suggests. Sanders [39] deduced that the methanol formation is independent from the formaldehyde formation by the fact that by reducing the oxygen concentration, the product concentrations decrease but the ratio of methanol to formaldehyde does not. However, a second interpretation of these findings can be found in a rapid equilibrium between both species.

Strickler [37] investigated the influence of CF_3Br on the deposition process. Only a small amount of the freon was used during the deposition process. He detected several additional gas products: C_2F_6, CF_3H, CF_2CH_2, and CH_3Br. Methyl bromide could be accounted for by methyl radical abstraction of Br from freon: CH_3 + CF_3Br → CH_3Br + CF_3. The recombination of the trifluoromethyl radicals then gives hexafluoroethane. Strickler measured that the deposition rate increases with increasing concentration of freon. CF_3 radicals may speed up the process by providing another route for DMTC decomposition by abstracting hydrogen. Many other radical reactions are involved in the oxidation of DMTC in the presence of freon, which makes the mechanism very complex.

2.2.6 $(CH_3)_2SnCl_2$ + H_2O/O_2

Adachi and Mizushima [35, 36] studied the reaction system DMTC+O_2+H_2O in the temperature range of 400 to 500 °C. In the presence of water vapour, the deposition

rate dependence on DMTC concentration increased from [DMTC]$^{0.46}$ to [DMTC]$^{0.65}$. They suggest that in the reaction of DMTC+O_2, the rate determining step is the oxidation of Sn-Cl bonds, while in the reaction of DMTC+O_2+H_2O, the oxidation of Sn-CH$_3$ bonds is rate determining. The hydrolytic decomposition of Sn-Cl bonds takes place much easier at these temperatures. They reported an activation energy of 38 kcal/mol for the hydrolysis of DMTC, as is shown in figure 2.9.

Sanders [39] compared the DMTC+O_2+H_2O reaction with the separate oxidation (DMTC+O_2) and hydrolysis (DMTC+H_2O) reactions, as is depicted in figure 10. She found that the oxidation and hydrolysis reactions were interdependent: the presence of oxygen increases the extent for DMTC hydrolysis whilst water increases the extent of oxidation. Sanders [39] measured the decrease of DMTC concentration during reaction with FTIR. The loss of DMTC in the DMTC+O_2+H_2O system is at every temperature more than in the DMTC+O_2 and DMTC+H_2O systems, with in each twice the concentration of O_2 or H_2O, respectively, compared to the combined system. A possible explanation for this phenomenon is that water forms a complex with DMTC, which weakens the Sn-Me bond and promotes the methyl radical formation.
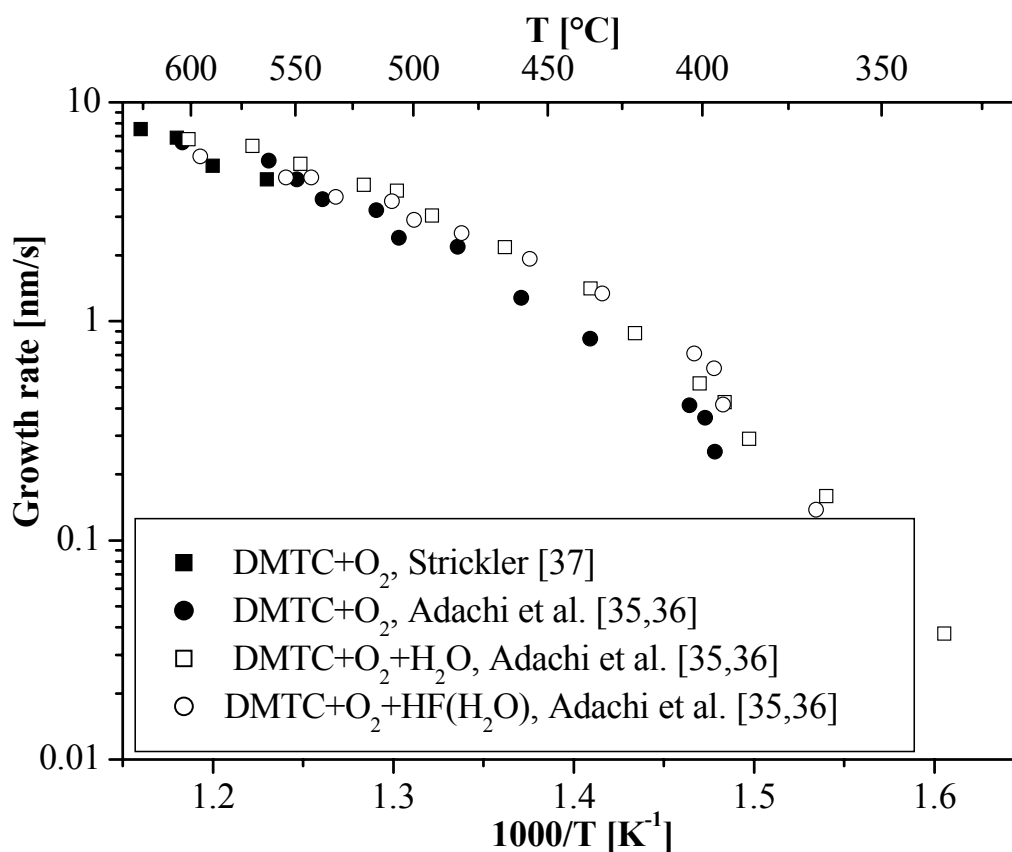
Figure 2.9: *Reported growth rate of tin oxide, prepared from (CH$_3$)$_2$SnCl$_2$ + O$_2$ or O$_2$/H$_2$O, as a function of temperature. The data of Strickler were obtained in a horizontal hot wall reactor with [DMTC]=4·10^{-3} and [O$_2$]=0.2. The data from Adachi were obtained in a stagnant point flow reactor, [DMTC]=1.1·10^{-4} mol/min, and [O2]=0.25 atm, [H$_2$O]=0.06 atm, and [HF]=3.3·10^{-3}.*
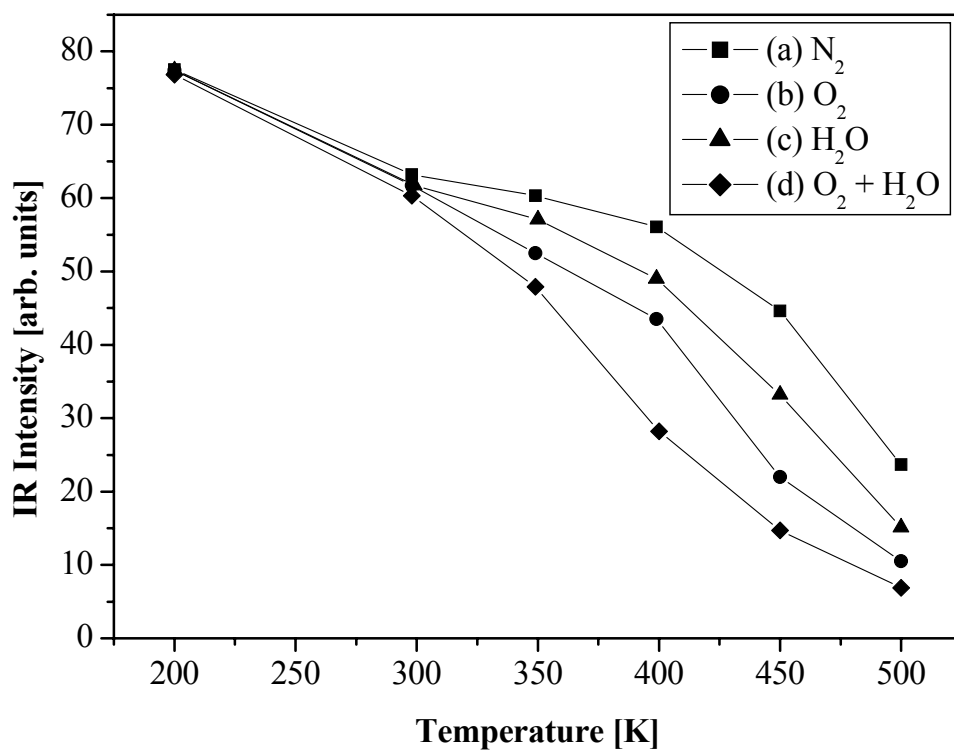
Figure 2.10: *Loss of DMTC as a function of temperature during reaction in (a) N₂, (b) O₂, (c) H₂O, and (d) H₂O + O₂ at concentrations half of those used in (b) and (c), respectively [39].*

2.3 Electrical properties

Completely stoichiometric undoped tin oxide would be an insulator, but a reasonable degree of conductivity can be achieved by stoichiometric deviation or by doping. Undoped tin oxide films often show some degree of conductivity because of unintentionally doping with Cl^- or due to non-stoichiometry, mostly caused by oxygen vacancies in the lattice. These vacancies contain electrons from the removed oxygen atom, which can be excited to the conduction band:

$$SnO_2 \rightarrow Sn_{Sn4+} + O_{O2-} + V_{O2-} + \frac{1}{2}O_2$$
$$V_{O2-} \rightarrow V_{O..} + 2e^-$$
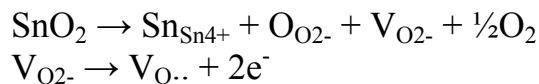
If too many oxygen vacancies are created, the structure can change into SnO with excess oxygen, which often has a negative influence on the conductivity. Another possibility for increasing the conductivity of tin oxide is the incorporation of a suitable ion in the lattice. Substituting Sb^{5+}, Sb^{3+}, In^{3+}, P^{5+}, or As^{3+} for Sn^{4+}, or substituting F^-, Cl^- for O^{2-}, results in a donor level in the energy band gap causing a higher conductivity. Tables 2.1 and 2.2 show the sheet resistance, electrical resistivity, carrier concentration, and mobility for undoped and doped tin oxide films, respectively, as prepared from various precursors.

The charge carriers generated by non-stoichiometry and doping are scattered by various mechanisms, like ionised impurity scattering, neutral impurity scattering, grain boundary scattering, and scattering at other defects and dislocations. The conductivity thus is dependent on the composition and the morphology of the layer, which in turn is dependent on deposition parameters like substrate temperature, film thickness, gas flow rate, precursor composition, and post-deposition annealing. The influence of these deposition parameters on the electrical properties of tin oxide thin films will be discussed in section 2.5.

Table 2.1: *Electrical properties of tin oxide films.*

Precursors	Temp [°C]	Sheet resistance [$\Omega/\square$]	Electrical resistivity [$\Omega\cdot$cm]	Carrier conc. [cm^{-1}]	Hall mobility [$cm^2 \cdot V^{-1} \cdot s^{-1}$]	Ref.
$SnCl_4 + O_2$	450	-	$1.1 \cdot 10^{-3}$	-	-	40
$SnCl_4 + O_2$	600	400	-	-	-	41
$SnCl_4 + O_2$	600-800	10^4	0.1	$1.2 \cdot 10^{15}$	$5 \cdot 10^3$	12
$SnCl_2 + O_2$	500	40	0.625	-	-	42
$SnCl_2 + O_2$	500	-	$1.4 \cdot 10^{-3}$	$6 \cdot 10^{20}$	7.8	10
$SnCl_2 + O_2$	500	420	$4.2 \cdot 10^{-3}$	-	18	43
$SnCl_2 + O_2$	500	-	$6.4 \cdot 10^{-4}$	-	-	7
$SnCl_2.2H_2O + O_2$	400	-	$4.4 \cdot 10^{-3}$	-	-	11
$SnCl_2.2H_2O + O_2$	500	115	-	-	-	6
$SnCl_4 + H_2O$	350	-	$1.7 \cdot 10^{-3}$	-	44	44
$SnCl_4 + H_2O$	350	23	$3.8 \cdot 10^{-3}$	$1.27 \cdot 10^{20}$	12.8	21
$SnCl_4 + H_2O$	525	-	$2.3 \cdot 10^{-3}$	$2.8 \cdot 10^{20}$	9.5	45
$SnCl_4 + H_2O$	400	-	$\sim 10^{-3}$	-	-	16
$SnCl_4 + H_2O_2$	400	-	$\sim 10^{-2}$	-	-	16
$SnCl_4 + H_2O$	550	-	$2.2 \cdot 10^{-2}$	$3 \cdot 10^{19}$	10	16
$SnCl_4 + H_2O + CH_3OH$	550	-	$2.5 \cdot 10^{-3}$	$1.5 \cdot 10^{20}$	16	16
$Sn(CH_3)_2Cl_2 + O_2$	400-500	-	$6\text{-}7 \cdot 10^{-4}$	$3\text{-}4 \cdot 10^{20}$	22	35
$Sn(CH_3)_2Cl_2 + H_2O$	400-500	-	$2 \cdot 10^{-3}$	$1 \cdot 10^{20}$	20	35
$Sn(acac)_2Cl_2$	500	40	0.625	-	-	46
$Sn(acac)_2 + air$	300	-	$1.27 \cdot 10^{-2}$	$6.33 \cdot 10^{19}$	7.8	47
$Sn(acac)_2$	400	-	$4.7 \cdot 10^{-4}$	-	-	48
$Sn(C_4H_9)_2(CH_3COO)_2 + O_2$	420	1.4	$4.5 \cdot 10^{-2}$	-	-	49
$Sn(C_4H_9)_2(CH_3COO)_2 + O_2 + H_2O$	430	-	0.1	-	-	50
$Sn(C_4H_9)_2(CH_3COO)_2 + O_2 + H_2O$	420	544	$5 \cdot 10^{-3}$	-	-	51
$Sn(CH_3)_4 + O_2$	500	-	$3.3 \cdot 10^{-2}$	-	-	52
$Sn(CH_3)_4 + O_2$	450	-	$1.1 \cdot 10^{-3}$	$1.0 \cdot 10^{20}$	8.6	26
$Sn(C_2H_5)_4 + O_2$	398	-	$1.6 \cdot 10^{-3}$	$1.8 \cdot 10^{20}$	23	26
$Sn(C_4H_9)_4 + O2$	466	-	$6.2 \cdot 10^{-3}$	$1.4 \cdot 10^{20}$	7.5	26
$Sn(C_4H_9)_2(CH_3COO)_2 + O_2$	466	-	$1.1 \cdot 10^{-2}$	$1.0 \cdot 10^{20}$	5.3	26

Table 2.2: *Electrical properties of doped tin oxide films.*

Precursors	Temp [°C]	Sheet resistance [$\Omega/\square$]	Electrical resistivity [$\Omega.cm$]	Carrier conc. [cm^{-1}]	Hall mobility [$cm^2.V^{-1}.s^{-1}$]	Ref.
$SnCl_4 + SbCl_5 + H_2O$	500	24	$7 \cdot 10^{-2}$	$4 \cdot 10^{20}$	20	53
$SnCl_4 + O_2(O_3) + HF/H_2O$	350	1.6	$3.4 \cdot 10^{-4}$	-	-	54
$DMTC + O_2 + HF/H_2O$	535	-	$3.2 \cdot 10^{-4}$	$5 \cdot 10^{20}$	35	54
$SnCl_2 + O_2 + SbCl_3$	500	55	$5.5 \cdot 10^{-4}$	-	8.3	55
$SnCl_2 + O_2 + TFA$	500	15	$2.2 \cdot 10^{-4}$	-	8.1	55
$SnCl_4 + H_2O + CH_3OH + SbCl_5$	550	-		$3 \cdot 10^{20}$	14	20
$SnCl_4 + air + PCl_5$	400	12	$1 \cdot 10^{-4}$	$3 \cdot 10^{20}$	30	56
$DMTC + HF/H_2O + O_2$	648	14.4	$4.6 \cdot 10^{-4}$	-	-	57
$MBTC + TFA/H_2O + O_2$	500	25	$5.3 \cdot 10^{-4}$	-	-	58
$MBTC + TFA/H_2O$	560	26	$5.2 \cdot 10^{-4}$	-	-	59
$SnCl_4 + HF/H_2O + CH_3OH$	500	9.9	$1.2 \cdot 10^{-3}$	-	-	60
$TMT + O_2 + C_3F_6$	-	5	$5 \cdot 10^{-4}$	-	-	61
$TMT + (CH_3)_3SnCF_3 + O_2$	500	2	$2 \cdot 10^{-4}$	-	50	62
$MBTC + TFA/H_2O + CH_3CO_2C_2H_5$	690	22	$4.1 \cdot 10^{-4}$	-	-	63
$DMTC + (CH_3)_2SnF_2$	540	7	$2 \cdot 10^{-4}$	-	-	64
$TMT + O_2 + CF_3Br$	560	3	$1.2 \cdot 10^{-4}$	-	-	65

2.4 Optical properties

Tin oxide films have a large transmittance in the visible region of the electromagnetic spectrum as a consequence of the large energy band gap of about 3.5-4.2 eV [5, 66]. In general the films are transparent from a wavelength of about 400 up to 2000 nm. The transparency decreases with increasing carrier concentration because of absorption by the free electrons. Above a wavelength of about 8 μm, the films become highly reflective. This high infrared reflection is associated with the interaction of the photons with the electrons in the conduction band and is directly related to the conductivity of the layer. This relationship approximately is given by [5]:

$$R_i = (1+2\varepsilon_0 c_0 R_s)^{-2} \tag{2.4}$$

where R_i, the infrared reflectivity, R_s, the sheet resistance, and $\varepsilon_0 c_0 = 1/376 \ \Omega^{-1}$.
Table 2.3 gives an overview of some optical properties as have been found by various authors. The optical transmissions are about 90% and an infrared reflectivity up to 90 % can be achieved. The band gap varies between 3.7 and 4.25 eV. The low values are probably the consequence of the presence of tin monoxide as a second phase [67].
The exact behaviour of the optical properties with varying wavelength is dependent on the deposition parameters used during deposition of the film.

Table 2.3: *Optical properties of undoped and doped tin oxide films.*

Precursors	Transmission visible region [%]	Reflection infrared region [%]	Bandgap [eV]	Refractive index	Reference
$SnCl_2.2H_2O + O_2$	87	-	-	-	11
$SnCl_4 + H_2O$	90	77	3.93	1.7 - 1.9	21
$Sn(C_4H_9)_2(CH_3OO)_2 + H_2O/O_2$	90	-	-	1.9	50
$SnCl_2 + O_2 + SbCl_3$	89.2	-	4.16	1.746	55
$SnCl_2 + O_2 + H_2O/TFA$	90.8	-	4.25	1.78	55
$SnCl_2 + O_2$	90.5	-	4.06	1.822	55
$Sn(CH_3)_4 + O_2 + H_2O/HF$	86	-	3.8	-	53
$SnCl_4 + O_2 + PCl_5$	83	-	3.68	-	56
$Sn(CH_3)_4 + O_2 + CF_3Br$	90	90	-	-	65

2.5 Influence of deposition parameters on properties of tin oxide films

Various authors have investigated the dependence of the optical properties of tin oxide layers on chemical vapour deposition parameters, such as the nature of the precursors or the substrate, deposition time, deposition temperature, flow rate of the various precursors, and doping. Also the effects of post-deposition annealing on film properties have been studied. In this section the effects of these deposition parameters and of annealing on structure and properties of CVD-grown tin oxide layers will be discussed.

2.5.1 Influence of the precursor composition

The influence of the tin-containing precursor on the structure and properties of tin oxide layers is difficult to determine, because of the influence of other parameters. In the case of Cl-containing precursors, the possibility exists that chlorine is incorporated in the film. If it replaces oxygen, more free carriers can be generated which lowers the resistivity. However, if it is located at other positions in the lattice, it can act as an electron trap. In that case the resistivity will be higher. An additional problem may arise when the substrate is bare glass, because of the possibility of the formation of NaCl crystals on the grain boundaries [20]. Which effect has the biggest influence depends on the type of substrate and on the various deposition parameters. By using hydrogen as the carrier gas, however, chlorine incorporation can be prevented. Chlorine is then removed as HCl [45].
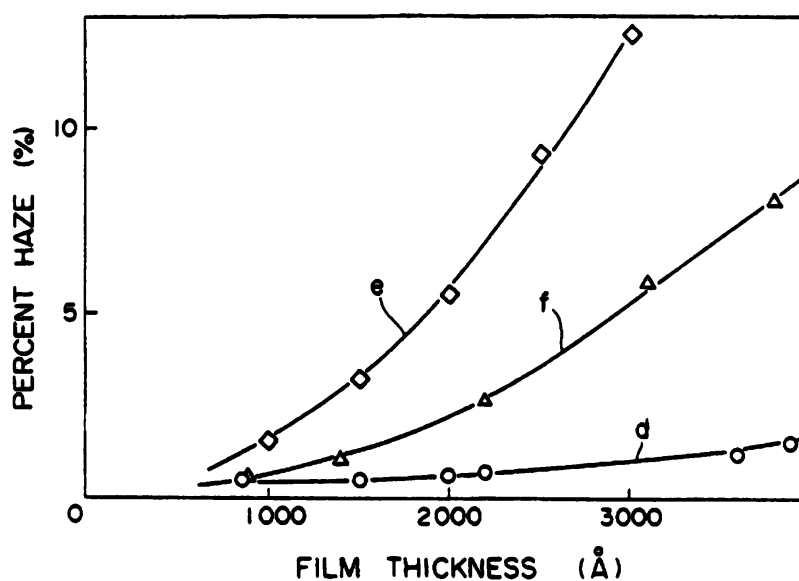
Figure 2.11: *Haze ratio for tin oxide formed from oxidation of (d) monobutyltin trichloride, (e) tin tetrachloride, and (f) dimethyltin dichloride [69].*

Kamimori and Mizuhashi [26] compared four organotin precursors. They found that also the size of the precursor has an influence on the film formation and structure. For the two "large" molecules, dibutyltin diacetate and tetrabutyltin, film formation was supposed to be controlled by reaction of an intermediate precursor-oxygen complex. The films consist of aggregates of small grains of around 5 nm. For tetraethyltin and tetramethyltin it was concluded that film formation is the result of reaction between chemisorbed oxygen and the gaseous precursor, as is discussed in section 2.2. The structure showed larger grains of good crystallinity.

The morphology of the coating has a large influence on its optical properties such as the haze ratio, which is defined as the ratio between the diffuse transmittance and the total transmittance. The haze ratio is larger for rough-grained layers than for fine-grained layers [68]. Kato [69] compared the haze ratio of undoped tin oxide on glass made from monobutyltin trichloride, tin tetrachloride, and dimethyltin dichloride, as is shown in figure 2.11. The haze ratio for tin oxide from monobutyltin trichloride (MBTC) is the lowest. Probably, this is caused by the large groups attached to the tin atom, which tend to decrease the surface diffusion rate. The nucleation rate will be larger and the crystal growth rate lower, so smaller grains are formed. At the same time the deposition rate and electrical resistivity are comparable to those obtained with dimethyltin dichloride (DMTC), and $SnCl_4$ as precursors. Another precursor, leading to tin oxide layers with a low haze ratio, was found by Lindner [70-72]. He used monophenyltin trichloride and oxygen to form a tin oxide layer of 250 nm with a haze ratio smaller than 1%. It was suggested that the low haze ratio might be ascribed to the absence of voids or pits in the coating.

2.5.2 Influence of the deposition time

When all other deposition parameters are kept constant, an increasing deposition time results in a higher thickness of the layer. In general the electrical resistivity of the film, doped and undoped, decreases with increasing thickness to a more or less constant value, see for example figure 2.12. A longer deposition time results in larger grains. The number of grain boundaries decreases and hence less grain boundary scattering will occur [16]. This implies that the mobility should increase. Indeed, this has been reported [41]. However, the proportional decrease in the number of grain boundaries compared to the bulk of the material will be much smaller at a higher thickness [7]. This would explain the tendency of the resistivity to approach to a constant value [6, 12, 44, 73-76]. The dependence of the layer thickness on the resistivity is more pronounced for films deposited at lower temperatures [11]. Some workers [49, 50] observed an increase in resistivity at high thickness. Possibly the high deposition time produces more stoichiometric tin oxide layers.
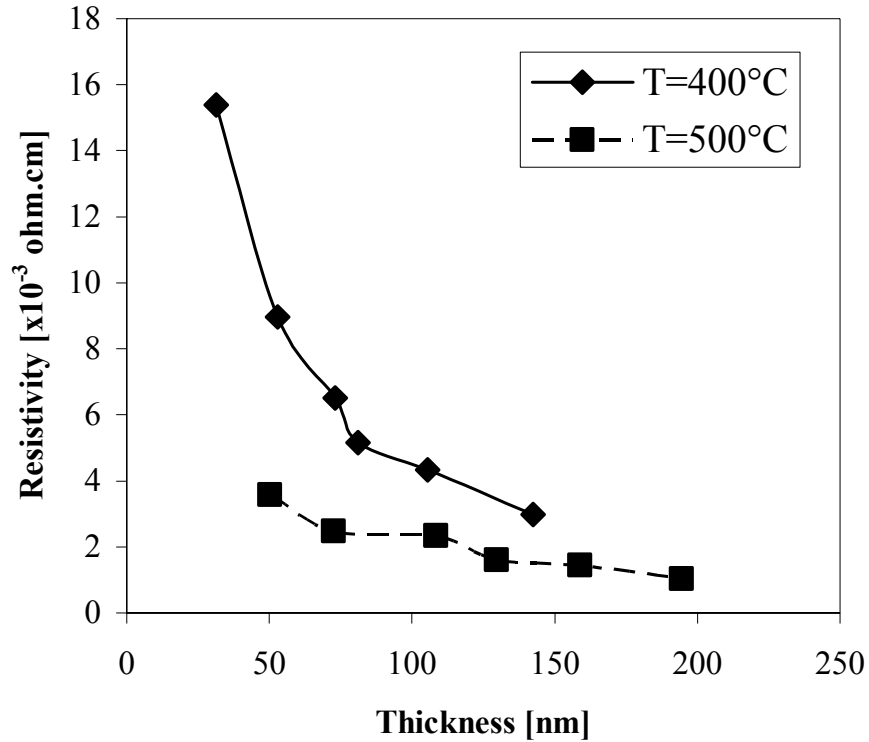
Figure 2.12: *Variation of the resistivity for layers deposited at 400 °C (♦) and 500 °C (■) [11].*

Because conductivity and infrared reflectivity depend on the same intrinsic properties, mobility and carrier concentration, the infrared reflectivity becomes higher for thicker films. The transmission decreases with thickness because of a higher absorption in the bulk of the film [41, 44]. Also the structure of the layer is dependent on the deposition time, i.e. thickness. Sanon et al. [44] found for tin oxide on glass starting from $SnCl_4$ and H_2O, that above a thickness of 1.3 μm the preferred orientation changed from (110) to (200). A change in orientation with thickness was also found by other authors, using other precursors. Maruyama and Ikuta [47] used tin(II) acetylacetonate and air to deposit tin oxide. Below a thickness of 200 nm there was no preferred orientation.

For film thicknesses between 200 and 1000 nm, the (200) peak in the X-ray diffraction spectrum increased, whereas the (310) peak remained constant and the other peaks decreased in intensity. Above a thickness of 1000 nm, the (200) diffraction peak is the main one. Belanger et al. [77] used dibutyltin diacetate, oxygen, and a dopant. X-ray diffraction showed the preferred orientation in the film changed from (110) to (200) when the film thickness was about 1 μm. In general, tin oxide films with a thickness above 100 nm are textured with an orientation dependent on the deposition parameters.

2.5.3 Influence of the deposition temperature

At low deposition temperatures the resistivity of the grown layers is high, but it decreases with increasing deposition temperature [7, 10, 16, 21, 35, 48] to a minimum at about 400-500 °C and then increases again [40]. Figure 2.13 shows the variation of the conductivity with deposition temperature for an undoped tin oxide layer deposited in a cold wall reactor starting from DMTC, and O_2 [35]. The resistivity initially decreases with increasing deposition temperature because the grain size and the crystallinity of the layer increase [48]. After a minimum value at about 450 °C, the resistivity of the layer increases as a result of a decreasing carrier concentration. This is caused by the elimination of oxygen vacancies (more complete oxidation) or by a lower concentration of active chlorine ions at high temperatures. However, Sanon et al. [21] found the carrier concentration to be independent of deposition temperature and attributed the change in resistivity to a change in mobility. They state that at low temperatures more and more defects are annealed out, causing an increase in mobility and thus in conductivity. At deposition temperatures above 350 °C, the mobility and thus the conductivity decreases, probably caused by re-evaporation of coating material and surface roughness which creates voids inside the film. Also the change in texture orientation with temperature [76, 78, 79] may have an influence on the mobility.

Except the influence of grain size, crystallinity, and the presence of a SnO-phase, Lou et al. [41] found that also the presence of sharp cornered pits on the surface has an influence on the resistance. The pits cause a lower mobility [80]. As the deposition temperature increases, the concentration of these pits decreases, resulting in an additional decrease of the resistivity.

Because for doped tin oxide the free electrons are supplied by the dopant, the resistivity does often not show an optimum on deposition temperature [20, 35, 76, 78, 79, 81, 82]. Figure 2.14 shows the dependence of the conductivity, mobility, and carrier concentration with deposition temperature for SnO_2:Sb made from $SnCl_2$, $SbCl_3$, and O_2 [81]. A higher

Figure 2.13: *Influence of the substrate temperature on the electrical resistivity (ρ), mobility (μ), and carrier concentration (n) [35].*

temperature results in larger grains and better crystallinity resulting in a higher carrier concentration, a higher mobility, and thus a higher conductivity.

The dependence of visible transmission on the deposition temperature shows a similar behaviour as the resistivity [10, 11]. The absorption coefficient increases with increasing carrier concentration due to absorption by more free electrons. Also an increase in the diffusive transmission has been observed with increasing deposition temperature, as is shown in figure 2.15 [78]. The deposition temperature also influences the type of texture formed in the layer. Ma et al. [78] formed fluorine doped tin oxide by oxidation of $SnCl_4$ and $C_2H_4F_2$. Below 450 °C the layers showed a preferential orientation of (110) planes, while above 450 °C the (200) planes had the highest XRD intensity. The exact type of texture is not only dependent on the thickness, but also on the temperature of the substrate.
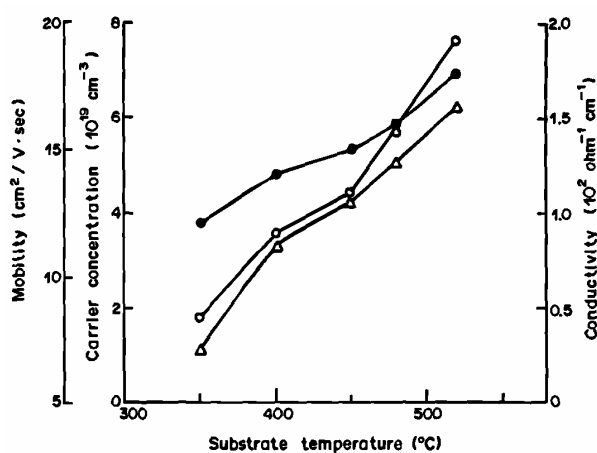
Figure 2.14: *Variations of carrier concentration (■), conductivity (o), and mobility (△) of doped tin oxide with substrate temperature [81].*
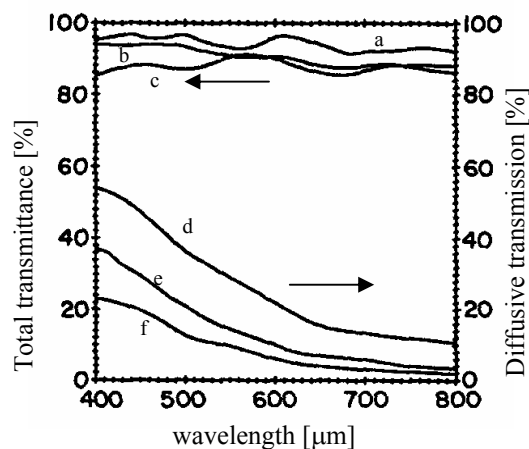
Figure 2.15: *The optical transmission vs. wavelength. a, b, c, total transmission and d, e, f, diffusive transmission. Curves a and d, SnO₂:F films, T_s=550°C; b and e, SnO₂:F films, T_s=450 °C; c and f, SnO₂, T_s=400 °C [78].*

2.5.4 Influence of the type of substrate

The morphology and composition of the substrate also has an influence on the properties of the coating. Yusta et al. [7] found a slightly lower resistivity for undoped tin oxide on Pyrex substrates, $6.4 \cdot 10^{-4}$ Ω.cm, compared to Si-substrates, $9 \cdot 10^{-4}$ Ω.cm, probably due to differences in surface morphology. The Pyrex substrates are more irregular than the polished Si-substrates, which could allow for bigger grains. Figure 2.16 shows the grain size, carrier concentration, resistivity, and Hall mobility as a function of the coating thickness for glass and fused silica substrates. For both substrates the grain size shows similar behaviour, but the resistivity for fused silica substrates is lower compared to glass substrates. A plausible explanation is the diffusion of alkali metal ions from the glass into the coating. This may result in neutralisation of charge carriers especially at low thickness and in lower mobility, because these ions can act as an additional impurity scattering site [44]. Gotoh and Mizuhashi [20] did a similar investigation,

but compared glass with silica coated glass substrates. The conductivity and the mobility for the silica coated glass substrate were higher, whereas the carrier concentration was lower. The higher resistivity of the glass substrate was thus mainly caused by the lower mobility. The latter was attributed to diffusion of Na-ions into the coating, thereby forming NaCl crystals at the grain boundaries. This would result in smaller grain size, which was also indicated by X-ray diffraction. Another difference they found was that the growth rate on glass was higher. Again the out-diffusion of alkali ions may provide additional absorption sites for water molecules which enhances the reaction.
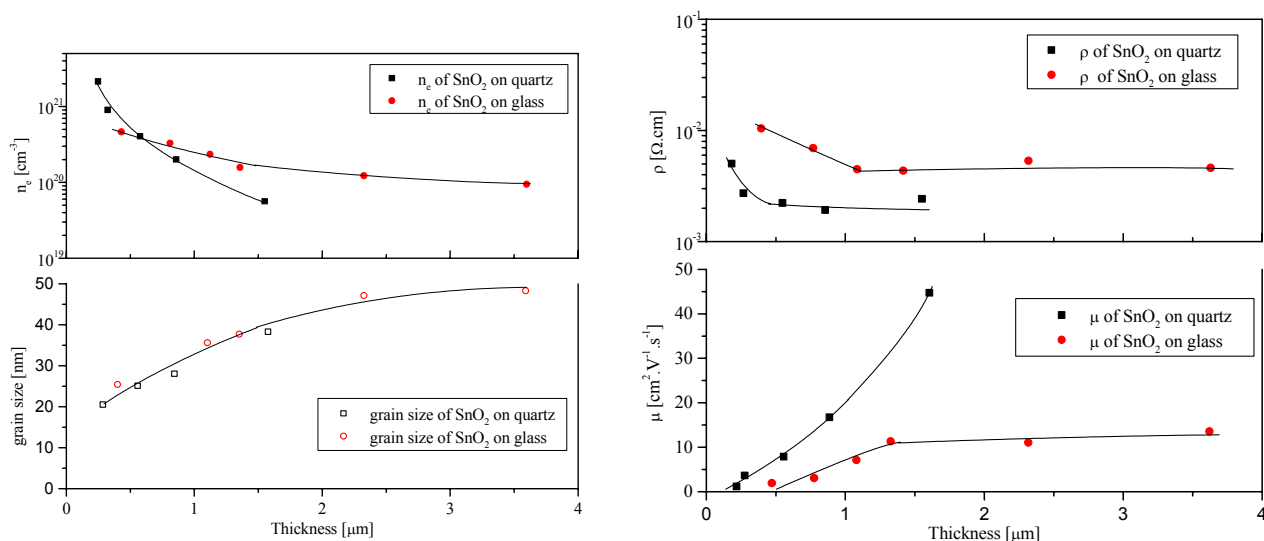
Figure 2.16: *Variation of the grain size, carrier concentration (n_e), Hall mobility (μ), and resistivity (ρ) with the thickness of the film on glass and fused silica substrates [44].*

2.5.5 Influence of the Sn-precursor flow rate

The flow rate of the tin-containing precursor has a very large influence on the resistivity of the films [12, 21, 41, 52, 83]. Sanon et al. [21] found that the sheet resistance decreases with increasing flow rate of $SnCl_4$, but for flow rates higher than 1.2 l/min the sheet resistance shows a saturation tendency. They attribute this tendency to the effect of a cancellation between a higher thickness and a lower conductivity at high flow rates. An increase in conductivity with increasing precursor flow rates has also been found for other precursors, like tetramethyltin [41, 52, 83].

Gordon et al. [76, 84] investigated the influence of the TMT flow rate on the amount of diffusive transmission, which is related to the haze ratio of the film. They found that for films grown from 0.1 mol% TMT and high oxygen concentration, the diffusive transmission decreased with increasing thickness; whereas for films grown from 0.5 mol% TMT and high oxygen concentration, the diffusive transmission increased with thickness.

The effect of the flow rate of $SnCl_4$ on the absorption coefficient of films deposited at 600 °C is shown in figure 2.17 [41]. The flow rates of $SnCl_4$ vapour for samples a, b, c, and d are 2.32×10^{-3}, 4.62×10^{-3}, 6.96×10^{-3}, and 9.28×10^{-3} mol/min,

respectively, with the oxygen flow rate fixed at 4.1×10^{-2} mol/min. Higher flow rates increase the absorption coefficient and decrease the transparency in the short wavelength range of the visible spectrum. X-ray diffraction and Hall effect measurements revealed that the films deposited at low flow rates, sample a and b, had a high sheet resistance and had broad SnO_2 peaks with respect to the films deposited with high flow rates of $SnCl_4$, samples c and d. Higher flow rates result in improved crystallinity and an increase in grain size, leading to a better conductivity and a higher absorption coefficient [41]. The mechanism underlying the above results, however, is not well understood to date.
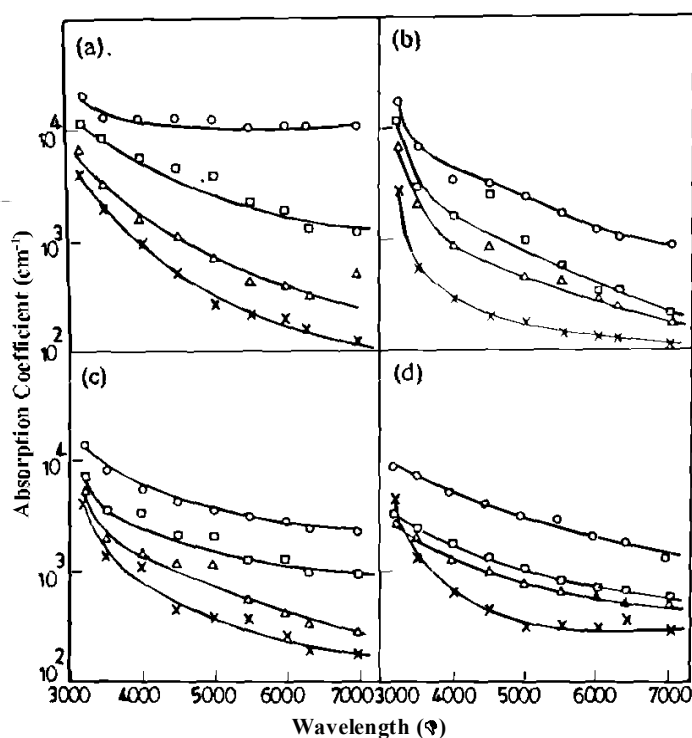
Figure 2.17: *Dependence of the deposition time on the absorption coefficient for films grown at 600°C with various flow rates of SnCl₄. Sample a (x 1min, Δ 2 min, 3min, o 6 min); sample b (x 0.5min, Δ 1 min, 2min, o 4 min); sample c (x 1min, Δ 2 min, 3min, o 4 min); sample d (x 0.5min, Δ 1 min, 2min, o 4 min) [41].*

2.5.6 Influence of the oxygen flow rate

Reddy et al. [6] investigated the influence of the oxygen flow rate and thus the oxygen partial pressure on the resistivity of undoped tin oxide layers grown by reaction between $SnCl_2$ and O_2. As can be seen in figure 2.18, the resistivity initially decreases, reaches a minimum and increases again with increasing oxygen flow rate. At low flow rates two factors may play a role. The growth rate increases, thereby the thickness, resulting in a lower resistivity as discussed previously. Also at low flow rates a highly resistive SnO-phase is present [41], which will be oxidised to SnO_2 with increasing flow rates. After a minimum is reached where the layer contains the optimal concentration of oxygen vacancies or unintentionally Cl-incorporation, the resistivity increases again as a result of filling of the oxygen

vacancies. Also the thickness becomes higher, so the influence of the thickness on the resistivity is much weaker [6, 11]. The influence of oxygen on the structure is dependent on the concentration and tin-precursor used. Using TMT and high concentrations of oxygen (>80%), Gordon et al. [84] produced very rough fluorine doped tin oxide (FTO) films with changing morphology along the flow direction. The film became more rough along the flow direction, probably caused by water formation from the CVD-reactions. Electron micrographs revealed a needle-like surface indicating a preferential growth along a single crystal direction. The transmittance showed the same dependence on the oxygen flow rate as the resistivity, as is depicted in figure 2.18 [6, 11]. At low flow rate the carrier concentration is low, so the absorption by the free carriers is low too. After an optimum at 1.16 l/min of oxygen the carrier concentration increased, causing an increase in absorption and thus a decrease in transmittance. Ma et al. [78] found that at high flow rate the diffusive transmission and the haze increases, as a consequence of a higher surface roughness.
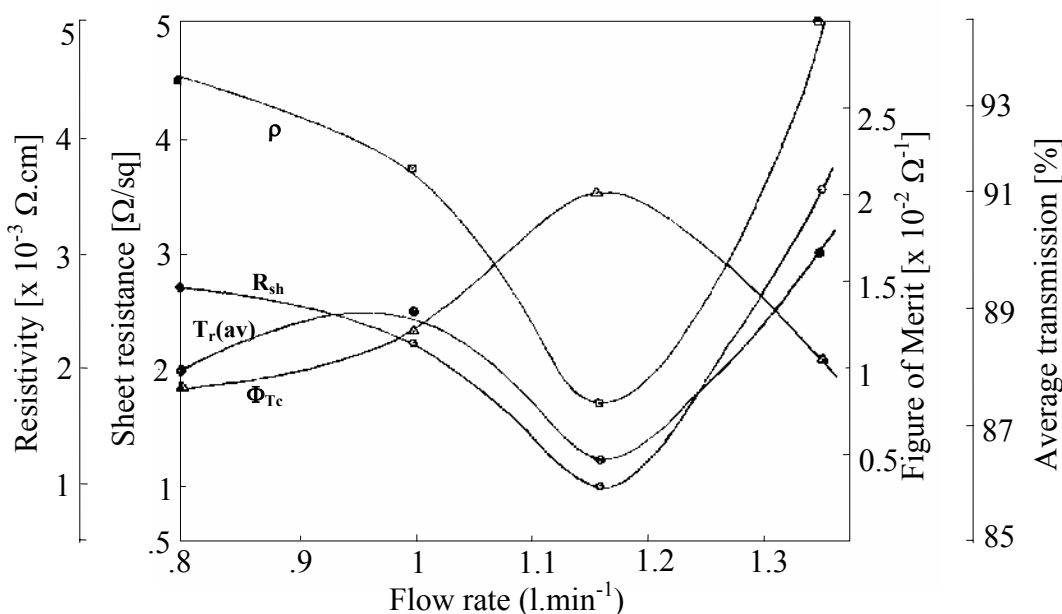
Figure 2.18: *Variation of sheet resistance (R_{sh}), resistivity ( ), average transmission (T_r), and figure of merit (Φ_{TC}) with oxygen flow rate F [6].*

2.5.7 Influence of water flow rate

Using water in addition to or instead of oxygen increases the growth rate and thus decreases in general the deposition temperature [16, 20]. Also the grain size and hence the visible haze increases with water addition [84, 35]. The effect on the resistivity is not completely clear. Figure 2.19 depicts the dependence of mobility and resistivity on the flow rate of water or hydrogen peroxide for films deposited at 300 °C in a hot wall reactor [16]. Although the growth rate increases, the mobility decreases and the resistivity increases [16, 50]. This effect is more serious for films deposited by using hydrogen peroxide [16]. Also Adachi and Mizuhashi [35] found that using H_2O/O_2 instead of pure O_2 resulted in a higher resistivity. Possible

explanations are particle formation in the gas phase and the onset of too-quick decomposition, which disturbs regular growth and crystallisation through wandering of adatoms along the surface. Gotoh and Mizuhashi [20] found the resistivity to decrease with increasing water content. They deposited tin oxide on glass from $SnCl_4$ and H_2O in a cold wall reactor at 500 °C. The difference with the observations of Adachi and Mizuhashi [35] can be explained by the fact that in a cold wall reactor powder formation is suppressed. The reaction is confined to an area close to the surface of the substrate.
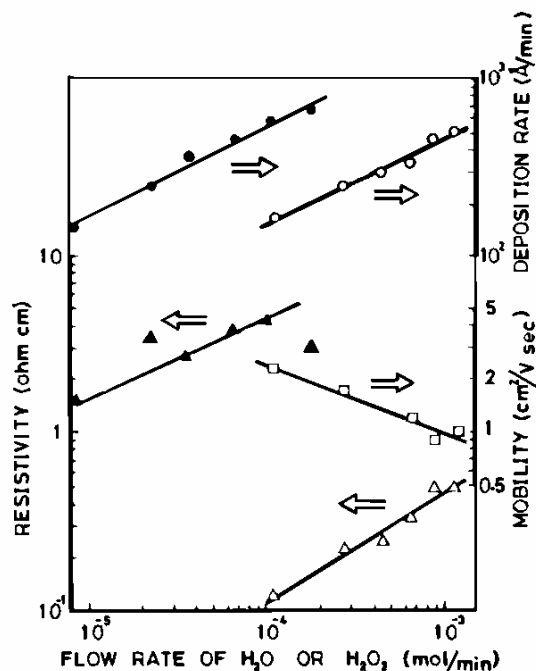
Figure 2.19: *Deposition rate, resistivity, and mobility vs. flow rate of water (open symbols) or hydrogen peroxide (closed symbols). Deposition was conducted at 300 °C with 2 mg/min of $SnCl_4$ [16].*

2.5.8 Influence of methanol addition

A possibility to increase the conductivity of undoped tin oxide layers is addition of methanol to the reacting gas mixture. Methanol acts as a reducing agent, which results in an increase in the carrier concentration. The mobility also increases by adding methanol, but the cause for this is less clear [20]. Because methanol absorbs competitive with oxygen or water to the surface, the film forming reaction is suppressed so the deposition rate decreases with methanol addition. Also chlorine incorporation in the grain boundaries is suppressed because of formation of less reactive CH_3Cl in stead of HCl.

2.5.9 Influence of doping

Doping of tin oxide films with a suitable ion creates a donor level in the band gap resulting in an enhanced conductivity of these films. Especially fluorine (F) and antimony (Sb) have been found to be the most useful dopants from an application

point of view. Adding a suitable amount of dopant to the film causes an increase in the carrier concentration through the controlled valency mechanism [85]:

SnO$_2$:Sb: $Sn^{4+}_{1-x}e_xSb^{5+}_xO^{2-}_2$

SnO$_2$:F: $Sn^{4+}e_xO^{2-}_{2-x}F^-_x$
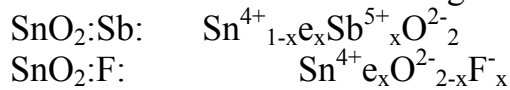
Various authors [20, 32 - 35, 53, 55, 56, 86 - 88] have investigated the effect of the amount of dopant on the resistivity, mobility, and carrier concentration.

Figure 2.20 shows this dependence for a SnO$_2$:Sb film deposited from SnCl$_4$, SbCl$_5$, and H$_2$O on Corning 7059 glass at 500 °C. Below P(SnCl$_4$)/P(SbCl$_5$)=0.05, the resistivity decreases because of an increase in the carrier concentration. Above this ratio, the resistivity raises, caused by an increase in ionised impurity scattering from the excessive Sb incorporation in the lattice and/or the formation of a Sb$_2$O$_5$ phase. However, also at low dopant concentrations, the carrier concentration has not the value as would be expected theoretically on the base of the concentration of dopant in the layer [70, 89]. Belanger et al. [77] state that in the case of antimony some of the dopant segregates to the grain boundaries. For crystallites with the crystallographic orientations (110), (211), and (301) it remains as Sb^{3+} at the surface to retain charge neutrality and acts as an electron trap. For crystallites with the (200) orientation, the antimony need not to be reduced and the dopant enhances the conductivity.

Figure 2.21 shows the influence of an increased ratio of HF/SnCl$_4$ on the spectral absorption. A higher dopant concentration results in general in a lower transmittance because of absorption of an increased number of free carriers, and increases the infrared reflectivity [32, 81].
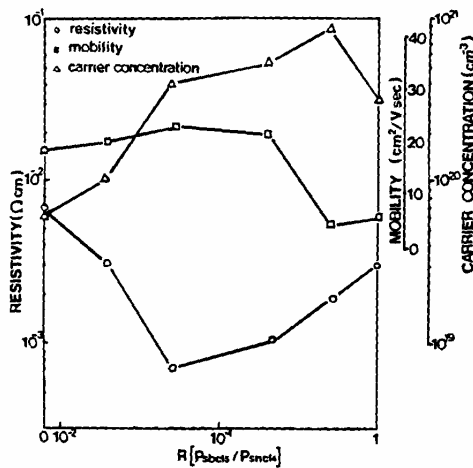
Figure 2.20: Resistivity, carrier concentration, and mobility of the films as a function of input gas ratio, R(P$_{SbCl5}$/P$_{SnCl4}$) [53].
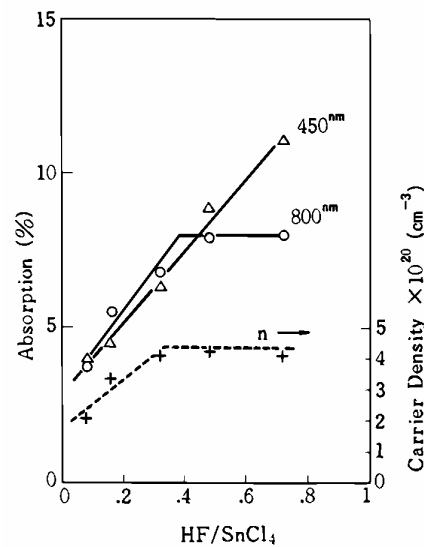
Figure 2.21: Carrier concentration and absorption at 450 and 800 nm as a function of the relative HF flow rate [75].

2.5.10 Influence of post-deposition annealing

The effect of post-deposition annealing is difficult to predict because several phenomena may occur [5, 42, 90]:
- Increase of the crystallinity and the grain size of the film.
- Oxidation of oxygen vacancies or decrease in chlorine concentration.
- Change of the highly resistive SnO phase into SnO_2 and/or Sn.
- Adsorption and desorption of oxygen at the surface or the grain boundaries. These oxygen sites can act as electron traps.
- Reorientation of existing crystallites.

The effect of annealing is thus dependent of the condition of the film right after deposition, the annealing ambient, the temperature, and time. Sundaram and Bhagavat [42] annealed undoped tin oxide in four different ambients, viz. Ar, N_2, O_2, and air. They observed for all ambients an initial decrease in sheet resistance with annealing temperature. After an optimum around 700 °C the sheet resistance increased again. Figure 2.22 shows these trends for films deposited at different temperatures. The same trend was found by Baliga and Ghandhi [83], who annealed their films in forming gas (80% N_2 and 20% H_2). Kane et al. [49] found the sheet resistance to increase after annealing for 15 min at 420 °C in air or nitrogen. For air the sheet resistance increased by a factor of about 20 compared to a factor of about 2 for annealing in nitrogen. This suggests that the increase in resistance is predominantly caused by oxidation of the oxygen vacancies.
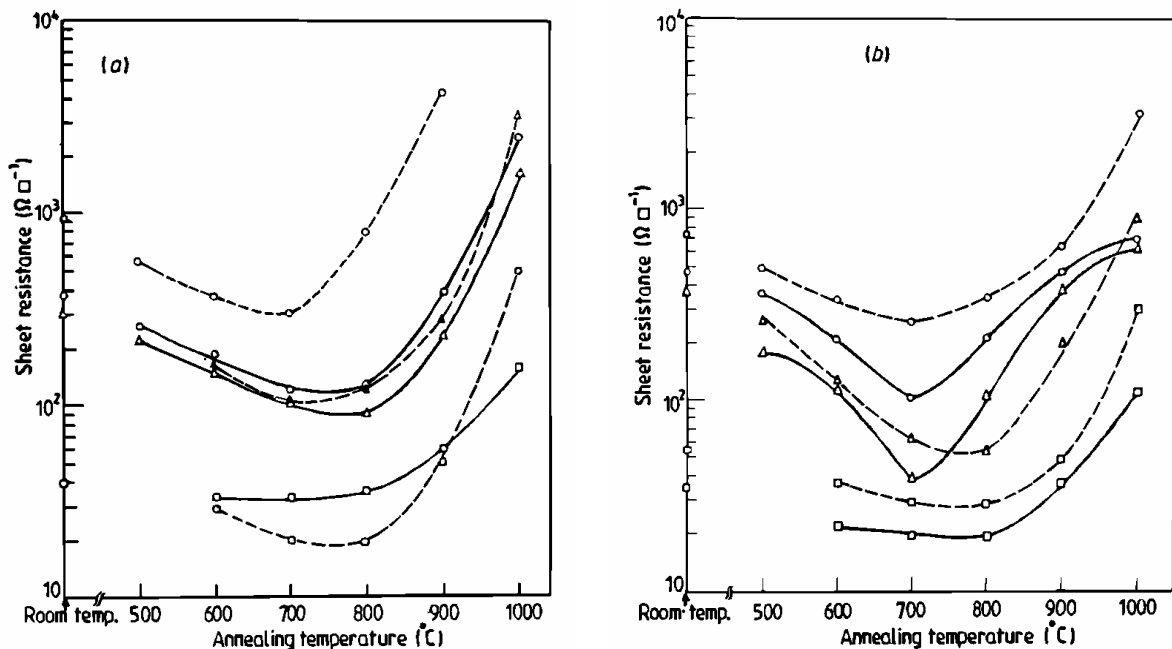
Figure 2.22: *Typical variation of sheet resistance as a function of annealing temperature. (a) Films annealed in argon (broken curves) and oxygen (full curves). (b) Films annealed in air (broken curves) and nitrogen (full curves). Deposition at 400°C (O), 450 °C (Δ), and 500 °C (□) [42].*

2.6 Applications

Because of the unique combination of electrical and optical properties listed in the preceding sections and the mechanical hardness and chemical stability, a wide variety of applications for tin oxide coatings exist. Among these applications are electrodes for liquid crystals, heated windscreens for cars, protective coatings on bottles, gas sensors, and electrodes in solar cells.

Depending on the deposition parameters used, the coating can be made according to the specifications required for a particular application. With most of these applications a trade-off between optical and electrical properties is necessary. Both electrical conductivity and visual transparency should be as large as possible. However, because of their fundamental relationship this is not possible in most cases. Haacke [91] defined a figure of merit that gives a balance between optical transmission and sheet resistance:

$$\Phi_{TC} = \frac{T^{10}}{R_S} = \sigma t \exp(-10\alpha t)$$

with Φ_{TC}, the figure of merit, T the average transmission in visible light, R_S the sheet resistance, σ the conductivity, t the thickness, and α the absorption coefficient. As is shown for the electrical conductivity and the visible transmission, also the figure of merit is dependent on the various deposition parameters. Table 2.4 compares the values of Φ_{TC} of doped and undoped tin oxide layers as deposited by various workers.

Table 2.4. *Comparison of values for the figure of merit, Φ_{TC}, for tin oxide layers deposited by various workers.*

Precursors	Sheet resistance [$\Omega/\square$]	Transmission [%]	Figure of merit [x10^{-3} Ω^{-1}]	Reference
$SnCl_2.2H_2O + O_2$	115	86.5	2.03	6
$SnCl_2 + O_2$	420	90.5	1.42	43
$SnCl_2 + O_2 + SbCl_3$	55	89.2	6.78	43
$SnCl_2 + O_2 + TFA$	14.89	90.8	25.8	43
$SnCl_4 + CH_3OH + H_2O/HF$	5	85	39.4	75
$SnCl_4 + O_2 + H_2O/HF$	6	83	25.9	87
$SnI_4 + SbI_3 + O_2$	54	85	3.6	66
$SnCl_4 + O_2 + F_2$	7.6	94	71	79
$Sn(CH_3)_4 + O_2 + C_3F_6$	5	85	39	61
$Sn(CH_3)_4 + O_2 + PF_5$	3	82	45.8	61
$Sn(CH_3)_4 + O_2 + CF_3Br$ [1]	3	90	116	65

[1]: The substrate (glass) has been coated with an intermediate layer of SiO_xN_y.

2.6.1 Low-E coatings

Low-Emissivity glass (low-E glass) is used to reflect the heat carried by infrared radiation with long wavelengths, typically around 10 μm [92]. This can be achieved by coating the glass with fluorine doped tin oxide (FTO). The desired properties of this coating are a high visible transmission and a high infrared reflectivity. The thickness of these layers plays thus an important role, because a higher thickness means a higher infrared reflectivity, but a lower visible transmission. Typically the FTO layer is 300-400 nm thick. To prevent out-diffusion of alkali ions, the glass is first coated with about 10 nm of silica [93]. Another intermediate layer is deposited before the FTO layer in order to prevent iridescence. These iridescent colours are due to the difference in refractive index of glass, about 1.5, and tin oxide, about 2.
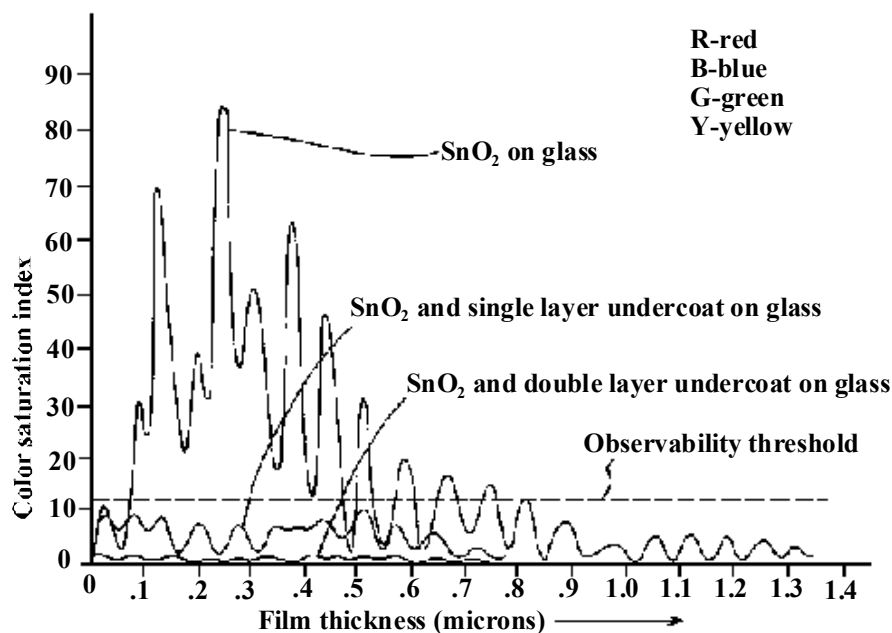
Figure 2.23: *Colour saturation index for SnO$_2$ on glass, tin oxide and a single layer undercoat on glass, and tin oxide with a double layer undercoat on glass [73].*

Figure 2.23 shows the colour saturation index for tin oxide on glass with no undercoat, with an undercoat consisting of a single layer, and with an undercoat consisting of two layers [65]. Below a certain observability threshold the human eye will not see any coloration in the reflected light. An intermediate layer with a refractive index n of around 1.7 and a certain thickness between the FTO layer and the glass can thus reduce the coloration below the level of what the human eye can observe. This layer can consist of a silicon oxynitride with a layer thickness of about 72 nm [65], or of a mixed silica/tin oxide for a gradual change in refractive index [94-97]. Another possibility is a two layer system consisting of 18 nm of SnO$_2$:F and 28 nm of SiO$_x$C$_y$ [98, 99], or two layers of mixed silica/tin oxide [100]. The glass is coated with a first layer of 54 nm of SiO$_2$/SnO$_2$ with n~1.7, and thereafter with a second layer of 45 nm of SiO$_2$/SnO$_2$ with n~1.8 [101].

Another requirement for low-E coatings is low haze, e.g. diffusive transmission should be as low as possible. Monobutyltin trichloride [102] or monophenyltin trichloride [72] are very suitable precursors for producing haze free coatings. The haze can further be reduced by using an undercoat of ZnO [103], SiO_2 [104], or a thin layer, 10-30 nm, of tin oxide formed by oxidation of monophenyltin trichloride [70, 71]. The FTO layer will be deposited on top of the undercoat layer using p.e. tin tetrachloride or monobutyltin trichloride, and will assume the haze free characteristics of the undercoating.

Control of the balance between nucleation rate and crystal growth rate is another possibility. In a conveyor belt system, where the injector head is in the middle of the heated area with two exhausts at both ends, the nucleation starts upstream of the injector head. By reducing the crystal growth in this area, nucleation is improved. Crystal growth can be reduced by injecting dry air upstream of the precursor injector thereby preventing water reaching the nucleation site [105], or injecting a crystal growth inhibiting gas, like an alcohol or 1,1 difluoroethane [106].

2.6.2 Solar cells

Tin oxide coatings have found also extensive use in thin film solar cells made from hydrogenated amorphous silicon (a-Si:H). This type of solar cell consists of a glass plate, coated with a transparent conducting oxide such as fluorine doped tin oxide, a p-i-n structure made from a-Si:H, and a metal electrode, as is shown in figure 2.24 [68]. The amorphous silicon layer is deposited on top of the FTO layer using a silane plasma. Therefore, doping with fluorine is preferred over antimony, because antimony will diffuse in the a-Si:H layer above 250 °C, while small concentrations of fluorine doping seem not to be harmful [68]. In addition to a good chemical stability with respect to the highly reactive silane plasma, the tin oxide layer should have a high conductivity, a high transparency in the visible region, and optimal light scattering for an optimal operation of the solar cell. By scattering the light at a rough surface the light can be trapped in the a-Si:H layer for an increased light absorption, as is shown in figure 2.25 [84].
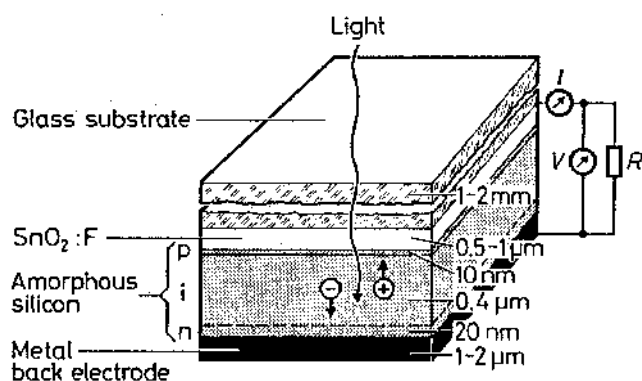
Figure 2.24: *Structure of a pin amorphous silicon solar cell [68].*
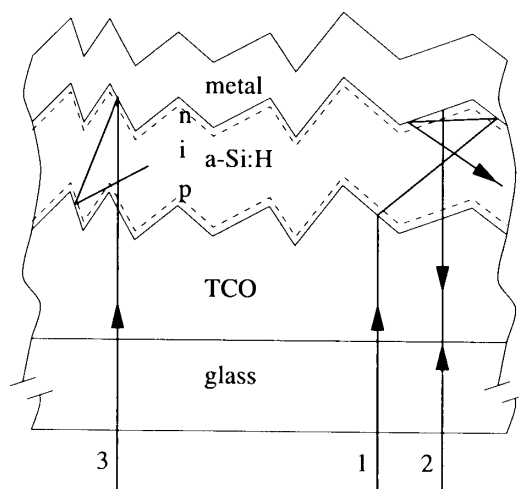
Figure 2.25: *Schematic representation of the light trapping effect [107].*

Gordon et al. [84] reported that only a small amount of haze, 4-6%, is needed to achieve the entire amount of light trapping. Very rough surfaces may introduce shunting which degrades the fill factor. In addition, also the morphology influences the performance of the solar cell. Jagged type surfaces, using low concentrations of TMT and oxygen, produced better quality cells than rod shaped surfaces [84]. This is supported by investigations of other authors [108, 109]. Sato et al. [109] investigated three types of surfaces, each with a different texture: a pyramidal shape with sharp edges (type A) , a hemi-spherical shape (type C), and an intermediate shape (type B. Their results are listed in table 2.5. A 1 cm^2 solar cell with a FTO layer with a pyramidal texture and a aluminium backcontact had the highest conversion factor of 12 %. Kim et al. [115] did a similar investigation with the same results. The highest conversion factor they obtained was 11.4% for a 3x3 mm^2 cell with a pyramidal-shaped FTO layer which had a haze ratio of 25%. In a later study Sato et al. [117] optimised the morphology even further to improve the conversion factors of a solar cell. They adjusted the morphology of type A to a more uniform surface structure with less steepened valleys or peaks. This type of morphology, designated by type U, was achieved by enhancing the crystallinity of the film. Because crystalline perfection is directly related to the concentration of impurities in the film, crystalline enhancement was achieved by decreasing the F-content of the film. Although the sheet resistance decreased, this effect was less important for application in a solar cell than the gain in conversion factor achieved by this type of morphology.

The thickness and surface roughness of a film are related to each other [12], but can be controlled separately by using a two-stage process [68]. The glass is first coated with a uniform, specular film from SnCl$_4$, HF/H$_2$O and methanol, and a second layer is deposited on top of it by using only SnCl$_4$ and HF/H$_2$O. The amount of texture is determined by the ratio of methanol to tin tetrachloride used in the first stage.

Table 2.5: *Properties of the four types of textured TCO films [109, 110].*

	Type A	**Type B**	**Type C**	**Type U**
Texture	pyramidal	medium	hemi-spherical	pyramidal without steep features
Thickness (Å)	8000	8000	8000	8000
Sheet resistance ($\Omega/\ $)	8	6	4	15-30
Optical absorption (%)	6	8	11	4
Pseudo-cell reflectance (%)	9	12	15	11
Effective transmission (%)	85	80	74	85

2.7 Conclusions

Although a vast number of investigations is present in the literature, with many different precursors for deposition of tin oxide, little is known about the chemistry of these processes. Tin oxide from oxidation or hydrolysis of tin tetrachloride is mainly formed by surface reactions, while tin oxide from dimethyltin dichloride (DMTC) and tetramethyltin (TMT) is formed by a combination of gas phase and surface reactions. Some attempts have been made to identify the reaction mechanisms of TMT+O_2 and DMTC+O_2 in the gas phase. Both processes include a branched chain reaction. The precursor looses a methyl radical in an initial step, followed by a sequence of reactions propagated by organotin radicals. A hydroxytin species, $(CH_3)Cl_2SnOH$ for DMTC oxidation and $(CH_3)_3SnOH$ for TMT oxidation, is proposed to be the key intermediate. Model simulations gave the same trends as found in experiments. However, the reported mechanisms only comprise reactions in the gas phase, the conversion of the key intermediate into solid tin oxide is not described. In addition the formation of by-products is not well described, and fitted kinetic parameters are often obtained from experiments in a reactor with transport limitations. Mechanisms for tin tetrachloride and for depositions with water still have to be constructed. For monobutyltin trichloride, a common precursor in industry, no growth rate data have even been reported yet.

In general there is little known about the specific steps of the mechanism of tin oxide deposition. In chapter 5 the mechanism and kinetics of tin oxide deposition from DMTC, O_2, and H_2O will be described and when possible compared to what has been proposed by Giunta et al. [38]

Tin oxide thin films with good optical and electrical properties can be made by chemical vapour deposition using organotin precursors as $SnCl_4$, TMT, DMTC, and MBTC. Sheet resistances down to 3 $\Omega/$ have been reported. Optical transmission and infrared reflectivity can be as high as 90%. The properties not only depend on the type of precursor used, but also on the deposition parameters, such as deposition temperature, deposition time, precursor flow rates and concentrations, annealing conditions, and additives used. Deposition temperature must be sufficiently high, in order to obtain high growth rates and high conductivity. Higher deposition times also lead to better layer quality. However, diffusion of alkali metal ions from glass substrates should be avoided.

The electrical properties of tin oxide from different tin precursors will be described in chapter 6 and compared with published values where possible.

Tin oxide layers are used in many different areas, such as low-emissivity windows in buildings, solar cells, flat-panel displays, and defrosting windows in vehicles. For each application a typical set of electrical and optical properties is required. Tin oxide layers applied in low-E windows need a very low haze value, which can be achieved by using MBTC as a precursor. Tin oxide layers in solar cells need a high haze value, which can be achieved by using $SnCl_4$ and water. Using methanol as an

additive in the beginning of the process the right type of morphology can be achieved for an optimal haze ratio.

References

[1] Jarzebski, Z. M., Marton, J. P. *J. Electrochem. Soc.*, **1976**, *123*, 199C.
[2] Jarzebski, Z. M., Marton, J. P. *J. Electrochem. Soc.*, **1976**, *123*, 299C.
[3] Jarzebski, Z. M., Marton, J. P. *J. Electrochem. Soc.*, **1976**, *123*, 333C.
[4] Chopra, K. L., Major, S., Pandya, D. K. *Thin Solid Films*, **1983**, *102*, 1.
[5] Hartnagel, H. L., Dawar, A. L., Jain, A. K., Jagadish, C. *Semiconducting transparent thin films*, IOP publishing Ltd., Bristol, **1995**.
[6] Reddy, S.R., Mallik, A.K., Jawalekar, S.R., *Bull. Mater. Sci.*, **1986**, 8, 357.
[7] Yusta, F.J., Hitchman, M.L., Shamlian, S.H. *J. Mater. Chem.*, **1997**, *7*, 1421.
[8] Oldershaw, G.A., Robinson, K. *J. Chem. Soc. A*, **1971**, 2963.
[9] Murty, N.S., Jawalekar, S.R. *Thin solid films*, **1983**, *102*, 283.
[10] Sundaram, K. B., Bhagavat, G.K., *J. Phys. D: Appl. Phys.*, **1981**, *14*, 333.
[11] Murty, N.S., Bhagavat, G. K., Jawalekar, S.R., *Thin solid films*, **1982**, *92*, 347.
[12] Tabata, O. *Proc. Int. Conf. Chem. Vap. Deposition*, **1975**, *5th*, 681.
[13] Ghoshtagore, R.N. *J. Electrochem. Soc.*, **1978***, 125(1)*, 110.
[14] Ghoshtagore, R.N. *Proc. Int. Conf. Chem. Vap. Deposition*, **1977**, *6th*, 433.
[15] Kleps, A.I., Battiston, G.A., Gerbasi, R., Guerriero, P., Podaru, C. . *Proceedings of the 14th International CVD conference and EuroCVD-11*, **1997**.
[16] Muranoi, T., Furukoshi, M. *Thin Solid Films*, **1978**, *48*, 309.
[17] Lou, J.C., Lin, M.S., Chyi, J.I., Shieh, J.H. *Thin Solid Films*, **1983**, 106, 163.
[18] Lindner, G.H., *US Patent 4737388*, **1988**.
[19] Advani, G.N.; Jordan, A.G.; Lupis, C.H.P.; Longini, R.L. *Thin Solid Films*, **1979**, *62*, 361.
[20] Gotoh, Y, Mizuhashi, M. *Asahi Garasu Kenkyu Hokoku*, **1984**, *34(2)*, 123.
[21] Sanon, G., Rup, R., Mansingh, A. *Thin Solid Films*, **1990**, 190, 287.
[22] Wartenberg, E.W., Ackermann, P.W., *Glastech. Ber.*, **1988**, 61, 256.
[23] Borman, C.G., Gordon, R.G., *J. Electrochem Soc.*, **1989**, 136, 3820.
[24] Vetrone, J., Chung, Y. W. *J. Vac. Sci. Technol. A*, **1991**, *9(6)*, 3641.
[25] Aleksandrov, Y.A., Baryshnikov, Y.Y., Zakharov, I.L., Lazareva, T.I., *Kinetika i Kataliz*, **1990**, 31, 727.
[26] Kamimori, T., Mizuhashi, M. *Proceedings of the 8th international CVD conference*, **1981**, 438.
[27] Wan, C. F., McGrath, R. D., Keenan, W. F., Frank, S. N. *J. Electrochem. Soc.*, **1989**, *136(5)*, 1459.
[28] Harrison, P.G., Ashworth, A., Clark, E.N., McManus, J., *J. Chem. Soc. Faraday Trans.*, 1990, 86, 4059.
[29] Zawadzki, A.G., Giunta, C. J., Gordon, R. G. *J. Phys. Chem.*, **1992**, *96(13)*, 5364.
[30] Johnson, R.P., Price, S.J.W. *Can. J. Chem.*, **1972**, *50*, 50.
[31] Fuller, M.J., Warwic, M.E., *J. Catal.*, **1973**, 29, 441.

[32] Chow, T.P., Ghezza, M., Baliga, B.J. *J. Electrochem. Soc.*, **1982**, *129*, 1040.

[33] Hsu, Y.-S., Ghandhi, S.K. *J. Electrochem. Soc.*, **1980**, *127*, 1592.

[34] Hsu, Y.-S., Ghandhi, S.K.. *J. Electrochem. Soc.*, **1979**, *126*, 1434.

[35] Adachi, K.; Mizuhashi, M. *Proceedings on the 10th international CVD conference*, **1987**, 999.

[36] Adachi, K.; Mizuhashi, M., *Reports Res. Lab. Asahi Glass Co., Ltd.*, **1988**, 38, 57.

[37] Strickler, D.A. *PhD. Thesis,* **1989**.

[38] Giunta, C. J., Strickler, D. A., Gordon, R. G. *J. Phys. Chem.*, **1993**, *97(10)*, 2275.

[39] Sanders, H. *Proceedings of the 14th International CVD conference and EuroCVD-11*, **1997**, 81.

[40] Kojima, M., Kato, H., Imai, A., Yoshida, A. *J. Appl. Phys.* **1988**, *64(4)*, 1902.

[41] Lou, J. C., Lin, M. S. *Thin Solid Films* **1983**, *110(1)*, 21.

[42] Sundaram, K. B., Bhagavat, G. K. *J. Phys. D: Appl. Phys* **1981**, *16(1)*, 69.

[43] Jawalekar, S. R. *Phys. Semicond. Devices, 3rd Proc. Int. Workshop* **1985**, 147.

[44] Sanon, G.; Rup, R.; Mansingh, A., *Phys. Status Solidi A* **1991**, *128(1)*, 109.

[45] Aboaf, J.A., Marcotte, V.C., Chou, N.J. *J. Electrochem. Soc.* **1973**, *120(5)*, 701.

[46] Ivashchenko, A.I., Khoroshun, I.V., Kiosse, G.A., Maronchuk, I. Yu., Popushoi, V., *Crystallography reports* **1997**, *42 (5)*, 901.

[47] Maruyama, T., Ikuta, Y., *Sol. Energy Mater. Sol. Cells* **1992**, *28(3)*, 209.

[48] Nishino, J., Ohshio, S., Saitoh, H., Kamata, K. *Mater. Res. Soc. Symp. Proc.* **1995**, *363*, 225.

[49] Sberveglieri, G., Nelli, P., Benussi, G. P., Depero, L. E., Zocchi, M., Rossetto, G., Zanella, P. *Sens. Actuators B* **1993**, *16(1-3)*, 334.

[50] Melsheimer, J., Ziegler, D. *Thin Solid Films* **1983**, *109(1)*, 71.

[51] Houng, K.H. *Bull. Inst. Chem., Acad. Sin.*, **1982**, *29*, 19.

[52] Baliga, B.J., Ghandhi, S.K. *J. Electrochem. Soc.* **1976**, *123*, 941.

[53] Kim, K.H., Lee, S.W., Shin, D.W., Park, C.G. *J. Am. Ceram. Soc.* **1994**, *77(4)*, 915.

[54] Ishida, T., Tabata ,O., Park, J.I., Shin, S.H., Magara, H., Tamura, S., Mochizuki, S., Mihara, T. *Thin Solid Films* **1996**, *282(1-2)*, 228.

[55] Jawalekar, S. R., *Phys. Semicond. Devices, Proc. Int. Workshop* **1985***, 3rd*, 147.

[56] Upadhyay, J. P., Vishwakarma, S. R., Prasad, H. C. *Thin Solid Films* **1998**, *169(2)*, 195.

[57] Soubeyrand, M.J., Halliwell, A.C. *US Patent 5698262* **1997**.

[58] Lindner, G. H. *US Patent 4,696,837* **1987**.

[59] Lindner, G. H. *US Patent 4,590,096* **1986**.

[60] O'Dowd, J. G., Catalano, A. W., Fortmann, C. M., Lee, O. J. *US Patent 4,880,664* **1989**.

[61] Akhtar, M. *US Patent 4,705,701* **1987**.

[62] Gordon, R. G. *US Patent RE31,708* **1984**.

[63] Russo, D. A., Lindner, G. H. *US Patent 4,601,917* **1986**.

[64] Yoldas, B.E., Mattox, D.M. *US Patent 4,293,594* **1981**.

[65] Gordon, R. G. *US Patent 4,187,336* **1980**.

[66] Vlahovic, B., Persin, M. *J. Phys. D: Appl. Phys* **1990**, *23(10)*, 1324.

[67] De, A., Ray, S. *J. Phys. D: Appl. Phys.* **1991**, *24*, 719.

[68] Plättner R., Stetter W., Köhler P. *Siemens Forsch.- u. Entwick.-Ber.* **1988**, *17(3)*, 138.

[69] Kato, Y., Kawahara, H., Hyohdou, M. *US Patent 4,500,567* **1985**.

[70] Lindner , G. H. *US Patent 4,737,388* **1988**.

[71] Lindner, G. H. *US Patent 4,788,079* **1988**.

[72] Lindner, G. H. *US Patent 4,600,654* **1986**.

[73] Bruno, L., Pijolat, C., Lalauze, R. *Sens. Actuators B* **1994**, *18(1-3)*, 195.

[74] Bruno, L., Lalauze, R., Pijolat, C., *Adv. Sci. Technol.* **1995**, *5*, 497.

[75] Mizuhashi, M., Gotoh, Y., Adachi, K., *Jpn. J. Appl. Phys., Part 1* **1988**, *27(11)*, 2053.

[76] Proscia, J., Gordon, R. G. *Thin Solid Films* **1992**, *214(2)*, 175.

[77] Belanger, D., Dodelet, J. P., Lombos, B. A., Dickson, J. I., *J. Electrochem. Soc.* **1985**, *132(6)*, 1398.

[78] Ma, H., Zhang, D., Chen, Y., Li, S., Ma, J., Zong, F. *Proc. SPIE-Int. Soc. Opt. Eng.* **1996**, *2897*, 104.

[79] Ma, H. L., Zhang, D. H., Win, S. Z., Li, S. Y., Chen, Y. P. *Sol. Energy Mater. Sol. Cells* **1986**, *40(4)*, 371.

[80] Kaneko, H., Miyake, K. *J. Appl. Phys.* **1982**, *53 (5)*, 3629.

[81] Choudhury, C., Sehgal, H. K. Energy Convers. Manage. **1989**, *29(4)* , 265.

[82] Hattori, T., Itoh, S., Tagawa, T., Murakami, Y. *Stud. Surf. Sci. Catal.* **1987**, *31*, 113.

[83] Baliga, B. J., Ghandhi, S. K. *Tech. Dig. - Int. Electron Devices Meet.* **1975**, 105.

[84] Gordon, R.G., Proscia, J., Ellis Jr., F.B., Delahoy, *A.E. Sol. Energy Mater.*, **1989**, *18*, 263.

[85] Vincent, C.A. *J. Electrochem. Soc.* **1972**, *119*, 515.

[86] Kane, J., Schweizer, H. P.; Kern, W., *J. Electrochem. Soc.* **1976**, *123(2)*, 270.

[87] Saxena, A. K., Thangaraj, R., Singh, S. P., Agnihotri, O. P., *Thin Solid Films* **1985**, *131(1-2)*, 121.

[88] Hu, J., Gordon, R. G. *AIP Conf. Proc.* **1992**, *268*, 381.

[89] Lindner, G.H. *US Patent 4737388* **1988**.

[90] Kim, K., Finstad, T. G., Chu, W. K., Cox, X. B., Linton, R. W., *Sol. Cells* **1985**, *13(3)*, 301.

[91] Haacke, G. *J. Appl. Phys*. **1976**, *47*, 4086.

[92] Gordon, R. G., *J. Non-Cryst. Solids* **1997**, *218*, 81.

[93] Mizuhashi, M., Gotoh, Y. *Repts. Res. Lab., Asahi Glass Co., Ltd* **1982**, *32 (2)*, 79.

[94] Athey, P.R., Dauson, D.S., Lecocq, D.E., Neuman, G.A., Sopko, J.F., Stewart-Davie, R.L., *US Patent 5464657* **1995**.

[95] Gordon, R G. US Patent 4,206,252 **1980**.

[96] Gordon, R G. US Patent 4,308,316 **1981**.

[97] Gordon, R. G. US Patent 4,440,822 **1984**.

[98] Gordon, R. G. US Patent 4,377,613 **1983**.

[99] Gordon, R. G. US Patent 4,419,386 **1983**.

[100]Gordon, R. G. US Patent 4,612,217 **1986**.

[101]Neuman, G. A., Stewart-Davis, R. L. US Patent 5,395,698 **1995**.

[102]Russo, D. A., Lindner, G. H. US Patent 4,743,506 **1988**.

[103]Terneu, R., Van Cauter, A. US Patent 4,329,379 **1982**.

[104]Neuman, G. A. US Patent 5,744,215 **1998**.

[105]Ellis, Jr., F. B. US Patent 5,393,563 **1995**.

[106]Ellis, Jr., F. B. US Patent 5,487,784 **1996**.

[107]Wallinga, J. Thesis Utrecht Univ. **1998**.

[108]Kim, W.-Y., Shibata, A., Kazama, Y., Konagai, M., Takahashi, K. *Jap. J. App. Phys.* **1989**, *28 (3)*, 311.

[109]Sato, K., Gotoh, Y., Hayashi, Y., Adachi, K., Nishimura, H. *Reports Res. Lab. Asahi Glass Co., Ltd.* **1990**, *40 (2)*, 233.

[110]Sato, K., Gotoh, Y., Wakayama, Y., Hayashi, Y., Adachi, K., Nishimura, H. *Reports Res. Lab. Asahi Glass Co., Ltd.* **1992**, *42(2)*, 129.

Chapter 3. Experimental system

Abstract

As was shown in chapter 2, some attempts have been made to identify the mechanism of tin oxide deposition. However, these studies were carried out in reactor systems, which also exhibited heat and mass transfer phenomena, thereby making it difficult to extract real kinetic data. This chapter describes a system, where the concentration and temperature distribution in the reactor is homogeneous by using a continuously stirred tank reactor (CSTR). Directly coupled to this reactor are an Fourier transform infrared spectrometer and a mass spectrometer, allowing in-situ study of the gas phase composition. The reactor can be fed by dimethyltin dichloride (DMTC), oxygen, water, nitrogen, and other gases. The flow rate of species, which are in the gas phase at room temperature are controlled by calibrated mass flow controllers. The flow of DMTC, which is a liquid at room temperature, is controlled by its vapour pressure, which will be discussed in chapter 4. Chapter 5 discusses the experimental results of a study of the kinetics of tin oxide deposition from DMTC using the system described here.

3.1 Introduction

In order to simulate the tin oxide deposition process in different types of reactors, it is imperative to know the intrinsic reaction kinetics. This means that when studying the reaction chemistry of tin oxide CVD, the influence of heat and mass transfer/transport must be excluded. A second requirement is in-situ monitoring of the reaction chemistry so that transient effects can be neglected and a direct comparison can be made between observed growth rates and the measured gas phase composition.

In section 3.2 a description is given of a continuously stirred tank reactor system for atmospheric tin oxide CVD, which deals with these requirements. In this reactor *in-situ* intrinsic deposition rates can be measured during continuous flow experiments, whereas also the gas phase composition in the reactor can be determined *in situ,* simultaneously. Section 3.3 deals with the feasibility of this reactor set-up. An overview of the experimental procedures, materials, and methods of data acquisition is given in section 3.4.

3.2 Reactor set-up

The reactor set-up, depicted schematically in figure 3.1, consists of a feed section, a reactor section, and an analysis section. In the following, these three sections will be discussed in detail.

Feed section

The deposition of tin oxide is carried out by oxidation or hydrolysis of the precursor dimethyltin dichloride (DMTC). It is evaporated at a temperature of 425 K, using nitrogen (quality 5.0, Hoekloos) as carrier gas. Extra nitrogen can be added to the nitrogen/DMTC flow to control the total volumetric flow of precursor and carrier gas. The evaporation of DMTC is established in a glass/stainless steel vessel, suspended in an oil bath. The oil bath temperature is controlled to within 0.2 K. Also the carrier gas entering the bubbler is preheated to 425 K, by passing it through the same oil bath by means of a coil of 1.5 m length. The gas leaving the bubbler is heated to 445 K to prevent condensation of DMTC.

The flow rate of DMTC can be calculated by using the vapour pressure of DMTC, of which its determination is described in chapter 4:

$$F_{DMTC} = \frac{X}{1-X} F_{N_2} \qquad (3.1)$$

with F_{DMTC} = Flow of DMTC leaving the bubbler [SLM]

F_{N_2} = Flow of nitrogen entering the bubbler [SLM]

X = Relative vapour pressure of methanol at the temperature of the bubbler [-]

The relative vapour pressure, X, of methanol can be calculated by the relation:

$$X = \frac{10^{8.94 - 2800/T}}{760} \qquad (3.2)$$

with T = temperature of the bubbler [K]

Both oxygen (quality 5.0, Hoekloos) and water can be used as oxidants. Again for these reagents nitrogen is used as carrier gas. Optionally, helium or argon can be used as carrier gas in both gas flows. Water is evaporated with a Controlled Evaporation Mixing-unit (Bronkhorst Hi-tec), which allows stable and reproducible flows of water vapour, or, optionally, with a reflux column if high flow rates are required. Nitrogen is used as purge gas to protect the electronic part of the microbalance and both sides of the optical windows of the Fourier Transform Infrared Spectrometer (FTIR). The flow rates of all process gases are established with thermal mass flow controllers (Bronkhorst Hi-tec or Brooks).

Reactor section

The atmospheric pressure laboratory reactor set-up consists of a fused silica continuous flow reactor, as shown in figure 3.2. Spherical geometry was chosen as it favours mixing and uniformity of heat transfer. The feed is injected through the four nozzles of a cross-shaped injector, located in the middle of the reactor. To prevent reaction in the inlet tubes, the tin oxide precursor and the oxidant are fed separately to the reactor by two nozzles for each feed. The nozzles are located in two orthogonal planes, midway between the centre of the reactor and the wall. To ensure good mixing, the inner diameters of the reactor, $1.2 \ 10^{-1}$ m, and of the nozzles, $1.0 \ 10^{-3}$ m, are derived on the basis of hydrodynamic criteria for jet stirred reactors, as proposed by David and Matras [1]. These criteria are presented in appendix A. They state: 1) that the jets originating from the four nozzles have to be turbulent and fully developed, 2) that the reactor content must be recycled by the jets, and 3) that the maximum velocity of the gases flowing through the nozzles should be kept below the sonic velocity of the particular gas at the pressure and temperature under consideration, to prevent shock waves in the reactor. The use of these criteria ensures that the residence time distribution of the reactor is very close to that of a perfect mixer. However, as was shown by Azay and Côme [2], such reactor still can exhibit very strong temperature gradients, which only can be eliminated by a sufficient preheating of the fed gases. Therefore, the gases were preheated to a maximal temperature of 773 K prior to introduction into the reactor. The highest temperature used in this study, 883 K, is sufficient to ensure a homogeneous temperature distribution in the reactor [2].

The above reactor configuration permits space (residence) times between 0.6 and 4.5 s at a reactor temperature of 673 K, between 0.5 and 2.8 s at 918 K, and between 0.5 and 2.2 s at 1073 K. The reactor temperature is regulated to obtain isothermal operating conditions. The reactor is heated by means of an electrical resistance oven of spherical shape, with a heating capacity of 1000 W. The temperature regulation of the oven is performed by means of a PID-controller (Watlow), using a thermocouple located in a thermo-well, placed near the glass substrate. Reactor temperatures up to 1100 K can be obtained.

In the middle of the reactor, just above the injector, a 10 x 10 mm^2 glass substrate is suspended from an electro-balance, to measure *in situ* deposition rates. To monitor the progress of the CVD reaction in the gas phase by means of FTIR, the reactor is equipped with two cylinders in line and level, protruding through the oven, as is shown in Figure 3.2. Both are fitted with a KBr-window, coated with BaF_2. The optical path in this configuration is located through the middle of the reactor, close to the substrate surface.

Analysis section

The weight increase of the substrate, due to deposition of tin oxide, is measured as a function of time by means of an electro-balance (C.I. Electronics). This balance can be operated in the weight range from 0 to 50 mg, with a resolution of 0.1 mg under ideal circumstances. Analysis of the gas phase in the reactor is performed by means of FTIR and mass spectrometry. The FTIR (MIDAC 2500) has a spectral resolution between 0.5 and 32 cm^{-1}, and is equipped with an MCT (Mercury
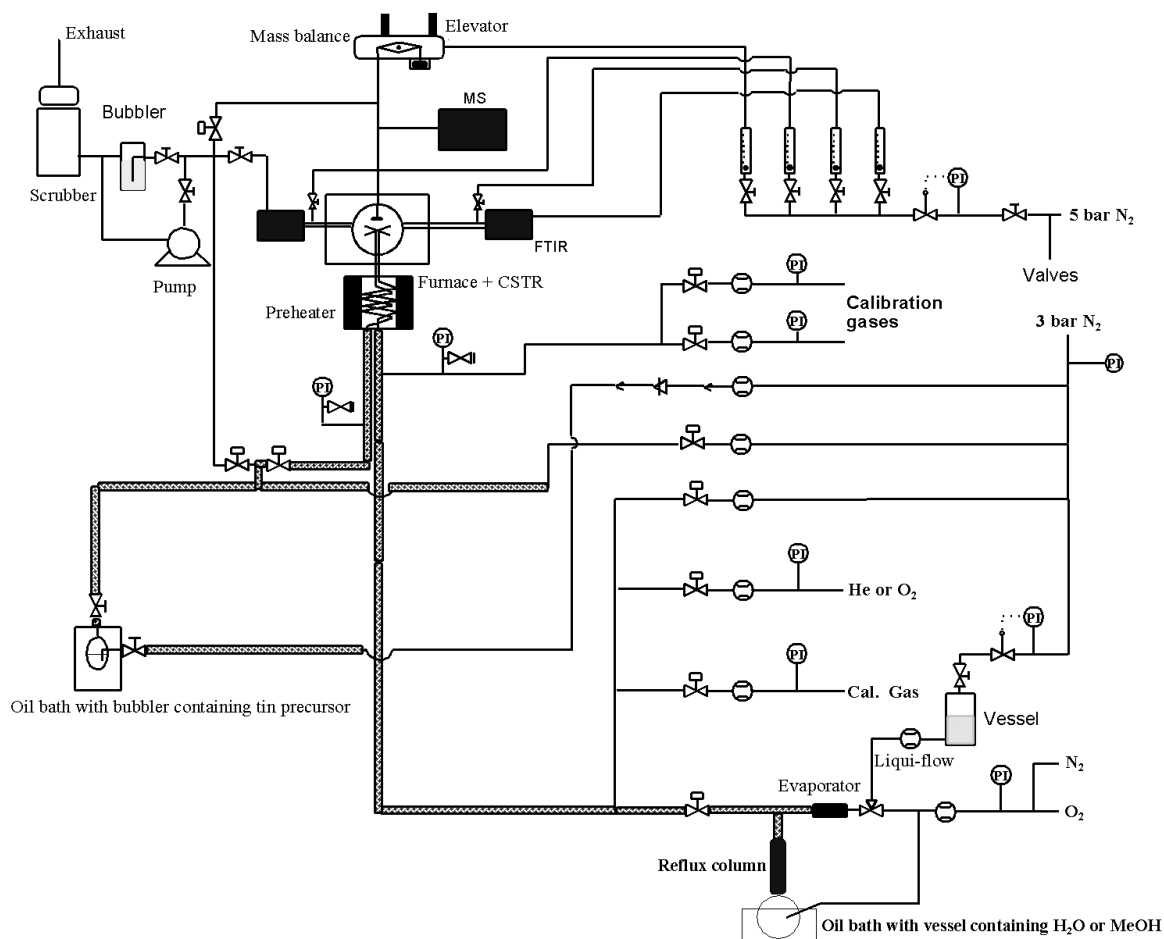
Figure 3.1: *Experimental set-up of CSTR-reactor system.*
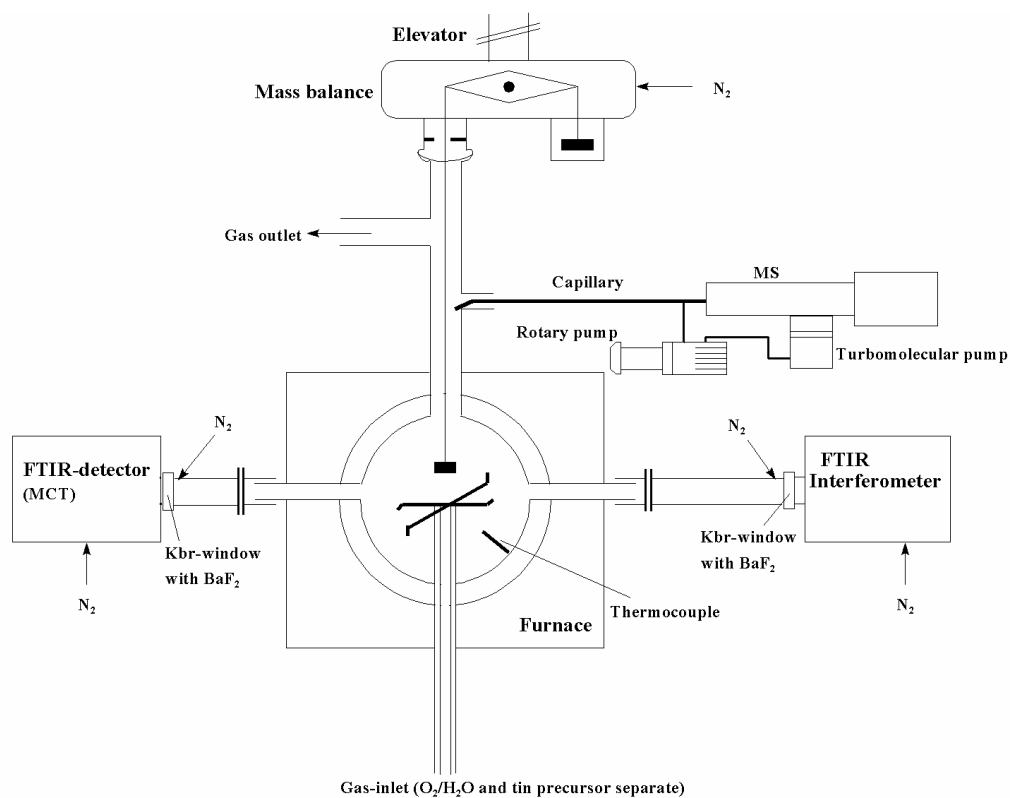
Figure 3.2: *CSTR reactor, including inlet nozzles, FTIR, Mass Spectrometer and Mass Balance.*

Cadmium Telluride) or a DTGS (Deuterated TriGlycine Sulfate) detector. The FTIR data are processed with multivariate calibration techniques, such as classical least squares (CLS) analysis, or partial least squares analysis (PLS). The mass spectrometer (Fisons SXP Elite) has a range of 600 amu and a resolution of 0.1 amu.

3.3 Reactor performance

The concentration uniformity of the reactor was checked by placing the capillary of the mass spectrometer at various positions in the reactor. The reactor was kept at room temperature. A flow of 5 mol% CO_2 in N_2 was maintained with a space time of 2s in the reactor. As can be seen in figure 3.3 the concentration distribution of CO_2 was uniform within the error margins of the measurements. In order to test the influence of the side arms with the purge gas, a second experiment measured the mass spectrum response from the middle of the reactor to the end of the side arms. The measured response was the same throughout the reactor, except when the capillary was placed in the opening of the nozzle which supplied CO_2. Here the response was somewhat higher. The response at the interface was still the same as in the rest of the reactor. After 1 cm (position O in figure 3.3) in the side arm the response of CO_2 drops towards practically zero. These experiments show that the flow regime in the CSTR reactor is sufficiently turbulent to ensure a homogeneous gas mixture throughout the reactor.
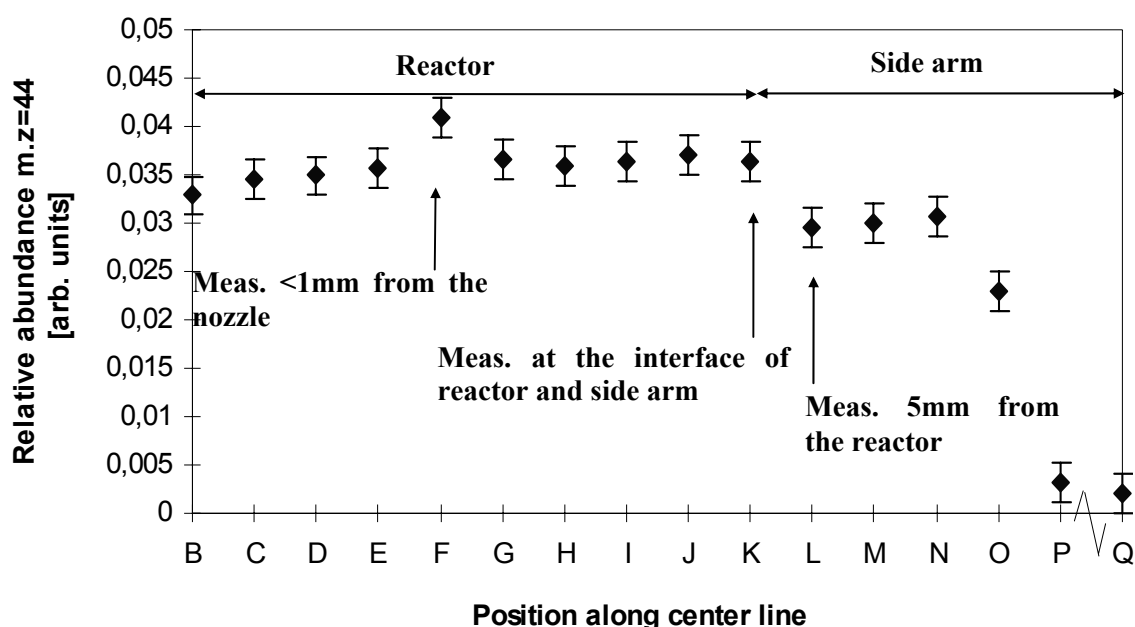
Figure 3.3: *The relative intensity of m/z = 44 as measured by the mass spectrometer from the middle of the reactor (B) to the end of the side arms (Q). The scale is approximately linear, except between P and Q. The distance B-P is about 100 mm. The reactor was at room temperature, space time was 2 s and the concentration of CO_2 in N_2 was continuously kept at 5 mol%.*

3.4 Analysis methods

The reactor system described in the preceding sections is used to study the intrinsic chemistry and kinetics of the CVD of tin oxide. Tin oxide is deposited in the reactor under a fixed set of process conditions, i.e. reactor temperature, space-time, and precursor, O_2, and H_2O concentration. During the deposition, FTIR and mass spectra are taken for revealing the gas phase composition in the reactor. In some cases the deposition is carried out with a substrate suspended in the reactor, providing a direct gravimetric measurement of the deposition rate of tin oxide. By conducting depositions under various conditions in terms of reactor temperature, and precursor, oxygen, and water concentrations, the mechanism and kinetics of the deposition process can be elucidated. In the subsequent sections, the theory and methods for quantification of FTIR and mass spectrometry data are given.

3.4.1 FTIR spectroscopy

A molecule can absorb radiation with a certain wavelength if a transition between energy states in the molecule corresponds to the energy of a photon with that wavelength. For vibrational energy transitions, the energy difference corresponds to the infrared (IR) regime in the electromagnetic spectrum. The selection rule for these transitions is that during transition change in dipole moment of the molecule. Therefore, almost all except homonuclear diatomic molecules absorb energy corresponding to IR-radiation, making IR-spectroscopy ideal for determination of the gas phase composition. The molecular composition of a sample can be probed by several methods among which Fourier Transform Infra Red (FTIR) spectroscopy has become increasingly more important by the advance of high-speed computers. This method is non-intrusive and is able to scan a large segment of the infrared spectrum in a short time (~1s) at high resolutions (~0.5 cm^{-1}).

In the next section a short overview of the background of FTIR is given, followed by an overview of some of the issues that have to be dealt with when probing the gas phase with the FTIR setup as described in section 3.2. The last section lists the frequency ranges used for quantifying the composition of the gas phase during a typical deposition experiment.

FTIR background

In an FTIR spectrometer, a Michelson interferometer divides a beam of radiation into two paths, which recombine again after a path difference has been introduced. A schematic representation is shown in figure 3.4. An infrared source, e.g. a SiC-rod, emits a beam of radiation, which hits the beam splitter. Here one half of the beam is transmitted to a moving mirror and one half is reflected to a fixed mirror. The two beams reflect at the mirrors and recombine at the beamsplitter, after which one half is transmitted and one half is reflected again. When the two beams meet at the beamsplitter, they interfere, resulting in a beam going back to the radiation source and a beam going to the detector. The intensities of the beams going back to the radiation source and passing to the detector depend on the difference in distance of the two mirrors to the beamsplitter. Although two beams come out the

interferometer containing equivalent information, only one beam is passed to the detector because of the difficulty separating the beam returning from the beamsplitter to the radiation source from the beam that is emitted from the radiation source.

After passing the beamsplitter the two beams reflected back by the two mirrors have a path length difference of 2(OM-OF) = δ (figure 3.4). This is called retardation. With zero retardation the beams are in phase and there is maximum constructive interference. If δ=½λ, with λ the wavelength of the light beam, the mirror has moved ¼λ, the beams are completely out of phase and there is maximum destructive interference. If δ=λ, there is maximum constructive interference again. In the case the IR-source is monochromatic with intensity $I''(\nu)$ with $\nu = 1/\lambda$ (cm^{-1}), the intensity I' of the beam reaching the detector can be described by:

$$I'(\delta) = 0.5I''(\nu)\left[1+\cos(2\pi\,^{\delta}/_{\lambda})\right] \quad = \quad 0.5I''(\nu)\left[1+\cos(2\pi\nu\delta)\right] \tag{3.3}$$

I'(δ) is composed of a component independent of the retardation, equal to 0.5I''(ν), and a modulated component, which is dependent on the retardation, equal to 0.5I''(ν)cos(2πνδ). In general only the modulated term is considered in spectroscopy and is referred to as the interferogram, I(δ).
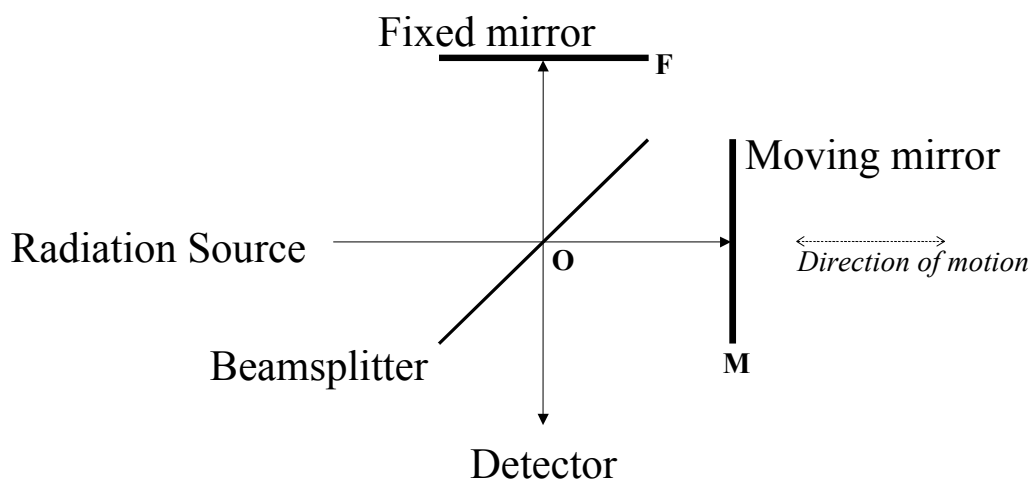
Figure 3.4: *Schematic representation of the Michelson interferometer. Radiation emitted by a source is split into two beams by the beamsplitter. One beam reflects on a fixed mirror and one beam reflects on a moving mirror. At the beamsplitter the two beams recombine. Because of a phase difference caused by the movement of one of the mirrors, the resulting beam is modulated.*

In practice, various other factors influence the signal measured by the detector:
· The beamsplitter may not have the ideal characteristics of 50% transmittance and 50% reflectance.
· Detectors and electronic amplifiers may not have a uniform response to all wavenumbers.

These effects can be taken into account by multiplying I''(ν) by a wavenumber dependent correction factor, H(ν), which then accounts for the beamsplitter efficiency, the detector response, and the amplifier characteristics. Setting B(ν) = 0.5H(ν)I''(ν) gives:

$$I(\delta) = B(\nu)\cos(2\pi\nu\delta) \qquad (3.4)$$

B(ν) represents the intensity of the radiation source at wavenumber ν as modified by the instrumental characteristics. I(δ) is the cosine transform of B(ν). With most interferometers the moving mirror has a constant velocity u, giving an interferogram that varies with time according to:

$$I(t) = B(\nu)\cos(2\pi\nu \cdot 2ut) \qquad (3.5)$$

If the radiation source is not monochromatic, but continuous, as in real life applications, the interferogram represented by equation 3.4 changes in an integral, with I(δ) and B(ν) being each others Fourier transform:

$$I(\delta) = \int_{-\infty}^{\infty} B(\nu)\cos(2\pi\nu\delta)d\nu \qquad \text{and} \qquad B(\nu) = \int_{-\infty}^{\infty} I(\delta)\cos(2\pi\nu\delta)d\delta \qquad (3.6)$$

However, real life applications put some constraints onto the applicability of equation 3.6. It is impossible to scan the moving mirror between distances 0 and ∞. Further, if the Fourier transform is carried out by a computer, the interferogram has to be digitised at a finite sampling range. The maximum resolution that can be obtained by a maximum retardation of the mirror of Δ_{max}, is then given by:

$$\Delta\nu = (\Delta_{max})^{-1} \qquad (3.7)$$

The response at a certain wavenumber or frequency is not an infinitely thin line anymore, but a function of wavenumber, with a certain width and side lobs. Especially the side lobs can be problematic when quantifying absorption bands. However by applying a mathematical weighting function in equation 3.6, the magnitude of these side lobs can be suppressed. This procedure is called apodisation of which a more thorough explanation can be found in [3].

The FTIR spectra described in this thesis were determined using an apodisation function called medium Norton-Beer [3] and have a resolution of 0.5 cm^{-1}. Because of the limited energy range of the mercury cadmium telluride (MCT) detector used in this work, only molecules with absorption characteristics between 400 and 5000 cm^{-1} can be detected. An example of an FTIR spectrum recorded during a typical deposition experiment is shown in figure 3.5.
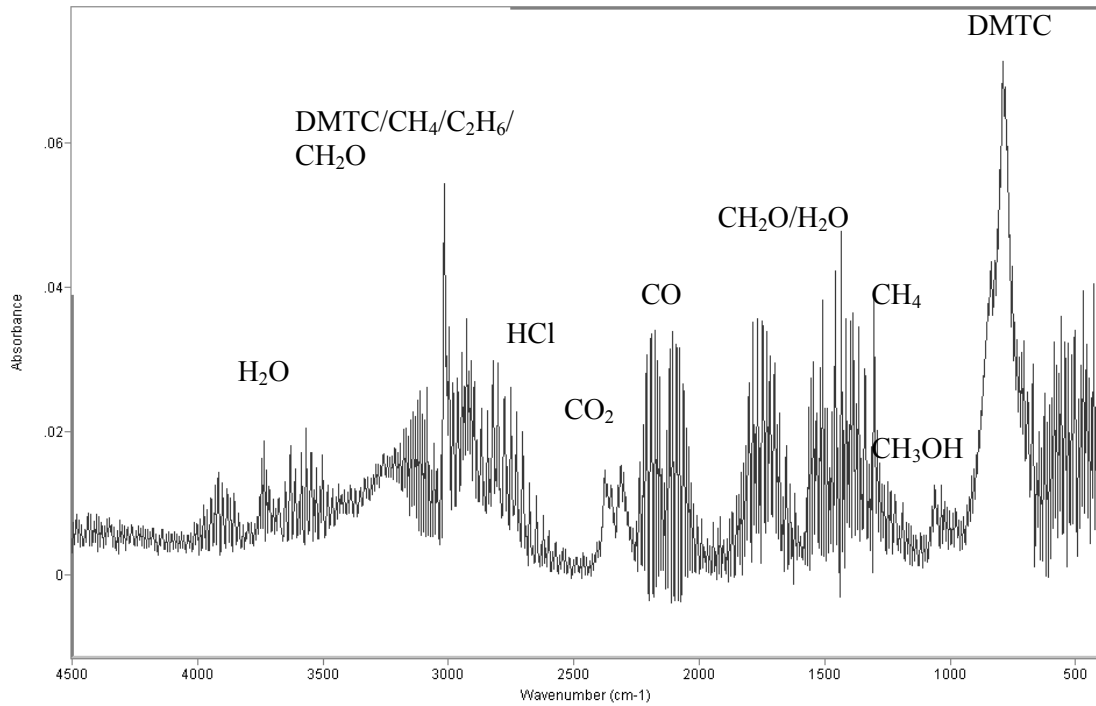
Figure 3.5: *FTIR spectrum (32 scans averaged) recorded during the deposition of tin oxide from 2 vol% DMTC and 20 vol% O$_2$, balance N$_2$. Reactor temperature is 530 °C, reactor space-time is 2 s.*

Quantification of FTIR spectra

The FTIR spectrum can be used for quantification of the composition of a sample by applying Beer's law, which states that the absorbance A of a compound j, is proportional to the concentration of that compound:

$$A = \log \frac{I(\nu)}{I_0(\nu)} = -\alpha_j \cdot [j] \cdot l \qquad (3.8)$$

with I(ν) = the intensity measured by the detector after the beam has passed a sample

     I$_0$(ν) = the intensity measured by the detector after the beam has passed the background, i.e. without the sample present.

    α_j = molar absorption coefficient or extinction coefficient of compound j

    [j] = the molar concentration of species j in the sample

    l = the pathlength of the beam through the sample

However, there are some issues, which have to be taken into account when using FTIR spectra for quantifying the composition of a gas sample:

71

1. Phase correction.

   In practice, an extra term -ε has to be added to the phase angle, $2\pi v\delta$, in equation 3.6, to describe the actual interferogram. These corrections to the phase angle may arise due to various optical, electronic, or sampling effects. The result of this is that equation 3.6 is modified into:

$$I(\delta) = \int_{-\infty}^{\infty} B(v)\cos(2\pi v\delta - \varepsilon)dv \qquad (3.9)$$

   Because of the trigoniometric property, cos (α - β) = cosα·cosβ + sinα·sinβ, the addition of a second term to the phase angle has the effect of adding sine wave components to the cosine wave interferogram. The removal of the sine components from an interferogram is known as phase correction. One of the major causes for phase correction in the case of this work was mirror misalignment. Unfortunately, this was concluded after the finalisation of the experiments. The software used in this work, GRAMS/32 4.1 (Galactic Instruments Inc.), has a standard phase correction method incorporated for calculating a spectrum from the data obtained from the detector. However, as can be seen in figure 3.6, the sine components, represented by the negative absorption peaks, are still present in the line shape. The current software has no options for modifying the phase correction method, so almost all spectra used in this work have sine wave components in the line shape, resulting in negative ghost peaks near an absorption feature. The calibration spectra were determined in the same manner, viz., with the same software without the phase correction option. Therefore, the influence of this lack of phase correction on the quantification of the compound concentrations is considered to be very limited.

2. Non-linearity of the MCT detector.

   MCT detectors are known not to be completely linear with respect to the response to the amount of infrared radiation reaching the detector. In order to quantify this non-linearity an experiment was conducted where the absorption of a sheet of plastic was measured at various IR beam intensities. The intensity of the beam was controlled by use of a diaphragm, which regulated the diameter of the modulated IR beam. The intensity of the beam was quantified by measuring the alignment percentage, which is a measure for the amount of light reaching the detector. As can be seen in figure 3.7, the IR response varies with the beam intensity over the whole range used in the measurements. If the FTIR is to be used for quantification of the gas phase composition in the reactor it is clearly very important to keep the alignment of the FTIR setup as constant as possible between experiments. In this way, the beam intensity on the detector, without the sample present, is constant, so that the non-linearity of the MCT detector has not to be taken into account.
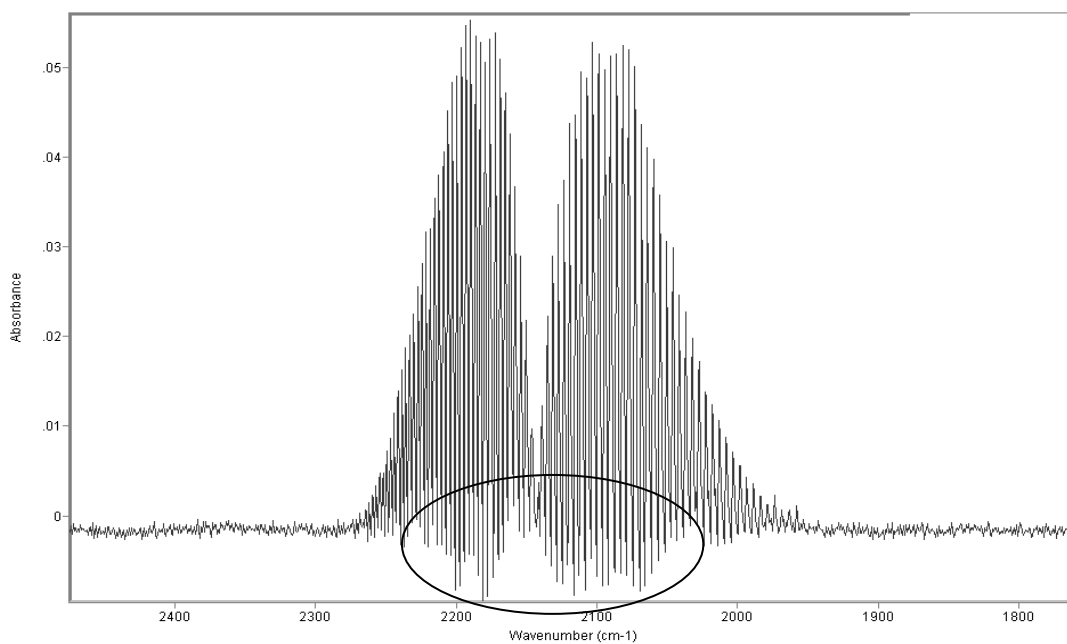
Figure 3.6*: Calibration spectrum of CO. The spectrum was recorded at 530 °C, with 1 mol% CO in N_2. The negative peaks (circled) are probably due to mirror misalignment and could not be corrected for.*
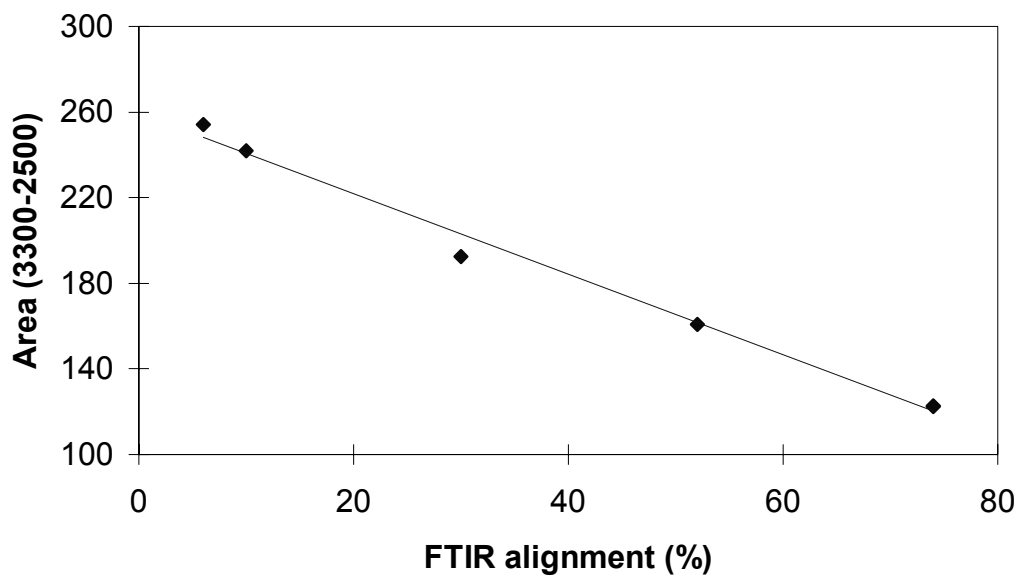
Figure 3.7: *Absorption area of a plastic sheet measured with various intensities of the IR beam.*

3. Interference.

In practice, an absorption feature can only be used if it originates from a single component, and has no interference with absorption features of other components. For some species such a feature is difficult to find, and therefore it is necessary to use an absorption peak of relatively low intensity. In the case of tin oxide deposition from DMTC and O_2, one of the by-products formed is HCl. The absorption peaks corresponding to the H-Cl stretch are located between 2600 and 3200 cm^{-1}. However, in this region also absorption occurs from other compounds as DMTC, CH_4, C_2H_6, CH_2O, and CH_3OH. For quantifying the amount of HCl,two small peaks are used in the spectrum between 2731.3 and 2695.1 cm^{-1}, resulting in a lower sensitivity. The identification and quantification of ethane is impossible because the absorption features are completely hidden by absorption features of other compounds.

4. Dependence on temperature.

Because most absorption features are not only due to a change in vibrational state, but also due to a change in rotational state, the spectra of most compounds are dependent on the temperature. In principle this would mean that every compound has to be calibrated at every temperature at which an experiment was conducted. However, for some compounds, such as DMTC, this is rather difficult because they decompose at higher temperatures. One way to circumvent this problem is to calibrate not for peak height at a certain wavenumber, but to calibrate the area under one or more absorption peaks. As is shown in figure 3.8 the calibration curve for peak height varies with temperature, because of the different distribution of rotational states. However, if the complete area under the P and R rotational absorption branches of CO is taken, the dependence on temperature for the calibration curve is negligible.
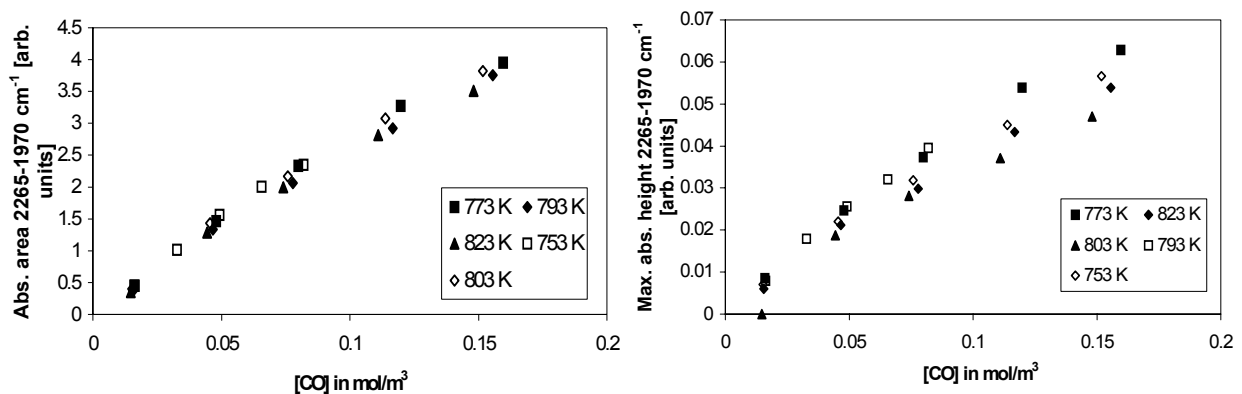
Figure 3.8: *Calibration graphs for CO at various temperatures. The left graph shows the calibration curves using the area under the absorption features between 2265 and 1970 cm^{-1}. The right graph shows the calibration curve for the height of the strongest absorption feature in the spectrum.*

Overview of frequencies used for calibration
Taken into account the problems stated above, the following wavenumbers or wavenumber ranges were selected for quantification of the concentration of various compounds in the gas phase:

DMTC: $970\text{-}635$ cm^{-1}
CO_2: 670 cm^{-1}
CO: $2265\text{-}1970$ cm^{-1}
CH_4: 1305 cm^{-1}
H_2O: $4080\text{-}3360$ cm^{-1}
CH_2O: 1742 cm^{-1}
CH_3OH: 1030 cm^{-1}
HCl: $2731.3\text{-}2695.1$ cm^{-1}

Reliability of measurements

The reproducibility of the FTIR-spectra was tested in two ways:
1. After a major system clean-up, a FTIR-spectrum was recorded using a set of standard deposition conditions, and compared with a spectrum recorded before the system clean-up.
2. Before every experimental series, a FTIR-spectrum of CO_2 was recorded and compared with previous measurements.

In general the spectra of an experiment with a set of standard conditions, but recorded on different times, differed less than 5%. This error margin is based on the area under the main peaks.

The signal-to-noise ratio (SNR) of the spectra is dependent on the absolute peak heights and the frequency. For quantification of compounds only those peaks are taken, so that the SNR<15%.

Determination of activation energy
The FTIR signals can be used to determine the overall activation energy of conversion of for example DMTC. It is calculated by solving the mass balance for DMTC:

$$F_V \cdot [DMTC]_{in} - F_V \cdot [DMTC]_{out} = R_V \cdot V \qquad (3.10)$$

with: F_V = volumetric gas flow rate in m^3/s
      $[DMTC]_{in}$ = molar concentration of DMTC going into the reactor in mol/m^3
      $[DMTC]_{out}$ = molar concentration of DMTC leaving the reactor in mol/m^3
      R_V = volumetric reaction rate in mol.m^{-3}.s^{-1}
      V   = volume of the reactor in m^3

In equation 3.10 the assumption has been made that the density of the gas stays constant during reaction. This assumption is valid, because the concentration of tin precursor used is always below 5%.

Assuming a first order reaction rate in DMTC, the volumetric reaction rate can be written as:

$$R_V = A \cdot e^{-E_{act}/R \cdot T} \cdot [DMTC] \tag{3.11}$$

with: A = overall Arrhenius pre-exponential factor in s^{-1}
  E_{act} = overall activation energy in J/mol
  R = universal gas constant, 8.3144 $J.mol^{-1}.K^{-1}$
  T = reactor temperature in K
  $[DMTC]$ = concentration DMTC in the reactor in mol/m^3

In a perfect CSTR reactor, the species concentration leaving the reactor is the same as the species concentration inside the reactor. Replacing R_V in equation 3.8 by the expression in equation 3.9, the mass balance can be rearranged to give the overall activation energy by:

$$\ln\left(\frac{[DMTC]_{in}/[DMTC]_{out} - 1}{\tau}\right) = \ln(A) - \frac{E_{act}}{R} \cdot \frac{1}{T} \tag{3.12}$$

with: τ = space time in the reactor in s

The inlet concentration of DMTC is known and the concentration of DMTC inside the reactor is measured by FTIR. By plotting the left hand side of equation 3.10 versus 1/T, the slope of a linear least-squares fit gives $-E_{act}/R$. This activation energy represents the overall activation energy of conversion of DMTC.

For determination of the overall activation energy of deposition of tin oxide, a similar approach exists. In this case, the conversion of tin precursor is not used, but the deposition rate of tin oxide:

$$R_A = R_V \cdot 1/a_V \tag{3.13}$$

with R_A = deposition rate of tin oxide on the surface in $mol.m^{-2}.s^{-1}$
  a_V = the surface-to-volume fraction of the reactor in m^2/m^3

Again assuming a first order dependence of the reaction process on the tin precursor, e.g. DMTC, equation 3.11 can be written as:

$$k = \frac{R_A \cdot a_V}{[DMTC]} \tag{3.14}$$

with: k = reaction rate coefficient in s^{-1}

The concentration DMTC can be solved from the mass balance as shown in equation 3.8, resulting in:

$$k = \cfrac{1}{\cfrac{[DMTC]_{in}}{R_A \cdot a_V} - \tau}$$
(3.15)

By plotting the natural logarithm of the right hand side of equation 3.13 versus 1/T, the slope of a linear least-squares fit gives -E_{act}/R. This activation energy represents the overall activation energy for the deposition of tin oxide.

3.4.2 Mass spectrometry

The gas phase composition was also monitored with a differentially pumped quadrupole mass spectrometer (Fisons SXP Elite 600), containing an enclosed ion source and an electron multiplier detector. The detection limit is about 1 ppm. The high vacuum inside the analysis chamber is maintained by a turbomolecular pump (Balzers), backed by a rotary vane pump (Leybolds). The reactor gas is sampled by a heated silica capillary, which is pumped by a rotary vane pump (Leybolds). The capillary is connected to the ion source via a silica grid. The pressure in the ion source can be regulated by a needle valve placed between the rotary vane pump and the capillary. This pressure is maintained at 1.10^{-4} Pa. Both the capillary and the mass spectrometer are kept at a temperature of about 170 °C for preventing condensation of precursor gases.
The mass spectrometer could only be effectively used for the study of the decomposition of DMTC. When oxygen or water is added, the mass spectrum becomes too complex to distinguish individual components.

References

[1] R. David and D. Matras, *Can. J. Chem. Eng.*, 53 (1975), 297-300.

[2] P. Azay and G.-M. Côme, *Ind. Eng. Chem. Process Des. Dev.*, 18 (1979), 754-756.

[3] P.R. Griffiths, Chemical infrared Fourier Transform Infrared Spectroscopy, Chemical Analysis Vol.43 (1975).

[4] P. W. Atkins, Physical Chemistry, 2nd Edition (1977).

[5] J.O. Hinze and B.G. van der Hegge Zijnen, *Appl. Sci. Res.*, A1, 435-461 (1949).

[6] M.L. Albertson, Y.B. Dai, R.A. Jensen, and H. Rouse, *Trans. Amer. Soc. Civ. Engrs.*, 115, 639-697 (1950).

[7] M.B. Donald and H. Singer, *Trans. Instn. Chem. Engrs.*, 37, 255-267 (1959).

[8] F.P. Ricou and D.B. Spalding, *J. Fluid Mechanics*, 11, 21-32 (1961).

[9] H.W. Liepmann and J. Laufer, *Techn. Notes Nat. Advs. Comm. Aeronaut.*, 1257 (1947).

[10] M.K. Thornton, P.C. Malte, and A.L. Crittenden, *Combust. Sci. And Techn.*, 54, 275-297 (1987).

[11] P.M. Sforza and R.F. Mons, *Int. J. Heat Mass Transfer*, 21, 371-384 (1978).

Appendix 3A: Design criteria CSTR

This appendix describes the construction rules for a jet stirred tank reactor following the rules established by David and Matras [1]. The reactor has a spherical geometry because it favours mixing and uniformity of heat transfer. Mixing is achieved by four jets emerging from nozzles of a cross-shaped injector, located in the middle of the reactor. To enhance complete mixing the nozzles are placed in two orthogonal planes. The diameters of the nozzle and reactor are evaluated using the fluidodynamic relations for axial symmetric jets proposed by David and Matras [1].

Working principle jet stirred reactor

The gas flowing out of a nozzle, as depicted in figure 3.9, forms a circular jet. This jet mixes violently with the surrounding fluid creating a certain degree of turbulence and the jet itself grows thicker.

The jet flow can be divided in two distinct regions. The first region which is close to the nozzle is the flow development region. In the second region the flow is fully developed. The turbulence penetrates inwards towards the axis of the centre line of the jet, where a core of flow with undiminished velocity equal to u_0 exists. At the interface between these two regions the turbulence generated at the boundaries of the jet reaches the centre line causing the mean velocity on the axis to decrease with increasing distance x.
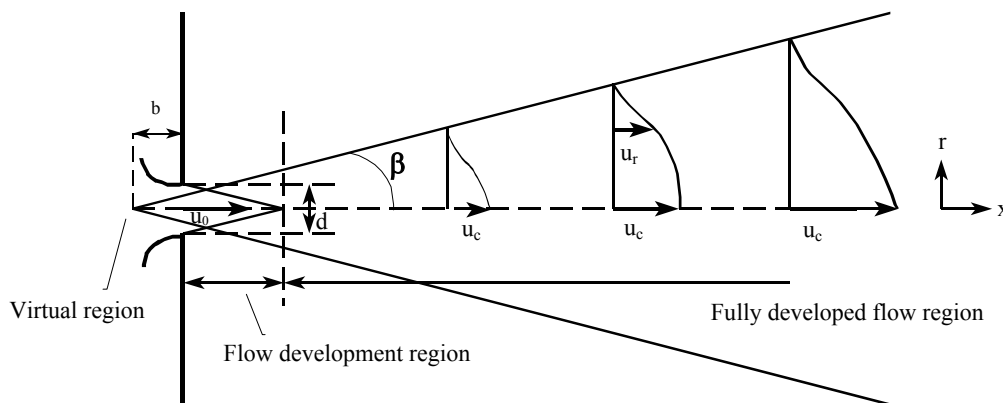
Figure 3.9: *Shape of a jet emerging from a nozzle. The meaning of the symbols is explained in the text.*

In the region close to the nozzle opening the axial velocity (u_c) remains constant and the velocity distribution in radial direction (u_r) changes from being flat to a Gaussian-like distribution, which is characteristic for the fully developed region.

For this region the following velocity distribution equations have been derived by Hinze and Van der Hegge Zijnen [5]:

$$u_r = \frac{u_c}{(1 + a_1 \dfrac{r^2}{(x+b)^2})^2} \quad , x/d > 8 \tag{3.16}$$

$$u_c = a_2 \, u_0 \frac{d_0}{x+b} \quad , x/d > 8 \tag{3.17}$$

The same authors determined experimentally the constants a_1 and a_2 for air at room temperature and atmospheric pressure:

a_1 = 63.8
a_2 = 6.39
b = $0.8 d_0$

The volumetric flow rate at distance x from the nozzle can be expressed as:

$$Q_x = 2 \int_0^R \frac{u_c}{(1 + a_1 \dfrac{r^2}{x^2})^2} \pi r \, dr = 2\pi u_c \left[\frac{-0.5\, x^2/a_1}{(1 + a_1 \dfrac{r^2}{x^2})} \right]_0^R = \pi u_c \frac{x^2}{a_1}(1 - \frac{1}{1 + a_1 \dfrac{R^2}{x^2}}) \tag{3.18}$$

Because $\tan\beta = R/x$, this can be rewritten to:

$$Q_x = \pi u_c x^2 \frac{\tan^2 \beta}{1 + a_1 \tan^2 \beta} \tag{3.19}$$

With $Q_0 = \pi/4 \cdot d_0^2 \cdot u_0$, this results in:

$$Q_x / Q_0 = 4 \cdot a_2 \cdot \frac{x}{d_0} \cdot \frac{\tan^2 \beta}{1 + a_1 \tan^2 \beta} = A \cdot \frac{x}{d_0} \tag{3.20}$$

Various values for the constant A are published in literature; it is found that A is a function of the medium used:

Hinze and Van der Hegge Zijnen [5]:   A=0.28 for air at ambient temperature
David and Matras [1]:   A=0.47*(2/π)=0.299 for air at room temperature and atmospheric pressure.
Albertson et al. [6]:   A=0.32 for air
Donald and Singer [7]:   A=1.625$v^{0.133}$ with v being the kinematic viscosity (m^2/s).
Ricou and Spalding [8]:   A=0.32 for air

Taking the average value, it is found that 0.3 seems to be a reasonable value for A in air at room temperature. It is unknown how this value changes at higher temperatures; according to David and Matras [1] A increases with increasing temperature.

Design rules

David and Matras [1] derived four criteria for the design of a jet-stirred spherical reactor with the mixing behaviour of a perfect mixer. If the dimensions of the reactor satisfy these criteria, a good homogeneity of concentration and temperature throughout the reactor is to be expected. These criteria are:

1) Condition for a fully developed jet:
A necessary condition for the system to function properly is that each turbulent jet should become fully developed. Liepman and Laufer [9] experimentally determined this condition, which can be expressed by a Reynolds number.
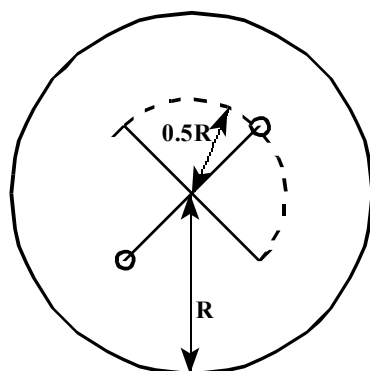
Figure 3.10: *Schematic cross section of the jet stirred reactor. The jet has to be developed before it reaches the other nozzle, located 0.5 πR away.*

$$\frac{u_0 x \rho}{\eta} \geq 7 \cdot 10^4 \tag{3.21}$$

For x the following expression holds: x ≤ 0.5·π·R, see figure 3.10. For a reactor with 4 jets, this results in:

$$\frac{2 \pi R^4 \rho}{3 \tau d_0^2 \eta} \geq 7 \cdot 10^4 \tag{3.22}$$

This is usually only a constraint for very small reactors. A few remarks can be placed with this expression. In the publication of Liepmann and Laufer [9] the expression as stated in equation 3.22 will not be found. They only said that under

their conditions (air at room temperature departed from a orifice with a diameter of 2.54 cm and a velocity of 18 m/s) the length of the flow development region is 30 cm. Expressing this result as a Reynolds number yields: Re> 4.10^5. However, in all literature concerning this subject a Reynolds limit of 7.10^4 is used.

2) Condition of a turbulent jet:

For a jet that opens as a cone with an apex angle of 22°, a minimal Reynolds number applies for the jet to be turbulent: Re > 800 [1]. The parameters in this Reynolds number are related to a cross section of the jet flow. The mean velocity across the jet can be expressed as:

$$u_m = \frac{\frac{1}{4}Q}{\pi r^2} = \frac{\frac{1}{4}A \cdot Q_0 \cdot x/d_0}{\pi x^2 \tan^2 \beta} = \frac{A \cdot R^3}{3 d_0 x \tan^2 \beta} \tag{3.23}$$

Wherein for the typical length scale the diameter of the jet, 2·x·tanβ, can be taken. It follows that:

$$Re = \frac{2\rho A R^3}{3\eta d_0 \tau \tan \beta}$$

Taking β=11°, the condition of Re>800 results in:

$$\frac{A R^3 \rho}{d_0 \tau \eta} \geq 230 \tag{3.24}$$

3) Condition of recycle limitations:

The reactor content must be recycled by the jets. David and Matras [1] determined experimentally that a recycling ratio of $Q/Q_0 \geq 30$ is necessary. Using equation 3.20 this leads to:

$$\frac{AR}{d_0} > 19 \tag{3.25}$$

4) Condition of sound velocity:

The maximum velocity of the gases flowing out of the nozzles has to be kept below the sonic velocity of the particular gas at the pressure and temperature under consideration. Otherwise shock waves will be formed, strongly interfering with the mixing process:

$$\frac{4 R^3}{3 d_0^2 \tau} < u_s \tag{3.26}$$

Design jet stirred CSTR

The precursors are fed to the reactor by excess nitrogen. Therefore the material constants of nitrogen are applied in the design rules of the CSTR (table 3.1).

Table 3.1: *Physical properties of nitrogen.*

	T=673 K	T=918 K	T=1073 K	Reference
Density [$g.l^{-1}$]	0.507	0.372	0.318	ideal gas law
Viscosity [10^{-7} Pa.s]	313	379.7	416.9	N.B. Vargaftik. Tables on the thermophysical properties of liquids and gases. 2nd ed., John Wiley & Sons (1975).
Sound velocity [$m.s^{-1}$]	523.7	606.3	652.3	id.

The respective design criteria as given by equations 3.23 to 3.26 can now be obtained as shown in table 3.2.

Table 3.2: *Four criteria for designing a fully turbulent jet stirred CSTR.*

Criterion	T=673 K	T=918 K	T=1073 K
$R^4/(\tau d_0^2)$ [m^2/s] >	2.06	3.41	4.38
$R^3/(\tau d_0)$ [m^2/s] >	$4.73\cdot10^{-2}$	$7.83\cdot10^{-2}$	0.100
R/d_0 [-] >	63	63	63
$R^3/(\tau d_0^2)$ [m/s] <	393	455	489

On the basis of graphs of log(R) against log(d_0) at different residence times (1-5 s) and temperatures (673-1073 K), the dimensions of the reactor and the nozzles can be chosen. An example of the design constraints for a process operated at a temperature of 873 K and a residence time of 2 s is given in figure 3.10. For the reactor a diameter of 120 mm and a nozzle diameter of 1 mm are chosen.
This means the following residence times are applicable:

T=400 °C : $0.6 < \tau < 4.5$
T=645 °C : $0.5 < \tau < 2.8$
T=800 °C : $0.5 < \tau < 2.2$
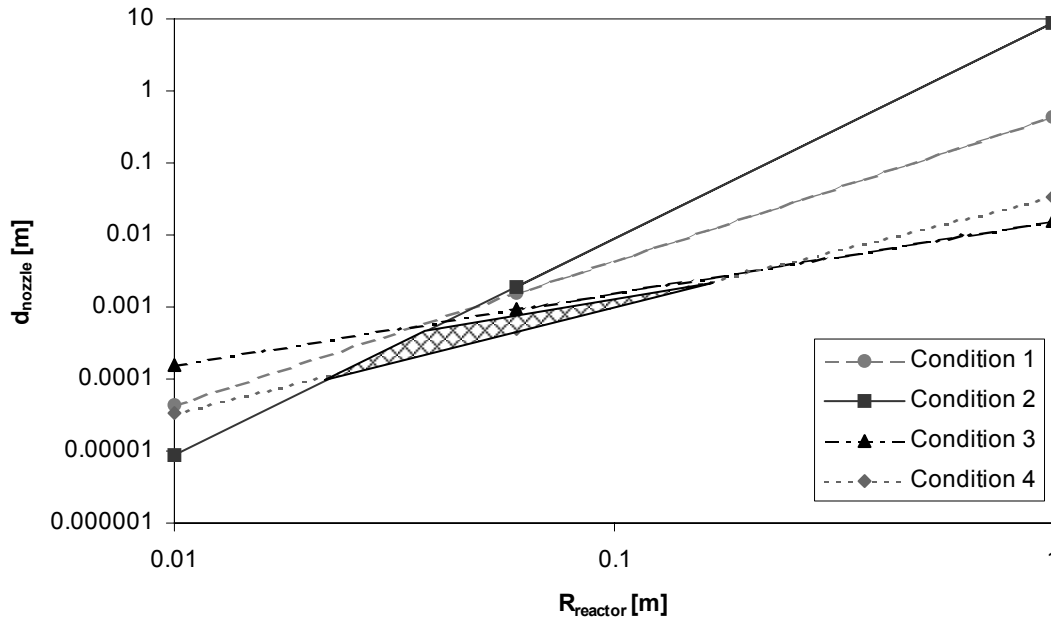
Figure 3.10: *The relation between reactor diameter and nozzle diameter for the four design criteria as proposed by David and Matras [1] for a reactor at 873K and a space time of 2 s. The shaded region is the set of reactor radii and nozzle diameters which satisfy all four criteria.*

Characteristic mixing times

In the reactor described in the preceding sections only those reactions can be studied whose reaction rates are slower than the rate of mixing in the reactor. A characteristic time for mixing is the time required for entrainment of a unit of mass flow rate equivalent to that of the inlet jet [8, 10].

If the densities of the entrained fluid and jet fluid are the same, equation 3.20 can be used:

$$\frac{\dot{m}}{\dot{m}_0} = A \cdot \frac{x}{d_0} \tag{3.27}$$

This means a characteristic length for mixing is given by:

$$\Delta x = d_0 / A \tag{3.28}$$

For the developed zone of a jet, the constant A is about 0.3. For the initial region $(x/d_0 < 8)$ this constant is about 0.2 [11]. By assuming the characteristic velocity to be the inlet jet mean velocity, u_0, the entrainment time in the initial region is:

$$t_{e1} = 5 \frac{d_0}{u_0} \tag{3.29}$$

For the developed region, the characteristic velocity is assumed to be the mean velocity across the jet at a distance x from the nozzle, $u_m(x)$, as defined in equation 3.23. The entrainment time in the developed region is then:

$$t_{e2} = 0.52 \left(1 + a_1 \frac{r^2}{x^2}\right) \frac{x}{u_0} \qquad (3.30)$$

The maximum values for both entrainment times are ($u_0=28$ m.s^{-1}, x=0.5R) t_{e1} = $2 \cdot 10^{-4}$ s, and $t_{e2} = 6 \cdot 10^{-3}$ s, respectively.

Another important characteristic time in obtaining concentration and temperature homogeneity in the reactor is the cycle time, t_c. This time is defined as the time required for a given particle of gas to transverse the path length L, approach the reactor wall at the position of the following jet, if present at the same level, where intense mixing occurs all without a great degree of chemical reaction occurring. Taking $(u_0+u_r(\frac{1}{2}R))/2$ as the average velocity between the inlet nozzle and the reactor wall, the cycle time is defined as:

$$t_c = \frac{R}{u_0 + u_r\left(\frac{1}{2}R\right)} \qquad (3.31)$$

The maximum value of t_c is then 2.10^{-3} s. From these considerations it can be concluded that only reaction rates for reactions with characteristic reaction times larger than 6.10^{-3} s, can be studied.

Symbol list

Roman symbols:

a_1:	dimensionless constant	[-]
a_2:	dimensionless constant	[-]
A:	dimensionless constant	[-]
C_p:	heat capacity at constant pressure	[J.mol^{-1}.K^{-1}]
d_0:	nozzle diameter	[m]
M:	molar molecular weight	[kg.mol^{-1}]
P:	power	[W]
Q_x:	volumetric flow rate at a distance x	[m^3.s^{-1}]
Q_0:	nozzle volumetric flow rate	[m^3.s^{-1}]
R:	reactor radius	[m]
u_c:	centerline gas velocity	[m.s^{-1}]
u_r:	gas velocity at a distance r from the centerline of the jet	[m.s^{-1}]
u_m:	mean gas velocity across the jet	[m.s^{-1}]
u_s:	sonic velocity	[m.s^{-1}]
u_0:	nozzle velocity	[m.s^{-1}]

V:	volume	[m^3]
x:	axial distance	[m]
$\dot{m}$:	mass flow rate	[kg.s^{-1}]
$\dot{m}_0$:	initial mass flow rate	[kg.s^{-1}]
t_{e1}:	entrainment time in the initial region of a jet	[s]
t_{e2}:	entrainment time in the fully developed region of a jet	[s]
t_c:	cycle time	[s]

Greek symbols:

η:	dynamic viscosity	[Pa.s]
ν:	kinematic viscosity	[m^2.s^{-1}]
ρ:	density	[kg.m^{-3}]
τ:	residence time	[s]
β:	jet angle	[deg]

Chapter 4. Vapour pressure measurements

Abstract

The vapour pressures of a number of precursors for the chemical vapour deposition of tin oxide were determined at various temperatures. For this purpose, a new experimental set-up was used for measuring vapour pressure at constant temperature. With this set-up, disrupting effects due to evaporation of volatile decomposition products, degassing of gas particles from walls, and small leaks can be readily detected and compensated for. The precursors studied were $SnCl_4$, CH_3SnCl_3, $(CH_3)_2SnCl_2$, $(CH_3)_3SnCl$, $Sn(CH_3)_4$, $(C_4H_9)SnCl_3$. For CH_3SnCl_3, $(CH_3)_2SnCl_2$, $(CH_3)_3SnCl$, and $(C_4H_9)SnCl_3$, no vapour pressure data have been previously reported. The values of the constants A and B for the integrated Clausius-Clapeyron equation, log P (Torr) = A - B / T(K), were determined. The next chapter describes a kinetic study of tin oxide deposition from dimethyltin dichloride. In order to quantify the amount of tin precursor entering the reactor, it is necessary to know its vapour pressure.

4.1 Introduction

For accurate control of the feed rate of the precursor to the CVD reactor, it is imperative to know the vapour pressure of the precursor. However, the measurement of the vapour pressure of a substance can be quite complex due to, for example, partial decomposition of the reactant at elevated temperatures or the presence of volatile contaminants in the precursor [1-3]. A new set-up was designed in order to avoid these problems and to measure the vapour pressure in a very accurate way. Commonly described systems for measuring vapour pressures like the boiling point method, the gas saturation method, the Langmuir method, or the Knudsen method [4, 5], do not take into account these additional effects. Precursors as described in this thesis are known for their instability at elevated temperatures and the pollution present in the compounds, making it necessary to design a new set up in order to avoid these problems. The set up and the measuring method is to some extent consistent with the system described by Waffenschmidt [3], also using a time-resolved static method in order to make a distinction between decomposition and the actual vapour pressure. This measuring method is further improved to discreet the vapour pressure from effects of decomposition, leakage of the system, degassing of walls, and pollution of the compounds. This system is

used to determine the vapour pressure vs. temperature relations of various tin oxide precursors.

4.2 Experimental system

The vapour pressure measurements were carried out using an experimental facility, configured in such a way that any disturbing effects, mentioned in the introduction, can be corrected for. In this way, an accurate estimate of the true vapour pressure is obtained. Figure 4.1 shows a schematic representation of the vapour pressure measurement apparatus. The heart of the system is a pressure gauge (MKS, MK 270), which measures the pressure difference, ±0.1 Torr, between two compartments. Compartment 1 is a stainless steel tube that connects the pressure gauge and valve 1. Compartment 2 consists of a stainless steel tube and a glass tube containing the sample, connecting the pressure gauge and valve 2. A fused silica temperature sensor (Hereaus Quat 100) is placed near the sample tube allowing an accurate measurement of the sample temperature, ±0.05 °C. Readings from the differential pressure sensor and the temperature sensor are recorded automatically by computer and displayed on screen in real time. The measuring system is placed in an oven in order to measure vapour pressures at temperatures up to 200 °C. The compartments can be evacuated with an oil diffusion pump backed up by a rotary vane pump. Because precursors for CVD processes are often hazardous, the gases are condensed in a cold trap.
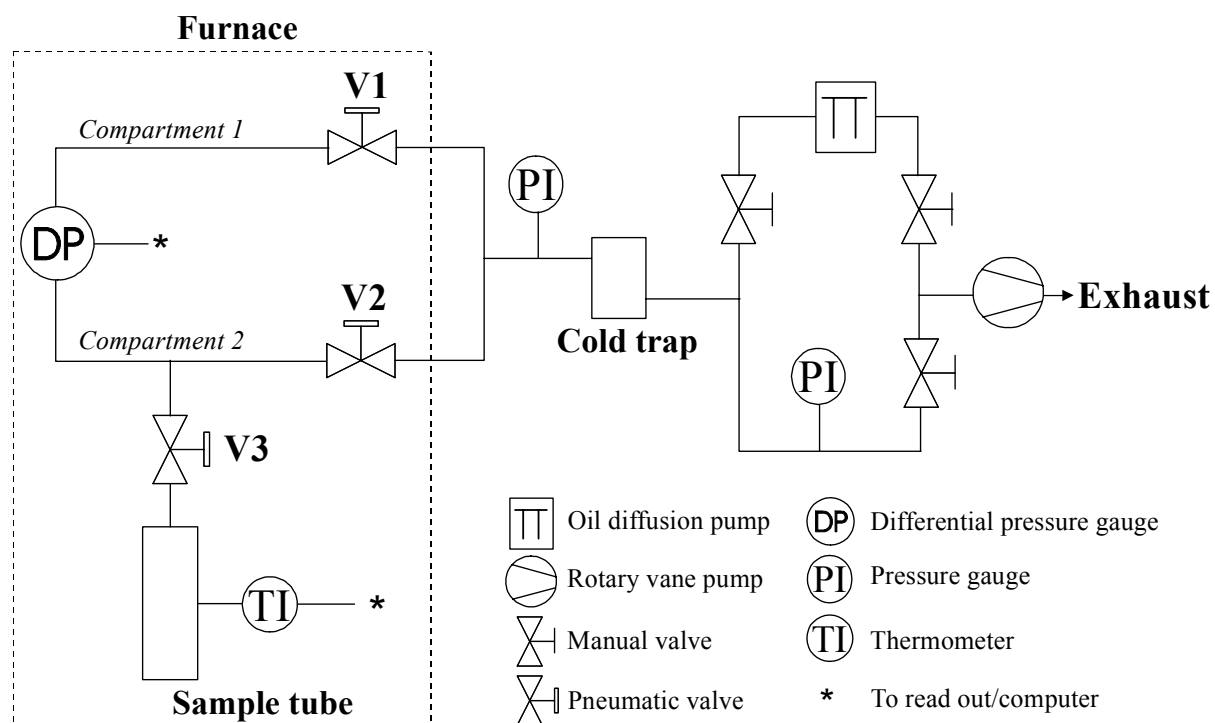
Figure 4.1: *Apparatus used for vapour pressure measurements.*

4.3 Measurement procedure

Six precursors for tin oxide deposition were investigated: tetramethyltin (Aldrich, 99+%), trimethyltin chloride (Aldrich, 97%), dimethyltin dichloride (97%), methyltin trichloride (Aldrich, 97%), tin tetrachloride (Aldrich, 99.9%), and monobutyltin trichloride (Elf-Atochem, 99%). All compounds were purified up to 99+%.

Tetramethyltin and tin tetrachloride were measured for comparison with literature values [6-11]. As a confirmation of the vapour pressure measurements of monobutyltin trichloride (MBTC), also its boiling point is determined by heating liquid MBTC in a nitrogen atmosphere under reflux.

The measurement starts by evacuating compartments 1 and 2. After a short period of pumping, to prevent loss of precursor material, valve 3 is closed (point A in figure 4.2). After also valves 1 and 2 are closed, valve 3 is opened again (point B in figure 4.2). The vapour of the sample spreads out through compartment 2, causing a jump in the pressure difference between the two compartments (point C in figure 4.2). In the ideal case the pressure difference should remain constant over time. However, the pressure difference increases gradually, due to possible small leaks in the system, desorption of molecules from the walls, possible decomposition of the precursor, and the evaporation of contaminants during the monitored time. In order to obtain the true vapour pressure, these effects have to be eliminated from the measured data. The effect of desorption of molecules from the wall can be compensated for by extrapolating the linear part of the vapour pressure curve to the time of the start of the measurement (point E in figure 4.2). This point will then represent the vapour pressure of the sample without the bias due to the presence of small leaks, volatile contaminants, or decomposition products. The presence of volatile contaminants can be detected by repeating the very first experiment, performed after attaching the sample vessel, several times under the same conditions. The first measurements will contain a contribution from these volatile compounds. However, this contribution decreases in time due to repeated evacuation of the vessel containing the sample. The extrapolated values of the vapour pressure at point E in figure 4.2 will decrease towards a constant value until no volatile contaminants are present anymore.

The effects of leaking and the decomposition of the precursor into gaseous products can be corrected for by repeating the same experiment several times but with different time periods between points A and B.
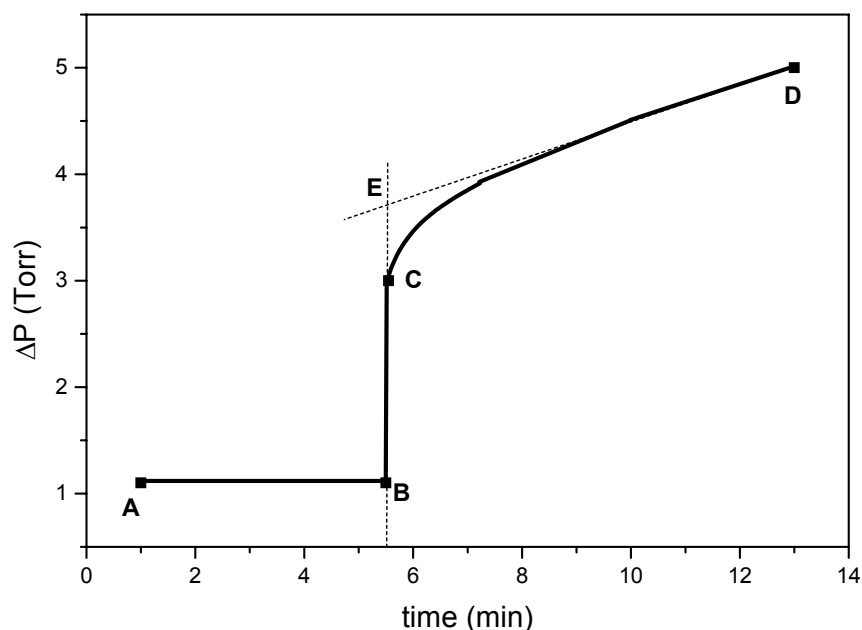
Figure 4.2: *A typical vapour pressure measurement.*

Before point A in figure 4.2 all gases are pumped away. At point A valve 3 is closed. If some decomposition of the precursor takes place during the time between A and B, or if small leaks are present, the jump at point C will show an extra increase. The obtained values of the vapour pressure at point E are then plotted as a function of this time period. Extrapolation of the measured vapour pressures towards a zero time period results in a value of the actual vapour pressure of the examined compound in the precursor vessel.

4.4 Vapour pressure curve

The vapour pressure curve, dp/dT, in the phase diagram of a specific compound is approximated by the integrated Clausius-Clapeyron equation [12]:

$$\ln (p/p_0) = \frac{-\Delta H}{RT} + \frac{\Delta H}{RT_0},$$ (4.1)

in which p is the vapour pressure in Torr, T is the temperature in Kelvin, R is the universal gas constant in $J.mole^{-1}.K^{-1}$, and ΔH is the enthalpy of evaporation or sublimation in J/mole. Furthermore, the second term on the right hand side is a constant, so p_0 can be set arbitrarily at 1 Torr for convenience with corresponding T_0:

$$\log p = A - B / T,$$ (4.2)

with A and B constants. The corresponding enthalpy of evaporation or sublimation can be deduced from the constant B. By plotting the logarithm of the vapour

pressure against reciprocal temperature, the slope of the resulting curve multiplied by –Rln(10) yields the heat of evaporation per mole [12].

4.5 Results and discussion

The results of the vapour pressure measurements of tetramethyl tin (TMT), trimethyltin chloride (TMTC), dimethyltin dichloride (DMTC), monomethyltin trichloride (MMTC), tin tetrachloride (TTC), and monobutyltin trichloride (MBTC) are depicted in figure 4.3. No significant decomposition was observed for all five precursors. Each set of data can be described by equation 4.2. A distinction is made between data obtained at temperatures below and beyond the melting points of three of the precursors. The numerical results are shown in table 1. The vapour pressures measured for $SnCl_4$ and $Sn(CH_3)_4$ are in agreement with the data reported in literature as is shown in figure 4.4. The enthalpy of evaporation of DMTC, 54 kJ/mol, is comparable to a previous reported value of 51 kJ/mol [13]. For methyltin trichloride and trimethyltin chloride no vapour pressure data could be found in literature. The enthalpy of evaporation for MBTC, 58.8±0.8 kJ/mol, is comparable to the value reported by Buchanan and McKown [14], 60 kJ/mol, but the values of A are significantly different. Extrapolation of their equation shows a boiling point of 205 °C. However, an independent boiling point measurement gave a value of 217 °C at 758 Torr, which is in agreement with the value of 220 °C calculated from the Clausius-Clapeyron equation with the data given in table 4.1.

Table 4.1: *Vapour pressure data for tin oxide, dimethyltin dichloride (DMTC), tin tetrachloride (TTC), tetramethyltin (TMT), monomethyltin trichloride (MMTC), and monobutyltin trichloride (MBTC). Data are fitted to log p (Torr) = A - 1000 * B / T (K). Error margins given are at 95% confidence intervals for the experimental fit.*

Precursor	A	B	ΔH (kJ/mol)	Temp. range (°C) of measurement
DMTC (s)	12.2±0.1	4.05±0.04	77.6±0.8	60 - 100
DMTC (l)	8.94±0.09	2.80±0.03	53.5±0.6	100 - 130
TTC (l)	7.99±0.08	1.98±0.02	37.8±0.4	0 - 40
TMT (l)	7.94±0.03	1.76±0.01	33.7±0.2	0 - 25
MMTC(s)	10.6±0.3	3.19±0.09	61±2	20 - 40
MMTC(l)	8.24±0.1	2.41±0.04	46.1±0.8	60 - 90
TMTC(s)	11.0±0.4	3.2±0.1	61±2	0 - 20
TMTC(l)	8.98±0.05	2.54±0.02	49±0.3	40 - 85
MBTC(l)	9.1±0.1	3.07±0.04	58.8±0.8	70 - 145
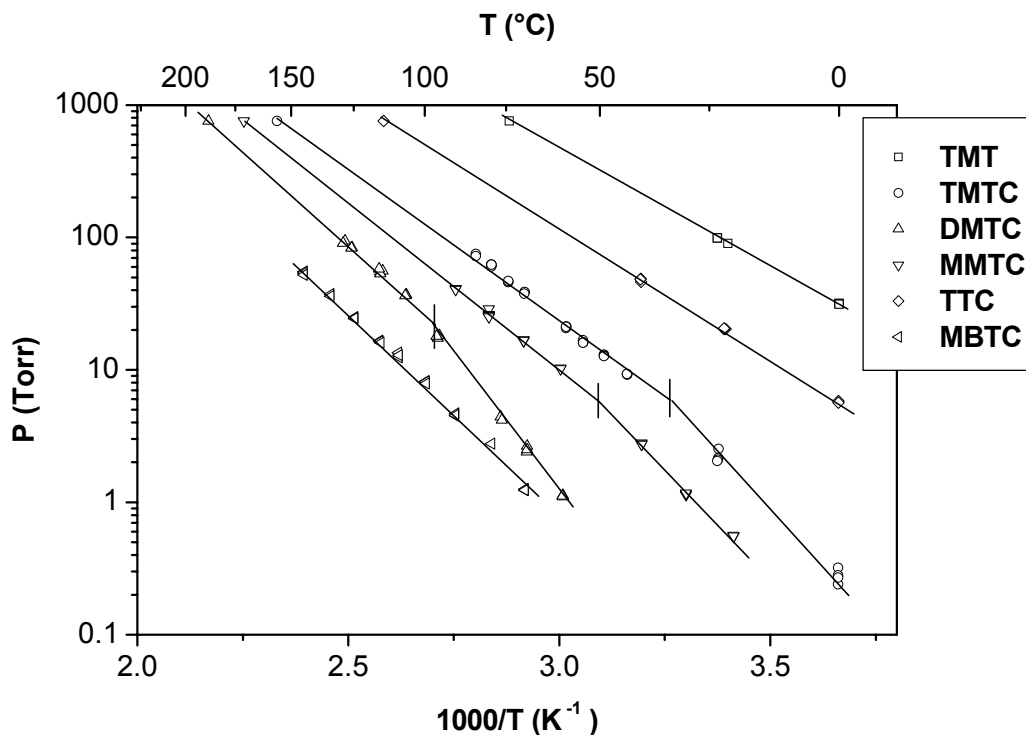
Figure 4.3: *Vapour pressure measurements of dimethyltin dichloride (DMTC),
monomethyltin trichloride (MMTC), trimethyltin chloride (TMTC), tin tetrachloride
(TTC), tetramethyltin (TMT), and monobutyltin trichloride (MBTC). The vertical lines
represent the melting point of a compound.*
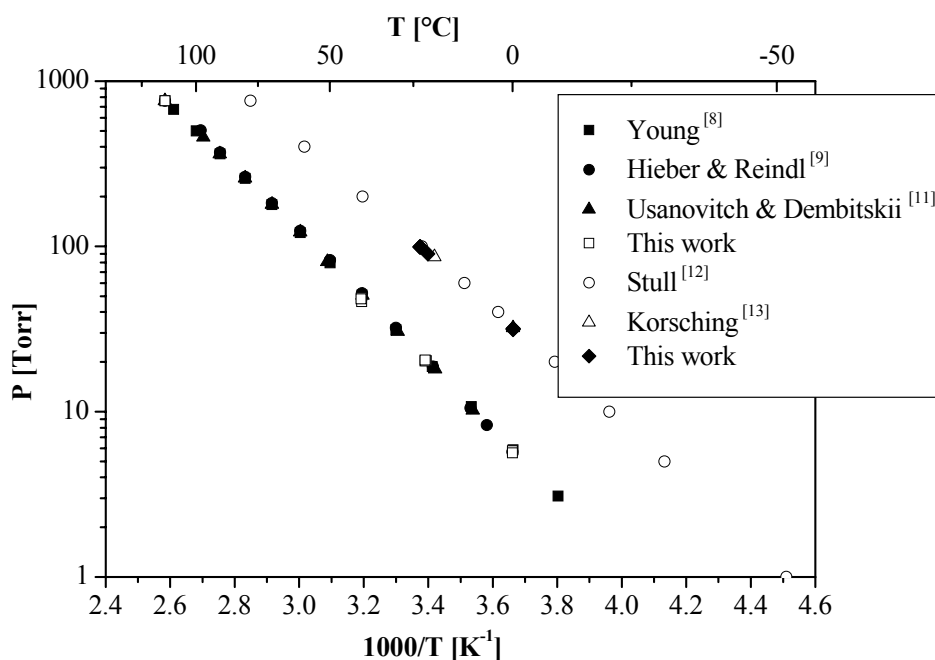
Figure 4.4: *Vapour pressure measurements of tin tetrachloride (TTC) and
tetramethyltin (TMT), compared to data known in literature.*

4.6 Conclusions

The vapour pressures of several precursors for tin oxide deposition were measured. The measurements were carried out in such a way that any disturbing effects due to pollution, decomposition, and the measurement system itself, could be accounted for. The system was tested by measuring the vapour pressures of $SnCl_4$ and $Sn(CH_3)_4$. The values measured are in good agreement with previous reported values for these compounds. Vapour pressure data for CH_3SnCl_3, $(CH_3)_2SnCl_2$, $(CH_3)_3SnCl$, and $(C_4H_9)SnCl_3$, were not reported before in literature.

References

[1] C.I.M.A. Spee, F. Verbeek, J.G. Kraaijkamp, J.L. Linden, T. Rutten, H. Delhaye, E.A. Van der Zouwen, and H.A. Meinema, *Mat. Sci. Eng.*, 1993, *B17*, 108.

[2] C.I.M.A. Spee, J.L. Linden, A. Mackor, K. Timmer, and H.A. Meinema, *Mat. Res. Soc. Symp. Proc.*, 1996, *425*, 93.

[3] E. Waffenschmidt, J. Musolf, M. Heuken, and K. Heime, *J. Supercond.*, 1992, *5*, 119.

[4] A. Weissberger, Physical Methods, Part 1, Interscience Publishers Inc., New York, 1960.

[5] A.N. Nesmeyanov, Vapor Pressure of the Chemical Elements, Elsevier Publ. Comp., Amsterdam, 1963.

[6] S. Young, *Scient. Proc. Roy. Dublin Soc.* 1909, *12*, 374.

[7] W. Hieber, E. Reindl, *Z. Electrochem.*, 1940, *46*, 559.

[8] A. Kabesh, R. S., Nyholm, *J. Chem. Soc.*, 1951, 3245.

[9] M. Usanovich, A. Dembitskii, *J. Gen. Chem. USSR*, 1959, *29*, 1744.

[10] D. R. Stull, *Ind. Eng. Chem.,* 1947, *39*, 517.

[11] H. Korsching, Z. *Naturforschung*, 1946, *1*, 219.

[12] W. J. Moore, *Physical Chemistry*, Longman, London, 1972.

[13] G. A. Nash, H. A. Skinner, W.F. Stack, *Trans. Faraday Soc.*, 1965, *61*, 640.

[14] J. L. Buchanan, C. McKown, *J. Non-Cryst. Solids*, 1997, *218*, 179.

Chapter 5. Mechanism and kinetics of tin oxide deposition from dimethyltin dichloride, oxygen, and/or water

Abstract

Using the reactor system described in chapter 3, the chemical mechanism of tin oxide deposition from dimethyltin dichloride (DMTC), O_2, and/or H_2O is studied. Thermal decomposition of DMTC in nitrogen starts at about 773 K. It is initiated by the cleavage of the Sn-C bond in DMTC, and is propagated by a branched radical mechanism. Also, when DMTC is mixed with oxygen, it appears that the cleavage of Sn-C is still the initiation step. However, subsequent reactions between O_2 and CH_3 lead to additional propagation steps that lead to more reactive radicals, which enhance the overall reaction rate. Addition of water leads to even more possible reaction paths, both in the gas phase as well as on the surface. From the CSTR measurements an overall lumped chemical mechanism for DMTC + O_2 is determined, which will be used in chapter 7 to simulate two types of CVD reactors. The growth rates obtained from these simulations will be compared to the experimental values.

5.1   Introduction

As is discussed in chapter 2, tin oxide coatings are used in a wide variety of applications and are used on a large scale. However, most production processes are based on empirical laws and experience. The most common tin precursors to produce tin oxide coatings are monobutyltin trichloride (MBTC), tin tetrachloride (TTC), and dimethyltin dichloride (DMTC). From these three precursors little is known about the mechanism for forming tin oxide. The first precursor is currently under investigation at Sandia National Laboratories [1], and some results will be discussed in chapter 6. Ghosthagore [2, 3] published some data on $SnCl_4$, of which a summary is given in chapter 2. Giunta et al. [4] published a detailed mechanism of tin oxide formation from DMTC and oxygen, but this mechanism was based on

data obtained from a laminar flow reactor, and for a large part taken from literature on combustion and chlorine chemistry.

This chapter reports on the mechanism and kinetics of tin oxide formation from DMTC, oxygen, and water. The mechanism is derived on the basis of the experimental results obtained in the CSTR reactor described in chapter 3, and contains only the most important steps for tin oxide formation.

This chapter is divided into two parts. The first part will describe the decomposition behaviour of DMTC in nitrogen. The second part discusses the deposition of tin oxide from DMTC, oxygen, and water.

5.2 Experimental conditions

All the experimentsthat are described in this chapter were conducted in the reactor system described in chapter 3. In order to keep the number of experiments within an acceptable level, all experiments were conducted at atmospheric pressure and at a reactor space time of 2 s. At this space time, the CSTR also satisfies all four criteria for a perfect stirred tank reactor, as described in the appendix of chapter 3, in the temperature range of 623 to 1000 K. Especially at higher temperatures, the optimal operation window for the residence time is very narrow, e.g. $0.5 < \tau < 2.7$ s at 925 K.

The temperature of the preheater is in principle set to the same temperature as the reactor. However, because above a temperature of 743 K, DMTC starts to decompose, the preheater temperature is kept at 743 K for experiments conducted at reactor temperatures of 743 K and above. In order to keep the surface conditions always the same, the walls of the reactor are coated with a thin layer of tin oxide prior to an experiment.

Decomposition of DMTC in N_2
The thermal behaviour of DMTC was studied between 643 and 903 K in steps of 20 K. The concentration of DMTC at every temperature was varied between 1 and 5 mol% with steps of 1 mol%. The gas phase reactions were studied with both MS and FTIR, as is described in chapter 3.

Deposition of SnO_2 from DMTC and O_2 and/or H_2O
A total of about 250 experiments was performed to study the deposition of tin oxide from dimethyltin dichloride, oxygen, and water. The experiments were divided in 10 series of which the experimental conditions are listed in table 5.1.

Table 5.1. *Range of experimental conditions used during the investigation of the deposition of tin oxide. All experiments were carried out in the CSTR system at atmospheric pressure and a reactor space time of 2 s.*

Exp. series	DTMC [mol%]	O_2 [mol%]	H_2O [mol%]	T [K]	FTIR	Grav.[1]
A	1 – 5	20	0	743 – 823	yes	no
B	2	1 – 10	0	743 – 823	yes	no
C	2	20	0	723 – 863	no	yes
D	3	15	0	703 – 783	yes	no
E	5	1 – 35.5	0	773	yes	yes
F	5	1 – 20	0	873	yes	yes
G	2	20	2	683 – 889	no	yes
H	2	20	0	786 – 807	yes	yes
I	0.25 – 5	20	0	743	yes	yes
J	2	20	0 – 15	743	yes	yes
K	1 – 3	20	0	763	yes	yes

[1]: Gravimetric analysis

Only a few depositions were carried out above 823 K, because control of the reactor temperature at these temperatures is difficult due to the released heat by the combustion reactions.

5.3 Results and discussion

5.3.1 Decomposition of DMTC in N_2

An analysis of the FTIR and mass spectra recorded during decomposition of DMTC in N_2 revealed that the decomposition products are $SnCl_2$, CH_4, C_2H_4, C_2H_6, and C_3H_8. Figure 5.1 shows the hydrocarbon products formed during decomposition of 5 mol% DMTC using the MS data. Around 773 K, DMTC starts to decompose to form methane, ethane, ethene, and propane. All products show the same trends as a function of temperature. No evidence was found for the presence of chlorinated hydrocarbons like HCl and CH_3Cl. The presence of methane, ethene, and ethane was confirmed by both MS and FTIR. The appearance of propane was concluded from MS data only, because the IR-response of propane is weak and overlaps with the IR-response of methane. The presence of $SnCl_2$, a liquid between 519 and 925 K, was based on visual observations and analysis of the deposit in the exhaust. During the experiments liquid droplets could be seen in the side arms of the reactor, which connect the FTIR. After the experiment a deposit was found in the exhaust line. X-ray diffraction showed this deposit contained DMTC, $SnCl_2$, and a small amount of an unknown substance. Inductively coupled plasma analysis (ICP) showed that the deposit almost solely contained tin and chlorine. Figures 5.2 and 5.3 show typical FTIR and MS spectra recorded during the decomposition of 5
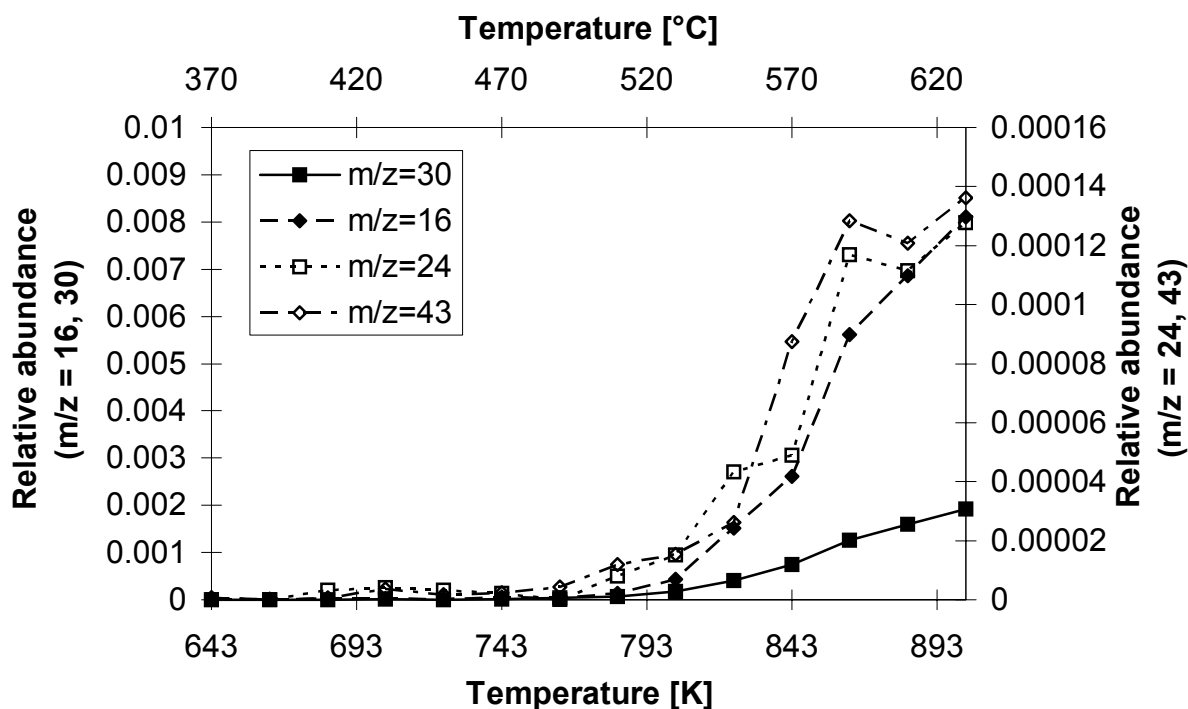
Figure 5.1: *Mass spectrometer measurements of the formation of methane, ethene, ethane, and propane during the decomposition of 5 mol% DMTC in N_2. Decomposition starts at about 773 K.*
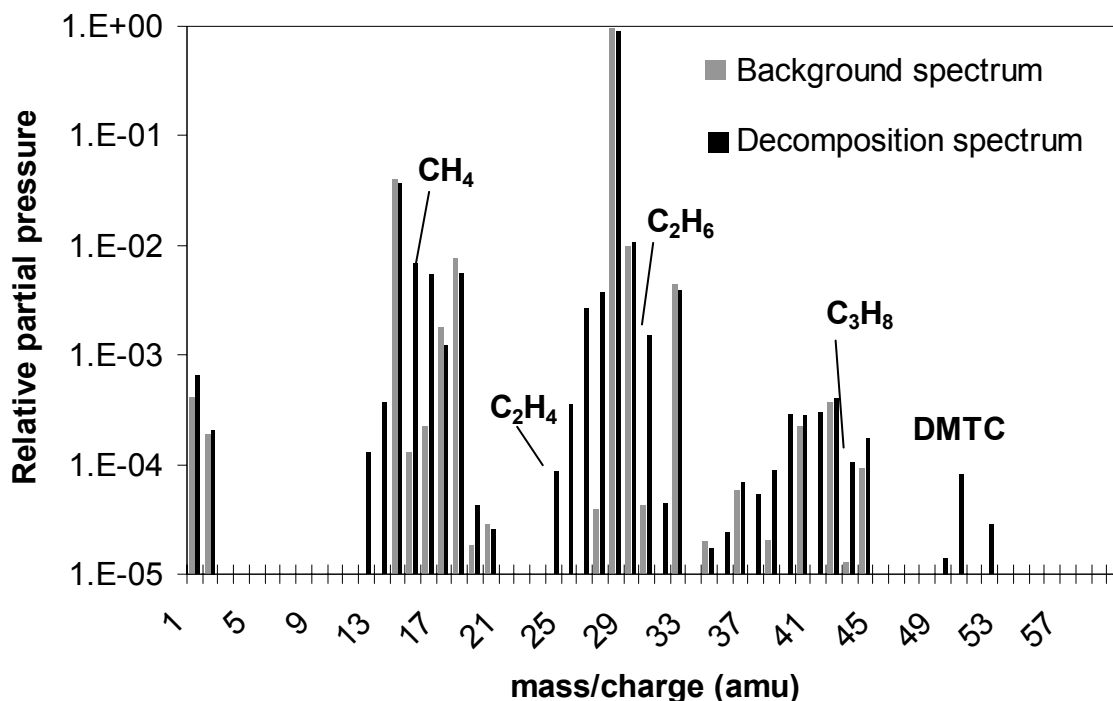
Figure 5.2: *Typical mass spectrum recorded during decomposition of DMTC. Experimental conditions were 5 mol% DMTC in N_2 at a reactor temperature of 903 K and a space time of 2 s. The fragments show the presence of methane, ethane, ethene, propane,*

mol% DMTC in N_2 at 903 K. The mass spectrum shows the presence of hydrocarbon fragments like CH_m^+ with m=0-4, $C_2H_n^+$ n=0-6, and $C_3H_p^+$ with p=0-8. These fragments are associated with the with formation of methane, ethene, ethane, and propane during decomposition. The fragments between 35 and 38 amu and between 47 and 52 amu are associated with Cl-fragments from DMTC. They can be found at all temperatures. Comparison with spectra of pure methane, ethene, ethane, and propane learns that some fragments only originate from one compound. Fragments at 16, 24, 30, and 43 amu can solely be attributed to methane, ethene, ethane, and propane, respectively. Calibration of these fragments allows monitoring the concentration of these hydrocarbons with temperature and inlet DMTC concentration.

The FTIR spectra clearly show besides DMTC, the presence of methane and ethene. The elevation of the methane peaks around 3000 cm^{-1} is caused by the presence of the broad ethane bands underneath. Propane also has an absorption band around 3000 cm^{-1}, but this band could not be unambiguously identified. At high temperatures the DMTC bands almost disappear and a band around 730 cm^{-1} appears, probably associated with $SnCl_2$. The baseline drift with increasing wavenumbers is caused by the absorption of the infrared light by the liquid tin dichloride droplets. For calibration of DMTC, methane, and ethene, the absorbance areas between 932-735 cm^{-1}, 1310-1180 cm^{-1}, and 970-925 cm^{-1}, respectively, were taken. Ethane and propane all interfere with features from other compounds and can therefore not be calibrated with univariate methods. Multivariate techniques such as partial least-squares methods have been investigated [5], but were found to be too complex too be used in this analysis.
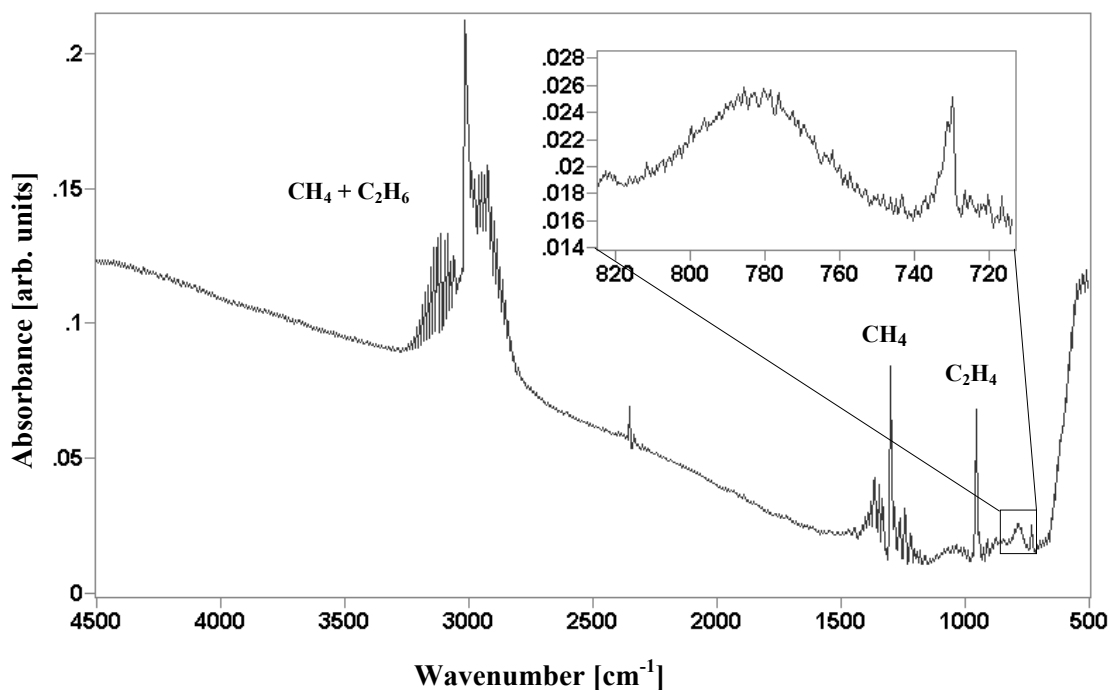
Figure 5.3: Typical FTIR spectrum recorded during decomposition of DMTC. Experimental conditions were 5 mol% DMTC in N_2 at a reactor temperature of 903 K and a space time of 2 s. The spectrum shows the presence of DMTC, methane, ethene, and ethane. The small peak at 730 cm^{-1} could not be identified but is thought to be associated

5.3.2 Mechanism of decomposition of DMTC

Figure 5.4 shows the decrease of absorbance of DMTC with increasing temperature. Up to 763 K there is no significant decomposition, so the absorbance of DMTC is the same at these temperatures. Using these data, a calibration curve for DMTC was derived using Beer's law: $A = \alpha \cdot c + \beta$, in which A is the absorbance area between 1310 and 1180 cm^{-1}, α the absorbance coefficient, β a baseline correction factor, and c the concentration DMTC in mol/m^3. Linear least-squares analysis of these data gave $\alpha = 23.3 \pm 1$ $cm^{-1} \cdot m^3 \cdot mol^{-1}$ and $\beta = -0.55 \pm 0.6$ cm^{-1}. Using this relation the absorbance data at higher temperatures can be converted into actual concentrations. Using the linear relationship between the decomposition rate and concentration of DMTC, as is shown in figure 5.4, a mass balance for DMTC over the CSTR reactor gives:

$$[DMTC]_{out} = [DMTC]_{in} / (1 + k * \tau) \tag{5.1}$$

where $[DMTC]_{out}$ is the concentration of DMTC in the reactor and as measured by the FTIR. This concentration is equal to the concentration of DMTC in the outlet of the reactor. $[DMTC]_{in}$ is the concentration of DMTC entering the reactor, τ the space time in the reactor, and k the overall rate constant. This overall rate constant is assumed to follow the Arrhenius equation:

$$k = A_0 * \exp(-E_{act}/RT) \tag{5.2}$$

with A_0 the pre-exponential factor, E_{act} the activation energy for the overall reaction, R the gas constant, and T the absolute temperature.
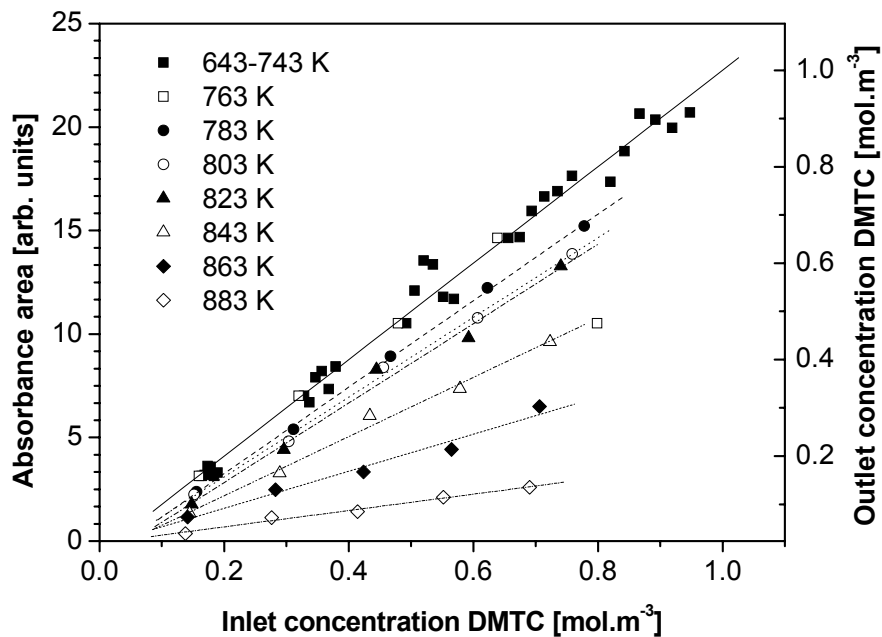
Figure 5.4: *Variation of the absorbance area between 932 and 735 cm^{-1} with inlet DMTC concentration. Between 763 and 783 K, DMTC starts to decompose, yielding lower concentrations of DMTC with temperature. The decomposition rate is linear in DMTC concentration. The data at 763 K are not considered because of the presence of an outlier.*

Inserting the values of the gradients in figure 5.4 in equation 5.1 and combining this with equation 5.2 will give the overall activation energy. The points corresponding to 763, 783, and 803 K are excluded in the linear regression analysis. The error in these data is very large because of little decomposition. Least-squares analysis gives an activation energy of 263 ± 12 kJ/mol and a pre-exponential factor of $9 \cdot 10^{15}$ s^{-1}. Within the error margin, the value for E_{act} is close to the value reported in literature, which was 235 kJ/mol. This overall activation energy is somewhat lower than the bond dissociation energy for Sn-C in DMTC, 292 kJ/mol [6].

Figure 5.5 shows the formation of methane at different inlet concentrations of DMTC. The concentrations are calculated from the absorbance area between 1310 and 1180 cm^{-1}. These values are in agreement with the values calculated by MS data. Figure 5.5 clearly shows a linear relation between the inlet concentration DMTC and the methane formation at each temperature. This linear relation is also found for the formation of ethane, ethene, and propane. Consequently, the underlying mechanism for the decomposition of DMTC has to predict a linear relationship between the rate of formation of hydrocarbons and the inlet DMTC concentration. A possible chain mechanism for the decomposition of DMTC is:

(1) $(CH_3)_2SnCl_2$ → $SnCl_2CH_3 \bullet$ + $CH_3 \bullet$

(2) $SnCl_2CH_3 \bullet$ → $SnCl_2$ + $CH_3 \bullet$

(3) $CH_3 \bullet$ + $(CH_3)_2SnCl_2$ → $SnCl_2CH_3 \bullet$ + C_2H_6

(4) $CH_3 \bullet$ + $(CH_3)_2SnCl_2$ → $SnCl_2CH_3CH_2 \bullet$ + CH_4

(5) $SnCl_2CH_3CH_2 \bullet$ → $SnCl_2$ + $C_2H_5 \bullet$

(6) $C_2H_5 \bullet$ + $(CH_3)_2SnCl_2$ → C_3H_8 + $SnCl_2CH_3 \bullet$

(7) $C_2H_5 \bullet$ + $(CH_3)_2SnCl_2$ → C_2H_6 + $SnCl_2CH_3CH_2 \bullet$

(8) $C_2H_5 \bullet$ + $(CH_3)_2SnCl_2$ → $SnCl_2CH_3 \bullet$ + C_2H_4 +CH_4

(9) $CH_3 \bullet$ + $SnCl_2CH_3 \bullet$ → $(CH_3)_2SnCl_2$
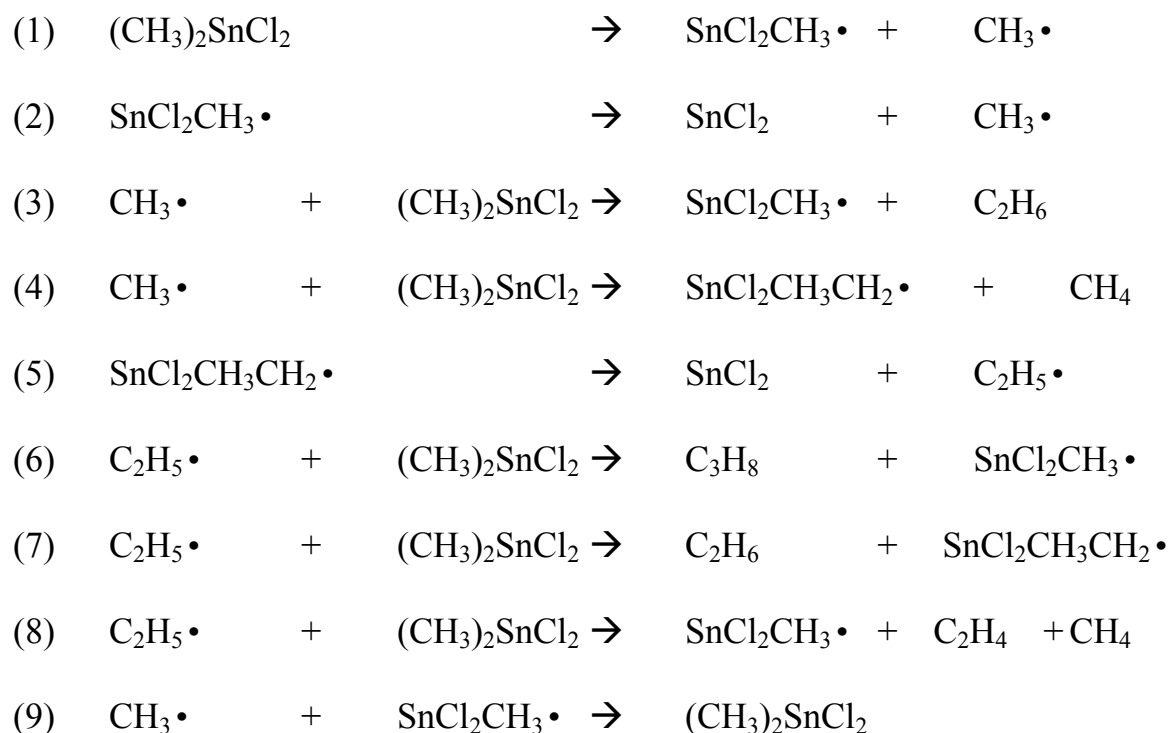
The initiation reaction (1) is almost certain because of the observed formation of various hydrocarbons during decomposition. It is also in agreement with the mechanisms proposed by Price and Trotman-Dickenson [7] and by Johnson and Price [8], who investigated the pyrolysis of DMTC and tetramethyltin (TMT) in toluene, respectively. However, their mechanisms assume the methyl radicals to react with the carrier gas toluene. Therefore, the propagation reactions (3) and (4) are between methyl radicals and DMTC, the second most abundant reactive species in the reactor. From these two propagation steps, the rate of reaction 4 is in general

at least one order of magnitude larger than the rate of reaction 3. For tetramethyltin (TMT) decomposition Borell and Platt [9] report for hydrogen abstraction, a rate which is three orders of magnitude higher with respect to the methyl abstraction.
Eventually through reaction (5) also ethyl radicals are produced which will react with DMTC too. Although Taylor and Milazzo [10] report intramolecular interaction between the methyl groups is possible in TMT, another route for ethyl radical production may involve the attack of a methyl group on the Sn radical:

(5a) $SnCl_2CH_3CH_2 \bullet + CH_3 \bullet$ → $SnCl_2CH_3 \bullet$ + $C_2H_5 \bullet$

Steps (6) and (7) represent, respectively, methyl and hydrogen abstraction from DMTC by the ethyl radical.
Step (8), the only step where ethene is formed, consists of several elementary steps. However, in order to explain the trends and the formation of by-products, and because the sequence of steps is unclear, the formation of ethene is summarised in step (8).
The formation of ethene may proceed through the formation of a tin hydride bond or the decomposition of the ethyl radical, although this last step requires an activation energy of 167 kJ/mol [11]:

(8a) $C_2H_5 \bullet$ → C_2H_4 + $H \bullet$

The termination reaction (9) which is the reverse reaction of (1), is also very likely, because all other recombination reactions, such as:

(9a) $CH_3 \bullet$ + $CH_3 \bullet$ → C_2H_6

(9b) $CH_3 \bullet$ + $C_2H_5 \bullet$ → C_3H_8

(9c) $C_2H_5 \bullet$ + $C_2H_5 \bullet$ → C_4H_{10}

give an order in the concentration of DMTC in the rate equation higher than one, which is not in agreement with the linear relationship found in the experiments. The branching mechanism proposed here also explains the somewhat lower activation energy for the overall decomposition reaction, 259 kJ/mol, compared to the Sn-C bond strength in DMTC, viz., 292 kJ/mol [6].
The proposed mechanism adequately explains the formation of the various hydrocarbons found during the experiments and predicts a linear dependence between the formation of the various hydrocarbons and the inlet DMTC concentration. For estimation of the various rate constants, more calibration data are necessary to significantly quantify also the ethene, ethane, and propane formation.
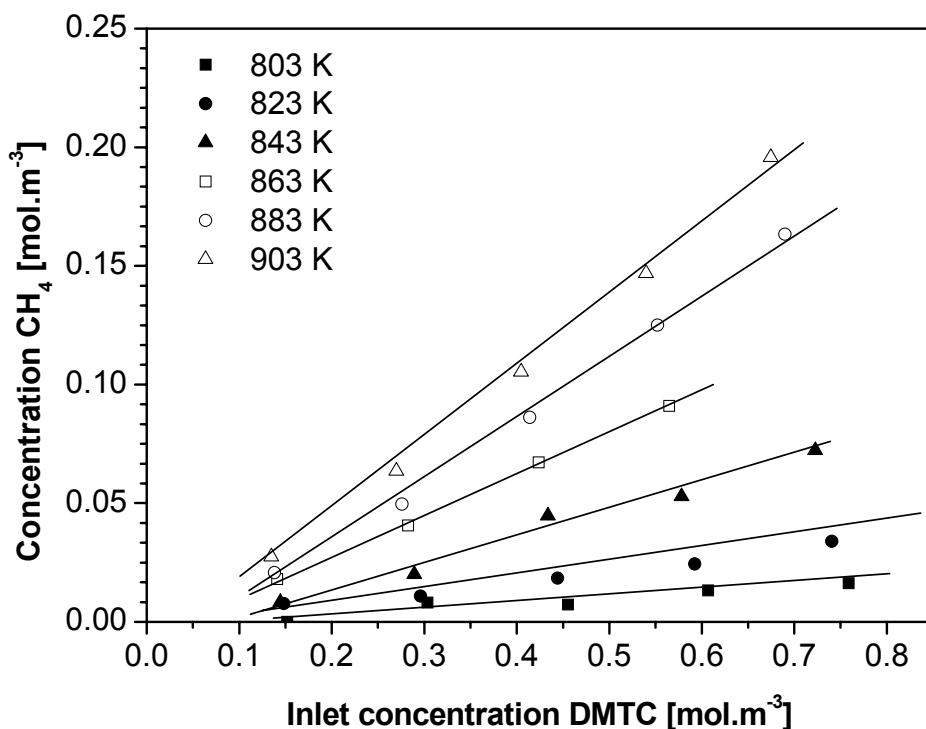
Figure 5.5: *Formation of methane as determined from the FTIR as a function of the inlet concentration DMTC. The different lines represent different reactor temperatures. As the temperature increases more methane is formed, linearly dependent on the inlet DMTC concentration.*

5.3.3 Deposition of SnO_2 from DMTC and O_2 and/or H_2O

Several experiments were conducted to study the reaction between DMTC and oxygen to form tin oxide under various conditions. Both FTIR and mass spectra were recorded. However, due to the large number of species present in the gas phase during the deposition process, the mass spectra were too complex to be deconvoluted, so most of the results are based on FTIR spectra.

According to FTIR analysis, the reaction process starts at about 683 K (410 °C). Figure 5.6 shows a typical spectrum of the gas phase composition recorded during the deposition process. As can be seen in this figure, several gas phase products are formed besides solid tin oxide, i.e. HCl, CH_2O, CH_3OH, CH_4, H_2O, CO_2, and CO. It is possible that also higher hydrocarbons like C_2H_6 and C_3H_8 are formed, but their presence can only be unambiguously detected by FTIR at concentrations higher than about 0.1 mol%. Mass spectra also showed the presence of small amounts of H_2.

In the following sections the results of the deposition experiments with FTIR analysis will be discussed by looking at the influence of DMTC concentration, temperature, oxygen concentration, and water concentration on the formation of by-products and the deposition rate of tin oxide. These results are then used to construct a mechanism of tin oxide formation. This mechanism is also used to propose a two-step reaction mechanism containing the overall deposition rate,
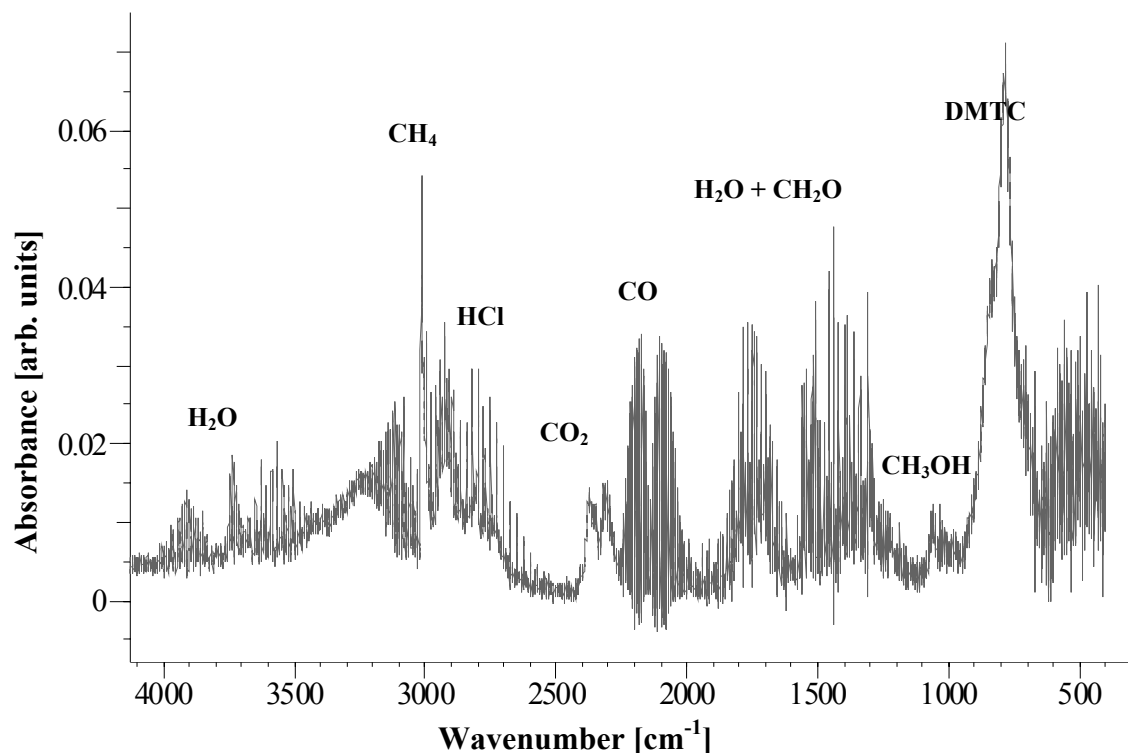
Figure 5.6: *FTIR spectrum of the gas phase composition during the deposition of tin oxide from 2 mol% DMTC and 20 mol% O_2. Reactor temperature is 803 K and the space time is 2 s.*

which will be used in the computational fluid dynamic modelling studies discussed in chapter 7.

Influence of DMTC concentration

Figure 5.7 shows the conversion of DMTC and the growth rate of tin oxide, respectively, at various inlet concentrations DMTC. The deposition rate of tin oxide depends linearly on the inlet concentration DMTC. However, the conversion of DMTC seems to have a non-linear relationship with the inlet concentration of DMTC. Comparison of the growth rate of tin oxide formed and the conversion rate of DMTC also show a significant difference. Expressing both values in $mol.m^{-3}.s^{-1}$ shows that only about 60% (low inlet concentration of DMTC) to 15% (high inlet concentration of DMTC) of the conversion of DMTC can be attributed to the formation of tin oxide. X-ray diffraction analysis of deposits in the exhaust after finalisation of the experiments shows besides residual DMTC also $SnCl_2.5H_2O$. This indicates that part of DMTC is converted into tin oxide and a part is converted into tin dichloride. Exact determination of the selectivity is difficult, because there is also the possibility that some homogeneous nucleation in the gas phase has taken place.
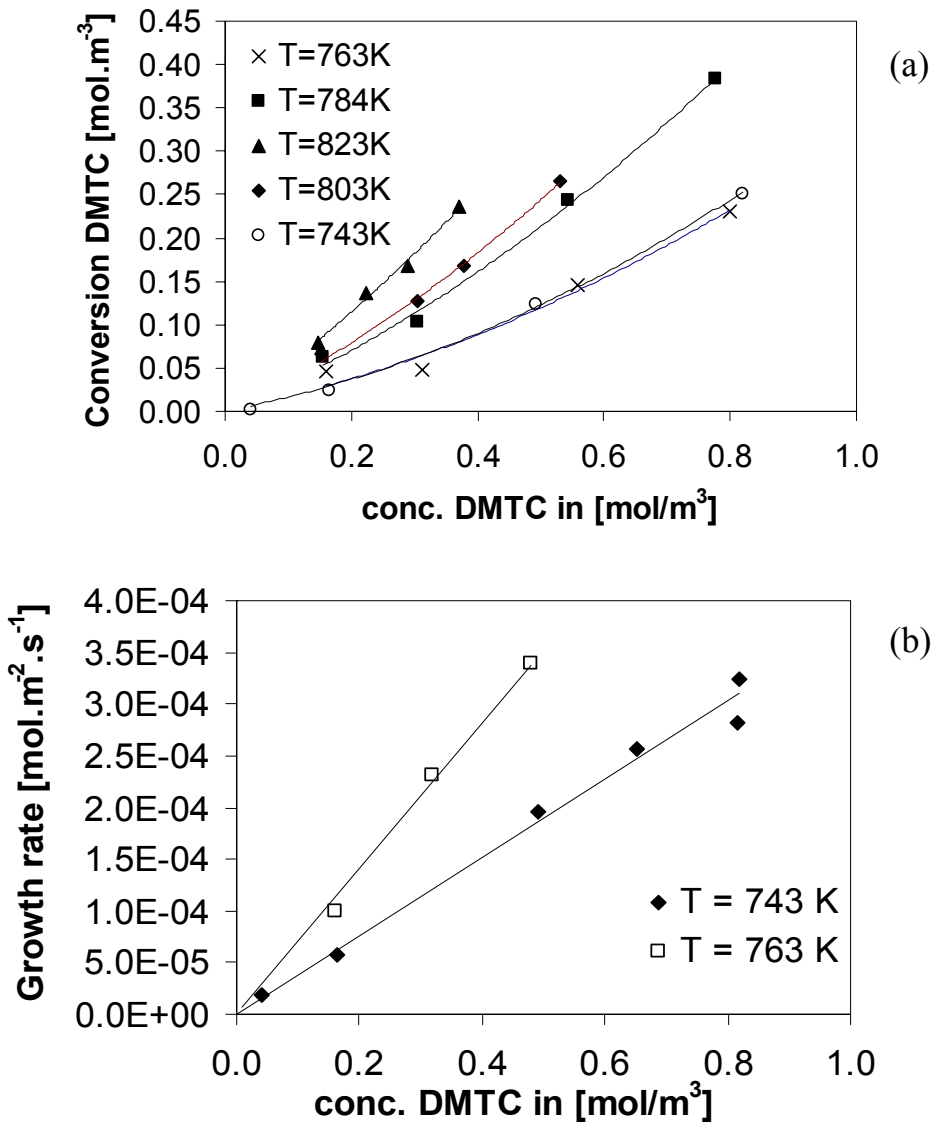
Figure 5.7: *Conversion of DMTC (a) and growth rate (b) of tin oxide as a function of the inlet concentration DMTC at various temperatures.*

The concentrations of gaseous by-products such as CH_4, CO, CO_2, CH_2O, CH_3OH, and H_2O all increase linearly with the inlet concentration of DMTC. However, the concentration of HCl has a sub-linear relationship with the inlet concentration of DMTC. Figure 5.8 shows the dependence of CH_4 and HCl formation on the inlet concentration DMTC at several temperatures. Again this indicates that at higher DMTC concentrations relatively more of the DMTC is converted to $SnCl_2$.

Influence of oxygen concentration

Variation of the concentration of oxygen reveals that for $[O_2]/[DMTC]$-ratios, larger than about 3.5, the influence of the oxygen concentration on the reaction process is neglible, as is shown in figure 5.9. Also FTIR analysis shows little influence above $[O_2]/[DMTC]$-ratios of 3. This implies that for all experiments, which were carried out with 20 mol% O_2, there was always excess oxygen. Using

the data in figure 5.9, the order in oxygen for the overall reaction has been determined. Linear regression of ln(growth rate) versus ln($[O_2]$) shows that the overall reaction order of oxygen changes from 0.34±0.1 at 773K to 0.22±0.1 at 873K. These values are in agreement with the value of 0.25 found by Strickler [12].
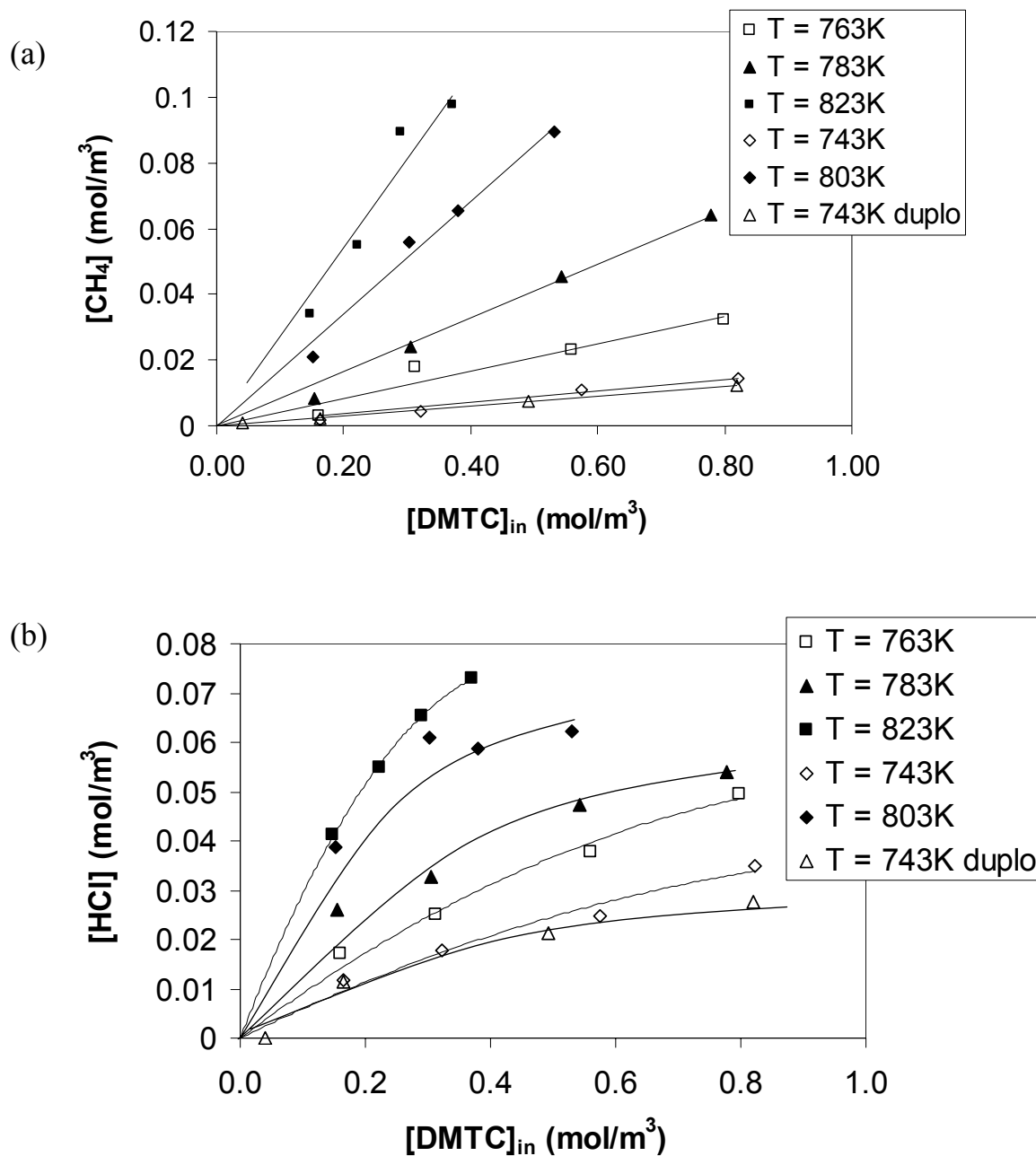
Figure 5.8: *Formation of methane (a) and hydrogen chloride (b) with varying inlet concentration of DMTC. Reactor space time is 2 s. Solid lines are to aid the eye.*
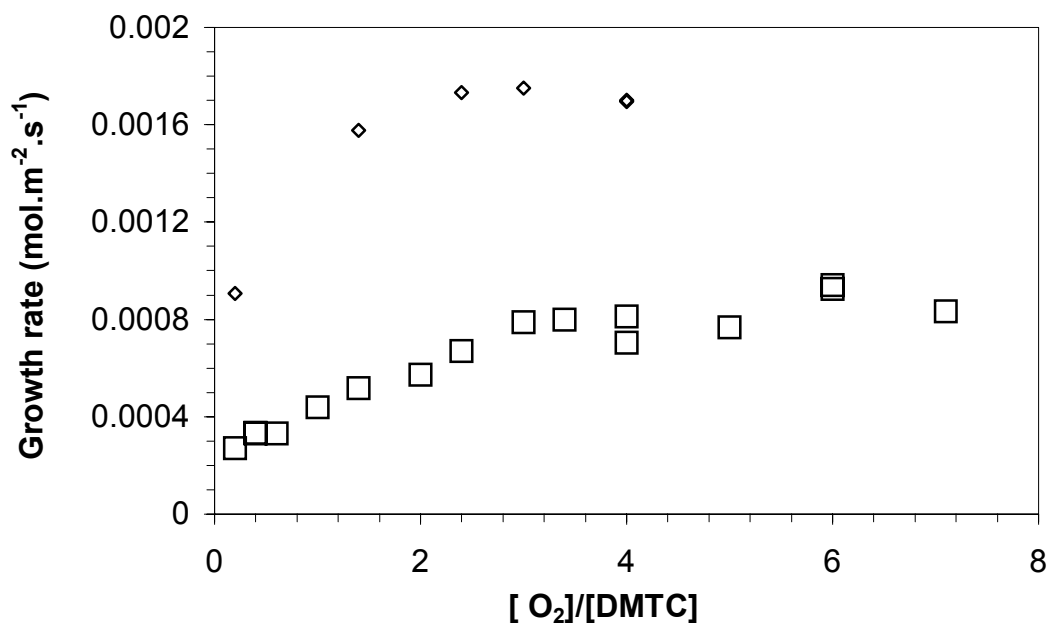
Figure 5.9*: Growth rate of tin oxide measured by mass increase as a function of the inlet [O₂]/[DMTC]-ratio. The squares represent data obtained at 873K, the diamonds represent data obtained at 773K. All data were conducted with 5 mol% DMTC and the reactor space time was 2 s.*

Influence of reactor temperature

As indicated in figure 5.10 the concentrations of CO, CO_2, CH_4, and HCl increase with temperature. The concentrations of CH_2O and CH_3OH decrease with temperature. At temperatures above 843 K both formaldehyde and methanol are not detected by FTIR anymore. FTIR results for experiments above 823 K are not shown in figure 5.9, because these spectra were taken under conditions where no calibration data was available.
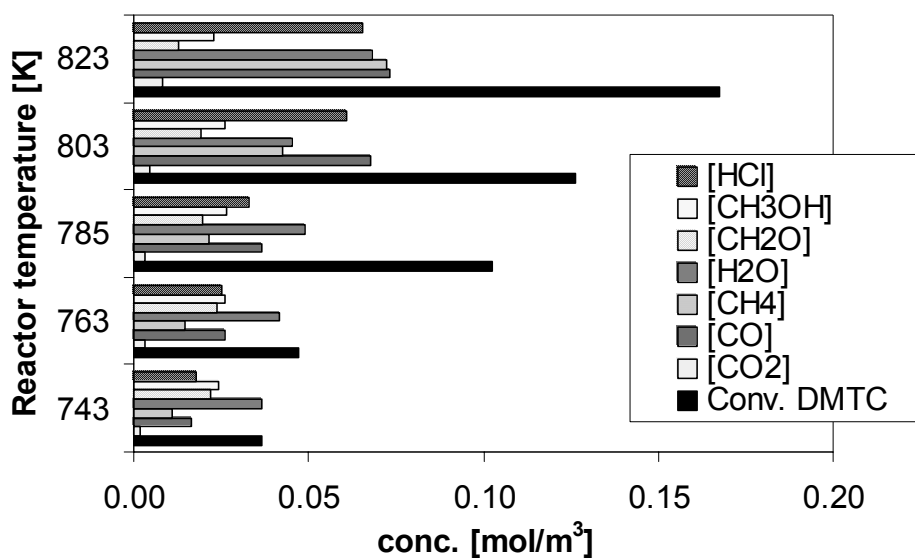
Figure 5.10*: Formation of by-products from the deposition of tin oxide from 2 mol% DMTC + 20 mol% O₂. Reactor space time was 2s.*

The concentration of H_2O is almost constant with temperature, see figure 5.11, indicating that water is both a product and a reactant in the reaction process.
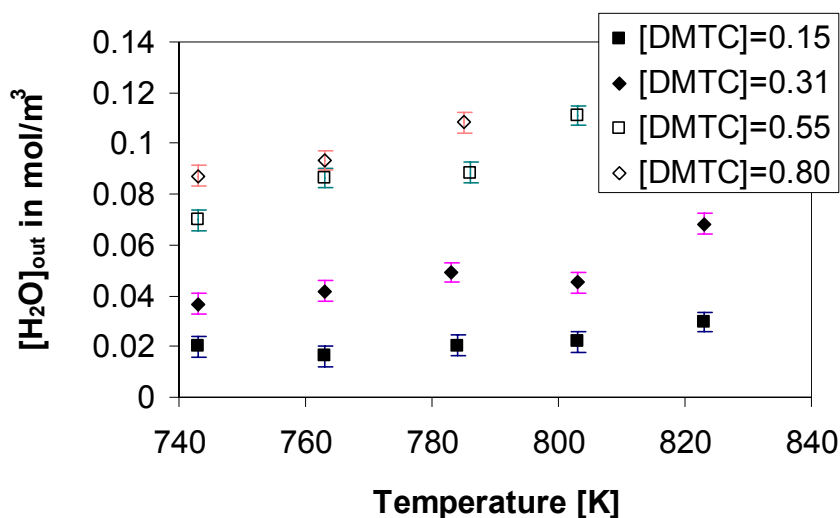
Figure 5.11: *Formation of H_2O from DMTC + 20 mol% O_2. Concentration of DTMC in the legend is given in mol/m^3. Reactor space time was 2 s.*

A comparison of the conversion of DMTC determined from FTIR analysis and the amount of converted DMTC into tin oxide from mass measurements learns, that as shown before, not all DMTC is converted into tin oxide, but a part is also converted into, probably, tin dichloride.

From figure 5.12a, an overall activation energy for tin oxide deposition is determined to be 148±5 kJ/mol. This value was determined without the data obtained at the highest temperature, 883 K. At these temperatures the reaction rate is so high that diffusion processes may influence the deposition rate measurements.

From FTIR analysis, an overall activation energy for the disappearance of DMTC of 92±10 kJ/mol is determined, as is shown in figure 5.12b. The overall error for both values is higher than expected from the nature of the measurements due to the difficulty of maintaining a constant reactor temperature at higher conversion/deposition rates. Both values are significant higher than the value found by Strickler [12], i.e. 75±15 kJ/mol.
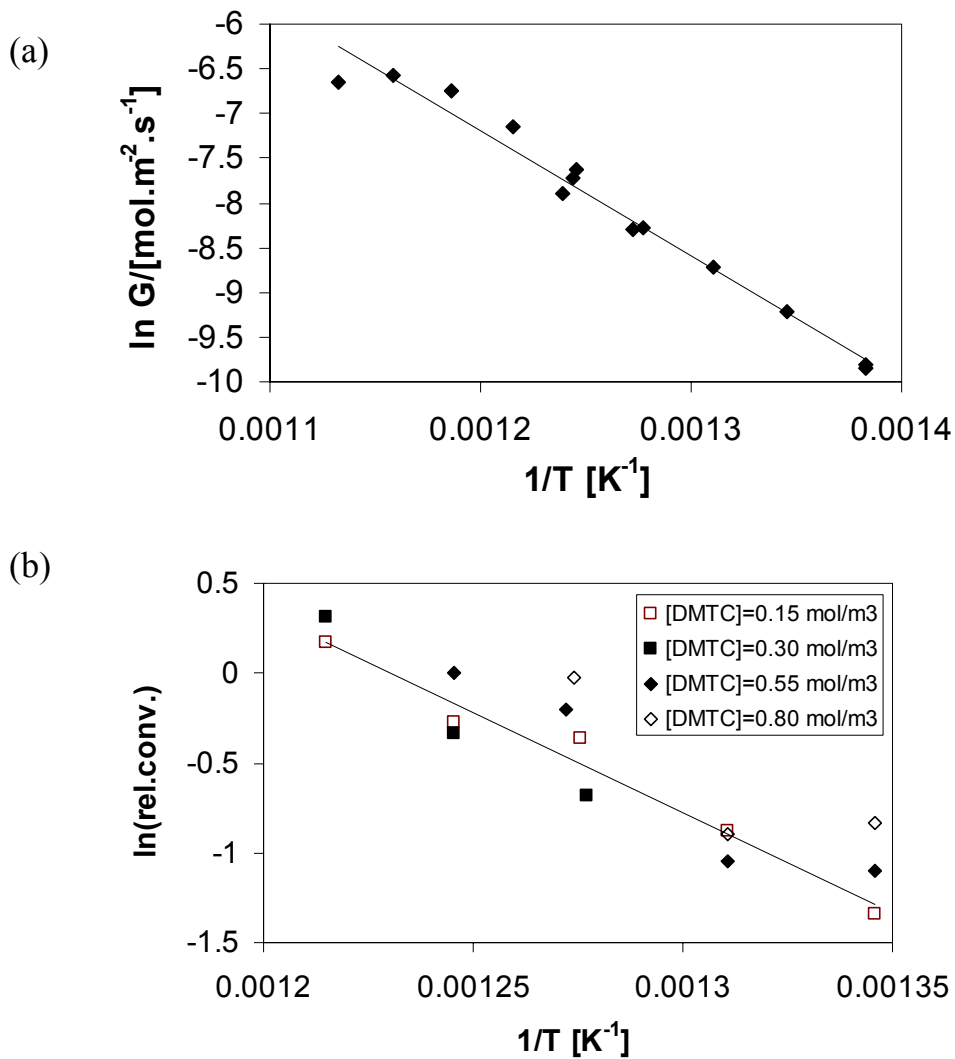
Figure 5.12: *Arrhenius plots for (a) the deposition of tin oxide from 0.34 mol/m³ DMTC, and (b) the conversion of DTMC. The reactor space time was kept at 2 s and [O₂]=3.4 mol/m³ in all experiments.*

Influence of water concentration

Adding water during deposition, increases the deposition rate dramatically, as is shown in figure 5.13a. Using 2 mol% DMTC and 20 mol% O_2 at 743K, addition of 4 mol% H_2O increases the growth rate of tin oxide by a factor of 3.4! Even if the water content was increased from 10 to 15 mol% in the precursor feed, still a significant rise in deposition rate was noticed. Higher water concentrations could not be achieved due to limitations of the experimental set-up. From figure 5.13a, an overall reaction order in water for the deposition process of 0.27±0.02 was determined.

Addition of water lowers the overall activation energy of the deposition process from 148±5 to 99±11 kJ/mol, figure 5.13b. The large error margin is due to the difficulty of maintaining a constant reactor temperature during the experiments. With higher conversion rates more reaction heat is released, which least to a problem with temperature control at higher temperatures.

(a)

(b)
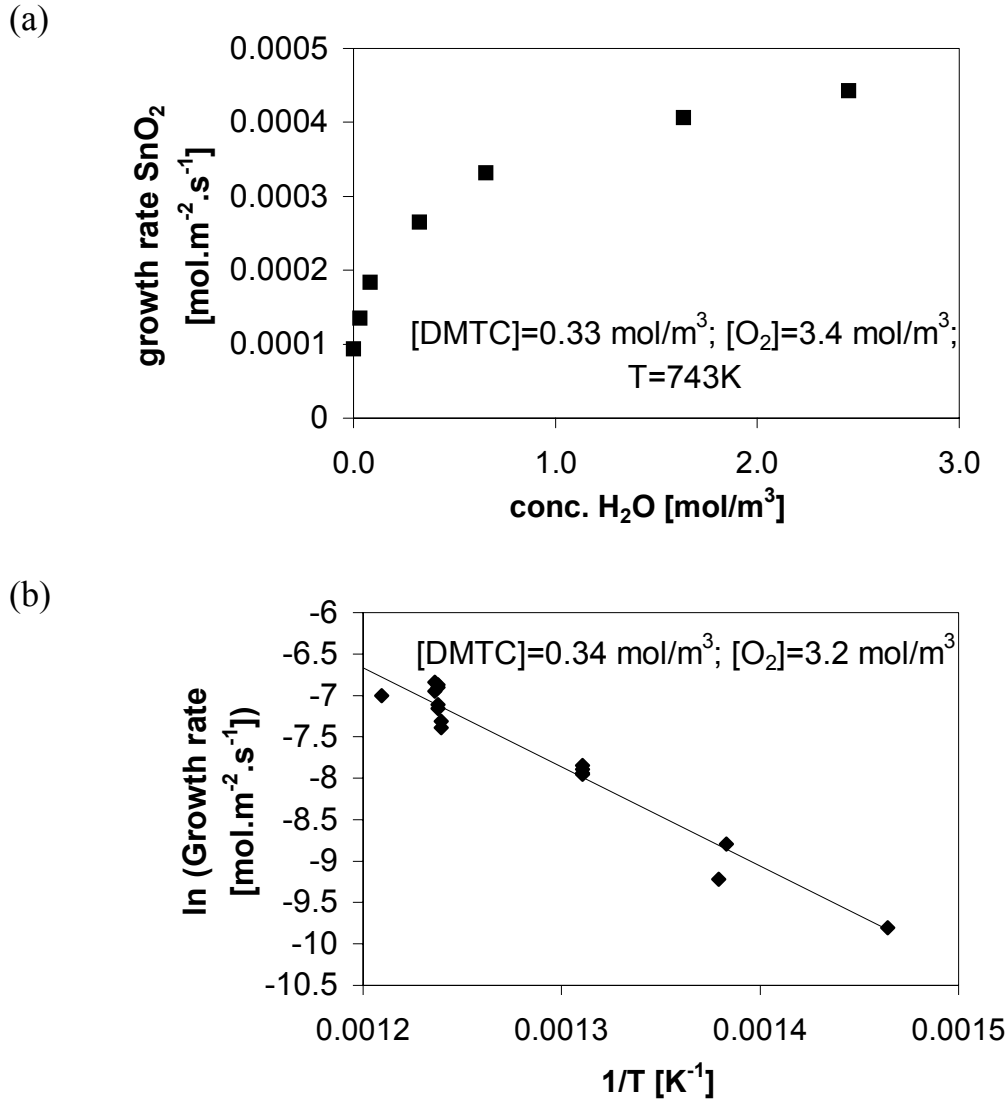
Figure 5.13: *(a) Deposition rate of tin oxide versus the water concentration, (b) Arrhenius plot for the deposition of tin oxide from DMTC, O_2, and H_2O. The reactor space time was kept at 2 s.*

5.3.4 Mechanism of tin oxide deposition from DMTC, O_2, and H_2O

Similar to the decomposition process of DMTC (section 5.3.2), the deposition of tin oxide from DMTC and oxygen begins with the loss of a methyl radical by DMTC:

(1) $(CH_3)_2SnCl_2$ $\rightarrow$ $CH_3SnCl_2\bullet$ $+ CH_3\bullet$

This initiation step has been reported for DTMC by Giunta et al. [4], and for TMT by several authors [8-10, 13-14]. The overall activation energy for the reaction between DMTC + O_2, 92±10 kJ/mol (section 5.3.3) is much lower than is expected from the activation energy of this initiation step, 263±12 kJ/mol (section 5.3.2). Two reasons may exist for this lower activation energy: (1) the radicals formed by the initiation reaction react with DMTC again (branched chain reaction) ; (2) the decomposition of DMTC is enhanced by surface reactions. For the oxidation of

DMTC, the second reason is not likely. Flow tube experiments [15-17] show that the highest growth rates are found at the end of the reactor, indicating that the rate-limiting step is a gas phase reaction. If the rate-limiting step would be on the surface, the highest growth rate would be at the beginning of the reactor, where the concentration of DTMC is highest. However, because gas phase reactions must first produce an intermediate species, which then reacts to tin oxide, a gas phase dominating mechanism would predict the highest growth rate much further from the reactor entrance. A branched chain mechanism has also been suggested for DMTC + O_2 by Giunta et al. [4] and for TMT + O_2 by Zawadski et al. [14].

After the initiation step, the remaining tin radical, will fall apart into tin dichloride and a methyl radical again:

(2) $CH_3SnCl_2\bullet$ → $SnCl_2$ + $CH_3\bullet$

Alternatively, the methyltin dichloride radical can also react with oxygen to produce a peroxide radical, as proposed by Giunta et al [4], but it is believed by those authors that reaction step (2) is faster, mainly because the bond strength of the Sn-C bond in CH_3SnCl_2 is relatively small, i.e. 23.6 kcal/mol [6].
The produced methyl radicals can either react with oxygen to form formaldehyde and OH radicals [18]:

(10) $CH_3\bullet$ + O_2 → CH_2O + $OH\bullet$

or react with unreacted DMTC to form ethane and methane:

(3) $CH_3\bullet$ + DMTC   → C_2H_6 + $SnCl_2CH_3\bullet$

(4) $CH_3\bullet$ + DMTC   → CH_4 + $SnCl_2CH_3CH_2\bullet$

The reaction between the $SnCl_2CH_3CH_2$ radical from reaction (4) and oxygen forms the peroxide $SnCl_2CH_3CH_2OO$. One subsequent reaction possible route is the decomposition of this peroxide radical into CH_3SnCl_2 and CH_2OO, followed by a fast decomposition of CH_2OO into CO and H_2O [18]:

(11) $SnCl_2CH_3CH_2\bullet$ + O_2 → $SnCl_2CH_3CH_2OO\bullet$

(12) $SnCl_2CH_3CH_2OO\bullet$ → $CH_3SnCl_2\bullet$ + $CH_2OO\bullet$

(13) $CH_2OO\bullet$ →   CO   + H_2O
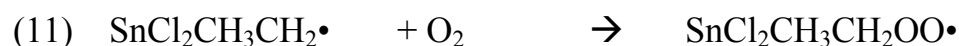
A second possibility is β-elimination of formaldehyde, resulting in the formation of $OSnCH_3Cl_2$, as is proposed by Giunta et al. [4]:

(12a) $SnCl_2CH_3CH_2OO\bullet$ → $OSnCH_3Cl_2\bullet$ + CH_2O

In contrast with the decomposition mechanism, the oxidation mechanism as proposed here, also produces OH radicals, which can react with DMTC to form water and methanol:

(14) OH• + DMTC → H_2O + $SnCl_2CH_3CH_2$•

(15) OH• + DMTC → CH_3OH + $SnCl_2CH_3$•
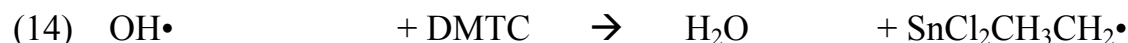
The gas phase reaction mechanism proposed in steps (1)-(4) and (10)-(15) results in the formation of the stable species tin dichloride. It is believed that $SnCl_2$ is the key intermediate for tin oxide formation on the surface. $SnCl_2$ can react in the gas phase with oxygen, or it adsorbs on the surface to undergo subsequent reactions to form $SnO_{2-x}Cl_x$.

The gas phase reactions possible for $SnCl_2$ are next evaluated based on the thermodynamic data on tin compounds, obtained from ab-initio BAC-MP4 calculations by Allendorf et al. [19]. Appendix 5A gives an overview of the heats of formation of the various compounds involved. According to the BAC-MP4 calculations the reaction between $SnCl_2$ and O_2 gives the cyclic compound – $O(SnCl_2)O$-:

(16) $SnCl_2$ + O_2 → $-O(SnCl_2)O-$
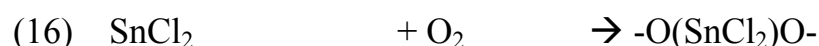
which is slightly endothermic by 28 kJ/mol at 800 K. Subsequent decomposition of this compound at the reactor temperatures is probably slow because they are both highly endothermic:

(17a) $-O(SnCl_2)O-$ → $-O(SnCl)O-$ + Cl•
ΔH_r = 160 kJ/mol at 800 K

(17b) $-O(SnCl_2)O-$ → $OSnCl_2$ + O•
ΔH_r = 207 kJ/mol at 800 K

However, subsequent reactions of $-O(SnCl_2)O-$ with the radicals produced during the decomposition of DMTC, such as H and OH, are very exothermic, and depending on the transition state, may react much faster to form $–O(SnCl)O-$:

(18) $–O(SnCl_2)O-$ + H• → $–O(SnCl)O-$ + OH•
ΔH_r = -147 kJ/mol at 800 K

(19) $–O(SnCl_2)O-$ + OH• → $–O(SnCl)O-$ + HOCl
ΔH_r = -83kJ/mol at 800 K
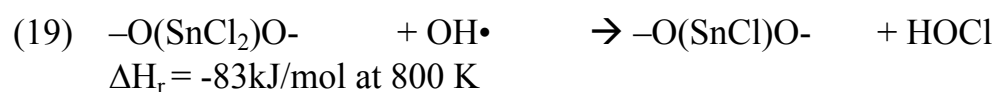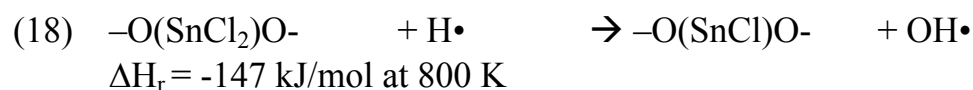
In any case the film precursor probably undergoes the Sn-Cl cleavage on the surface. The Sn-Cl dissociation energies for both $SnCl_2$ and $–O(SnCl_x)O-$ are very high, in the order of 400 kJ/mol [19], so cleavage in the gas phase is improbable.

The surface is also a good sink for CH_x species, as has become clear in the decomposition experiments, showing a black residue on the tin oxide coated walls of the reactor, which upon treatment with high temperature oxygen produced CO, CO_2 and H_2O.

In an oxygen atmosphere the CH_3 radicals produce OH and CO on the tin oxide surface, as is summarised in the following reaction step:

(20) CH_3 $+ 4O*$ $\rightarrow CO$ $+ OH*$ $+ *$

where O* is adsorbed oxygen, OH* is adsorbed OH, and * is a free surface site. The adsorbed OH groups react with $SnCl_2$ or $OSnCl_2$ to form $SnO_{2-x}Cl_x$:

(21a) $SnCl_2$ $+ (2-x)OH* \rightarrow SnO_{2-x}Cl_x$ $+ (2-x)HCl$

(21b) $OSnCl_2$ $+ (2-x)OH* \rightarrow SnO_{2-x}Cl_x$ $+ (2-x)HCl$ $+ O*$
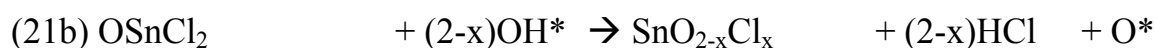
The mechanism explains the formation of the by-products of the decomposition and deposition process as is observed with FTIR analysis. In order to validate this mechanism quantitatively the rates of the individual reaction steps must be known. Due to the extensive research done in the field combustion, the rates of reactions in the C-H-O-Cl system are known. However, for the rates of reaction involving the tin species neither quantitative data have been measured yet directly nor theoretical results, such as Rice-Ramsperger-Kassel-Marcus (RRKM) calculations, are available.

The rates of the reaction steps in the C-H-O system were used to verify if methanol and formaldehyde are readily oxidised to CO, CO_2 and H_2O at the temperatures used during the experiments. The mechanism of Marinov [18] was used to predict what would happen with CH_2O and CH_3OH if these species were exposed to an oxygen rich atmosphere at temperatures between 673 and 973 K. Chemical mechanism evaluation with the software package Chemkin–Aurora [20] show that no significant decomposition of CH_2O and CH_3OH has taken place. However, during the deposition process also reactions with OH radicals are possible. These reactions result though in the production of CHO or CH_2OH radicals, which are not as good hydrogen abstractors as OH is. These reaction steps would eventually slow down the reaction process, of which no indication has been found. Another possibility is that the tin oxide surface catalyses the conversion of CH_3OH and CH_2O, as it is known that tin oxide catalyses the oxidation of CO to CO_2 [21]. The CSTR reactor was used to test this hypothesis.

Without the tin oxide coating on the reactor walls a mixture of methanol and oxygen did not react below a temperature of 873 K. When the walls of the CSTR were precoated with a layer of tin oxide, methanol without oxygen in a nitrogen atmosphere started to decompose at 773 K, giving CO, CO_2, CH_2O, and H_2O. In the presence of oxygen, conversion was detected at temperatures as low as 573 K!

Although nothing was found in existing literature on the thermal decomposition or oxidation of methanol over tin oxide, this same type of behaviour has been reported for other metal oxides as CuO [22] and ZrO_2 [23]. This means that, besides the reaction of $OSnCl_2$ or $SnCl_2$, also other surface reactions take place, which compete with each other for the available active sites on the surface. This would mean that addition of methanol as a precursor in the deposition of tin oxide may lead to a lowering of the deposition rate, which has also been reported [24].

Another important species, which is almost always added to the precursor feed in commercial tin oxide processes, is water. As is shown in section 5.3.3 water increases the deposition rate tremendously. Several possible reaction routes may explain this increase in the rate of tin oxide formation:

1. Water enhances the formation of OH groups on the growing surface [25], thereby enhancing reactions 21a or 21b.
2. Water forms a complex with DMTC in the gas phase. This complex may weaken the Sn-Cl bond, thereby forming an additional film precursor to $OSnCl_2$ or $SnCl_2$. This film precursor may be present in the form of $Sn(OH)_2$, which on the surface forms SnO_x.
3. Water reacts with the decomposition product $SnCl_2$. This may have two effects. More radicals are produced to enhance the decomposition rate of DMTC, or the deposition rate of SnO_2 is enhanced due to the formation of a more favourable intermediate.

The first two options are difficult to probe both experimentally and theoretically. The third option has been evaluated again by thermodynamical data based on ab-initio quantum mechanical calculations [19]. Figure 5.14 lists an overview of the possible routes and their heats of reaction at 800 K.
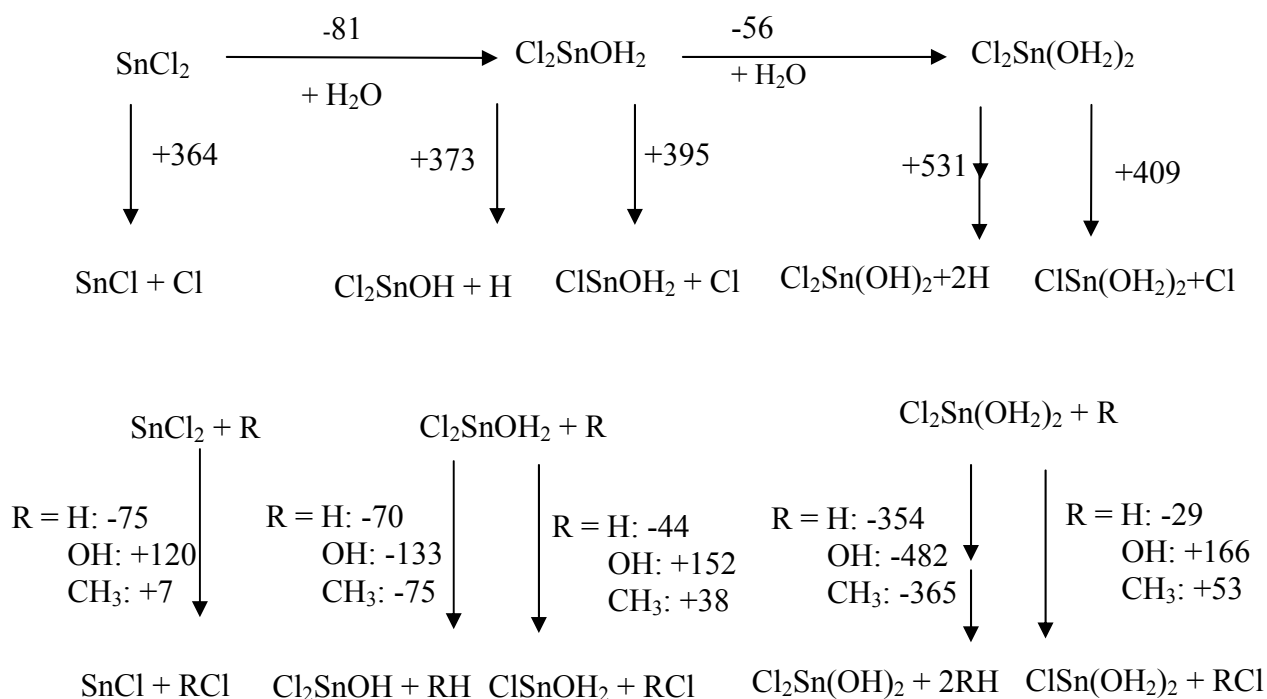
Figure 5.14: *Possible reaction pathways during for hydrolysis of $SnCl_2$. The heats of reaction (kJ/mol) are based upon the heats of formation listed in appendix 5A.*

Unimolecular decomposition of $SnCl_2$ into $SnCl$ and Cl is very endothermic. Because it is an unimolecular reaction step the calculated heat of reaction, 364 kJ/mol, is close to the activation barrier for this step. Complex formation of water with tin dichloride can occur exothermally:

(22) $SnCl_2$ + H_2O $\rightarrow$ Cl_2SnOH_2
ΔH_r = -81.4 kJ/mol
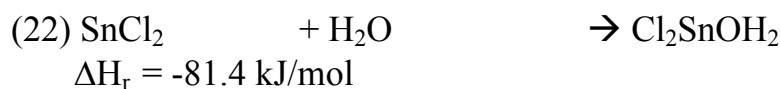
Subsequent loss of a hydrogen or a chlorine atom is still very endothermic, i.e. 370 kJ/mol for loss of H, and 395 kJ/mol for loss of Cl. So, instead of unimolecular decomposition, the tin dichloride-water complex probably undergoes a subsequent reaction with water or it undergoes H or Cl-abstraction by a radical. For example, H-abstraction of Cl_2SnOH_2 by OH is exothermic by 133 kJ/mol at 800 K. However, another addition of a water molecule seems even more thermodynamically favourable:

(23) Cl_2SnOH_2 + H_2O $\rightarrow$ $Cl_2Sn(OH_2)_2$
ΔH_r = -56.0 kJ/mol

The oxygen-hydrogen bonds in this $Cl_2Sn(OH_2)_2$ complex seem to have weakened with respect to Cl_2SnOH_2. The decomposition of the tin dichloride dihydrate complex into dichloro tindihydroxide is endothermic by 531 kJ/mol. This is an average of 265 kJ/mol for each loss of a hydrogen atom. This route would produce more H-radicals, which can enhance the decomposition rate of DMTC. However, radicals can also react with the tin dichloride-water complexes themselves. Although the heats of these reactions are negative, there may be a barrier for these bimolecular reactions steps.

5.4 Conclusions

The CSTR system described in chapter 3 was used to study the reaction mechanism and kinetics of DMTC with and without oxygen or water. Pyrolysis experiments with DMTC in nitrogen reveal that DMTC decomposes to tin dichloride, methane, ethane, ethene, and propane. A linear relation was found between hydrocarbon formation and the inlet DMTC concentration, and between the DMTC concentration present in the reactor and the inlet DMTC concentration. An elementary step reaction mechanism has been proposed which could adequately explain these results. Through calibration of the FTIR for DMTC, an activation energy for the overall reaction of 263 ± 12 kJ/mol was derived which is in agreement with previous results reported in literature.
In the presence of oxygen, the initiation step is the same as for pyrolysis, cleavage of the Sn-C bond in DMTC. However, the methyl radicals present after this initiation step react with oxygen eventually leading to a branched radical chain

mechanism. As shown in the discussion section the reaction mechanism of tin oxide is very complex, and the final intermediate, which will form tin oxide on the surface is not apparent.

Even without the addition of water, it is still necessary to incorporate its influence because oxidation of the methyl ligands of DMTC eventually leads to the formation of water. Figure 5.14 only shows some of the possible paths $SnCl_2$ can take. It is also possible that water forms complexes with DMTC itself. Only a combined theoretical and experimental approach will succeed in identifying the individual reaction steps that lead to the deposition of tin oxide.

The results presented in this chapter will form the basis to propose a lumped mechanism that will be used to simulate two types of CVD reactors in chapter 7.

References

[1] M. D. Allendorf, A.H. McDaniel, A. M. B. Van Mol, *Proceedings of the 4th ICCG*, 195 (2002).

[2] Ghoshtagore, R.N. *J. Electrochem. Soc.*, **1978**, *125(1)*, 110.

[3] Ghoshtagore, R.N. *Proc. Int. Conf. Chem. Vap. Deposition*, **1977**, *6th*, 433.

[4] Giunta, C. J., Strickler, D. A., Gordon, R. G. *J. Phys. Chem.*, **1993**, *97(10)*, 2275.

[5] Alcott, R.G., Van Mol, A.M.B., Spee, C.I.M.A., *Chem. Vap. Deposition*, **2000**, *6(5)*, 261.

[6] Allendorf, M.D., *personal communication*.

[7] Price, S.J.W., Trotman-Dickenson, A. F., *Trans. Faraday Soc.*, **1958**, *54*, 1630.

[8] Johnson, R.P., Price, S.K.W., *Can. J. Chem.*, **1972**, *50*, 50.

[9] Borrell, P., Platt, A.E., *Trans. Faraday. Soc.*, **1970**, *66*, 2286.

[10] Taylor, J.E.; Milazzo, T.S., *J. Phys. Chem.*, **1978**, *82*, 847.

[11] Baulch, D.L.; Cobos, C.J.; Cox, R.A.; Frank, P.; Hayman, G.; Just, Th.; Kerr, J.A.; Murrells, T.; Pilling, M.J.; Troe, J.; Walker, R.W.; Warnatz, J., *J. Phys. Chem. Ref. Data*, **1994**, *23*, 847.

[12] Strickler, D.A. *PhD. Thesis,* Harvard University*, **1989**.

[13] Aleksandrov, Y., Baryshnikov, Y.Y., Zakharov, I.L., Lazareva, T.I., *Kinet. Catal.*, **1990**, *31*, 637.

[14] Zawadzki, A. G.; Giunta, C. J.; Gordon, R. G., *J. Phys. Chem.*, **1992**, *96*, 5364.

[15] Sanders, H.E., *Proc. of the 14th Int. Conf. And EuroCVD-11*, **1997**, *97-25*, 81.

[16] Rivero, J.M., Marsh, J., Raisbeck, D., *J. Phys. IV France*, **1999**, *9*, Pr8-1003.

[17] Hopfe, V., Sheel, D.W., Raisbeck, D., Rivero, J.M., Graehlert, W., Throl, O., Van Mol, A.M.B., Speee, C.I.M.A., *J. Phys. IV France*, **2001**, *11*, Pr3-1153.

[18] Marinov, N. M., Pitz, W. J., Westbrook, C. K., Vincitore, A. M., Castaldi, M. J., Senkan, S. M., *Combustion and Flame*, **1998**, *114*, 192.

[19] Allendorf, M.D., Nielson, I, Melius, C., *to be published*.

[20] Kee, R., Rupley, F.M., meeks, E., Miller, J.A., Chemkin III: A fortran chemical kinetics package for the analysis of gas-phase chemical and plasma

kinetics. *Technical Report SAND96-8216,* Sandia Nat. Lab., Albuquerque, New Mexico, **1996**.

[21] Fuller, M.J.; Warwick, M.E., *J. Catal.,* **1973**, *29*, 441.

[22] Poulston, S., Rowbotham, E., Stone, P., Parlett, P., Bowker, M., *Catal. Letts.*, **1998,** *52*, 63.

[23] Fisher, I.A., *J. Catal.*, **1999**, *184*, 357.

[24] Gotoh, Y, Mizuhashi, M. *Asahi   Garasu Kenkyu Hokoku*, **1984**, *34(2)*, 123.

[25] Wartenberg, E.W., Ackermann, P.W., *Glastech. Ber.*, **1988**, 61, 256.

[26] Chase, Jr. M.W., Davies, C.A., Downey, Jr. J.R., Frurip, D.J., McDonald, R.A., Syverud, A.N., JANAF Thermochemical Tables, *J. Phys. Chem. Data*, **1985**, *14.*

Appendix 5A: Heats of formation

Table A5.1: *Heats of formation in kJ/mol of various species, involved in the CVD of tin oxide.*

species	$\Delta H_f(298K)$	$\Delta H_f(600K)$	$\Delta H_f(700K)$	$\Delta H_f(800K)$	$\Delta H_f(900K)$	reference
$SnCl_2$	-189.3	-172.2	-166.5	-160.7	-154.9	[19]
H_2O	-241.8	-231.3	-227.6	-223.8	-219.9	[26]
O_2	0.0	9.3	12.5	15.8	19.2	[26]
$-O(SnCl_2)O-$	-167.4	-137.6	-127.3	-116.8	-106.3	[19]
$-O(SnCl)O-$	-127.5	-104.9	-97.0	-89.1	-81.1	[19]
$SnCl$	70.4	70.4	70.4	70.4	70.4	[19]
Cl_2SnOH_2	-517.6	-487.2	-476.7	-466.0	-455.1	[19]
$Cl_2Sn(OH_2)_2$	-823.4	-777.6	-761.8	-745.8	-729.5	[19]
Cl_2SnOH	-364.3	-339.1	-330.3	-321.4	-312.4	[19]
$Cl_2Sn(OH)_2$	-732.9	-697.2	-684.7	-671.9	-658.9	[19]
$ClSnOH$	-17.6	-0.9	4.8	10.5	16.2	[19]
$ClSnOH_2$	-245.3	-221.1	-212.6	-204.0	-195.2	[19]
$ClSn(OH_2)_2$	-532.8	-495.5	-482.5	-469.3	-455.7	[19]
H	218.0	224.3	226.3	228.4	230.5	[26]
O	249.2	255.7	257.8	259.9	262.0	[26]
OH	39.0	47.9	50.9	53.9	56.9	[26]
Cl	121.3	128.1	130.4	132.6	134.9	[26]
OCl	122.2	132.5	136.1	139.7	143.3	[26]
H_2	0.0	8.8	11.8	14.7	17.7	[26]
Cl_2	0.0	10.7	14.4	18.1	21.9	[26]
$HOCl$	-78.0	-65.7	-61.3	-56.7	-52.0	[20]
HCl	-92.3	-83.5	-80.5	-77.5	-74.4	[26]

Chapter 6. Tin Oxide Deposition in a Stagnant Point Flow Reactor

Abstract

The deposition kinetics and film properties of tin oxide films grown from five different tin precursors are compared in an atmospheric pressure stagnant point flow reactor. Deposition was performed on glass and aluminum substrates using the precursors monobutyltin chloride (MMTC), dimethyltin chloride (DMTC), monomethyltin trichloride (MBTC), tin tetrachloride (TTC), and tetramethyltin (TMT) with oxygen as an oxidant. Apparent activation energies were calculated for each precursor using the Arrhenius equation, giving different activation energies for both substrates. The highest deposition rates on both glass and aluminum substrates at temperatures below 650°C were achieved using monobutyltin trichloride. Optimum film resistivity of 1.2x10^{-3} ohm.cm was found for a tin oxide layer of 550 nm grown at 675 °C from monomethyltin trichloride.

The growth rates of tin oxide from DMTC + O$_2$, experimentally determined in this reactor system will be compared with computational simulations discussed in chapter 7.

6.1 Introduction

A comparison is made with respect to deposition kinetics and film properties for tin oxide thin films grown from a variety of precursors using atmospheric pressure chemical vapour deposition. The system used is a stagnant point flow reactor, of which a description is given in section 6.2. Deposition was performed on glass and aluminum substrates using the precursors monobutyltin trichloride (MBTC), dimethyltin dichloride (DMTC), monomethyltin trichloride (MMTC), tin tetrachloride (TTC), and tetramethyltin (TMT) with oxygen as oxidant. The use of aluminum as a substrate is tested for solar cell applications as is described in chapter 1. This reactor set-up will also be used to compare growth rates for DMTC and O$_2$ with growth rates predicted by Fluent® simulations (chapter 7).

The growth rates of these precursors and their apparent activation energies for both substrates are discussed in section 6.3. A comparison of resistivities of the layers grown from each precursor is given in section 6.4.

6.2 Experimental system

Deposition experiments were conducted using a cold wall stagnant point flow reactor (SPFR) at atmospheric pressure as depicted in figure 6.1. The reactor consists of a fused silica tube (length 200 mm, internal diameter 46 mm), which is clamped in a vertical position via two stainless steel flanges. The substrate (17.5 mm^2 x 4 mm glass or 30 mm^2 aluminum foil) is supported in the centre of the reactor by a steel susceptor that is heated inductively. Standard process conditions are a total flow rate of 2 standard litres per minute (SLM), an inlet temperature of 180 °C, and an inlet concentration of 20 vol% oxygen. The other process conditions for the various experiments are given in table 6.1.

Table 6.1: Process conditions used for deposition of tin oxide in the SPFR.

Precursor	Molfraction	Substrate	Temperature range [K]
MBTC	0.01	glass	673-923
MBTC	0.02	glass, aluminum	673-923
MBTC	0.03	glass	673-923
DMTC	0.02	glass, aluminum	823-998
DMTC	0.02	glass	823-998
MMTC	0.02	glass, aluminum	823-998
MMTC	0.04	glass	823-998
TMT	0.01	glass	823-1023
TMT	0.02	glass, aluminum	823-1023
TMT	0.03	glass	823-1023
TTC	0.03	glass, aluminum	823-1023

Controlled evaporation and transportation of tin precursors to the reactor is achieved using a bubbler system with heated gas lines. Precursor concentrations and flows were calculated from their vapour pressures (chapter 4) assuming a 100% saturated flow from the bubbler. After each refill of the bubbler, the deposition process is repeated until the deposited layers are reproducible. After refilling the bubbler, the deposition rate is initially higher due to small concentrations of impurities, which can act as a tin oxide source, present in the precursor supply, or due to the presence of water. When these contaminants are exhausted due to the deposition reactions, the deposition rate becomes stable.

All gas flows were controlled using thermal mass flow controllers (Bronkorst HiTec). Layer thickness and sheet resistance measurements were made in the centre of each substrate, which lies immediately below the stagnant point in the reactor geometry during film deposition. Electrical measurements were made using the 4-point probe technique (Probe head: Jandel Engineering Universal Probe, current source and nanovoltmeter: Autolab PGSTAT20 from Ecochemie). The distance *s* between neighbouring collinear electrode tips was about 1 mm for all spaces. Thus the area characterised with each measurement was of the size of about 3 mm^2 on a sample of about 17.5 by 17.5 mm. Because the sheet resistance was always measured in the middle of the sample, edge effects are excluded. For the
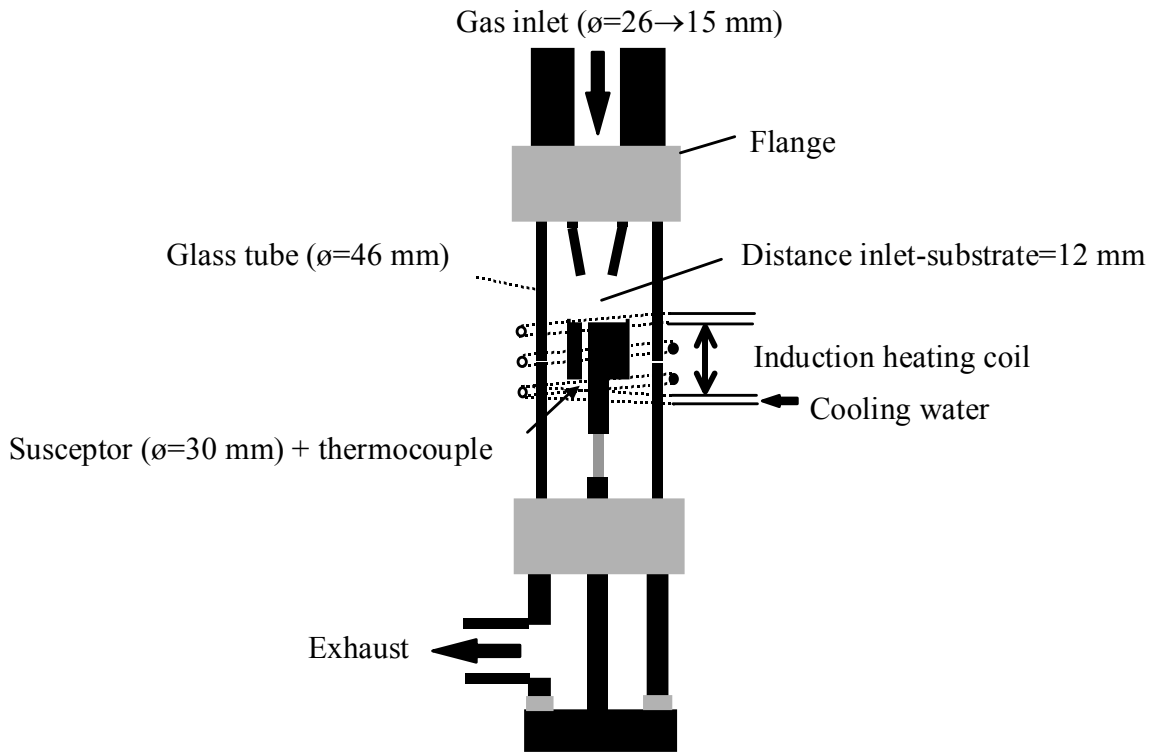
Figure 6.1: *Schematic presentation of the stagnation point flow reactor.*

films, the sample thickness (in the order of 1 μm) is much lower than the distance between the probes. Under these conditions, sheet resistance and bulk resistivity are calculated as:

$$R_{sh} = \frac{\pi}{\ln 2} \cdot \frac{V}{I} \qquad\qquad (6.1)$$

$$\rho = R_{sh} \cdot th \qquad\qquad (6.2)$$

with R_{sh} = sheet resistance [ohm/square]
V = measured voltage drop [V]
I = applied current [A]
ρ = resistivity [ohm.cm]
th = thickness of the film [cm]

For glass samples, film thickness and hence growth rate were determined by first etching a step across the coating using a Zn/HCl slurry, followed by step profile measurements performed on either a Tencor Alfa Step or a Tencor R-10 Surface Profiler. Growth rates for deposition on aluminum foil were determined from mass balance (Mettler AT261 Delta range, accuracy 0.01 mg) measurements made before and after deposition experiments. The density of the layer was assumed to be the same as the density of bulk tin oxide, i.e. 6.95 g/cm³.
Atomic Force Microscopy (AFM) measurements were conducted with an Autoprobe CP AFM from Park Scientific (100 μm contactmode scanner), using Proscan software version 1.511b.001 (Park Scientific Instruments). The vertical

resolution is 0.1 nm and the horizontal resolution is ca. 2nm (a scan of 1 μm corresponds to 512 lines).

The scans are analysed with Autoprobe Image software version 2.1.15 from Thermo Microscopes.

The crystalline properties of the film are measured with X-ray diffraction (XRD) using a Philips Xpert MPD. A wavelength of 0.15405 nm was used. The measurements were done from $2\theta = 10°$ to $95°$ with a step size of $0.02°$ and an interval of 2 s. From these measurements, the preffered crystallographic planes for each sample were determined from the integral peak height.

Deposition was performed using technical grade monobutyltin trichloride (MBTC, 95%, Elf Atochem), monomethyltin trihloride (MMTC, 99%, Alfa), tin tetrachloride (TTC, 99% Aldrich), tetramethyltin (TMT, 95% Aldrich), and purified dimethyltin dichloride (DMTC, Pilkington).

6.3 Results

6.3.1 Deposition rates

An overview of the growth rates of the deposited layers on glass and aluminum are depicted in figures 6.2a and 6.2b. The highest deposition rates on both glass and aluminum substrates up to temperatures of 650 ºC, were achieved using MBTC precursor. To achieve the same deposition rate using the other precursors, considerable higher substrate temperatures had to be used. Thick films deposited from MBTC (>1000 nm), exhibited poor adhesion to the glass substrates and could be pulled off with PVC electrical tape. Films of equal thickness deposited from either DMTC or MMTC exhibited better adhesion to the glass substrates. Only very poor quality films or no films at all were obtained from the TTC/O_2 precursor system on the glass substrates. In cases where deposition did occur, it is thought to be because of water contamination in the system or the occurrence of gas phase reactions due to the exceptionally high susceptor temperatures. In cases where deposition on aluminum foil did occur, the material deposited consisted of a white crystalline solid, not a transparent thin film. These observations for TTC are in agreement with the experiments by Ghoshtagore [2] who deposited tin oxide from TTC and O_2 only above 973 K.

Table 6.2 shows some roughness data measured by AFM. With MBTC, very reproducible smooth tin oxide films could be produced at relatively low temperatures on both substrates. TMT and MMTC also generated smooth tin oxide coatings, but they contained more pinholes, and higher reaction temperatures were needed to achieve comparable growth rates to that of MBTC. Films deposited from DMTC were much rougher.
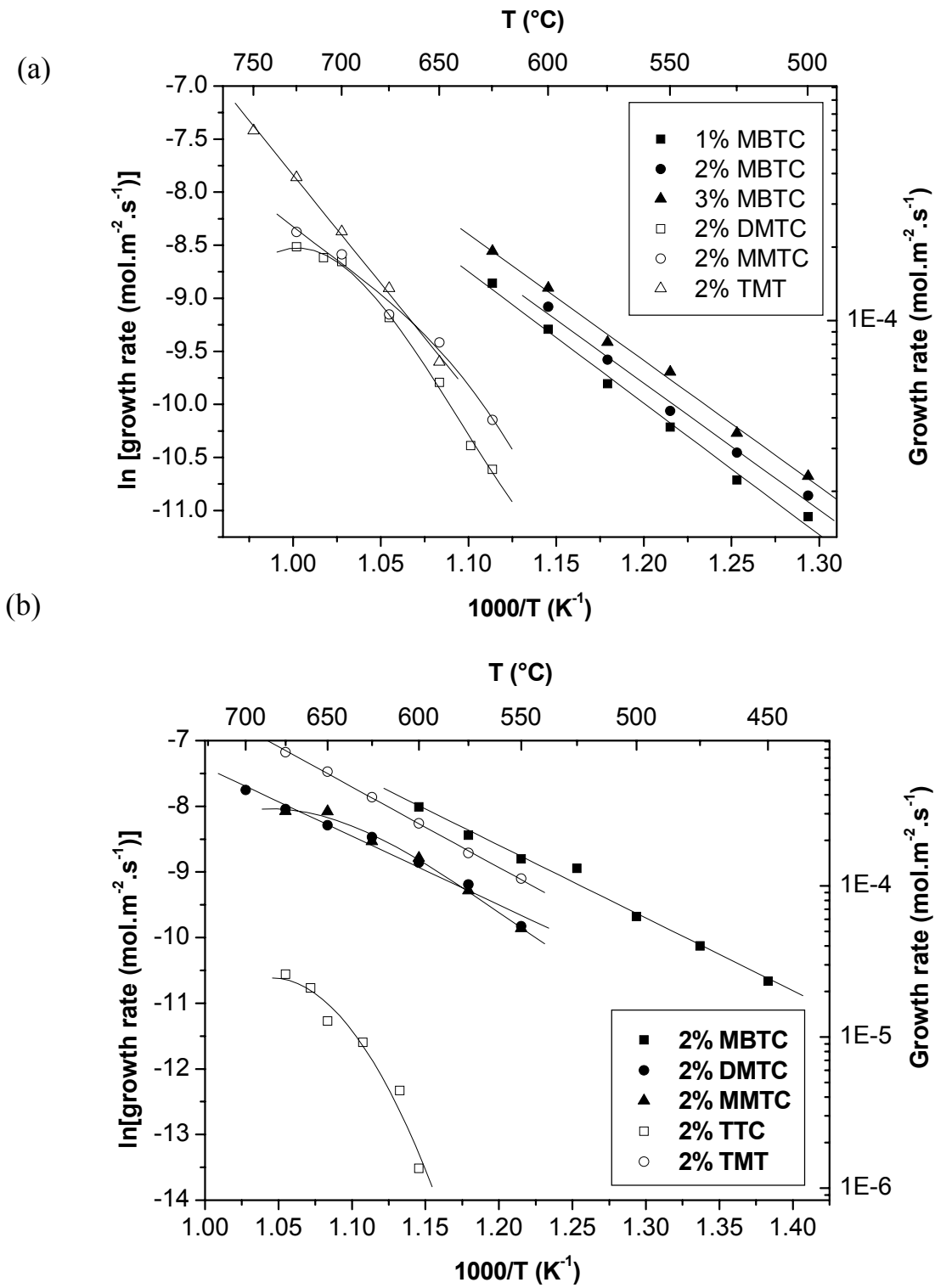
Figure 6.2*: Arrhenius plots of the growth rate of various tin precursors on aluminum (a) and glass (b). All depositions were carried out with 20% O_2 using a total flow rate of 2 SLM. The solid lines are an aid to the eye only.*

Table 6.2: *Surface roughness as measured by AFM for tin oxide layers of 1 μm deposited from four different precursors.*

Precursor	Thickness [nm]	RMS roughness [nm][1]	% RMS roughness/thickness
MMTC	970	11	1.1
MBTC	1000	10.5	1.0
DMTC	1043	38.8	3.7
TMT	997	18.5	1.9

[1]: RMS roughness is defined as $R_{RMS} = \sqrt{\dfrac{\sum\limits_{n=1}^{N}(z_n - \bar{z})^2}{N-1}}$, where $\bar{z}$ = mean z height, and N is the number of data points in an area of 20x20 μm^2.

Figure 6.3 a-d show a 3D representation of the tin oxide layers on glass. Relationships between growth rate and temperature could be described using the Arrhenius equation. Table 6.3 shows an overview of the activation energies determined for the various precursors on glass and aluminum.

The activation energy found for DMTC on glass, 150±15 kJ/mole, agrees with the activation energy found in the CSTR reactor, i.e. 148±5 kJ/mole, see chapter 5. The activation energies for MMTC and DMTC on glass are approximately equal, which is probably due to their similarity in chemical composition. Also the film growth rate and the sheet resistance (section 6.3.2) are about the same. The activation energy for TMT on glass, 170±11 kJ/mole, is also in agreement with previous reported values of 157-174 kJ/mole [1-4]. Deposition of tin oxide on glass from MBTC had the lowest activation energy, i.e. 99±9 kJ/mole.

Deposition on aluminum substrates gave different activation energies than for the glass substrates (Figure 6.2 and table 6.3). As with the glass substrates, deposition from MBTC was achieved at lower substrate temperatures with good substrate coverage. Deposition using the two methylated precursors MMTC and DMTC needed to be done at higher temperatures to achieve comparable growth rates.

Table 6.3: *Apparent activation energies for the deposition of tin oxide from a variety of precursors on glass and aluminum substrates.*

Precursor	Apparent E_a on glass (kJ/mole)	Apparent E_a on Al (kJ/mole)
MBTC	99 ± 9	92 ± 10
DMTC	150 ± 15	87 ± 12
MMTC	158 ± 12	109 ± 16
TTC	Not attainable	(190 ± 75)
TMT	170 ± 11	102 ± 4
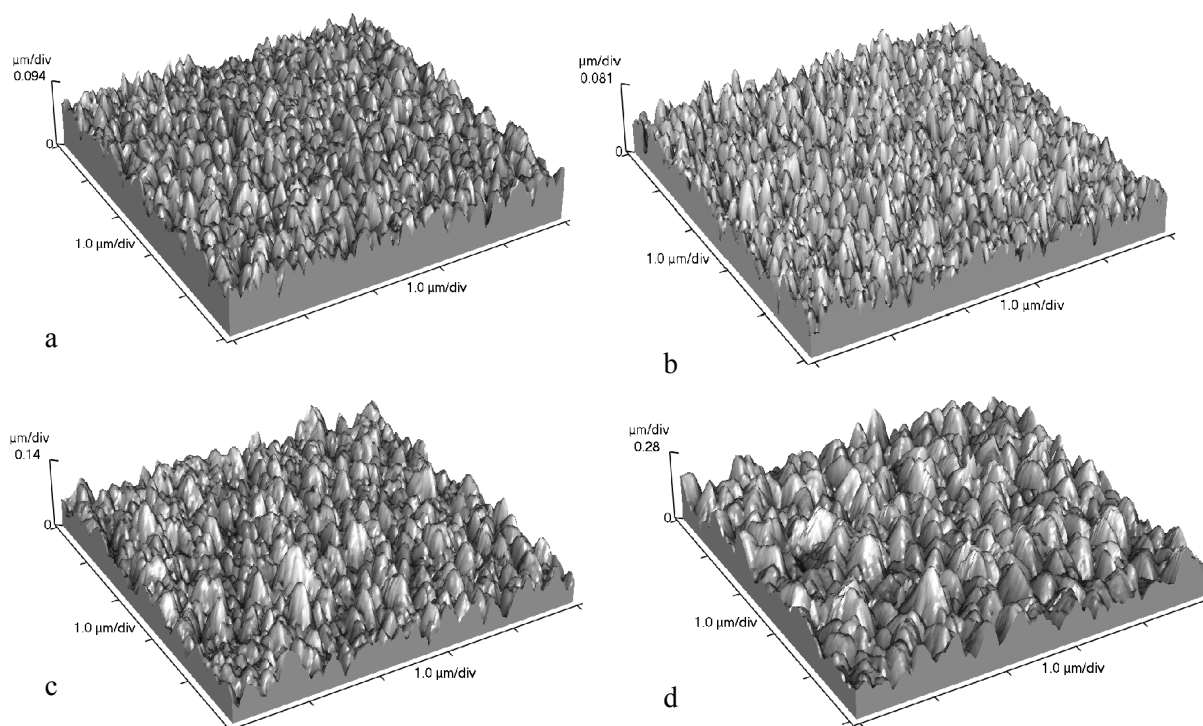
Figure 6.3: *AFM surface scan of a 5x5 μm^2 area of a 1μm tin oxide layer on glass deposited by oxidation of (a) MMTC, (b) MBTC, (c) TMT, and (d) DMTC.*

Deposition using TTC was very difficult, with very poor surface coverage. The material deposited from TTC could not be described as a thin film, but as small white particles adhering to the surface. Activation energies for the organometallic precursors are comparable at around 100 kJ/mole.

The difference in activation energies for glass and aluminum substrates can be caused by a number of factors. The overall deposition mechanism is complex and is likely to involve a mixture of gas phase as well as surface reactions (chapter 5). The different activation energies found for aluminum substrates as compared to the glass substrates suggest that surface reactions play an important role in the mechanism. However, it also is possible that other processes such as surface diffusion play a role, because the aluminum substrates used had a very rough surface compared to the glass substrates. Also the thermal conductivity of aluminum is much higher with respect to the glass substrate, resulting in a higher surface temperature for aluminum. Without in-situ measurements of either the surface or the gas phase composition during deposition it is difficult to quantify the extent of their influence on the overall deposition rate.

6.3.2 Resitivities

Four point probe measurements could not be made for films deposited on aluminum substrates due to the uneven surface and the high conductivity of aluminum. The most conductive film on glass was deposited from the MMTC

precursor using a deposition temperature of 675 °C, which exhibited a resistivity of $1.2 \cdot 10^{-3}$ ohm.cm for a tin oxide coating of 550 nm thickness. Resistivity results for each precursor are summarised in figure 6.4.

Films deposited from MBTC above 600 °C were in excess of 1 μm thickness and peeled off the glass before electrical measurements could be made. No reproducible conductive coatings could be made from the TTC/O_2 precursor system at any substrate temperature. Coatings deposited from TMT exhibited very poor conductivity in comparison to the conductive films deposited from other precursors.

For all chlorine containing precursors, film resistivity decreased with increasing deposition temperature up to 675 °C, above 675 °C the film resistivity began to increase. Such trend has been reported before [5-10], see also figure 2.13. The resistivity initially decreases with increasing deposition temperature because grain size and crystallinity increases [10]. However, at higher temperatures the carrier concentration decreases. This is caused by the elimination of oxygen vacancies (more complete oxidation) or by a lower concentration of active chlorine ions at higher temperatures.
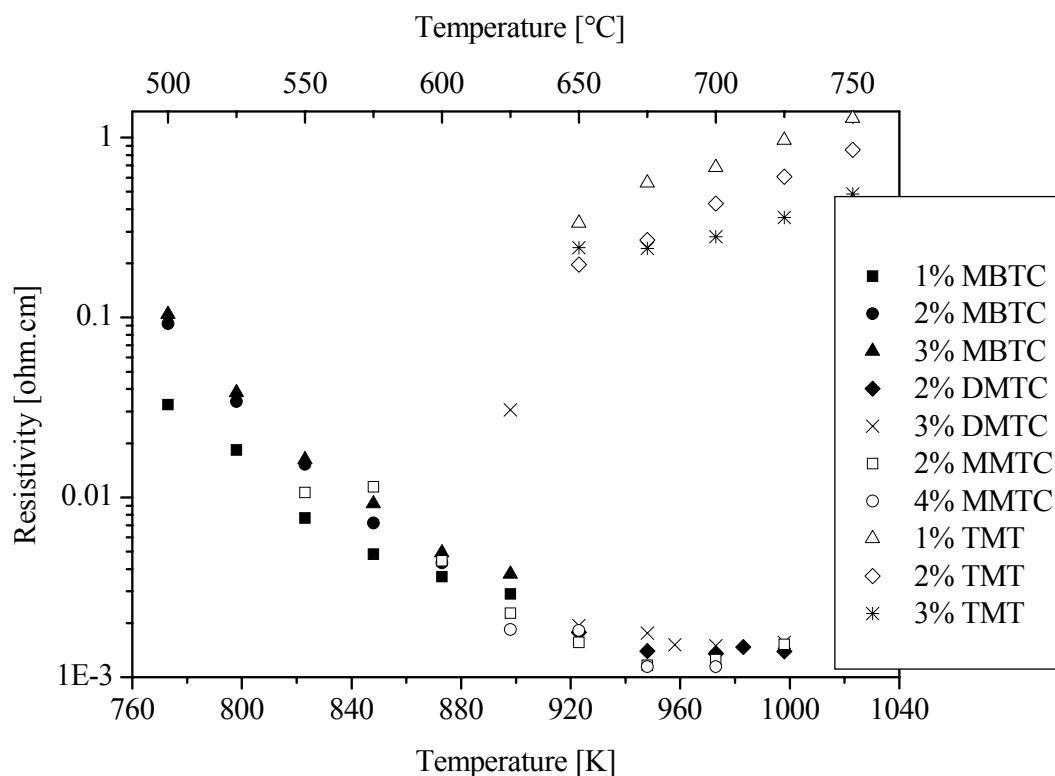
Figure 6.4: *Measured resistivities of tin oxide coatings on glass substrates. No reproducible conductive coatings could be made from the TTC/O_2 system at any susceptor temperature.*

The resistivity of films deposited from chlorine containing precursors was much lower than for the chlorine free precursor, namely TMT. The lower resistivity of these precursors is therefore likely to be caused by chlorine doping from the precursor ligands, as discussed in section 2.5.1.

As is shown in figure 6.4, film resistivity decreases with decreasing precursor concentration for MMTC, DMTC, and MBTC. At low precursor concentrations,

the nucleation rate is lower, and the adsorbed molecules have more time to diffuse across the substrate to form larger grains. This would result in fewer but larger crystals, with fewer grain boundaries. Conduction across grain boundaries is more difficult than through the crystallites, and as there are fewer grain boundaries the global resistivity decreases. Conversely, higher precursor concentrations would result in more nucleation sites and more, but smaller, grains. For TMT the opposite trend is observed, the resistivity increases with decreasing precursor concentration. A possible explanation is an increasing incorporation of carbon atoms with increasing growth rates at the high temperatures employed. The higher carbon content in the film causes a higher conductivity.

6.3.3 Film structure

Tin oxide films deposited from the various precursors with a molfraction of 0.02 were analysed with XRD. All precursors produced a polycrystalline tin oxide film on both glass and aluminum substrates, with the exception of TTC. Table 6.4 lists the main crystal plane present in each of the tin oxide films. The most abundant crystal planes on the surface of the tin oxide films are (200) and (211). The preferred orientation of the layers is not only dependent on the substrate material, but also on film thickness and deposition temperature.

Table 6.4: Main crystal planes (hkl) present on surface of tin oxide coatings on glass and aluminum substrates. No reproducible coatings could be made from the TTC/O_2 system at any susceptor temperature.

Precursor	Thickness [nm]	Preferred orientation	Deposition temperature [K]
Glass			
DMTC	128	(110)	898
DMTC	291	(211)	923
DMTC	907	(200)	973
DMTC	1043	(200)	1003
MMTC	423	(211)	923
MBTC	222	(211)	823
MBTC	593	(211)	873
TMT	352	(211)	923
TMT	1204	(211)	973
TMT	2003	(301)	1003
Aluminum			
DMTC	369	(200)	973
MMTC	396	(200)	973
MBTC	865	(200)	973
MBTC	563	(200)	848
MBTC	339	(211)	798
MBTC	163	(211)	773
TMT	1346	(211)	873

6.4 Conclusions

In this chapter, five different tin precursors, dimethyltin dichloride (DMTC), monobutyltin trichloride (MBTC), monomethyltin trichloride (MMTC), tetramethyltin (TMT), and tin tetrachloride (TTC), were used to grow tin oxide films on both glass and aluminum substrates. Oxygen was used as an oxidant. All precursors, except TTC, produced tin oxide layers within the temperature frame of the experiments, 673-1023 K. MBTC proved to give the highest growth rate, an important criterion in the commercial production of tin oxide coatings. Layers above 1 μm and grown with MBTC had a poor adhesion to the substrate. Although commercial tin oxide coatings are most often less than 800 nm thick, the reason why this only occurs with MBTC is still unknown.

Large differences were observed in growth rates between tin oxide deposited on glass and aluminum foils. Although the difference in actual surface temperature on both substrates is different due to their different thermal properties, the surface morphology of the substrates also may play a role. The aluminum films have a very rough surface with a lot of grooves due to the rolling process during their manufacturing, while the glass substrate has a very smooth surface.

The properties of the deposited tin oxide layers were qualitatively compared with each other through electrical four point probe measurements and GAXRD. The Cl-containing precursors, with the exception of TTC, all showed a low resistivity, in the order of 1.10^{-3} - 1.10^{-2} Ω.cm for layers grown above 823 K. The layers deposited from TMT all had resitivities in excess of 10^{-2} Ω.cm. The lowest resistivity was observed for a tin oxide coating grown from MMTC at 848 K, $1.2.10^{-3}$ Ω.cm. These low resistivities suggest that the layers grown from MBTC, MMTC, and DMTC were all doped with Cl. TMT lacks chlorine ligands, and has consequently a higher resistivity.

The XRD measurements mainly showed that the preferred orientation of the layers is dependent on various conditions, such as type of precursor and substrate, thickness of the layer, and temperature.

Overall, it can be concluded that the type of precursor has a large influence on the growth rate of the tin oxide layer, but more importantly also in the properties of the layer. This suggests that some tin precursors are more suitable for producing tin oxide films for a certain application than others, depending on the required properties of tin oxide for that application.

References

[1] Borman, C.G., Gordon, R. G. *J. Electrochem. Soc.*, **1989**, *136(12)*, 3820.

[2] Ghoshtagore, R.N. *J. Electrochem. Soc.*, **1978***, 125(1)*, 110.

[3] Kamimori, T., Mizuhashi, M. *Proceedings of the 8th international CVD conference*, **1981**, 438.

[4] Baliga, B.J., Ghandhi, S.K. *J. Electrochem. Soc.*, **1976**, *123*, 941.

[5] Yusta, F.J., Hitchman, M.L., Shamlian, S.H. *J. Mater. Chem.*, **1997**, *7*, 1421.

[6] Sundaram, K. B., Bhagavat, G.K., *J. Phys. D: Appl. Phys.*, **1981**, *14*, 333.

[7] Muranoi, T., Furukoshi, M. *Thin Solid Films*, **1978**, *48*, 309.

[8] Sanon, G., Rup, R., Mansingh, A. *Thin Solid Films*, **1990**, 190, 287.

[9] Adachi, K.; Mizuhashi, M. *Proceedings on the 10th international CVD conference*, **1987**, 999.

[10] Nishino, J., Ohshio, S., Saitoh, H., Kamata, K. *Mater. Res. Soc. Symp. Proc.* **1995**, *363*, 225.

Chapter 7. Modelling of tin oxide CVD from DMTC

Abstract

The kinetic data from chapter 5 have been used to extract a lumped mechanism for tin oxide deposition from dimethyltin dichloride (DMTC) and oxygen. Using a two step reaction mechanism with the rate-limiting step in the gas phase followed by a very fast surface deposition reaction, growth rate profiles of tin oxide in two different types of reactors have been successfully predicted with computational fluid dynamic (CFD) modelling. The first reactor simulated was a horizontal laminar flow reactor. The model contained a 3D description of the reactor together with experimentally determined temperature boundary conditions. The simulations done on this model were both qualitatively and quantitatively in good agreement with experiments done in this reactor. The validity of the kinetic data was also tested at various temperatures using a model for a stagnant point flow reactor. Again the predictions of the growth rate made by this model are in good agreement with experiments done in this reactor.

7.1 Introduction

As was already mentioned in chapter 1, tin oxide CVD is a complicated process. Commercial injector and reactor systems are therefore often based on experience and empirical rules. Sometimes the injector design is based on the results of a computational fluid dynamics (CFD) calculation. However, seldom the complete reactor system, from injector to exhaust is simulated, with inclusion of the chemistry. The main reason is that this chemistry is almost never known. More extensive simulation of a reactor system including the chemistry can help improve injector or reactor design and provide guidelines to improve the precursor utilisation.

This chapter aims to show that the chemical kinetics for DMTC + O2, discussed in chapter 5, can be used to simulate the deposition rate of tin oxide. Two different types of tin oxide CVD reactors were simulated using CFD calculations. The first reactor to be discussed is the stagnant point flow reactor (SPFR), described in chapter 6. The second reactor is a laminar flow CVD reactor (LFR). This reactor is

used by Pilkington for studying the CVD process and is designed to mimic the performance of an on-line CVD coater. This chapter presents the simulation results of these reactors and compares the results with the data obtained from experiments. The simulations are done with the Fluent 5.3 software package. Section 7.2 will give a short overview of the methods this commercial package uses for simulating chemically reacting flows. Section 7.3 discusses the estimation of the molecular properties needed for solving the transport equations. In section 7.4 the geometry and meshing used for the reactors are given, together with the boundary conditions and the model parameters, such as viscosity, chemical reactions steps and kinetic constants, etc, used during the simulations. After a presentation of the results in section 7.5, the deposition rates calculated by the simulations are compared in section 7.6 with experimental values where possible.

This chapter will end with a discussion of the usefulness and the drawbacks of the simulation efforts.

7.2 Computational fluid dynamics modelling

Modelling of the CVD of tin oxide involves the simulation of the flow dynamics together with the heterogeneous and homogeneous chemistry in the CVD reactor. The transport behaviour of gas depends on the degree of rarification, expressed by the Knudsen number Kn=λ/L, the ratio of the mean free path of molecules, λ, and a typical length scale of the smallest detail of interest in the reactor, L. According to the kinetic gas theory, the mean free path is described by [1]:

$$\lambda = \frac{1}{\pi \sqrt{2}} \cdot \frac{k_B T}{p \sigma^2}$$

(7.1)

where T is the gas temperature, p the reactor pressure, k_B the Boltzmann constant, and σ is the collision diameter. Most tin oxide CVD processes are operated at atmospheric pressure and at temperatures between 700 and 1000 K with nitrogen as carrier gas ($\sigma \approx 3.8$Å). Under these conditions, the mean free path is about 0.2 μm. For Kn<0.01, simulation of the gas flow can be performed using the theory of continuum mechanics, meaning that as long as the reactor characteristic length scales of interest are larger than 20 μm, the gas flow can be described by the continuum equations, which is the case in this study. The flow conditions discussed in this chapter are also such that laminar flow can be assumed, i.e. the Reynolds number is always lower than 2300.

In order to solve the continuum equations for the CVD reactors studied in this chapter, the commercial CFD-package Fluent$^®$ is used, which is capable of handling complex 3D geometries and coupled gas phase and surface reactions. Fluent uses the following steps to solve a CFD-problem:
  1. The geometrical domain of interest is outlined.
  2. This domain is divided in non-overlapping grid cells or control volumes.

3. The physical and chemical phenomena of interest are selected.
4. The material and fluid properties are defined.
5. The boundary conditions at the cells, which coincide with or touch the domain, are specified.

Subsequently the simulation can be started, which involves solving the continuum equations according to the phenomena selected in 3. In Fluent the numerical solution of the total problem is found using the finite difference or finite volume method [2], of which a detailed description can be found in Versteeg and Malalasekera [3]. The physical and chemical phenomena are described by the transport equations for mass, momentum, heat, and concentrations of the various chemical species involved in the CVD process.

The conservation of mass is given by the continuity equation, stating the net accumulation of mass in a fluid element is equal to the net rate of flow of mass into the fluid element:

$$\frac{\partial \rho}{\partial t} = -\nabla \cdot \left(\rho \vec{v} \right) \tag{7.2}$$

where ρ is the average density, and $\vec{v}$ the mass average velocity of the gas.
The conservation of momentum is given by the equation of motion:

$$\frac{\partial \rho \vec{v}}{\partial t} = -\nabla \cdot \left(\rho \vec{v} \vec{v} \right) + \nabla \cdot \vec{v} - [\nabla \cdot \tau] + \rho \vec{g} \tag{7.3}$$

where τ is the viscous stress tensor describing the viscous momentum flux, and g is a vector describing the gravitational force. The term of the left side of the equality sign describes the accumulation of momentum in a fluid element. The first term on the right side is the rate of momentum addition by convection, the second and third term describe the rate of momentum addition by molecular transport, and the last term represents the external force on the fluid. For a Newtonian fluid, such as gases at 1 atm., the viscous stress tensor can be written as:

$$\tau = -\eta \left(\nabla \vec{v} + \left(\nabla \vec{v} \right)^T \right) + \left(\frac{2}{3} \eta - \kappa \right) \left(\nabla \cdot \vec{v} \right) I \tag{7.4}$$

where η is the viscosity of the fluid, κ is the dilatational viscosity, which can be neglected for gases at 1 atm. I is the unit tensor, $\nabla \vec{v}$ is the velocity gradient tensor, $\left(\nabla \vec{v} \right)^T$ is the transpose of this tensor, and $\left(\nabla \cdot \vec{v} \right)$ is the divergence of the velocity vector.

Commercial tin oxide reactors are in general non-isothermal with in some cases a very steep thermal gradient perpendicular to the substrate surface. Therefore the

transport equation for thermal energy needs to be included in the model. Equation 7.5 depicts the energy balance for a multi-component mixture in terms of the temperature T:

$$c_p \frac{\partial \rho T}{\partial t} = -c_p \nabla \cdot \left(\rho \vec{v} T \right) + \left(\nabla \cdot \vec{q} \right) + \frac{Dp}{Dt} - \left(\tau : \nabla \vec{v} \right) - \sum_{i=1}^{N} \sum_{j=1}^{K} H_i v_{ik} \left(R_k^f - R_k^b \right) + \Delta E_r$$

(7.5)

where c_p is the heat capacity at constant pressure, $\vec{q}$ is the molecular heat transport vector, H_i is the partial enthalpy of species i, v_{ik} is its stoichiometric coefficient in reaction k, and R_k^f and R_k^b are respectively the forward and backward reaction rates of reaction k. The term of the left side of the equality sign describes the accumulation of energy in a fluid element. The first term on the right side is the rate of energy increase due to convective transport. The second term is the energy increase due to molecular transport mechanisms, and the third term is the energy increase due to compression. The quantity $-\left(\tau : \nabla \vec{v} \right)$ is the viscous dissipation heating, which describes the degradation of mechanical energy into thermal energy. For systems with relatively small viscosity and velocity gradients, like CVD reactors, this term is small, and is therefore neglected in this modeling study.

The next term is the energy increase due to the reactions. Finally, ΔE_r represents radiative energy transport, which is also neglected in this study. In CVD systems, a transparent gas such as nitrogen is often used as a carrier gas, while possible non-transparent reactants or products, such as CO_2, are highly diluted. This term may have an influence on the temperature of walls, which have to be simulated, but in this study the temperature of the walls of the reactor are set as a boundary condition. The temperature of the walls of the laminar flow reactor was experimentally determined using thermocouples by the University of Salford.
The molecular heat transport vector $\vec{q}$ in a multi-component system is expressed as [4]:

$$\vec{q} = -\lambda \nabla T + \sum_{i=1}^{N} j_i \frac{H_i}{M_i} + RT \sum_{i=1}^{N} \frac{D_i^T}{M_i} \nabla \left(\ln x_i \right)$$

(7.6)

where λ is the thermal conductivity, j_i the diffusive mass flux of species i, D_i^T the thermal diffusion coefficient of species i. M_i and x_i are, respectively, the molecular mass and the mole fraction of species i. The molecular heat flux consists of three terms: the heat conduction, the transport of enthalpy due to diffusion of species, and the Dufour term, transport of heat due to concentration gradients. This last term has usually very little effect on the total molecular heat flux and is neglected in this study.
Finally, because CVD systems contain multiple components, the transport equations for individual species i are needed:

$$\frac{\partial p\omega_i}{\partial t} = -\nabla \cdot \left(\rho \vec{v}\omega_i\right) - \nabla \cdot \vec{j_i} + M_i \sum_{i=k}^{K} v_{ik}\left(R_k^f - R_k^b\right) \qquad (7.7)$$

where ω_i is the mass fraction of species i. The sum of mass fractions over all constituents is equal to unity. Again the term on the left hand side is a transient term representing the accumulation of species i in a fluid element. The first term on the right hand side corresponds to convection, the second to diffusion, and the last term to chemical reactions.

The diffusive flux is defined as:

$$\vec{j_i} = \rho\omega_i\left(\vec{v_i} - \vec{v}\right) \qquad (7.8)$$

in which the mass average velocity $\vec{v}$ is defined as:

$$\vec{v} = \sum_{i=1}^{N} \omega_i \vec{v_i} \qquad (7.9)$$

The diffusive flux $\vec{j_i}$ represents the molecular mass flux of species i as the result of a concentration gradient, a thermal gradient, or additional driving forces, such as pressure, gravity, or electrical potential. In the case of atmospheric pressure CVD systems, only concentration and thermal gradients have to be considered. For a multi-component dilute gas mixture, where a single component l is in excess, such as the carrier gas in CVD systems, the diffusive flux is given by the generalized Fick's law [4]:

$$\vec{j_i} = -\rho D_{il}\nabla\omega_i - D_i^T\nabla(\ln T) \qquad ; i = 1..N, i \neq l \qquad (7.10)$$

where D_i is the binary mass diffusion coefficient of species i in l, and D_i^T the thermal diffusion coefficient of species i. Alternatively, if there is no single component in large access, the Stefan-Maxwell equations can be used [1]:

$$\vec{j_i} = \frac{c^2}{\rho} \sum_{j=1}^{N} M_i M_j D_{ij}(\nabla x_j) - D_i^T\nabla(\ln T) \qquad (7.11)$$

where c is the total molar concentration of the gas mixture, D_{ij} the multi-component diffusion coefficients, and x_j the mole fraction of species j.

Both definitions for the diffusive mass flux $\vec{j_i}$ can be used in Fluent, but the latter is computationally more expensive.

7.3 Molecular properties

Equations 7.2 to 7.11 describe the complete CVD system, and can be numerically solved by Fluent if the molecular properties of all the species in the system are known. In general these properties are a function of temperature, pressure, and composition of the gas mixture. Experimental data for the coefficients of viscosity, thermal conductivity are available among others for air, nitrogen, oxygen, helium, and argon, common carrier gases in CVD, as a function of temperature and pressure. The mass and thermal diffusion coefficients have only been measured for a limited set of gas mixtures. With a few exceptions, experimental data on organometallic compounds and the intermediates formed during the deposition process are lacking. Therefore, it is necessary to use models for predicting their molecular properties. Good estimates for these coefficients can be obtained by applying the kinetic gas theory [1, 4, 5], which is based on an assumed intermolecular potential. For gas molecules, a good interaction potential is given by the Lennard-Jones potential:

$$\phi(r)=4\varepsilon\left(\left(\frac{\sigma}{r}\right)^{12}-\left(\frac{\sigma}{r}\right)^{6}\right) \tag{7.12}$$

where r is the distance between the molecules, and the Lennard-Jones parameters, σ and ε, represent the molecular collision diameter, and a characteristic interaction energy, respectively. In the following, each of the molecular transport properties is discussed.

Density

According to the kinetic gas theory, in gases that are sufficiently diluted the volume of the molecules and their interaction forces can be neglected. In these gases, the equation of state is given by the perfect gas law: $pV = nRT$. This leads to the density ρ:

$$\rho=\frac{Mp}{RT} \tag{7.13}$$

where M is the average molar mass:

$$M=\sum_{i=1}^{N}x_{i}M_{i} \tag{7.14}$$

For APCVD systems the ideal gas law is quite accurate.

Viscosity

In general the viscosity of a mixture can be calculated from the viscosities of the individual components, which again can be approximated, with errors typically less than 5% [5], from the kinetic gas theory. Although this approach is available in Fluent, it requires a certain computational effort. In this study the carrier gas N_2 is present in excess of 75 mol%. Therefore, the viscosity is simulated by a polynomial fit of the temperature dependent experimental values for the viscosity of N_2 at 1 atm [6]:

$$\eta = 7.473 \cdot 10^{-7} + 4.084 \cdot 10^{-8} T - 8.245 \cdot 10^{-12} T^2 + 1.306 \cdot 10^{-15} T^3 - 8.178 \cdot 10^{-20} T^4$$

(7.15)

where η is the viscosity and T the absolute temperature.

Thermal conductivity

Similar to the viscosity, the thermal conductivity of a gas mixture can be predicted from thermal conductivities of the individual components, which again can be approximated, with errors typically less than 3% [5], from the kinetic gas theory. Again, to prevent the computational effort, the thermal conductivity in this study is based on a polynomial fit of the temperature dependent experimental values for N_2:

$$\lambda = 4.737 \cdot 10^{-3} + 7.272 \cdot 10^{-5} T - 1.122 \cdot 10^{-8} T^2 + 1.455 \cdot 10^{-12} T^3 - 7.872 \cdot 10^{-17} T^4$$

(7.16)

where λ is the thermal conductivity.

Mass diffusion coefficient

As has been discussed in the previous section, there are several possibilities to assess the diffusion coefficients in a multi-component mixture. In this study, the diffusion coefficients are not based on a complete multi-component model, but are based on the binary diffusion coefficient of species i in N_2 (equation 7.10). The binary diffusion coefficient D_{ij} of a gas mixture i, j may be calculated, with errors typically within 5-10%, from:

$$D_{ij} = 0.0188 \cdot \sqrt{\frac{1}{M_i} + \frac{1}{M_j}} \frac{T^{3/2}}{p \sigma_{ij} \Omega_{D,ij}}$$

(7.17)

where M_i, and M_j are, respectively, the molecular mass of species i and j, and p is the pressure. The parameter σ_{ij} is set equal to ½($\sigma_i + \sigma_j$), where σ_i and σ_j are the molecular collision diameters of species i and j, respectively. The dimensionless quantity $\Omega_{D, ij}$ is the collision integral for diffusion and is a function of the parameter kT/ε_{ij} with $\varepsilon_{ij} = (\varepsilon_i \varepsilon_j)^{1/2}$, where ε_i and ε_j are the characteristic energy

potentials of species i and j, respectively. Equation 7.17 is quite accurate for non-polar molecules, but larger errors are introduced if one of the species has a polar character. It is possible to correct for this through the dimensionless quantity $\Omega_{D, ij} = f(kT/\varepsilon_{ij}, \delta)$, where δ is the dipole moment [7]. However, this option is not yet available in Fluent 5.3, and care must be taken when diffusion is the main transport mechanism.

Thermal diffusion coefficient

Molecular transport of species driven by a temperature gradient is called thermal diffusion or Soret diffusion. It causes large and heavy molecules to accumulate in the cold regions of the reactor, and small and light molecules to diffuse to the hot regions of the reactor. Thermal diffusion effects become significant in reactors with steep thermal gradients, and large differences between the molecular masses of the various species in the reactor. The CVD systems discussed in this chapter exhibit both phenomena.

In Fluent the thermal diffusion coefficient can be derived from the empirical expression [8]:

$$D_i^T = -2.59 \cdot 10^{-7} \, T^{0.659} \left[\frac{M_i^{0.511} x_i}{\sum\limits_{i=1}^{n} M_i^{0.511} x_i} - \omega_i \right] \cdot \left[\frac{\sum\limits_{i=1}^{n} M_i^{0.511} x_i}{\sum\limits_{i=1}^{n} M_i^{0.489} x_i} \right] \qquad (7.18)$$

Heat capacity

Although it is possible to calculate the heat capacity of a mixture from the heat capacity of the individual components, the heat capacity of the gas phase was assumed to be similar to the heat capacity of N_2 [6]:

$$c_p = 938.899 + 0.302T - 8.109 \cdot 10^{-5} T^2 + 8.264 \cdot 10^{-9} T^3 - 1.537 \cdot 10^{-13} T^4 \qquad (7.19)$$

where c_p is the heat capacity at constant pressure.

Thermodynamic properties

The thermodynamic properties of the various species are required in order to calculate the molecular heat transport, the heat of the reaction, and in the case of an elementary reaction mechanism, the equilibrium constant of an elementary reaction step. For a large number of individual gases the values for the standard heat of formation, H_{298}^0, the standard entropy, S_{298}^0, and the specific heat as a function of temperature, $c_p(T)$, have been tabulated, such as in Knacke [9], JANAF [10], Kubaschewski [11], and in the Chemkin® database [12]. From these tables the standard heat of formation, $H^0(T)$, and the standard entropy, $S^0(T)$, at temperature T may be calculated from:

$$H^0(T) = H^0_{298} + \int\limits_{298}^{T} c_p(T)dT \qquad (7.20)$$

$$S^0(T) = S^0_{298} + \int\limits_{298}^{T} \frac{c_p(T)}{T}dT \qquad (7.21)$$

Unfortunately, for some of the species in the chemical reaction mechanism used in this study, the heat capacities as a function of temperature were not known. Therefore only the standard heats of formation were used for calculating the molecular heat flux, and the heat of reaction. The error introduced by these approximations is small, because the molecular heat flux and the heat of reaction have only a minor contribution to the total heat transport. This study uses a lumped reaction mechanism, so it is not required to calculate reverse rate constants from the equilibrium constant.

Lennard-Jones parameters

Lennard-Jones parameters for common gases can be found in the Svehla [13] and Chemkin databases [14]. These parameters are often based on measurements of the viscosity or diffusion coefficient. If these data are not available, the Lennard-Jones parameters can be estimated from the critical constants [15]:

$$\sigma = 0.809 V_c^{0.333} \qquad (7.22)$$

$$\varepsilon/k_B = \frac{T_c}{1.2593} \qquad (7.23)$$

where V_c is the critical volume, and T_c is the critical temperature.
If even these constants are unknown, as is often the case with organometallic CVD precursors and intermediates, the critical constants can be estimated from compounds, which have a similar molecular composition and structure [15]. Fishtine [16] has developed such empirical rules for organometallic compounds, which are based on the group contribution rules of Lydersen [15]. The critical constant of a molecule is calculated from the critical constant of a reference compound. The difference in ligands (groups) between the molecule and the reference compound is taken into account by substitution of the contribution of these ligands (groups) to the critical constant. The contribution of various molecular groups to the critical constant has been tabulated. Appendix 8A gives the group contributions according to Fishtine [16].
The critical temperature can be derived from:

$$\sum \Delta T_R = 0.5 \cdot \left[1 - \sqrt{1 - 4\left(T_{bR}/T_{cR} - 0.567\right)} \right] \qquad (7.24)$$

$$\sum \Delta T = \sum \Delta T_R + \sum \Delta ' T \qquad (7.25)$$

$$T_b \big/ T_c = 0.567 + \sum \Delta T - (\sum \Delta T)^2 \qquad (7.26)$$

where:

$\sum \Delta T_R$ = Sum of increments for the critical temperature for a reference compound

T_{bR} = normal boiling point for the reference compound

T_{cR} = critical temperature for the reference compound

$\sum \Delta T$ = Sum of increments for the critical temperature of the desired compound

$\sum \Delta ' T$ = calculated change in group or atomic increments for the critical temperature going from the reference to the desired compound

The critical volume can be derived from:

$$V_c = V_{cR} + \sum \Delta ' V \qquad (7.27)$$

where:

V_{cR} = critical volume of the reference compound

$\sum \Delta ' V$ = sum of change in group increments for the critical volume

In the case of DMTC for example, the critical constants can be derived from the critical constants of $SnCl_4$ [17]. The Lennard-Jones parameters for the compounds used in this study are depicted in appendix 7B.

Chemical reaction mechanism

As is discussed in chapter 5, the complete mechanism of DMTC oxidation to form tin oxide layers is very complicated. From experiments in a laminar flow reactor, where the highest growth rate is at the end of the reactor, it is assumed that the rate-limiting step is in the gas phase. Therefore the following lumped mechanism is used to simulate the deposition rate:

(1) $(CH_3)_2SnCl_2$ $+ O_2$ $\rightarrow CH_3SnCl_2OH$ $+ ½CO_2$ $+ ½CH_4$

(2) CH_3SnCl_2OH $+ O_2$ $\rightarrow SnO_2$ $+ 2HCl$ $+ CH_2O$

The reaction steps are constructed to reflect the formation of the most abundant by-products. The tin-intermediate in this mechanism is chosen to balance the atomic composition, it does not represent the actual intermediate.

The reaction rate for step 1 was taken from the overall reaction rate in the CSTR reactor, as plotted in figure 5.12a. The reaction rate of step 2 is set to be much faster than step 1, such that as soon as the intermediate hits the wall it is converted to tin oxide:

$$k_1 = 4.43 \cdot 10^8 \, e^{-\frac{1.48 \cdot 10^8 \, J/kmol}{RT}} \quad s^{-1}$$

$$k_2 = 1 \cdot 10^8 \, e^{-\frac{1 \cdot 10^3 \, J/kmol}{RT}} \quad s^{-1}$$

From the results of chapter 5, it is known that the rate of tin oxide deposition is first order in DMTC. Because in both the simulations and the experiments, oxygen is always in excess, both reactions were considered pseudo-first order in the tin reactant.

7.4 Reactor description

Two types of reactors were simulated and the deposition rates predicted by the model are compared with the deposition rates measured during experiments. The first reactor to be discussed is the stagnant point flow reactor (SPFR) from chapter 6. The second reactor is a laminar flow reactor (LFR). This reactor has been used in the in-situ monitoring project, mentioned in chapter 1. Experiments in this reactor have been performed at the University of Salford (USAL) and in the laboratory of a glass manufacturer, Pilkington (Pilk). Their experimental results will be compared with the simulation results.

7.4.1 SPFR reactor

A schematic drawing of this reactor was shown in figure 6.1. The reactor is assumed to be axi-symmetric, so the simulation is based on a 2D geometry with the centre line of the reactor defined as an axi-symmetric axis. The simulation domain is shown in figure 7.1b. In figure 7.1a, a schematic view of the reactor is given together with an overview of the boundary conditions. The top boundary is the top flange of the reactor, also containing the inlet. The bottom part ends with the bottom flange. One side of the domain coincides with the axis of symmetry; the other side ends 0.5 m from the outer fused silica wall of the reactor. This side does not coincide with the reactor wall in order to be able to predict the heat flux through the part of the reactor wall that is not heated or insulated. It is assumed that the temperature 0.5 m from the reactor wall is ambient temperature (300 K) and that there is only a slight extraction of air along the reactor walls. Typical inlet conditions for the experiments are 2 mol% DMTC + 20 mol% O_2 with balance N_2. The total flow rate was in all experiments 2 SLM as described in chapter 6. These conditions were also applied in the model through the boundary conditions for the

inlet. In the model the velocity profile at the inlet is assumed to be fully developed laminar.

The inlet to the fused silica reactor is kept at T = 453 K with heating tape. Also the top 60 cm of the reactor is heated till T = 453 K with heating tape.

Inlet: v_{max}=0.19 m/s
Laminar profile
T=453K

Heating wire
T = 453K

Symmetry axis

Ambient
T= 300K
v=-0.01 m/s

Inlet tube

Glass substrate

Fused silica reactor wall

Outlet

Steel Susceptor
Uniform temperature
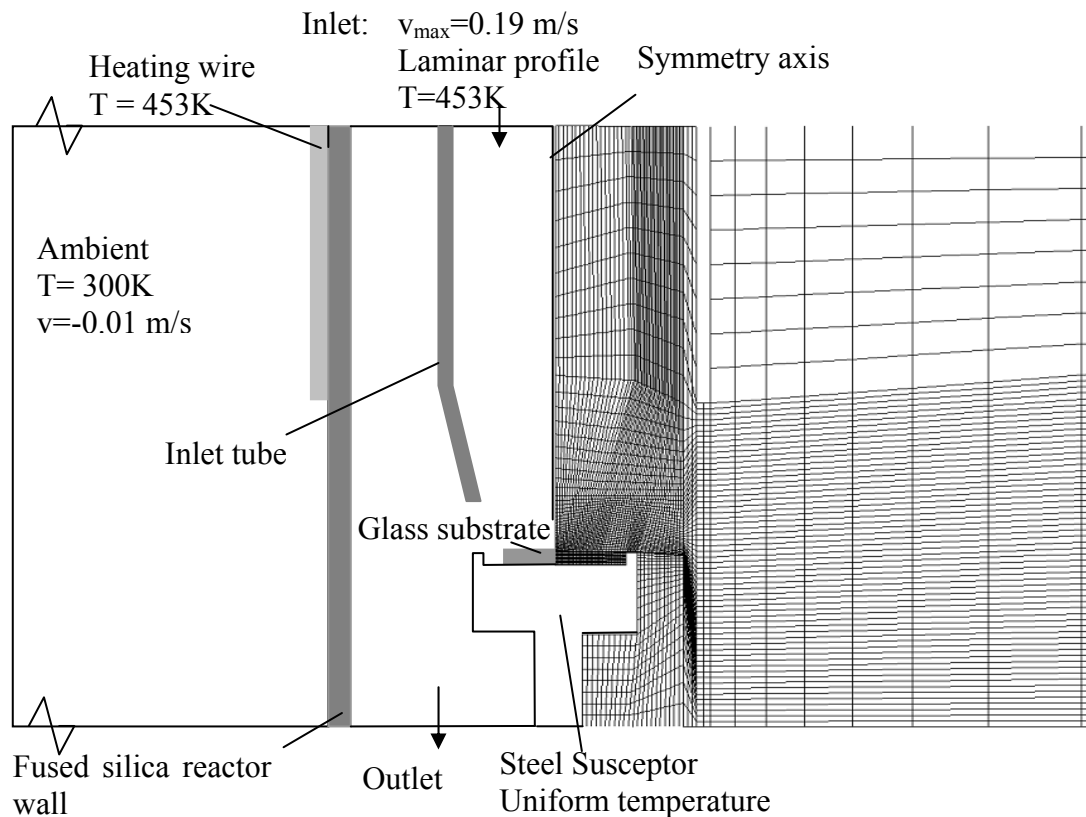
Figure 7.1: (a) Schematic overview of the boundaries in the computation domain, (b) grid used for simulation of the SPFR. The boundary on the right side is more extended.

Gas Inlet
(Precursors)

Quartz Reactor

Glass
Substrate

Graphite Block
holding heaters

Exhaust
Gases
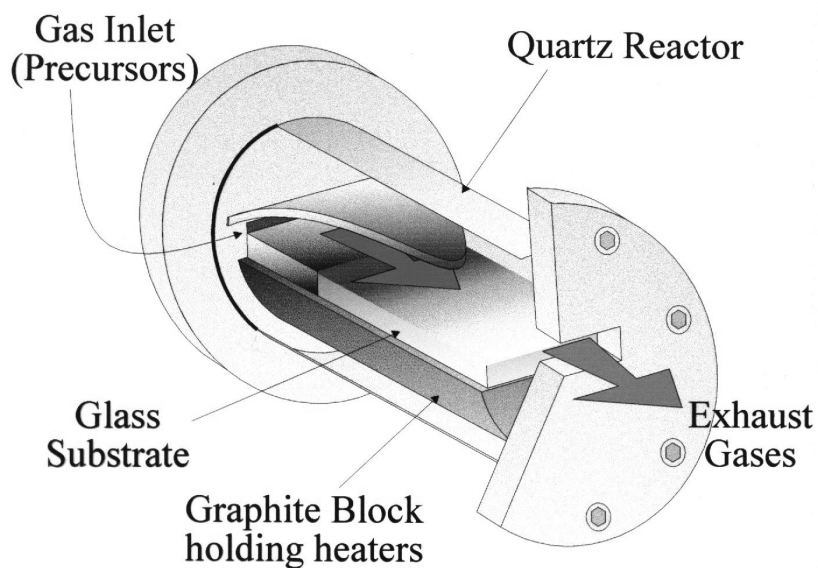
Figure 7.2: Schematic representation of the laminar flow reactor (LFR).

7.3.2 LFR reactor

The reactor consists of two parallel plates of which the bottom plate is heated. These plates are positioned 7 mm apart in a glass cylinder. The cylinder is kept between two flanges. One flange is connected to an inlet block and the second flange is connected to a flat conical outlet section that ends in a pipe leading to the exhaust. The inlet block is a metal chamber containing three baffles to spread the flow entering from a ¼" pipe over the width of the reactor. In the middle of the bottom half of the cylinder is a graphite block containing three heating elements. On top of this block lie a graphite foil and the glass substrate. Before and after the graphite block, the reactor is filled with fused silica plates to level with the substrate. Figure 7.2 shows a schematic of this reactor.

It would take a huge amount of computer time to model the complete reactor as described above. Therefore only the most important part of the reactor is chosen as domain for simulation, i.e. the part between the graphite block, the last baffle of the inlet block, the top plate, the outlet flange, and the side-walls of the cylinder. The details are shown in figure 7.3. Because there is a symmetry plane in the reactor, only half of the reactor needs to be modelled. In order to keep the computer time at an acceptable level some further restrictions have to be made:

- The temperature of the walls will be set according to the measurements done at USAL (figure 7.4).
- The domain is on one side limited by the last baffle of the inlet block. The inlet flow is assumed to be uniform. Because of the small dimensions of the inlet, only some small errors in the space just after the baffle will be made.
- There are no gas leaks between the top plate and the cylinder wall. Test trials at Pilkington using ink to visualise the flow patterns showed that only a small amount of the ink leaked through.
- The reactor to be modelled does not contain turrets, normally used to accommodate a Fourier transform infrared spectrometer (FTIR) attachment.

The domain was divided in 404 x 49 x 10 grid cells. The density of the grid cells was taken higher in the space just above the substrate in order to simulate the large gradients present there more accurately. Simulations using higher grid densities did not show any other results after convergence.
The inlet velocity of the gas was set at 2.1 m/s, which is based on a total flow rate of 8 SLM and an inlet temperature of 473 K. The inlet gas contained 5 mole% DMTC, 20 mole% O_2, and balance N_2. USAL has measured temperatures on various spots on the substrate, top plate, and sidewalls of the reactor. These measurements are used to define a temperature profile over the walls of the reactor as is shown in figure 7.4. The profiles are obtained by linear interpolation of the temperatures measured by USAL.

(a) side view

Inlet →

Quartz top plate

Steel inlet block

Quartz plates

Outlet →

Substrate

Quartz plates

Steel plate supporting quartz plates

Graphite heating block

(b) front view

Quartz top plate

Symmetry plane

Substrate

Graphite heating block
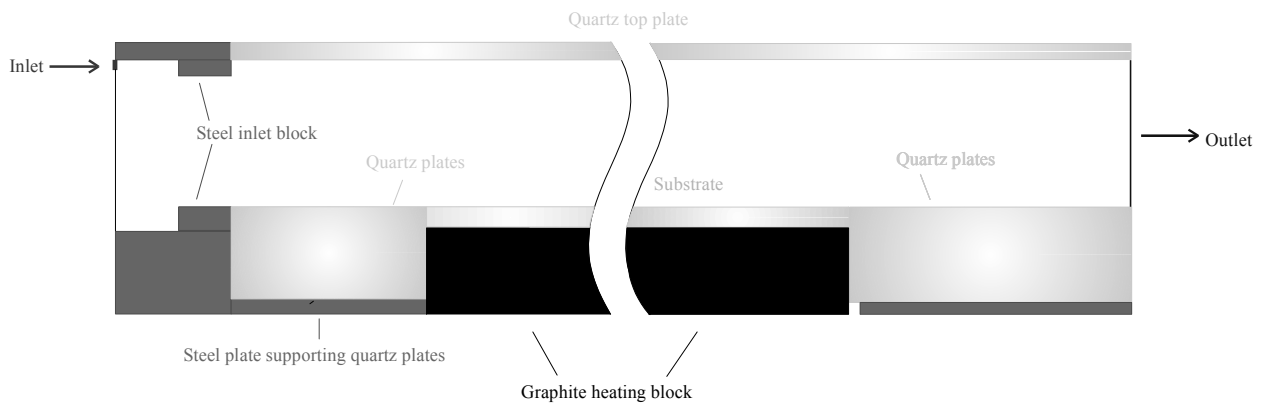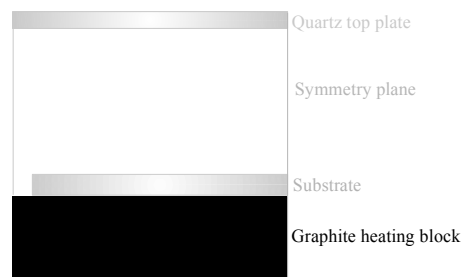
Figure 7.3: Schematic representation of the domain used for modelling laminar flow tin oxide reactor. Because of the presence of a symmetry plane through the middle of the reactor, only half of the reactor has to be modelled.

9.10e+02
8.59e+02
8.08e+02
7.57e+02
7.06e+02
6.55e+02
6.04e+02
5.53e+02
5.02e+02
4.51e+02
4.00e+02
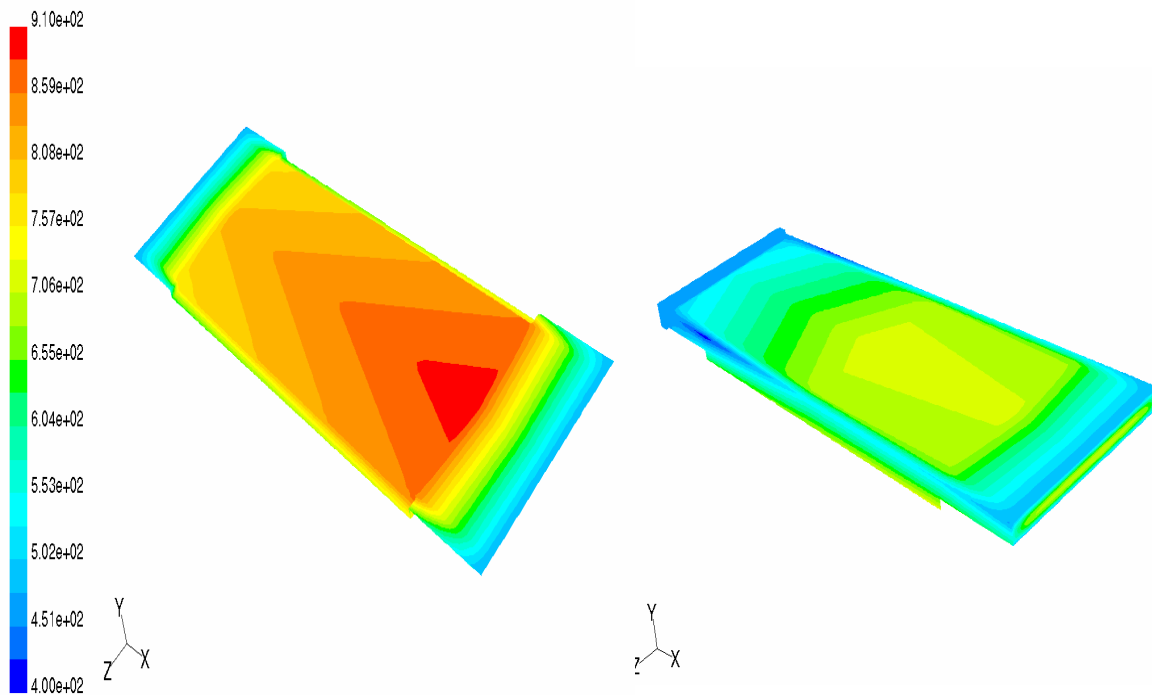
Figure 7.4: Temperature profiles of the bottom plates (a), and the top plates (b) used for modelling the laminar flow reactor (LFR).

144

7.5 Simulation results

7.5.1 SPFR reactor

Figure 7.5 shows, respectively, the velocity and temperature distribution in the SPFR reactor. About 1 mm above the substrate the temperature has dropped from 998 K at the surface of the substrate to below 700 K. Because of recirculation flow between the inlet and the reactor wall, this area is somewhat hotter than its surroundings, but the temperature does not exceed 650 K. At this temperature the reaction rates of any tin precursor and oxygen are very low, so no powder formation is expected, which is confirmed by the experiments. Because of the stagnant flow the impinging gas heats the walls of the reactor. Some deposition on the walls is therefore to be expected and indeed this was observed in experiments.
Using the lumped chemical mechanism of section 7.3 the growth rate of tin oxide on a glass substrate has been simulated. In the simulation the mole fraction of DMTC was set at 2 vol% and oxygen was set at 20 vol%, balance was nitrogen. Figure 7.6 shows the growth rate in the middle of the substrates. For comparison the growth rates measured after the experiments described in chapter 6 are also shown. The simulated growth rates are in accordance with the experimentally determined growth rates within the experimental error.
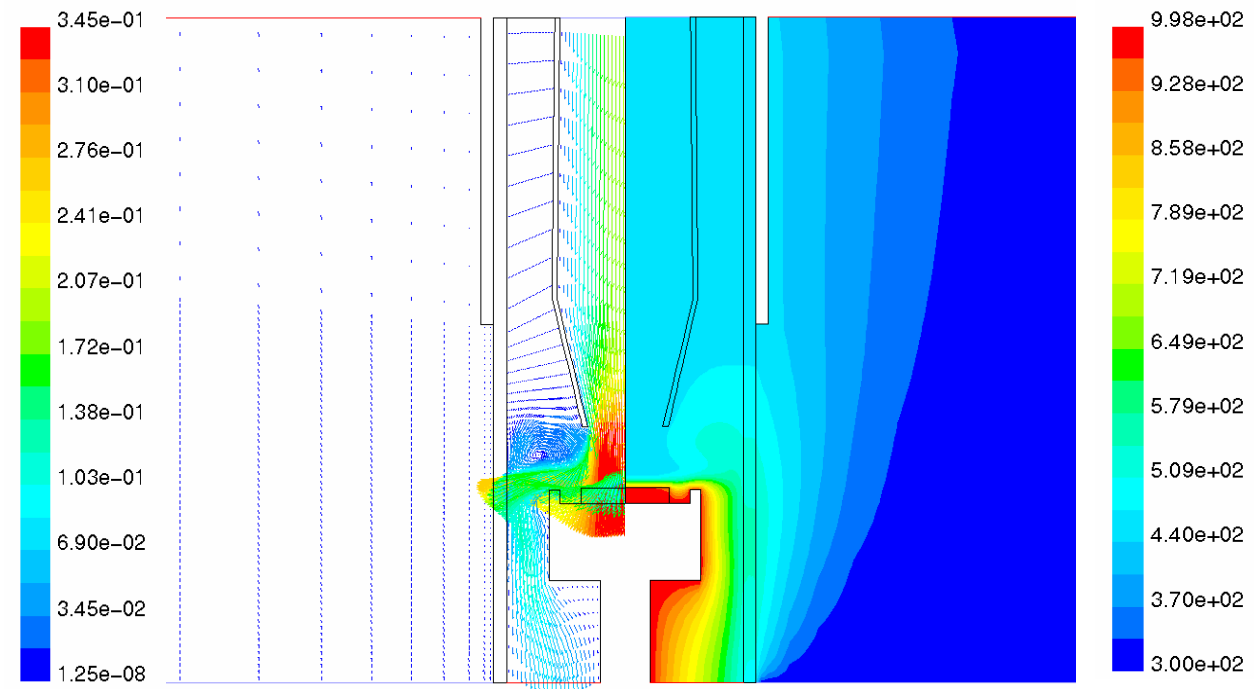
Figure 7.5: *Velocity (left) and temperature (right) distribution in the SPFR reactor.*
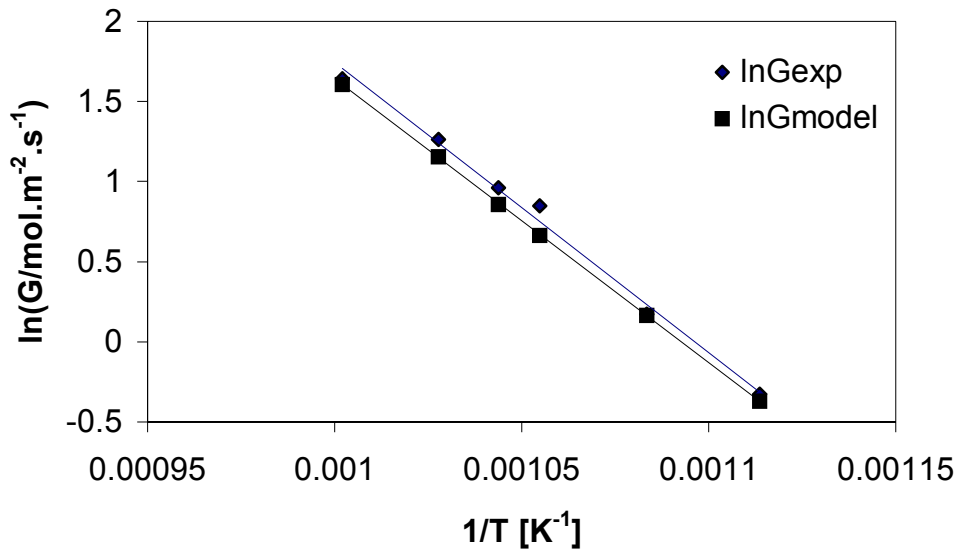
Figure 7.6*: Experimentally determined and simulated deposition rate of tin oxide on glass in a stagnant point flow reactor. Process conditions are 3% DMTC and 20% O_2. Total flow rate is 2SLM.*

7.5.2 LFR reactor

The lumped chemical mechanism of section 7.3 has also been used to simulate the growth profile in a laminar flow reactor. Figure 7.7 shows the growth rate of tin oxide on the symmetry axis of the bottom of the reactor, including the substrate, and the top plate. Figure 7.8 shows the total growth profile on the substrate.

Qualitatively the growth rate profile on the substrate corresponds with the measurements done at PTML using only DMTC and oxygen diluted in nitrogen, where they also found that the layer has its highest thickness at the end and in the middle of the substrate. Also visually the interference fringes correspond with the profile shown in figure 7.8.

Also, quantitatively the growth rate predictions made by the model are in good agreement with the measurements done at PTML. They found that the highest growth rate measured at the end of the substrate is about 20 nm/s while the model predicts 16 nm/s. The predictions made by the model are obtained purely on basis of the geometry of the reactor, the temperature profiles measured by USAL, and the reaction parameters obtained from the experiments done in the CSTR reactor, so no fitting algorithms have been used.

Both the quantitative and the qualitative experimental results support the validity of the chemical model used, where the rate-limiting step is proposed to be a gas phase reaction. In the case of a diffusion limited or a rate-limiting step at the surface, the highest growth rate would be expected at the beginning of the reactor where the concentration of precursor is highest. However, in the case of a rate-limiting step in the gas phase, the gas has to be heated up to form the intermediate film forming precursor. The highest growth rate is expected at the end of the reactor, because

here the gas has reached its highest temperature, and most of the intermediate film forming precursor is formed here.
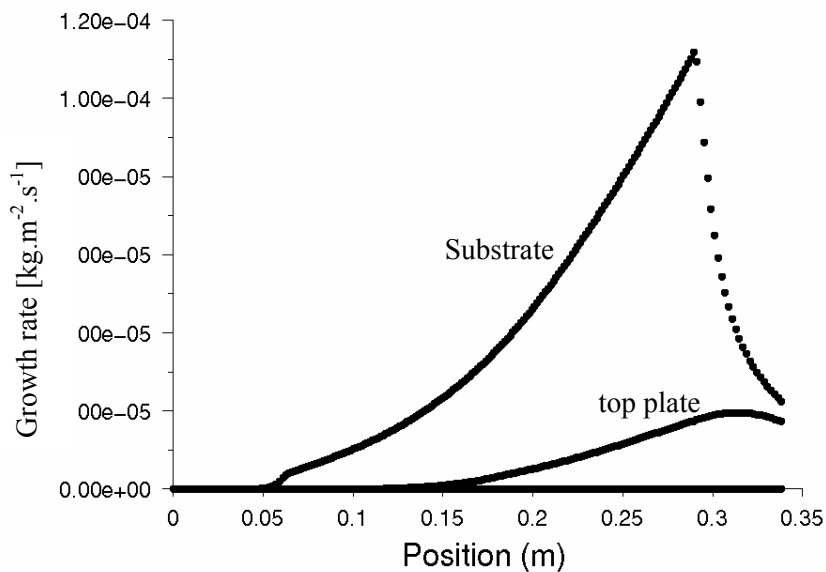
Figure 7.7: *Growth rate profile on the symmetry line of the botom of the reactor and the top plate. Growth rate is given as $kg.m^{-2}.s^{-1}$. The substrate is positioned between 0.0525 and 0.2905 m.*
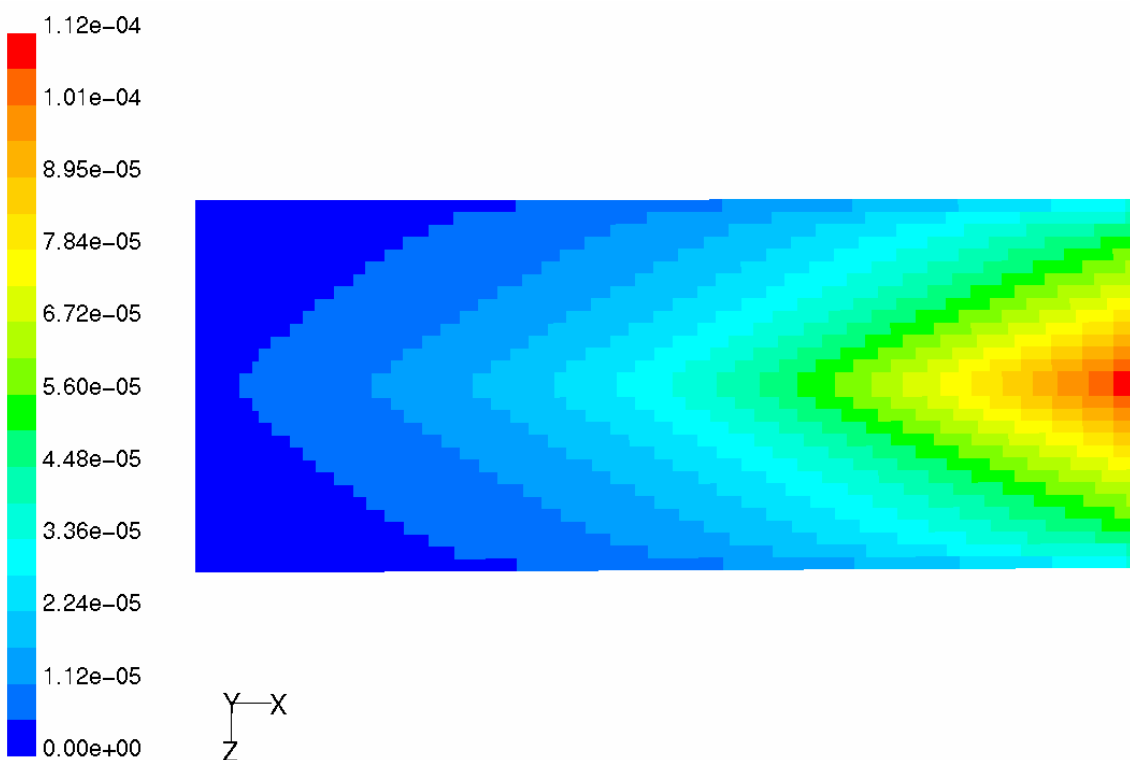
Figure 7.8: *Total calculated growth rate profile of tin oxide on a glass substrate, placed in the LFR. Growth rates are given in $kg.m^{-2}.s^{-1}$.*

In order to compare the growth rates in the case of gas phase reaction or surface reaction limited growth, approximate analytical solutions are plotted in figure 7.9. In this figure four cases are compared with the Fluent solution. These cases are:

1)   Growth of tin oxide on the substrate in the case the growth was purely limited by the gas phase diffusion of DMTC.

2)   Growth of tin oxide on the substrate in the case the growth was purely limited by a surface reaction. The surface reaction rate used in this case is deduced from the results of chapter 5.

3)   Growth of tin oxide on the substrate in the case the growth is limited by a gas phase reaction where DMTC first has to be converted into an intermediate, which subsequently immediately forms tin oxide on the substrate. Because it proved very difficult to obtain an analytical solution if there was a temperature gradient present in the reactor, the growth rate was calculated at two temperatures:

   (a) T = 782 K, the average temperature of the top plate.
   (b) T = 869 K, the average temperature of the substrate.
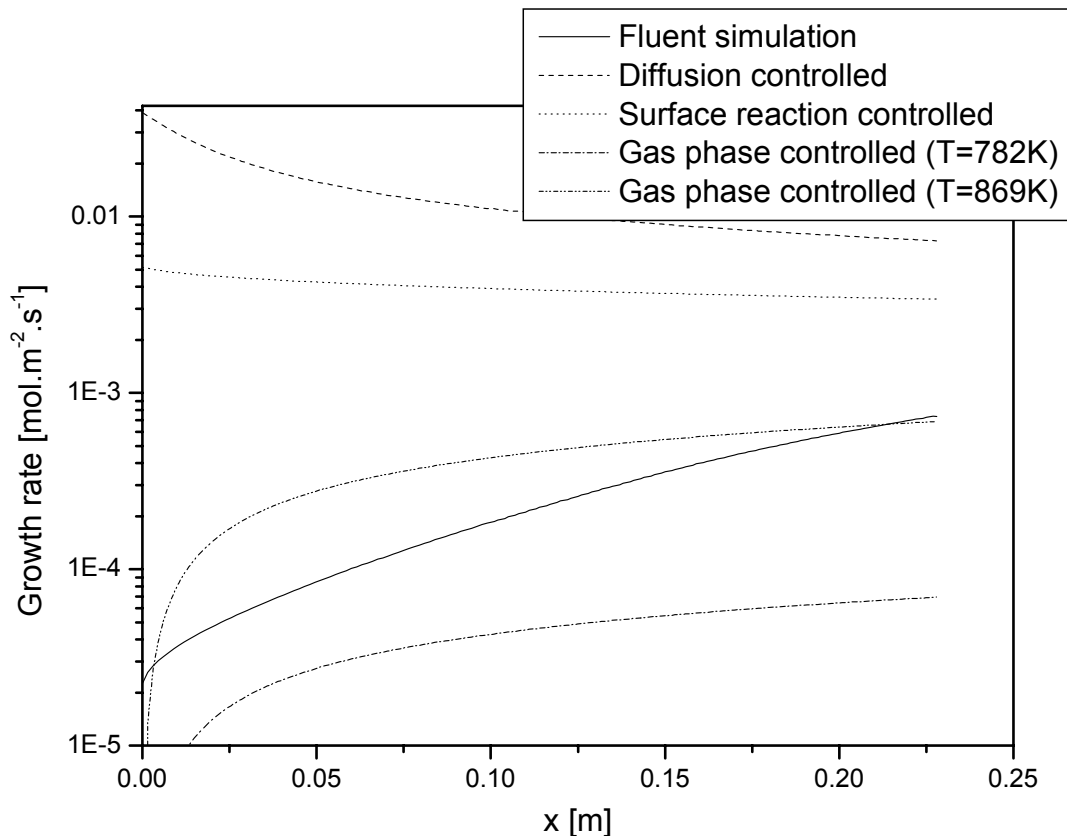
Figure 7.9: *The growth rate of tin oxide in the laminar flow reactor, as predicted by a Fluent simulation, and compared with analytical solutions discussed in the text. The deposition conditions are the same as mentioned in section 7.3.2.*

As can be seen the growth rate will drop as the gas flows through the reactor for cases (1) and (2). The cases where the analytical solutions were found by assuming a gas phase limited process show the same trend as the Fluent simulation. As expected the growth rate predicted by the Fluent simulation lies between the

analytical solutions for respectively the average temperature of the top plate and the substrate.

It follows that the growth rate of tin oxide from DMTC and O_2 is clearly limited by gas phase reactions. Although it is possible to obtain analytical solutions for the growth rate, much better predictions can be done with numerical fluid dynamics calculations. The main reason is that CFD calculations can deal much better with temperature variations in the reactor, which have a large influence on the growth rate.

7.6 Conclusion

With the advance of computer power over time and the availability of mature computational fluid dynamic packages, such as Fluent, it has become fairly straightforward to simulate chemical vapour deposition processes. In this chapter, two reactors are modelled with few assumptions. The first reactor is based on stagnation point flow and can be modelled in only two dimensions because of the presence of a symmetry axis. The second reactor, based on laminar flow between two plan parallel plates, is modelled in three dimensions. Both reactors were simulated using thermal diffusion and a simplified reaction mechanism, which is based on the experiments described in chapter 5. The growth rates predicted are in good agreement with experiments, thereby enhancing the validity of the chemical mechanism proposed. The laminar flow reactor was also subjected to an analytical analysis in order to clearly show the difference in growth rate behaviour in the case of (1) diffusion limited growth, (2) surface reaction rate limited growth, and (3) gas phase reaction limited growth. As expected, in cases (1) and (2) the growth rate decreases over the length of the reactor. For a gas phase reaction limited process the growth rate reaches its maximum at the end of the reactor. The Fluent simulation (and experimental trend) falls exactly between analytical solutions for a similar isothermal reactor with temperatures of, respectively, the average top plate and average substrate temperature.

References

[1]   Hirschfelder, J.O., Curtiss, C.F., Bird, R.B., *Molecular Theory of Gases and Liquids*, **1967**, John Wiley & Sons Inc., New York, USA.
[2]   Fluent 5 User's Guide, **1998**, Fluent Inc.
[3]   Versteeg, H.K., Malalasekera, W., *An introduction to computational fluid dynamics*, **1995**, Longman Group Ltd., London, England.
[4]   Bird, R.B., Stewart, W.E., Lightfood, E.N., *Transport phenomena*, **1960**, John Wiley and sons, New York, USA.

[5]   Reid, R.C., Sherwood, T.K., *The properties of gases and liquids, 2nd ed.*, **1966**, McGraw-Hill, New York, USA.

[6]   Vargaftik, N.B., Vinogradov, Y.K. Yargin, V.S., *Handbook of physical properties of liquids and gases, pure substances and mixtures, 3rg ed.*, **1996**, Begill House Inc, New York, USA.

[7]   Monchick, L., Mason, E.A., *J. Chem. Phys.*, **1961**, *35*, 1676.

[8]   Kuo, K.K.Y., *Principles of combustion*, **1986**, John Wiley and Sons, New York, USA.

[9]   Knacke, O., Kubaschewski, O., Hesselmann, K., *Thermochemical properties of inorganic substances II, 2nd ed.*, **1991**, Springer-Verlag, Berlin, Germany.

[10]   Chase, M.W. Jr., Davies, C.A., Downey, J.R. Jr., Frurip, D.J., McDonald, R.A., Syvarud, A.N., JANAF Thermochamical Tables, *J. Phys. Chem. Ref. Data*, **1985**, 14.

[11]   Kubaschewski, O., Alcock, C.B., Spencer, P.J., *Materials Thermochemistry, 6th ed.*, **1993**, Pergamon Press, Oxford, England.

[12]   Kee, R.J., Rupley, F.M., Miller, J.A., *The Chemkin Thermodynamic database*, **1989**, Sandia National Laboratories, USA.

[13]   Svehla, R.A., *Estimated Viscosities and Thermal Conductivities of Gases at High Temperatures*, **1962**, NASA Technical Report R-132.

[14]   Kee, R.J., Dixon-Lewis, G., Warnatz, J., Coltrin, M.E., Miller, J.A., *Chemkin Transport*, **1986**, Sandia National Laboratories, USA.

[15]   Benson, S.W., *Thermochemical Kinetics, 2nd ed.*, **1976**, John Wiley and sons, New York, USA.

[16]   Fishtine, S.H., *Zeitschrift fur Physikalische Chemie Neue Folge*, **1980**, *123*, 39.

[17]   Kobe, K.A., Lynn, R.E., *Chem. Rev.*, **1953**, *52*, 117.

[18]   Van Sark, W.G.J.H.M., Jansen, G., De Croon, M.H.J.M., Gilling, L.J. *Semicond. Sci. Technol.*, **1990**, *5*, 16.

[19]   Kleijn, C. PhD thesis 1991.

[20]   Van Sark, W.G.J.H.M., De Croon, M.H.J.M., Jansen, G., Gilling, L.J. *Semicond. Sci. Technol.*, **1990**, *5*, 36.

[21]   Spiegel, M.R. Schaum's outline of theory and problems of Fourier analysis, New York, USA, McGraw-Hill, 1974.

[22]   Handbook of Mathematical Functions, ed. M. Abramowitz, I.A. Stegun, New York, USA, 1972.

Appendix 7A. Group contributions for predicting critical constant according to the method of Fishtine

Table: Atomic and group contributions for Lydersen's method [6]

Atoms and atomic groups	ΔT	ΔP	ΔV
-CH_3 and -CH_2-	0.02	0.227	55
-CH_2- in ring	0.013	0.184	44.5
CH	0.012	0.21	51
CH in ring	0.012	0.192	46
=CH and =CH_2	0.018	0.198	45
=CH in ring	0.011	0.154	37
C	0	0.21	41
C in ring	-0.007	0.154	31
=C and =C=	0	0.198	36
=C and =C= in ring	0.011	0.154	36
≡C- and ≡CH	0.005	0.153	36
-F	0.018	0.224	18
-Cl	0.017	0.32	49
-Br	0.01	0.5	70
-I	0.012	0.83	95
-O-	0.021	0.16	20
-O- in ring	0.014	0.12	8
-OH in alcohols	0.082	0.06	18
-H in phenols	0.035	-0.02	3
>CO	0.04	0.29	60
>CO in ring	0.033	0.2	50
-CHO	0.048	0.33	73
-COO-	0.047	0.47	80
-COOH	0.085	0.4	80
-NH_2	0.031	0.095	28
>NH	0.031	0.135	37
>NH in ring	0.024	0.09	27
>N-	0.014	0.17	42
>N- in ring	0.007	0.13	32
-CN	0.06	0.36	80
-SH and -S-	0.015	0.27	55
-S- in ring	0.008	0.24	45
=O	0.02	0.12	11
-NO_2	0.055	0.42	78
=S	0.003	0.24	47

Appendix 7B. Molecular weight, formation enthalpy, and Lennard-Jones parameters of all the species present during the deposition process.

Species	Molecular weight [g/mol]	Formation enthalpy [kJ/mol]	σ [Å]	ε/k [K]
DMTC	219.67	-297.06	5.739	558.22
O_2	31.9988	0	3.467	106.7
N_2	28.01	0	3.798	71.4
HCl	36.46	-92.3	3.339	344.7
CH_4	16.04	-74.85	3.758	148.6
CH_2O	30.03	-115.897	3.590	498
CH_3SnCl_2 OH	221.66	-300	5.568	589.8
CO_2	44.01	-393.3	3.941	195.2
SnO_2	150.71	-580.74	-	-

Formation enthalpies were taken from the Chemkin database [5], and the Lennard-Jones parameters were taken from Svehla [4]. The Lennard-Jones parameters for DMTC and CH_3SnCl_2OH were calculated using critical constants [3], which were estimated according to the modified Lydersen method described in Fishtine [6]. The reference compound was $SnCl_4$.

Appendix 7C. Analytical expressions for the growth rate in a parallel flow reactor.

The growth of a solid layer deposited from a CVD process can be described if the set of partial differential equations given by equations 7.2 to 7.7 is solved. These equations can only be solved analytically if a number of simplifications are used. In this appendix these equations are solved for three different growth regimes in a horizontal rectangular reactor. All solutions are based on the same set of basic assumptions to come to the level of simplification required to be able to get an analytical solution. These assumptions will be physically justified to get a solution, which is still physically relevant.

The top plate of the reactor is at constant temperature, as is the bottom plate, which coincides with the substrate. The height of the reactor is h, and the width b. The coordination system used is depicted in figure 7C.9.
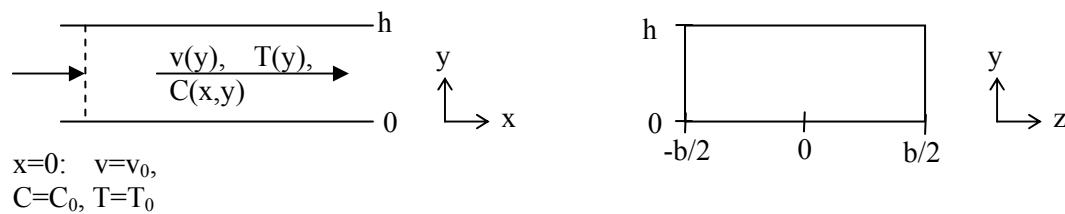
Figure 7C.9: *Definition of reactor geometry and coordination system used.*

The assumptions are listed below with their physical justification. They are based on the work by Van Sark et al. [18]:

1. The concentration of reactant and products is small as compared to the carrier gas, i.e. N_2, meaning the fluid dynamics is solely determined by N_2. In the case if tin oxide deposition the mole fraction of DMTC is 0.05, so DMTC does not contribute much. However, the concentration of oxygen is 20 mol%, but because its molecular properties are close to nitrogen, it is still safe to assume that the fluid dynamics are determined by N_2.
2. The deposition process is (quasi) stationary. The concentration, temperature, and velocity profiles are time independent.
3. The flow is assumed to be constant in vertical direction. Van Sark et al. [18] have shown that only a small error, <5%, is introduced if plug flow is assumed instead of laminar flow.
4. No deposition occurs on the top plate. As can be seen from the Fluent calculations in section 7.5.2 only some small deposition occurs et the end of the reactor.

5. The concentration, temperature, and velocity profiles are independent of z. This implies that either the reactor is considered to be of infinite width or that no deposition tales place at the side walls of the reactor.
6. Transport of growth species in the x-direction occurs only due to convective transport. Van Sark et al. [18] showed that axial diffusion only has a small effect on the growth rate.

Using the assumptions above it suffices to solve only equation 7.7, which is rewritten to a more convenient form:

$$v(y)\frac{\partial C_i(x,y)}{\partial x} = \frac{\partial}{\partial y}\left[D(T(y))\left(\frac{\partial C(x,y)}{\partial y} + (\alpha_T + 1)\frac{C(x,y)}{T(y)}\frac{\partial T(y)}{\partial y}\right)\right] + \sum_{i=k}^{K} v_{ik}(R_k^f - R_k^b)$$

(7.28)

The diffusion coefficient, D(T(y)), is calculated according to:

$$D = D_0 (T/T_0)^\gamma$$

(7.29)

which is different from equation 7.17. However, within the temperature range considered in this study, the difference in diffusion coefficient resulting from both calculation methods is less than 1%.

In equation 7.27, the thermal diffusion factor, α_T, is used instead of the thermal diffusion coefficient because it is less dependent on the mixture composition and temperature. The relation between both properties for a binary mixture is given by [19]:

$$D_1^T = \frac{p}{M_{av}RT}M_1M_2D_{12}x_1x_2\alpha_T$$

(7.30)

In this study the thermal diffusion factor is assumed to be constant, i.e. independent of temperature and mixture composition.

Three models will be presented, which will describe the growth rate in the case of:

1) Diffusion limited growth
2) Surface reaction limited growth
3) Gas phase reaction limited growth

Model 1: Diffusion limited growth.

In this model it is assumed that the top plate has a constant temperature T_0, and the bottom plate a constant temperature of T_s. In order to calculate the mean plug flow velocity, v_T, the following continuity equation has to be solved [20]:

Flux at x=0 = Flux at x>0

$$bhv_0\rho_0 = \int_0^h bv_T\rho(y)dy = bv_T\rho_0T_0\int_0^h \frac{1}{T(y)}dy$$

This leads to:

$$v_T = \frac{t_s-1}{\ln t_s}v_0 \tag{7.31}$$

where t_s is defined as T_s/T_0.

The temperature profile across the reactor is assumed to be linear:

$$T(y) = T_s - (T_s - T_0)y/h \tag{7.32}$$

Using equations 7.31 and 7.32, and after a coordinate transformation from y to t=T(y)/T$_0$, differential equation 7.28 can be rewritten to:

$$\frac{1}{t_s-1}\frac{1}{\ln t_s}\frac{h^2v_0}{D_0}\frac{\partial C(x,t)}{\partial x} = \frac{\partial}{\partial t}\left[t^\gamma\left(\frac{\partial C(x,t)}{\partial t}+(\alpha_T+1)\frac{C(x,t)}{t}\right)\right] \tag{7.33}$$

In this equation C(x,t) denote the concentration of DMTC.
Using the separation of variables method, and equating the resulting expression to $-\lambda^2$ gives:

$$C(x,t) = C_0\sum_{n=1}^{\infty}\alpha_n P(t)X(x) \tag{7.34}$$

where X(x) is found to be:

$$X(x) = e^{-\lambda_n^2(t_s-1)\ln t_s\frac{D_0}{v_0h^2}x} \tag{7.35}$$

P(t) is found by solving the differential equation:

$$\frac{d}{dt}t^\gamma\left(\frac{dP(t)}{dt}+(\alpha_T+1)\frac{P(t)}{t}\right) = -\lambda^2 P(t) \tag{7.36}$$

After multiplication with $t^{2-\gamma}$, this differential equation can be rewritten to:

$$t^2 \frac{d^2 P(t)}{dt^2} + (\gamma + \alpha_T + 1)t\frac{dP(t)}{dt} + \left[(\gamma - 1)(\alpha_T + 1) + \lambda^2 t^{2-\gamma} \right] P(t) = 0 \qquad (7.37)$$

Under certain conditions, i.e. $\alpha_T \geq$-1 and $1 \leq \gamma <$2, the solution of equation 7.37 is given by a combination of Bessel functions of the first and second kind and fractional order [21, 22]:

$$P(t) = t^{\theta + \varepsilon\varsigma} \left[J_\varsigma(\frac{\lambda_n t^\varepsilon}{\varepsilon}) - \beta_n Y_\varsigma(\frac{\lambda_n t^\varepsilon}{\varepsilon}) \right] \qquad (7.38)$$

where the following substitutions are used:

$$\varsigma = \frac{|\alpha_T - \gamma + 2|}{2 - \gamma} \qquad (7.39)$$

$$\varepsilon = \frac{2 - \gamma}{2} \qquad (7.40)$$

$\theta = $-$(\alpha_T + 1)$ \qquad\qquad if α_T-γ+2$\geq$0
$\theta = 1$-γ \qquad\qquad\qquad\quad if α_T-γ+2<0 \qquad (7.41)

In most practical situations, and also in this study, α_T-γ+2 is always larger than 0, so
$\theta = $-$(\alpha_T + 1)$.

The parameters α_n, β_n, and λ_n, have to be determined from the boundary conditions (a) to (c):

(a)   The growth on the substrate is diffusion controlled, so the concentration of tin precursor, DMTC, is zero at the surface: $C(x, t_s) = 0$.
      Substitution by equations 7.34, 7.35, and 7.38 yields:

$$P(t_s) = 0 \qquad (7.42)$$

which gives for β_n:

$$\beta_n = \frac{J_\varsigma\left(\dfrac{\lambda_n t_s^\varepsilon}{\varepsilon}\right)}{Y_\varsigma\left(\dfrac{\lambda_n t_s^\varepsilon}{\varepsilon}\right)} \qquad (7.43)$$

(b) No growth takes place on the top plate, so the flux of DMTC to the top plate is zero: $N(x,1) = 0$, where the flux $N(x,t)$ is defined as:

$$N(x,t) = D_0 \frac{1-t_s}{h} t^\gamma \left[\frac{\partial C}{\partial t} + (\alpha_T + 1) \frac{C}{t} \right] \tag{7.44}$$

Substitution by equations 7.34, 7.35, and 7.38 yields:

$$\left[\frac{\partial P}{\partial t} + (\alpha_T + 1) \frac{P}{t} \right]_{t=1} = 0 \tag{7.45}$$

Substituting the derivative of $P(t)$:

$$\frac{dP(t)}{dt} = \theta t^{\theta + \varepsilon\varsigma - 1} \left[J_\varsigma \left(\frac{\lambda_n t^\varepsilon}{\varepsilon} \right) - \beta_n Y_\varsigma \left(\frac{\lambda_n t^\varepsilon}{\varepsilon} \right) \right] + \lambda_n \left[J_{\varsigma-1} \left(\frac{\lambda_n t^\varepsilon}{\varepsilon} \right) - \beta_n Y_{\varsigma-1} \left(\frac{\lambda_n t^\varepsilon}{\varepsilon} \right) \right] \tag{7.46}$$

into equation 7.45 gives eventually:

$$\beta_n = \frac{J_{\varsigma-1}\left(\dfrac{\lambda_n}{\varepsilon} \right)}{Y_{\varsigma-1}\left(\dfrac{\lambda_n}{\varepsilon} \right)} \tag{7.47}$$

The values for β_n and λ_n can be found graphically or numerically from equations 7.43 and 7.47.

(c) The entrance concentration of DMTC is equal to C_0, corrected for the entrance temperature profile: $C(0,t)=C_0/t$. Substituting equation 7.34 yields:

$$\sum_{n=1}^{\infty} \alpha_n t^{0.5(2-\alpha_T-\gamma)} \left[J_\varsigma \left(\frac{\lambda_n t^\varepsilon}{\varepsilon} \right) - \beta_n Y_\varsigma \left(\frac{\lambda_n t^\varepsilon}{\varepsilon} \right) \right] = 1 \tag{7.48}$$

The values for α_n can be found using a linear least-squares fit procedure. Assuming that for example only the first five terms have any significant contribution to the calculation of $C(x,t)$, the values of α_n can be found by using a multivariate least-squares analysis of:

$$\sum_{n=1}^{5} \alpha_n t^{0.5(2-\alpha_T-\gamma)} \left[J_\varsigma \left(\frac{\lambda_n t^\varepsilon}{\varepsilon} \right) - \beta_n Y_\varsigma \left(\frac{\lambda_n t^\varepsilon}{\varepsilon} \right) \right] = 1$$

for $t = 1$ to t_s with a step size of 0.001 in order to have a large enough number of values for the fitting procedure.

From equations 7.43, 7.47, and 7.48 the values for α_n, β_n, and λ_n are found, so the concentration profile of DMTC throughout the reactor can be calculated according to equation 7.34. The growth rate R(x) can be subsequently calculated from:

$$R(x) = N(x,t)_{t=ts}$$

Using the definition of the flux N in equation 7.44, gives:

$$R(x) = \frac{D_0 C_0}{h} \sum_{n=1}^{\infty} A_n e^{-B_n \frac{D_0}{v_0 h^2} x} \tag{7.49}$$

with:

$$A_n = \alpha_n \lambda_n \left(\frac{T_s}{T_0} - 1\right) \left(\frac{T_s}{T_0}\right)^{-0.5\alpha_T} \cdot \left[-J_{\varsigma-1}\left(\frac{\lambda_n}{\varepsilon}\left(\frac{T_s}{T_0}\right)^{\varepsilon}\right) + \beta_n Y_{\varsigma-1}\left(\frac{\lambda_n}{\varepsilon}\left(\frac{T_s}{T_0}\right)^{\varepsilon}\right) \right] \tag{7.50}$$

$$B_n = \lambda_n^2 \left(\frac{T_s}{T_0} - 1\right) \ln\left(\frac{T_s}{T_0}\right) \tag{7.51}$$

Using the inlet conditions mentioned in section 7.3.2, equation 7.49 can be used to predict the growth rate in the laminar flow reactor (LFR) shown in figure 7.2, assuming the growth is gas phase diffusion limited.
For the top plate and substrate the average temperatures are taken over the centreline of the reactor.
D_0 and γ of DMTC in N_2 are determined by fitting equation 7.29 against the values of D_{ij} obtained from equation 7.17.
The thermal diffusion factor of DMTC is determined from equation 7.30.
This results in the following conditions:

v_0 = 2.1 m/s
C_0 = $[DMTC]_0$ = 0.717 mol/m^3
H   = 0.007 m
T_0 = 695 K
T_s = 869 K
D_0 = 3.68·10^{-5} m^2/s
γ = 1.55
α_T = 0.74

Substituting these values in equations 7.43, 7.47, and 7.48 gives α_n, β_n, and λ_n. Table 7C.1 shows the values of these constants, and also for A_n and B_n for n=1 to 5.

Table 7C.1: Parameters of model 1.

n	α_n	β_n	λ_n	A_n	B_n
1	5.718	1.21	6.559	1.952	2.406
2	1.874	-2.827	20.470	2.163	23.440
3	-3.584	0.551	34.219	2.036	65.499
4	-2.469	-1.053	47.945	2.112	128.587
5	1.556	1.734	61.664	2.081	212.705

Model 2: Surface reaction limited growth.

In the case the growth rate is surface reaction limited, the same differential equation as given in 7.33, and solution, as given by 7.34-7.36, can be used. However, boundary condition (a) is different giving different values for the constants α_n, β_n, and λ_n.

If the growth would be controlled by the surface reaction rate, boundary condition (a) gives:

$$N(x,t_s) = k_1^s \cdot C(x,t_s) \tag{7.52}$$

First order kinetics is assumed with a rate constant that equals k_1 from section 7.3, but corrected for the surface-to-volume ratio, a_V, of the CSTR: $k_1^s = k_1/a_V$.

Combining equation 7.52 with equation 7.44 yields:

$$\left[\frac{dP(t)}{dt} \right]_{t=t_s} + \left(\frac{\alpha_T + 1}{t_s} + \frac{Da_{II}^s}{t_s - 1} \right) P(t_s) = 0 \tag{7.53}$$

with $Da_{II}^s = \dfrac{k_1^s(T_s) \cdot h}{D(T_s)}$, which is known as the CVD-number or the Damköhler-II number.

Substitution the derivative of P(t) into equation 7.53 gives subsequently:

$$\lambda_n t_s^{\varepsilon-1} \left[J_{\varsigma-1}\left(\frac{\lambda_n t_s^{\varepsilon}}{\varepsilon} \right) - \beta_n Y_{\varsigma-1}\left(\frac{\lambda_n t_s^{\varepsilon}}{\varepsilon} \right) \right] + \frac{Da_{II}^s}{t_s - 1}\left[J_{\varsigma}\left(\frac{\lambda_n t_s^{\varepsilon}}{\varepsilon} \right) - \beta_n Y_{\varsigma}\left(\frac{\lambda_n t_s^{\varepsilon}}{\varepsilon} \right) \right] = 0 \tag{7.54}$$

Boundary condition (b) is the same as in model 1, no growth on the top surface, and results in the same expression as 7.47:

$$\beta_n = \frac{J_{\varsigma-1}\left(\dfrac{\lambda_n}{\varepsilon}\right)}{Y_{\varsigma-1}\left(\dfrac{\lambda_n}{\varepsilon}\right)} \qquad (7.55)$$

By substituting the expression for β_n into equation 7.54, λ_n can be solved graphically or numerically, after which β_n follows from 7.55.

The values for α_n are found by the same boundary condition (c) as in model 1 again, $C(0,t)=C_0/t$:

$$\sum_{n=1}^{\infty} \alpha_n \, t^{0.5(2-\alpha_T-\gamma)}\left[J_\varsigma(\frac{\lambda_n t^\varepsilon}{\varepsilon}) - \beta_n Y_\varsigma(\frac{\lambda_n t^\varepsilon}{\varepsilon})\right] = 1 \qquad (7.56)$$

The values for α_n can be found using the same linear least–squares fit procedure as in model 1.

The growth rate is found from equation 7.52:

$$R(x) = k_1^s \, C_0 \sum_{n=1}^{\infty} \alpha_n \, X_n(x) \, P_n(t_s) \qquad (7.57)$$

with $X_n(x)$ and $P_n(T_s)$ given by:

$$X_n(x) = e^{-\lambda_n^2 (t_s-1)\ln t_s \frac{D_0}{v_0 h^2} x} \qquad (7.58)$$

$$P_n(t_s) = t_s^{-0.5 \cdot (\alpha_T+\gamma)}\left[J_\varsigma(\frac{\lambda_n t_s^\varepsilon}{\varepsilon}) - \beta_n Y_\varsigma(\frac{\lambda_n t_s^\varepsilon}{\varepsilon})\right] \qquad (7.59)$$

For determination of α_n, β_n, and λ_n, the same conditions and material properties are used as mentioned in model 1. For calculation of the surface reaction rate k_1^s, the lumped mechanism of section 7.3 is even further simplified to a single surface reaction step:

$(CH_3)_2SnCl_2 \qquad + xO_2 \qquad \rightarrow SnO_2 \qquad + \text{By-products}$
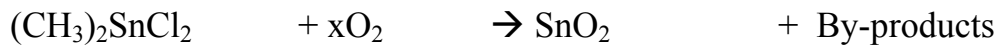
The reaction rate is equal to k_1, but modified by the surface-to-volume ratio of the CSTR.

Table 7A.2 shows the values for α_n, β_n, and λ_n for n=1 to 5.

Table 7A.2: Parameters of model 2.

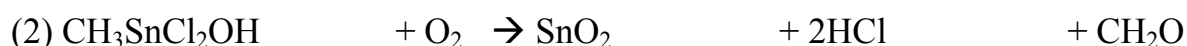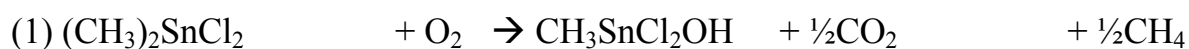| n	α_n	β_n	λ_n
1	6.320	-0.174	3.962
2	-2.439	-0.303	15.311
3	0.009	-103.621	28.321
4	0.020	-33.052	41.747
5	-0.181	1.641	55.308

Model 3: Gas phase reaction limited growth.

In the case the growth rate is gas phase reaction limited, at least two differential equations of the type of equation 7.33 have to be solved. However, in the case of a temperature gradient in the reactor, these equations prove difficult to solve. Therefore, a different approach is taken here. The temperature in the reactor is assumed to be homogeneous. In order to get a feeling of the influence of the temperature, the growth rate will be calculated for the average temperature of the top plate and the bottom plate. These values will subsequently represent the extremities, between which the "real" value will lie.

The same lumped mechanism is used to simulate the deposition rate as was used in section 7.3:

(1) $(CH_3)_2SnCl_2$ $+ O_2$ → CH_3SnCl_2OH $+ \frac{1}{2}CO_2$ $+ \frac{1}{2}CH_4$

(2) CH_3SnCl_2OH $+ O_2$ → SnO_2 $+ 2HCl$ $+ CH_2O$

In order to shorten the notations in equations this mechanism is simplified, without losing any necessary information for solving the corresponding differential equations, to:

$$A(x,y) \overset{k_1}{\leftrightarrow} B(x,y) \overset{D_B}{\leftrightarrow} B(x,0) \overset{k_2}{\leftrightarrow} SnO_2(x,0)$$
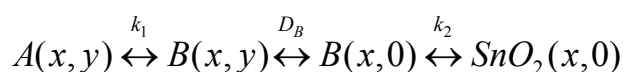
where A represents dimethyltin dichloride, and B an intermediate (such as $SnCl_2$). The rate constants k_1 and k_2 have the same values as in the lumped mechanism of section 7.3.
The difference in diffusion coefficients for A and B is assumed to be small, so $D = D_A = D_B$.
In order to obtain the growth rate for SnO_2, two differential equations of the type of 7.7 have to be solved in order to calculate the concentration profiles of A and B, respectively.

Again starting from equation 7.7 and using the geometry depicted in figure 7C.9, the differential equation for A becomes:

$$v_0 \frac{\partial A}{\partial x} = D \frac{\partial^2 A}{\partial y^2} - k_1 A \tag{7.60}$$

Using the following coordination transformation:

$$\hat{x} = \frac{D x}{v_0 h^2} \tag{7.61}$$

$$\hat{y} = \frac{y}{h} \tag{7.62}$$

and introducing the dimensionless Damköhler number:

$$Da_{II}^g = \frac{k_1 h^2}{D} \tag{7.63}$$

yields:

$$\frac{\partial A}{\partial \hat{x}} = \frac{\partial^2 A}{\partial \hat{y}^2} - Da_{II}^g A \tag{7.64}$$

Using the separation of variables method, $A(\hat{x}, \hat{y}) = X(\hat{x}) \cdot Y(\hat{y})$, and equating the resulting expression to $-\lambda^2$ gives:

$$\frac{1}{X} \frac{dX}{d\hat{x}} + Da_{II}^g = \frac{1}{Y} \frac{dY}{d\hat{y}} = -\lambda^2 \tag{7.65}$$

The solution for $X(\hat{x})$ and $Y(\hat{y})$ is given by:

$$X(\hat{x}) = e^{-(\lambda^2 + Da_{II}^g)\hat{x}} \tag{7.66}$$

$$Y(\hat{y}) = \alpha \sin(\lambda \hat{y}) - \beta \cos(\lambda \hat{y}) \tag{7.67}$$

The constant α, β, and λ can be found by applying the following boundary conditions:
-   No concentration gradients at the walls
-   The concentration of A at the entrance is A_0.
These lead to:

(a) $\left[\dfrac{\partial A}{\partial \hat{y}}\right]_{\hat{y}=0} = 0$ => $\alpha = 0$.

(b) $\left[\dfrac{\partial A}{\partial \hat{y}}\right]_{\hat{y}=1} = 0$ => $\sin(\lambda \hat{y}) = 0$ <=> $\lambda_n = n{\cdot}\pi$ with n= 0, 1,2,…

(c) $[A]_{\hat{x}=0} = A_0$ => $\displaystyle\sum_{n=0}^{\infty} \beta_n \cos(n\pi \hat{y}) = A_0$

From this last boundary condition follows that $\beta_n = 0$ for all n except n = 0. The final solution for A is:

$$A = A_0\, e^{-Da_{II}^{g}\,\hat{x}} \tag{7.68}$$

For species B an analogous differential equation as 7.64 can be stated:

$$\frac{\partial B}{\partial \hat{x}} = \frac{\partial^2 B}{\partial \hat{y}^2} + Da_{II}^{g} A \tag{7.69}$$

However the boundary conditions for B makes this equation more difficult to solve. These boundary conditions are:

(a) Only deposition on the substrate:

$$\left[\frac{\partial B}{\partial \hat{y}}\right]_{\hat{y}=0} = Da_{II}^{s} B \qquad \text{where } Da_{II}^{s} = \frac{k_2 h}{D} \tag{7.70}$$

(b) No concentration gradient near the top wall:

$$\left[\frac{\partial B}{\partial \hat{y}}\right]_{\hat{y}=1} = 0 \tag{7.71}$$

(c) No B is present at the entrance of the reactor:

$$[B]_{\hat{x}=0} = 0 \tag{7.72}$$

Due to the presence of the concentration of B in the first boundary condition, the solution is not as straightforward as 7.64, but can be found by a Laplace transformation of 7.69:

$$s \cdot \overline{B} = \frac{\partial^2 \overline{B}}{\partial \hat{y}^2} + Da_{II}^g \, \overline{A} \tag{7.73}$$

where $\overline{B}$ represents the Laplace transform of B.
Using the expression for A from 7.68, this can be rewritten to:

$$\frac{\partial^2 \overline{B}}{\partial \hat{y}^2} = s\overline{B} - \frac{Da_{II}^g \, A_0}{s + Da_{II}^g} \tag{7.74}$$

The solution of this second order ordinary differential equation is given by:

$$\overline{B} = \frac{Da_{II}^g \, A_0}{s(s + Da_{II}^g)} + \alpha' \sinh(\sqrt{s} \, \hat{y}) + \beta' \cosh(\sqrt{s} \, \hat{y}) \tag{7.75}$$

Applying boundary condition (a) yields:

$$\left[\frac{\partial \overline{B}}{\partial \hat{y}} \right]_{\hat{y}=0} = \alpha' \sqrt{s} = Da_{II}^s \cdot \left[\frac{Da_{II}^g \, A_0}{s(s + Da_{II}^g)} + \beta' \right] \tag{7.76}$$

Applying boundary condition (b) yields:

$$\left[\frac{\partial \overline{B}}{\partial \hat{y}} \right]_{\hat{y}=1} = \alpha' \sqrt{s} \cosh \sqrt{s} + \beta' \sqrt{s} \sinh \sqrt{s} = 0 \tag{7.77}$$

from which follows that:

$$\alpha' = - \beta' \tanh \sqrt{s} \tag{7.78}$$

Equations 7.76 and 7.78 can be solved simultaneously to give α' and β':

$$\alpha' = A_0 \cdot \frac{Da_{II}^g}{s(s + Da_{II}^g)} \frac{Da_{II}^s \cdot \tanh \sqrt{s}}{Da_{II}^s + \sqrt{s} \tanh \sqrt{s}} \tag{7.79}$$

$$\beta' = - A_0 \cdot \frac{Da_{II}^g}{s(s + Da_{II}^g)} \frac{Da_{II}^s}{Da_{II}^s + \sqrt{s} \tanh \sqrt{s}} \tag{7.80}$$

Substitution into 7.75 finally gives for the Laplace transform of B:

$$\overline{B} = A_0 \cdot \frac{Da_{II}^g}{s(s + Da_{II}^g)} \cdot \left[1 + \frac{Da_{II}^s \cdot \tanh\sqrt{s}}{Da_{II}^s + \sqrt{s}\,\tanh\sqrt{s}} \cdot \sinh\left(\sqrt{s}\,\hat{y}\right) - \frac{Da_{II}^s}{N_2 + \sqrt{s}\,\tanh\sqrt{s}} \cdot \cosh\left(\sqrt{s}\,\hat{y}\right) \right]$$

(7.81)

The Laplace transform of the growth rate R is given by:

$$\overline{R} = k_2 \cdot \left[\overline{B} \right]_{\hat{y}=0} = \frac{D \cdot A_0}{h} \frac{Da_{II}^g}{s(s + Da_{II}^g)} \cdot \frac{Da_{II}^s \cdot \sqrt{s}\,\tanh\sqrt{s}}{Da_{II}^s + \sqrt{s}\,\tanh\sqrt{s}}$$

(7.82)

The inverse Laplace transform is difficult to obtain. However, because k_2, and therefore N_2 is very large, $\overline{R}$ can be approximated by:

$$\overline{R} = \frac{D \cdot A_0}{h} \frac{Da_{II}^g}{s + Da_{II}^g} \frac{\tanh\sqrt{s}}{\sqrt{s}}$$

(7.83)

After inverse transformation of 8.83, the following expression for the growth rate is obtained in the case of gas phase reaction limited deposition:

$$R = 2\frac{D\,A_0}{h} \sum_{n=0}^{\infty} \left[\frac{e^{-\left(2n-\frac{1}{2}\right)^2 \cdot \pi^2 \cdot \hat{x}} - e^{-Da_{II}^g \cdot \hat{x}}}{1 - \dfrac{\left(2n - \frac{1}{2}\right)^2 \cdot \pi^2}{Da_{II}^g}} \right]$$

(7.84)

List of symbols

Roman symbols:

A: concentration of species A [mol.m^{-3}]
A_0:   concentration of species A at x=0 [mol.m^{-3}]
A_n: pre-exponential factor of growth rate [-]
B: concentration of species B [mol.m^{-3}]
B_0:   concentration of species B at x=0 [mol.m^{-3}]
B_n: exponential factor of growth rate [-]
b: width of reactor [m]

c_P: heat capacity at constant pressure [J.kg^{-1}.K^{-1}]

c: total molar concentration of the gas [mol.m^{-3}]

C_i: concentration of species i [mol.m^{-3}]

C_0: concentration at x=0 [mol.m^{-3}]

D_i^T: thermal diffusion coefficient of species i [kg.m^{-1}.s^{-1}]

D_{ij}: ordinary diffusion coefficient of species i in j [m^2.s^{-1}]

D_0: ordinary diffusion coefficient at T=T$_0$ [m^2.s^{-1}]

Da_{II}^g: dimensionless Damköhler number representing the gas phase reaction rate-to-diffusion ratio [-]

Da_{II}^s: dimensionless Damköhler number representing the surface reaction rate-to-diffusion ratio [-]

ΔE_r: radiative energy transport [W.m^{-2}]

h: height of reactor [m]

H_i: enthalpy of species i [J.mol^{-1}]

k_B: Boltzmann's constant [1.38·10^{-23} J.K^{-1}]

k_i: reaction rate of reaction i [s^{-1}]

I: unit tensor [-]

j_i: diffusive mass flux of species i [kg.m^{-2}.s^{-1}]

J_ζ: Bessel function of the first kind of fractional order ζ [-]

M_i: molecular mass of species i [kg.mol^{-1}]

M: average molecular mass [kg.mol^{-1}]

N: molar mass flux [mol.m^{-2}.s^{-1}]

p: pressure [Pa]

$\vec{q}$: molecular heat transport vector [W.m^{-2}]

R_{ik}: reaction rate of species i in reaction k [mol.m^{-3}.s^{-1}]

R: growth rate of tin oxide [mol.m^{-2}.s^{-1}]

s: Laplace coordinate [-]

S_i: entropy of species i [J.mol^{-1}.K^{-1}]

t: time [s]

t: normalised temperature [-]

t_s: normalised temperature of the substrate [-]

T: temperature [K]

T_c: critical temperature [K]

T_s: temperature of the substrate [K]

T_0: temperature of the top plate [K]

$\vec{v}$: velocity vector [m.s^{-1}]

v_0: plug flow velocity [m.s^{-1}]

v_T: plug flow velocity corrected for the thermal gradient [m.s^{-1}]

V_c: critical volume [m^3]

x: axial coordinate [m]

$\hat{x}$: dimensionless coordinate transform of x [-]

x_i: mole fraction of species i [-]

y: vertical coordinate [m]

$\hat{y}$:   dimensionless coordinate transform of y [-]

Y_ζ: Bessel function of the second kind of fractional order ζ [-]

Greek symbols:

α_T: thermal diffusion factor [-]
α_n: pre-exponential factor [-]
α':   constant of equation [-]
β_n: pre-exponential factor [-]
β':   constant of equation [-]
ε: Lennard-Jones interaction energy [J]
ε: help parameter $(=(2-\gamma)/2)$
γ: coefficient of temperature dependence of D [-]
θ: help parameter $(=-(\alpha_T+1)$ in most practical cases)
η: viscosity [Pa.s]
κ: dilatational viscosity [Pa.s]
λ: mean free path [m]
λ: thermal conductivity $[W.m^{-1}.K^{-1}]$
λ, λ_n: roots of equation [-]
ν: stoichiometric coefficient
ρ: density $[kg.m^{-3}]$
σ: collision diameter [m]
σ: Lennard-Jones collision diameter [m]
τ: viscous stress tensor $[N.m^{-2}]$
ϕ: Lennard-Jones interaction potential [J]
ζ: help parameter $(=|\alpha_T-\gamma+2|/(2-\gamma))$
ω_i: mass fraction of species i [-]
Ω_D: collision integral for diffusion [-]

Chapter 8. Conclusions

The goals of this thesis, as formulated in section 1.4, were to develop a working mechanism for the deposition of tin oxide from dimethyltin dichloride (DMTC), oxygen, and water, and subsequently use this mechanism to simulate two lab scale reactors.

As was shown in chapter 2, little was known up till 2002 about the chemistry behind tin oxide deposition. The main reason is the complexity of the process, as is schematically depicted in figure 1.2.

This complexity manifests itself again in the development of a mechanism for DMTC, O_2, and H_2O. The first step in both the decomposition as well as the oxidation of DMTC is the cleavage of the tin carbon bond. This results in the formation of methyl radicals. In the presence of oxygen, a whole avalanche of propagation reactions follows in the C-H-O range. Reaction kinetics of this subset of reactions can be taken from the combustion literature. Reaction kinetics involving Cl-C-O-H can be taken from studies of stratospheric phenomena. However, little is known of reactions involving Sn-containing species, both experimentally and theoretically. Therefore, it has proven very difficult to compose a complete reaction mechanism with kinetics of the individual elementary reaction steps.

However, studying the composition of the gas phase during deposition, gave great insight into the mechanism. Decomposition of DMTC results in $SnCl_2$, CH_4, and some higher order carbon species. No HCl was found, suggesting that Sn-Cl is a strong bond, which does not break on its own. When oxygen is present it is believed that $SnCl_2$ acts as an intermediate in the gas phase, and converts to tin oxide on the surface by reacting with surface-OH.

In the presence of water, the mechanism becomes even more complex. *Ab-initio* calculations showed that $SnCl_2$ can form complexes with water, suggesting that different intermediates form, which will convert to tin oxide on the surface.

Using gravimetric measurements it was possible to determine the overall reaction kinetics of tin oxide deposition from DMTC and O_2. Assuming the rate-limiting step is in the gas phase, a lumped two-step mechanism is suggested, which is used to simulate two types of lab-scale reactors. The simulations were carried out with Fluent®, a computational fluid dynamics package, and compared with experimental results. These results were also compared with analytical solutions, which are based on some crude assumptions.

The first reactor is based on stagnant point flow and can be modelled in only two dimensions because of the presence of a symmetry axis. This same reactor was also used in an experimental set-up, to get a direct comparison between the simulation and experimental results.

The second reactor is based on laminar flow between two plane-parallel plates. It is modelled in three dimensions. Both reactors were simulated the lumped two step reaction mechanism, and including thermal diffusion effects. The growth rates predicted are in good agreement with experiments, thereby enhancing the validity of the chemical mechanism proposed.

The laminar flow reactor was also subjected to an analytical analysis in order to clearly show the difference in growth rate behaviour in the case of (1) diffusion limited growth, (2) surface reaction rate limited growth, and (3) gas phase reaction limited growth. As expected, in cases (1) and (2) the growth rate decreases over the length of the reactor. For a gas phase reaction limited process the growth rate reaches its maximum at the end of the reactor. The Fluent$^{®}$ simulation (and experimental trend) falls exactly between analytical solutions for a similar isothermal reactor with temperatures of, respectively, the average top plate and average substrate temperature.

This thesis describes only the first steps in understanding the complicated mechanism of tin oxide precursors. Much more work will be necessary to construct a mechanism, which will really capture all the aspects of the tin oxide system. Some examples of these aspects are the direct reaction of water with DMTC (or MBTC or TTC) or with tin intermediates such as $SnCl_2$, the influence of addition of a fluor species for doping the tin oxide layer, and the influence of methanol, which is added to the precursor mixture in commercial reactors.

These aspects can not only be investigated purely from experiments, but use has to be made from theoretical methods such as *ab-initio* and RRKM calculations.

Even more important is the role of the surface in the mechanism, more specifically what type of surface reactions are taking place and what is their importance? This last aspect will be a real challenge in the future as both experimental and theoretical methods are still under development for studying elementary reaction steps on the surface.

Dankwoord

Dit proefschrift is het resultaat van vijf jaar van experimenteren, schrijven, discussiëren, mopperen, lachen, etc. Gelukkig heb ik in die tijd voldoende hulp gehad om deze jaren tot een goed einde te brengen en het proefschrift te maken dat nu voor U ligt. De mensen die me geholpen hebben, ben ik dan ook zeer dankbaar.

In het bijzonder wil ik bedanken Mart de Croon en Karel Spee, die de afgelopen jaren mijn mentors zijn geweest. De conferentie in Boston met het bijbehorende bezoek aan Cheers zullen we niet snel vergeten. Het in goede banen leiden van de totstandkoming van het proefschrift is gedaan door mijn promotor Jaap Schouten, wie ik dan ook veel dank verschuldigd ben. Ik ben deze mensen ook zeer erkentelijk dat ze zo geduldig met me zijn geweest. Het heeft even geduurd voordat het boekje af was.

Bij het experimentele werk heb ik gelukkig hulp gehad van een aantal studenten met wie ik zeer prettig gewerkt heb. Mijn dank gaat uit naar Danny de Klijn, Andries Habraken, Armand Bergsma, Suzanne Steins, Ross Archer en Fred Catseman.

Een speciale plaats wil ik reserveren voor Greg Alcott, waarmee ik ook na zijn Marie Curie-grant heel plezierig heb samengewerkt. Niet alleen in het lab, maar ook in de AOR en op de kermis.

Het werk beschreven in dit proefschrift is uitgevoerd bij TNO TPD en ik ben mijn collegae veel dank verschuldigd voor hun hulp. Vooral in mijn eerste jaar heb ik veel ervaring opgedaan over de experimentele kant van CVD. Hans Linden en Gerwin Kirchner hebben me geleerd hoe met VCR, Swagelok, massaspectrometers, etc. om te gaan. Maar niet alleen zij, ook mijn andere collegae hebben me experimenteel of moreel ondersteund in deze periode en daarna. Dus Elma, Petra, Johan K., Klaas, Henny, Roelant, Joost D., Han, Jan, Joost v. E, Hans M., Johan Z., Cor, Peter, Serge, Jurgen, Ivo, Miranka, Frank en Leo: bedankt!

Ik heb de eer en het plezier gehad om onder de afdelingshoofden Dick en daarna Ando te werken. Zij hebben me de ruimte gegeven om mijn proefschrift te voltooien.

In het bijzonder wil ik Zeger Vroon noemen, die mijn "kruiwagen" was en zonder wie ik misschien hier niet was terechtgekomen.

This work was part of a Brite Euram project and I am indebted to all the partners in this project, especially I want to thank Martin Davies, Martin Pemble (University of Salford), David Sheele, Deborah Raisbeck, Helen Sanders, Juan Rivero (Pilkington), Wulf Grählert, Volkmar Hopfe (Fraunhofer IWS), and Andreas Beil (Bruker) for a very pleasant collaboration.

Although my work at Sandia National Laboratories has not been included in this thesis, I am grateful to Mark Allendorf and Tony McDaniel for my very enjoyful

stay in California. Their valuable insights helped me to interpret some of my experimental results.

Ter afsluiting wil ik mijn familie en Elle bedanken. Hun vertrouwen en geduld waren een absolute voorwaarde om dit boekje tot stand te brengen. Mijn ouders hebben me altijd gesteund, zowel tijdens mijn studie als mijn promotie ondanks mijn soms "wilde haren". Elle wil ik speciaal bedanken voor haar liefde en begrip tijdens de afgelopen vijf jaar. Haar energie en onvoorwaardelijke steun hebben me door de moeilijke "laatste loodjes" geholpen

Curriculum Vitae

Antonius Maria Bernardus van Mol is geboren op 23 september 1972 in Eindhoven. In 1990 behaalde hij zijn Atheneumdiploma aan het Anton van Duinkerkencollege in Veldhoven. In datzelfde jaar begon hij de studie Scheikundige Technologie aan de Technische Universiteit Eindhoven. Begin 1997 behaalde hij zijn ingenieursdiploma met lof na een voltooiing van zijn afstudeerproject "Sintering behaviour and properties of barium aluminum oxynitrides with the β-alumina structure" bij de Vakgroep Vaste Stof en Materiaalchemie.

Direct na zijn afstudeerperiode begon hij aan zijn promotieproject bij de afdeling Coatingtechnologie van TNO TPD onder supervisie van prof.dr.ir. J.C. Schouten. Dit werk was onderdeel van het Brite Euram project "Improve CVD process control by spectroscopic in-situ monitoring tools", en resulteerde uiteindelijk in dit proefschrift. Na zijn promotieperiode van vier jaar, is hij in 2001 bij TNO gaan werken. Na gewerkt te hebben aan de ontwikkeling van atmosferische druk plasmatechnologie, is hij van januari tot juni 2002 gedetacheerd geweest bij Sandia National Laboratories (VS) onder leiding van Dr. M.D. Allendorf. Hier werkte hij aan de chemie en kinetiek van tinoxide CVD vanuit MBTC. Na terugkomst bij TNO werd hij projectleider voor TNO van het Helianthos project. In dit project werken verschillende universiteiten, TNO, en Akzo-Nobel/Shell Solar samen om een roll-to-roll pilot lijn te ontwikkelen voor de produktie van flexibele zonnecellen.

List of publications

A.M.B. van Mol, M.H.J.M. de Croon, C.I.M.A. Spee, J.C. Schouten, "Kinetic mechanism of the decomposition of dimethyltin dichloride", *J. Phys. IV France*, **9**, PR8-165 (1999).

A.M.B. van Mol, G.R. Alcott, M.H.J.M. de Croon, C.I.M.A. Spee, J.C. Schouten, "Kinetic study of the chemical vapour deposition of tin oxide: reactor design", *Proceedings of the 2nd ICCG*, 178 (1999).

G.R. Alcott, A.M.B. van Mol, C.I.M.A. Spee, "Evaluation of chemometric models in an FTIR study of the gas phase during atmospheric pressure CVD of tin oxide thin films", *Adv. Mat.: CVD*, **6**, 261 (2000).

A.M.B. van Mol, G.R. Alcott, M.H.J.M. de Croon, C.I.M.A. Spee, J.C. Schouten, "Evaluation of precursors for the chemical vapour deposition of tin oxide", *Proceedings of the 197th Electrochemical Society – Chemical Vapor Deposition XV*, Toronto May 2000, 765 (2000).

A.M.B. van Mol, R. Archer, M.H.J.M. de Croon, C.I.M.A. Spee, J.C. Schouten, "Kinetic study of the chemical vapour deposition of tin oxide from dimethyltin dichloride and oxygen", *Proceedings of the 3rd ICCG*, 301 (2000).

A.M.B. van Mol, R. Archer, M.H.J.M. de Croon, C.I.M.A. Spee, J.C. Schouten. "Kinetic Study of the chemical vapour deposition of tin oxide from various precursors", *Proceedings of the 3rd ICCG*, 379 (2000).

A.M.B. van Mol, S.J.B. Steins, M.H.J.M. de Croon, C.I.M.A. Spee, J.C. Schouten. "Modelling of chemical vapour deposition of tin oxide in a cold conveyor belt reactor", *Proceedings of the 3rd ICCG*, 381 (2000).

A.M.B. van Mol, J.P.A.M. Driessen, J.L. Linden, M.H.J.M. de Croon, C.I.M.A. Spee, J.C. Schouten, "Vapor Pressures of precursors for the CVD of titanium nitride and tin oxide", *Adv. Mat: CVD*, **7**, 101 (2001).

V. Hopfe, D.W. Sheel, D. Raisbeck, J.M. Rivero, W. Graehlert, O. Throl, A.M.B. van Mol, C.I.M.A. Spee, "NIR diode laser based process control for industrial CVD reactors", *Proceedings of the thirteenth European Conference on Chemical Vapor Deposition*, Pr3-1153 (2001).

M. D. Allendorf, A.H. McDaniel, A. M. B. Van Mol, "Decomposition of Monobutyltintrichloride in a High Temperature Flow Reactor: Rate constants and Product Formation", *Proceedings of the 4th ICCG*, 195 (2002).

M. D. Allendorf, I. B. Nielsen, C. F. Melius, A. M. B. Van Mol, "Thermodynamics and Reaction Pathways in the Decomposition, Oxidation, and Hydrolysis of Monobutyltintrichloride", *Proceedings of the 4th ICCG*, 231 (2002).

C.I.M.A. Spee, A.M.B. van Mol, J. Zijp, Y.L.M. Creyton, A. Fiala, M.P. de Goeje, "Review on atmospheric plasma deposition technology", *Proceedings of the 4th ICCG*, 161 (2002).

J.L.Linden, A.M.B. van Mol, C.P.G.Schrauwen, R.Groenen, M.C.M. van de Sanden, A.D.Kuypers, "Property control of transparent conducting oxides", *Proceedings 46th Annual SVC Technical Conference*, (2003).

M. D. Allendorf, I. B. Nielsen, C. F. Melius, A. M. B. Van Mol, "Thermodynamics and Reaction Pathways in the Decomposition, Oxidation, and Hydrolysis of Monobutyltintrichloride", *Proceedings of Chemical Vapour Deposition XVI and EuroCVD 14*, 55 (2003).

A.M.B. van Mol, M. D. Allendorf, "Decomposition, Oxidation, and Hydrolysis of Monobutyltintrichloride", *Proceedings of Chemical Vapour Deposition XVI and EuroCVD 14*, 65 (2003).

A.M.B. van Mol, F. Grob, K. Spee, K. van der Werf, R. Schropp, "Comparison of Photovoltaic Performance of SnO2:F coated substrates made using APCVD with different precursors", *Proceedings of Chemical Vapour Deposition XVI and EuroCVD 14*, 408 (2003).

M.D. Allendorf, A.M.B. van Mol. "Gas-Phase Thermochemistry and Mechanism of Organometallic Tin Oxide Precursors" *To be published as a chapter in "Topics in Inorganic Chemistry"* (2003).

A.M.B. van Mol, M.H.J.M. de Croon, J.C. Schouten. "Comparison of analytical and CFD models for the chemical vapour deposition of tin oxide", *To be published in AIChE* (2004).